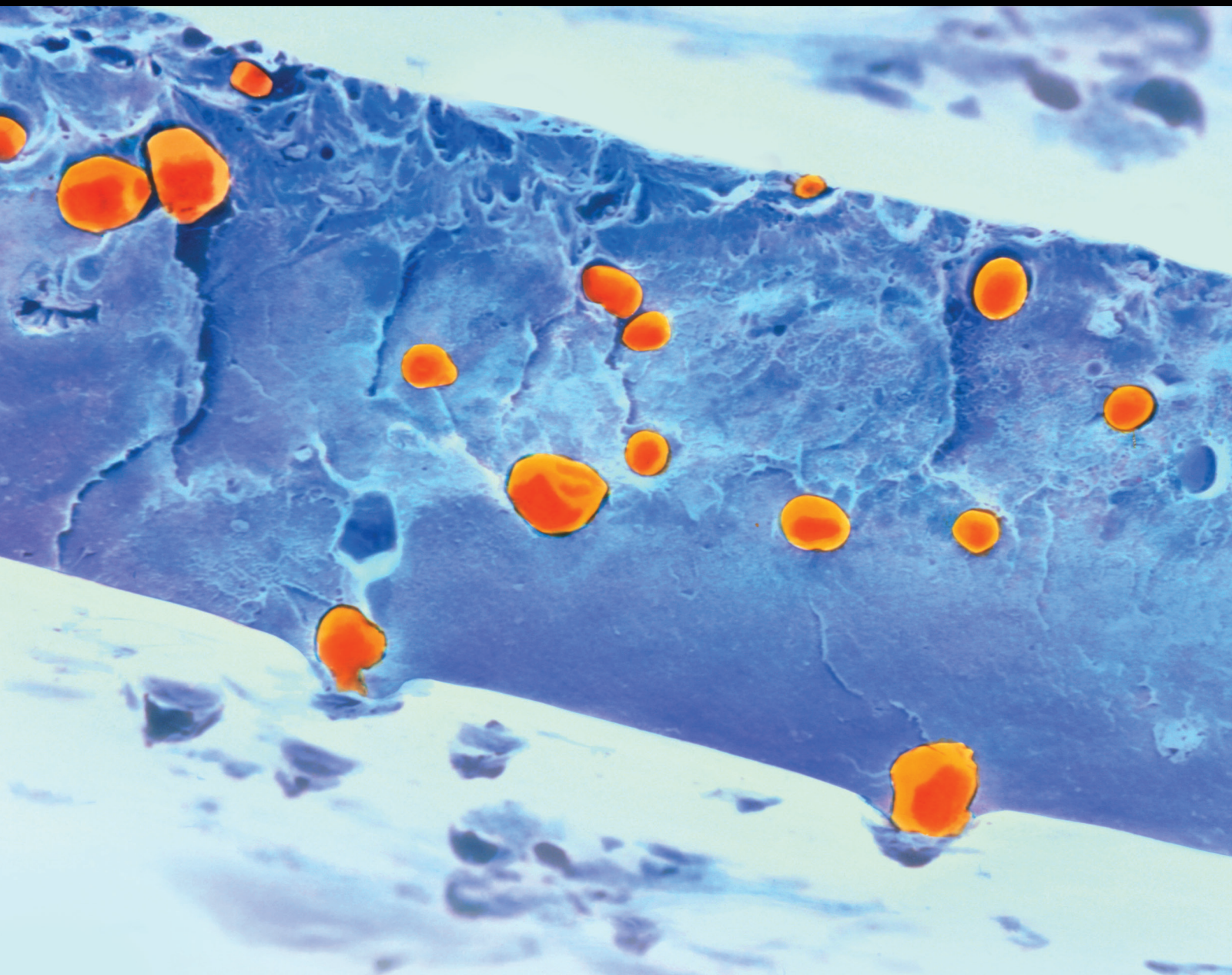


International Journal of Polymer Science

Fibre Reinforced Polymer Composites for Structural Applications in Construction

Lead Guest Editor: Jun Deng

Guest Editors: Marcus M. K. Lee, Baolin Wan, and Giuseppina Amato





Fibre Reinforced Polymer Composites for Structural Applications in Construction

International Journal of Polymer Science

Fibre Reinforced Polymer Composites for Structural Applications in Construction

Lead Guest Editor: Jun Deng

Guest Editors: Marcus M. K. Lee, Baolin Wan,
and Giuseppina Amato



Copyright © 2017 Hindawi. All rights reserved.

This is a special issue published in "International Journal of Polymer Science." All articles are open access articles distributed under the Creative Commons Attribution License, which permits unrestricted use, distribution, and reproduction in any medium, provided the original work is properly cited.

Editorial Board

Domenico Acierno, Italy
Sharif Ahmad, India
Luc Averous, France
M. Barletta, Italy
Christopher Batich, USA
Marc Behl, Germany
Filippo Berto, Norway
Laurent Billon, France
Andrea Camposeo, Italy
Wen Shyang Chow, Malaysia
Yoshiki Chujo, Japan
Angel Concheiro, Spain
Marek Cypryk, Poland
Li Ming Dai, USA
Yulin Deng, USA
Maria Laura Di Lorenzo, Italy
Eliane Espuche, France
Antonio Facchetti, USA
M. Fernández-García, Spain
Benny Dean Freeman, USA
J.-F. Gérard, France
Peng He, USA
Jan-Chan Huang, USA
Wei Huang, China
Nabil Ibrahim, Egypt

Tadashi Inoue, Japan
Patric Jannasch, Sweden
Nobuhiro Kawatsuki, Japan
J.M. Kenny, Italy
M. A. Khan, Bangladesh
Ruhul A. Khan, Canada
Saad Khan, USA
Jui-Yang Lai, Taiwan
Jose Ramon Leiza, Spain
Evangelos Manias, USA
Ulrich Maschke, France
Jani Matisons, Australia
G. R. Mitchell, UK
Subrata Mondal, India
Christian Nielsen, UK
Toribio F. Otero, Spain
Alessandro Pegoretti, Italy
Önder Pekcan, Turkey
Zhonghua Peng, USA
Antje Potthast, Austria
Debora Puglia, Italy
Miriam H. Rafailovich, USA
Arthur J. Ragauskas, USA
Subramaniam Ramesh, Malaysia
Bernabé L. Rivas, Chile

Juan Rodriguez-Hernandez, Spain
Hossein Roghani-Mamaqani, Iran
Mehdi Salami-Kalajahi, Iran
Erol Sancaktar, USA
A. P. H. J. Schenning, Netherlands
Markus Schmid, Germany
Matthias Schnabelrauch, Germany
Shu Seki, Japan
Vitor Sencadas, Australia
R. A. Shanks, Australia
B. Siddaramaiah, India
Atsushi Sudo, Japan
Hideto Tsuji, Japan
Stefano Turri, Italy
Hiroshi Uyama, Japan
Cornelia Vasile, Romania
Alenka Vesel, Slovenia
De-Yi Wang, Spain
Qinglin Wu, USA
Frederik Wurm, Germany
Huining Xiao, Canada
Yiqi Yang, USA
Michele Zappalorto, Italy

Contents

Fibre Reinforced Polymer Composites for Structural Applications in Construction

Jun Deng, Marcus M. K. Lee, Baolin Wan, and Giuseppina Amato
Volume 2017, Article ID 9218529, 1 page

Prestress Loss of CFL in a Prestressing Process for Strengthening RC Beams

Xinyan Guo, Dong Liu, Peiyan Huang, and Xiaohong Zheng
Volume 2017, Article ID 3832468, 11 pages

Bond-Slip Behavior of Basalt Fiber Reinforced Polymer Bar in Concrete Subjected to Simulated Marine Environment: Effects of BFRP Bar Size, Corrosion Age, and Concrete Strength

Yongmin Yang, Zhaoheng Li, Tongsheng Zhang, Jiangxiong Wei, and Qijun Yu
Volume 2017, Article ID 5156189, 9 pages

Study on Axial Compressive Capacity of FRP-Confined Concrete-Filled Steel Tubes and Its Comparisons with Other Composite Structural Systems

Jun Deng, Yifeng Zheng, Yi Wang, Tonghua Liu, and Hui Li
Volume 2017, Article ID 6272754, 7 pages

Combined Effects of Curing Temperatures and Alkaline Concrete on Tensile Properties of GFRP Bars

Wen-rui Yang, Xiong-jun He, Kai Zhang, Yang Yang, and Li Dai
Volume 2017, Article ID 4262703, 8 pages

Bond-Slip Models for FPR-Concrete Interfaces Subjected to Moisture Conditions

Justin Shrestha, Dawei Zhang, and Tamon Ueda
Volume 2017, Article ID 4031565, 14 pages

Fatigue Crack Propagation Behavior of RC Beams Strengthened with CFRP under High Temperature and High Humidity Environment

Dongyang Li, Peiyan Huang, Guang Qin, Xiaohong Zheng, and Xinyan Guo
Volume 2017, Article ID 1247949, 11 pages

Mechanical Properties of Steel-FRP Composite Bars under Tensile and Compressive Loading

Zeyang Sun, Yu Tang, Yunbiao Luo, Gang Wu, and Xiaoyuan He
Volume 2017, Article ID 5691278, 11 pages

Experimental Study on Bond Behavior of FRP-Concrete Interface in Hygrothermal Environment

X. H. Zheng, P. Y. Huang, X. Y. Guo, and J. L. Huang
Volume 2016, Article ID 5832130, 12 pages

Effect of Chloride on Tensile and Bending Capacities of Basalt FRP Mesh Reinforced Cementitious Thin Plates under Indoor and Marine Environments

Yan Xie, Kunhua Guan, and Lin Lai
Volume 2016, Article ID 7162313, 7 pages

Mechanical Behavior and Chloride Penetration of Precracked Reinforced Concrete Beams with Externally Bonded CFRP Exposed to Marine Environment

Yan Xie, Kunhua Guan, Lei Zhan, and Qichen Wang
Volume 2016, Article ID 1790585, 8 pages

Effect of Temperature Variation on Bond Characteristics between CFRP and Steel Plate

Shan Li, Tao Zhu, Yiyang Lu, and Xiaojin Li

Volume 2016, Article ID 5674572, 8 pages

Discussion of a Coupled Strength Attenuation Model for GFRP Composites in Hydrothermal Environments

Wei Chen, Yongxin Yang, and Biao Li

Volume 2016, Article ID 4258729, 6 pages

Investigation of Mechanical Properties of Basalt Particle-Filled SMC Composites

Kadir Cavdar and Mahmut Bingol

Volume 2016, Article ID 1231606, 6 pages

Editorial

Fibre Reinforced Polymer Composites for Structural Applications in Construction

Jun Deng,¹ Marcus M. K. Lee,² Baolin Wan,³ and Giuseppina Amato⁴

¹*Guangdong University of Technology, Guangzhou, China*

²*Curtin University Sarawak, Miri, Malaysia*

³*Marquette University, Milwaukee, WI, USA*

⁴*Queen's University Belfast, Belfast, UK*

Correspondence should be addressed to Jun Deng; jdeng@gdut.edu.cn

Received 28 May 2017; Accepted 28 May 2017; Published 2 July 2017

Copyright © 2017 Jun Deng et al. This is an open access article distributed under the Creative Commons Attribution License, which permits unrestricted use, distribution, and reproduction in any medium, provided the original work is properly cited.

In recent years, advanced fibre reinforced polymer (FRP) composites have become increasingly popular following the rapid growth in structural applications in construction around the world. These high-performance materials have been utilized in construction both for new structures and for strengthening/rehabilitation of existing buildings and bridges. Despite their widespread use, their full potential has still not been realized because of a number of fundamental concerns including high material costs, durability issues, bonding integrity, long-term interaction between loading and damage, and so forth. This special issue is aimed at providing a platform for the dissemination and discussion of recent research and achievements which address the issues on this topic from the theoretical and practical viewpoints.

A total of 13 original research papers were published in this special issue. These papers deal with materials and products, bond behavior, strengthening of concrete structures, and durability. Six papers focus on the mechanical and durability performances of FRP materials and products including BFRP bars, GFRP bars, steel-FRP bars, BFRP mesh, GFRP sheets, and basalt particle-filled SMC composites. Three papers report investigations on bond behavior of both FRP-concrete and FRP-steel after environmental exposure. Two more papers deal with prestressing systems designed to strengthen reinforced concrete beams and concrete-filled steel tubes and especially the prestress loss and bearing capacity. Theoretical and experimental studies on the durability behavior of FRP strengthened reinforced concrete beams

subjected to fatigue loading and hygrothermal environment are reported in two papers as well.

These recent theoretical and experimental investigations that have been disseminated in this special issue address some critical fundamental issues, especially the long-term performance of both the FRP materials and strengthened structures. We expect that this special issue will be of interest to both researchers and engineers and contribute toward the developments in FRP applications in construction.

Acknowledgments

We greatly appreciate all the authors for their contributions and reviewers for their constructive comments and suggestions.

*Jun Deng
Marcus M. K. Lee
Baolin Wan
Giuseppina Amato*

Research Article

Prestress Loss of CFL in a Prestressing Process for Strengthening RC Beams

Xinyan Guo,¹ Dong Liu,¹ Peiyan Huang,^{1,2} and Xiaohong Zheng¹

¹School of Civil Engineering and Transportation, South China University of Technology, Guangzhou 510640, China

²State Key Laboratory of Building Science, South China University of Technology, Guangzhou 510640, China

Correspondence should be addressed to Xinyan Guo; xyguo@scut.edu.cn and Peiyan Huang; pyhuang@scut.edu.cn

Received 29 September 2016; Revised 13 January 2017; Accepted 20 April 2017; Published 9 May 2017

Academic Editor: Giuseppina Amato

Copyright © 2017 Xinyan Guo et al. This is an open access article distributed under the Creative Commons Attribution License, which permits unrestricted use, distribution, and reproduction in any medium, provided the original work is properly cited.

A prestressing system was designed to strengthen reinforced concrete (RC) beams with prestressed carbon fiber laminate (CFL). During different prestressing processes, prestress loss was measured using strain gauges attached on the surface of CFL along the length direction. The prestress loss was 50–68% of the whole prestress loss, which is typically associated with CFL slipping between the grip anchors. Approximately 20–27% of the prestress loss was caused by the elastic shortening of the RC beam. An analytical model using linear-elastic theory was constructed to calculate the prestress loss caused by CFL slipping between the anchors and the elastic shortening of the strengthened beams. The compared results showed that the analytical model of prestress loss can describe the experimental data well. Methods of reducing the prestress loss were also suggested. Compared to other experiments, the prestressing system proposed by this research group was effective because the maximum percentage of prestress loss was 14.9% and the average prestress loss was 12.5%.

1. Introduction

The application of bonded fiber-reinforced polymer (FRP) to the surfaces of concrete members provides an efficient, lightweight, and noncorrosive alternative to other repair methods. Although bonding nonprestressed FRP to reinforced concrete (RC) members can increase their ultimate bearing capacity, only a portion of the strength of FRP is utilized in nonprestressed strengthening systems. Furthermore, nonprestressed FRP strengthening techniques do not significantly change the cracking load of RC members. Compared to nonprestressed strengthening techniques, prestressing FRP can close cracks, delay the opening of new cracks, and restore prestress to a system that has suffered a loss of internal prestressing [1].

Currently, there are three prestressing systems that have been proposed for FRP strengthening technology. One method indirectly prestressed FRP sheets by cambering the flexural member [2]. Using this method, the levels of prestress generated in the FRP plate or sheet were low. The second method applied direct tension to FRP by jacking against an

external reaction frame [3]. The prestressed FRP was bonded to an RC member with epoxy. When the epoxy resin was cured, the prestressing system was released. If the prestress level was high, additional anchoring was needed to be provided. The third method involved prestressing FRP by reacting it directly on a RC member [4]. A permanent mechanical anchorage system was fixed to the RC member, and the FRP sheets were prestressed directly by jacking and reacting against the RC member. After reaching the required prestress force, the movable anchors were locked, and the prestressed FRP sheets were bonded to the surface of the RC member.

For the first and second kinds of prestressing systems, in the prestressing process, after releasing the prestressed FRP plate, sheet, or laminate, high interfacial shear stress would be generated at two ends of the FRP and would result in the FRP debonding. In the third method, because wave-shape grip anchors were directly installed on the strengthened beam, no high interfacial shear stress occurred. There were two arrangements on the end of the prestressed FRP before it was cut at both ends of the RC members. One was bolt anchorage [5]. The anchor bolts were fixed on the RC member to fasten

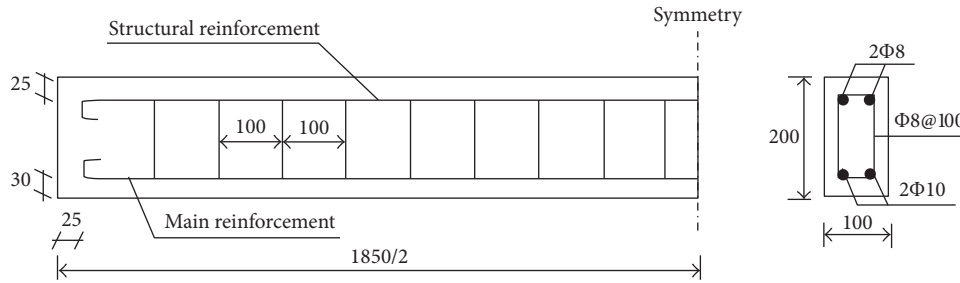


FIGURE 1: Steel bars used in an RC beam.

the FRP. The second arrangement was wrapping FRP around the RC member.

During the process of applying prestress to the plate, sheet, or laminate and bonding the prestressed FRP to an RC member, initial prestress loss was always generated [6, 7]. Importantly, the actual prestress resulted when the external forces were released. However, currently, studies on prestress loss are limited. Garden and Holloway [8] carried out an experimental study on strengthening RC beams using prestressed FRP plates. The plates were bonded with prestress levels ranging from 25% to 50% of the strength of the FRP plate. Prestressing was achieved using the second method described above and the nonanchored arrangement on the ends of the FRP plate. During the process of applying prestress to the plate and bonding the prestressed FRP plate to the RC beams, the prestress loss was influenced by the size of RC beams and the prestress level of the FRP applied. El-Hacha et al. [2] used the third prestressing system described above to prestress FRP. The FRP composite materials used included CFRP plates and CFRP sheets, and the prestress levels ranged from 15% to 30% and 50% of the strength of the FRP plate. The percentages of prestress loss were recorded as ranging from 13.4% to 46.64%. Diab et al. [9] utilized the second prestressing system to investigate rectangular beams bonded to prestressed FRP sheets, including anchored or unanchored FRP sheet ends. Using different layers of FRP sheet, the prestress levels of the FRP sheets varied from 21% to 40% of the tensile strength. The strains of the FRP sheets were measured when the FRP sheets were cut at both ends. Quantrill and Holloway [3] carried out an experiment on strengthening RC beams using prestressed FRP plates with prestress levels ranging from 21.7% to 46.3% of their strength. The percentages of prestress loss were recorded as ranging from 26% to 40%.

The prestress losses identified above were large, and long-term prestress loss was not measured.

Moreover, although the bolt anchorage arrangement can reduce shear stress and prestress loss [10], it to some extent caused damage to the RC members because some predrilled holes were used to fix the anchor bolts. It is important to choose a prestressed FRP strengthening method that does not cause secondary damage to concrete structures and determine the short- and long-term prestress loss laws of strengthened concrete members. In this paper, an experimental study was carried out to investigate the short- and long-term prestress loss law using the second prestressing system

described above and the FRP wrapping arrangement at the ends of FRP. The results were compared to those reported by other researchers using different prestressing system and different arrangement on the ends of FRP.

2. Experimental Program

2.1. Test Materials and Specimens. A total of fifteen specimens were designed for this study. The typical geometry and reinforcement of the tested beams are shown in Figure 1. The size of the RC beams was 1850 mm length \times 100 mm width \times 200 mm height. The composition proportion of concrete was $m_c : m_w : m_s : m_a = 1.0 : 0.5 : 2.06 : 3.66$ (cement : water : sand : gravel). The cube compressive strength and the elastic modulus of the concrete were 53.3 MPa and 35.2 GPa, respectively. The main steel bars exhibited a yield strength of 307 MPa and an elastic modulus of 206 GPa. In this paper, the RC beams were strengthened with prestressed carbon fiber laminate (CFL) [11] as the specimens. The CFL used in this paper was knitted by unidirectional carbon fiber silk and epoxide resin, which possessed the combined advantages of carbon fiber sheets and plates. The size and thickness of CFL can be determined and knitted according to the project requirements and reduce the effect of multilayer bonding. The elastic modulus of the CFL was 230 GPa with an ultimate tensile strength of 4750 MPa. The width of CFL was 100 mm, and the normal thickness was 0.23 mm. The adhesive used between concrete and CFL was A and B epoxy adhesive. The thickness of the A and B epoxy adhesive layer was in total approximately 0.2 mm, and most of the adhesive penetrated into the concrete. The shear strength of the epoxy adhesive was 14 MPa.

In total, 15 beams were divided into three groups based on the three different levels of prestress applied to CFL. Each group consisted of five strengthened beams. The three groups were strengthened by CFL with the prestress levels of 8%, 15%, or 22% with the CFL wrapping arrangement on the ends of CFL.

2.2. Prestressing System. A prestressing system for stretching CFL and strengthening RC beams was designed and constructed by our research group as shown in Figures 2 and 3. In this prestressing system, CFL was placed between two movable wave-shape grip anchors. The target RC beam was positioned under the prestressing bed. The prestressing system consisted of a stiff steel frame, movable wave-shape

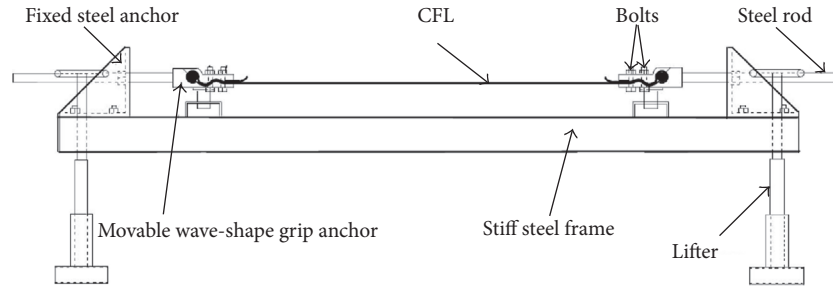


FIGURE 2: Bed of the prestressing system.



FIGURE 3: Photo of prestressing system.

grip anchor, fixed steel anchor, steel rod, and hydraulic jack. One roller and two wave-shape steels were set up in the movable wave-shape grip anchor. CFL was wrapped around the roller, and the two wave-shape steels were fastened by four bolts. The fixed steel anchors were welded to the end of frame to prevent any possible bending due to prestressing. The steel rods were inserted through the holes in both the movable wave-shape grip anchor and the fixed steel anchor and used at the jacking end. The CFL was prestressed by jacking and reacting against the stiff steel frame. The tensile loads and strains of CFL were measured by load cells and strain gauges attached along the length of the CFL. The lifter was used to adjust the height of the prestressing bed. It should be noted that the dimensions of all components of the anchorage system were based on finite-element analysis and several tests.

2.3. Prestressing and Bonding of CFL. The method of strengthening RC beams with prestressed CFL is illustrated in Figure 4 and summarized as follows:

- (1) The concrete surface was prepared using a sander to remove the cement cover and cleaned with acetone. Then, the beam was positioned near the prestressing bed.
- (2) The prestressing bed was hoisted to enable easy operation. The CFL was placed between the movable

wave-shape grip anchors, and the bolts were used to fasten the grip anchors.

- (3) By pumping oil into the hydraulic jack, the movable wave-shape grip anchors moved forward in the direction of the fixed steel anchor and exerted tensile force on CFL. CFL was prestensioned to 2.4% of its strength, and the loose nut was rotated until it locked the movable anchor in place. The bolts on the movable anchor were fastened to reduce the gap of the anchor, and then the loose nut was rotated opposite direction to release the prestressing load. The operating step is shown in Figure 4(a)
- (4) A and B epoxy adhesive was brushed on the surface of the beam with a spatula as shown in Figure 4(b).
- (5) The CFL was prestressed again, and the movable anchor was locked when the tensile load reached the desired prestressing force. In this study, three prestress levels (8%, 15%, and 22%) were used.
- (6) The RC beam was moved under the prestressing bed as shown in Figure 4(c).
- (7) The lifter was lowered down, and the prestressed CFL was bonded to the surface of the concrete. CFL was wrapped and bonded to the two ends of the strengthened RC beam as shown in Figure 4(d). After 5–7 days of curing time, the applied prestress was gradually alleviated by releasing the hydraulic jacks, and then the CFLs were cut at both ends.

The whole procedure of the prestressing and bonding of CFL was divided into four steps: tension, bonding, curing, and release.

2.4. Strain Measurement. Before loading the prestressing force, strain gauges were attached on the middle and quarter of CFL in the length direction. To monitor the effect of CFL wrapping, 28 strain gauges were attached near the corner of the wrap before the prestressing force was released. The distribution of the strain gauges on the CFL wrapping is shown in Figure 5. The strain gauges on the prestressed CFL and CFL wrapping were connected to a data acquisition system to measure and record the strains during the whole prestressing process.

The details of the experimental conditions are shown in Table 1.

TABLE 1: Measuring results for the strains of CFL ($\mu\epsilon$).

| Specimen | Initial strain | Prestress levels | Strain loss | | | | | Total strain loss (proportion) |
|----------|----------------|------------------|-----------------------------|-----------------------------|----------------------------|-----------------------------|------------------------|--------------------------------|
| | | | During tension (proportion) | During bonding (proportion) | During curing (proportion) | During release (proportion) | Long-term (proportion) | |
| PB-8-1 | 1566 | 8% | -140 (-8.9%) | 55 (3.5%) | -43 (-2.7%) | -41 (-2.6%) | -34 (-2.2%) | -203 (-13.0%) |
| PB-8-2 | 1597 | 8% | -146 (-9.1%) | 63 (3.9%) | -51 (-3.2%) | -58 (-3.6%) | -42 (-2.6%) | -234 (-14.7%) |
| PB-8-3 | 1569 | 8% | -120 (-7.6%) | 56 (3.6%) | -48 (-3.1%) | -50 (-3.2%) | -52 (-3.3%) | -214 (-13.6%) |
| PB-8-4 | 1533 | 8% | -98 (-6.4%) | 58 (3.8%) | -44 (-2.9%) | -37 (-2.4%) | -39 (-2.5%) | -160 (-10.4%) |
| PB-8-5 | 1599 | 8% | -154 (-9.6%) | 67 (4.2%) | -49 (-3.1%) | -50 (-3.1%) | -53 (-3.3%) | -239 (-14.9%) |
| PB-15-1 | 2908 | 15% | -209 (-7.2%) | 52 (1.8%) | -67 (-2.3%) | -73 (-2.5%) | -53 (-1.8%) | -350 (-12.0%) |
| PB-15-2 | 2932 | 15% | -190 (-6.5%) | 65 (2.2%) | -81 (-2.8%) | -91 (-3.1%) | -67 (-2.3%) | -364 (-12.4%) |
| PB-15-3 | 2970 | 15% | -214 (-7.2%) | 62 (2.1%) | -62 (-2.1%) | -82 (-2.8%) | -62 (-2.1%) | -358 (-12.1%) |
| PB-15-4 | 3060 | 15% | -235 (-7.7%) | 69 (2.2%) | -83 (-2.7%) | -94 (-3.1%) | -73 (-2.4%) | -416 (-13.6%) |
| PB-15-5 | 2931 | 15% | -190 (-6.5%) | 55 (1.9%) | -55 (-1.9%) | -77 (-2.6%) | -50 (-1.7%) | -317 (-10.8%) |
| PB-22-1 | 4313 | 22% | -280 (-6.5%) | 49 (1.1%) | -59 (-1.4%) | -110 (-2.6%) | -95 (-2.2%) | -495 (-11.5%) |
| PB-22-2 | 4386 | 22% | -320 (-7.3%) | 65 (1.5%) | -82 (-1.9%) | -128 (-2.9%) | -69 (-1.6%) | -534 (-12.1%) |
| PB-22-3 | 4389 | 22% | -327 (-7.5%) | 71 (1.6%) | -94 (-2.1%) | -133 (-3.0%) | -68 (-1.5%) | -551 (-12.6%) |
| PB-22-4 | 4357 | 22% | -268 (-6.2%) | 53 (1.2%) | -63 (-1.4%) | -121 (-2.8%) | -99 (-2.3%) | -498 (-11.4%) |
| PB-22-5 | 4368 | 22% | -291 (-6.7%) | 73 (1.7%) | -91 (-2.1%) | -148 (-3.4%) | -76 (-1.7%) | -533 (-12.2%) |

Note. In the name of each specimen, PB means prestressed beam, the first number is the prestress level, and the second number is a serial number.

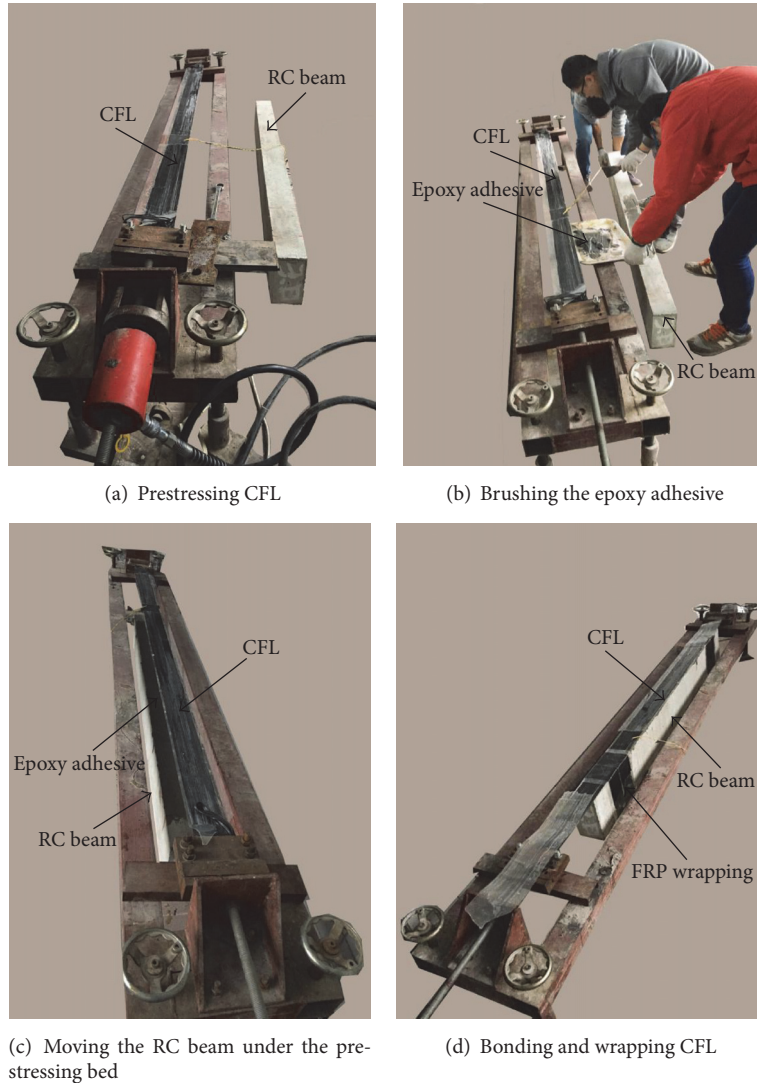


FIGURE 4: Strengthening method with prestressed CFL for RC beams.

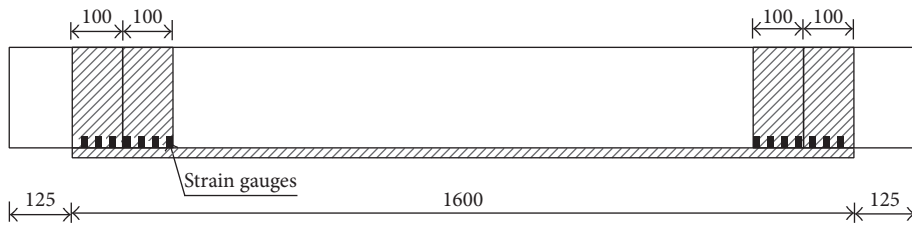


FIGURE 5: CFL wrapping and strain gauges.

3. Experimental Results and Discussions

After releasing the prestressed CFL, the prestressing force was transferred to the RC beam. The experimental investigation includes the short-term and long-term behavior of the bonding performance of prestressed CFL. Typically, the short-term was defined as immediate responses of CFL when

the prestressing force was transferred, and the long-term behavior included those up to 30 days.

The strain measurement results used for calculating the prestress loss of CFL are shown in Table 1.

3.1. *Prestress Loss during Tension.* As shown in Table 1, prestress loss was significant during the prestressing process.

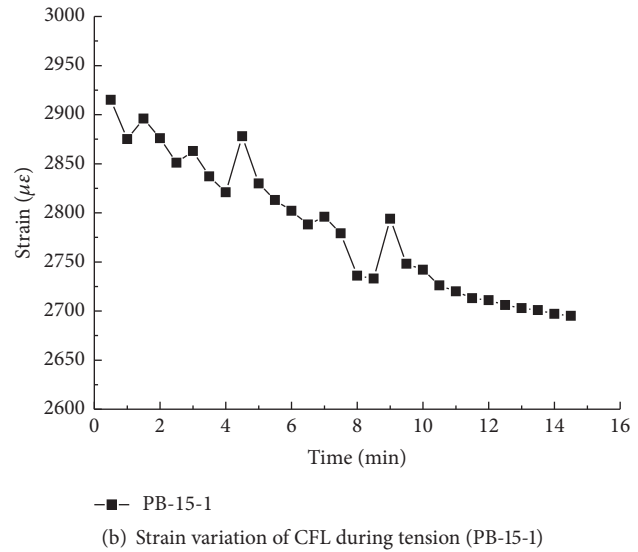
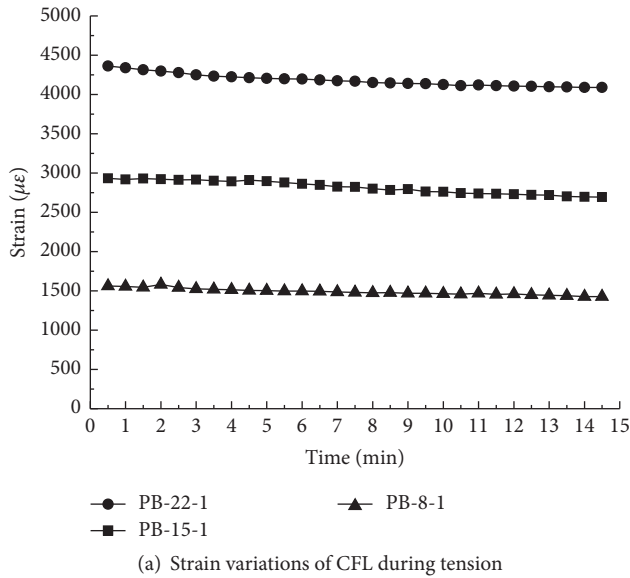


FIGURE 6: Strain variations of CFL during tension.

There were two main reasons that caused the noticeable prestress loss. One was deflection of the anchor when the hydraulic jack was released from the steel rod. The second was CFL slipping between the movable wave-shape grip anchors.

Figure 6(a) shows the changes in strain on CFL during the application of tension. Three groups of specimens were strengthened by CFL with the prestress levels of 8%, 15%, and 22%. The strain variation of CFL on specimen PB-15-1 is plotted in Figure 6(b). As shown in Table 1 and Figure 6, the prestress loss during tension was higher when the CFL was tensioned at a higher prestress level, but the relative prestress loss decreased as the prestress level increased.

3.2. Prestress Increase during Bonding. When the loading reached the desired prestressing force, the lifter was lowered and the prestressed CFL was bonded to the surface of the RC beam. During bonding, downward forces were applied to CFL to ensure that it bonded closely, which led to an increase in strain increment of prestressed CFL. During the test, the lifter was lowered down, and the CFL was moved as close to the surface of beam as possible. The strain increment was not relevant to the prestress levels and was influenced by the thickness of layer of epoxy adhesive between the CFL and the surface of the beam. The strain variation of CFL on specimen PB-15-1 is plotted in Figure 7.

3.3. Prestress Loss during Curing. After 5–7 days, the epoxy adhesive between the prestressed CFL and the surface of the RC beam was cured. The prestress loss during curing was caused by slipping between the CFL and the movable wave-shape grip anchor. The strain loss increased slightly as the prestress level increased and was generated during the first 10 hours of the curing process. The strain changes on CFL during the curing are shown in Figure 8.

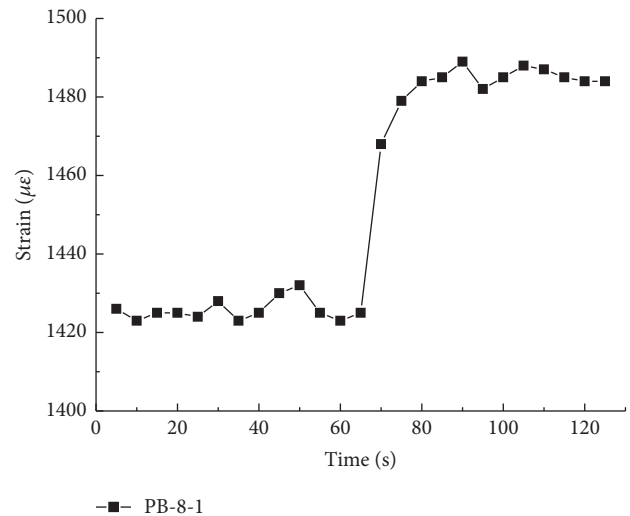


FIGURE 7: Strain variation of CFL during bonding.

3.4. Prestress Loss during Release. The last step of the prestressing operation was releasing the prestressing system. During the release, the applied prestress was gradually alleviated by releasing the hydraulic jacks, and then the CFL was cut at both ends. After releasing the prestressed CFL, the prestressing force was transferred to the RC beam. The prestress loss during the releasing step was caused by the elastic shortening of the RC beam, and the strain changes in CFL during this step under the three different prestress levels (8%, 15%, and 22%) are shown in Figure 9(a). The strain variation of CFL on the specimen PB-15-1 during the release is plotted in Figure 9(b). As shown in Table 1 and Figure 9, the prestress loss during the release step was higher when the CFL

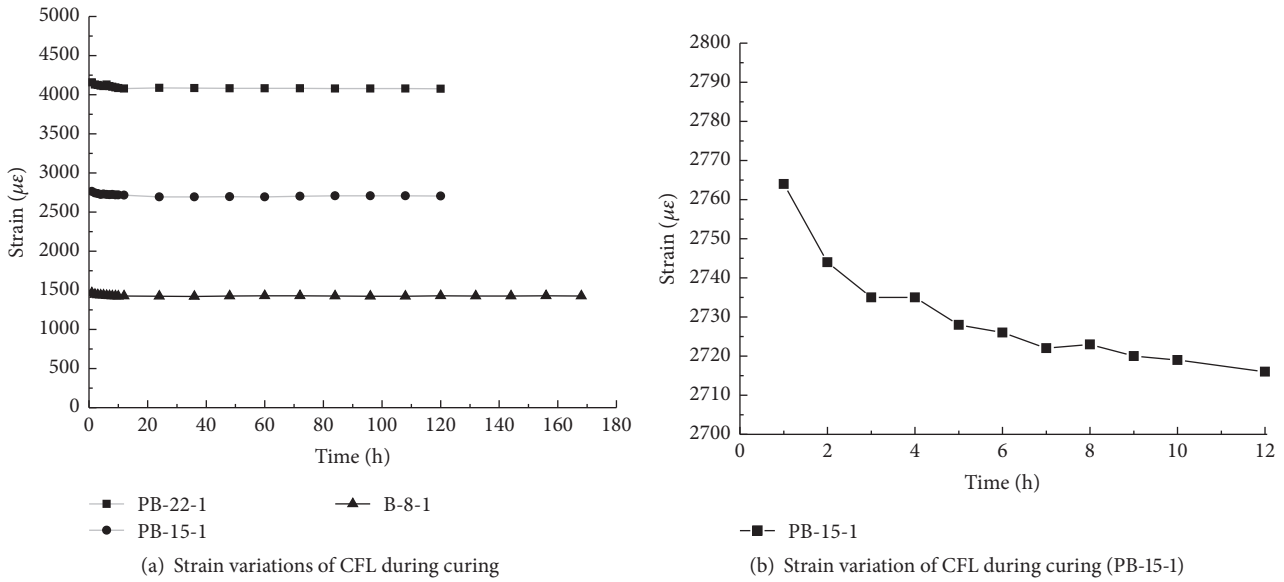


FIGURE 8: Strain variations of CFL during curing.

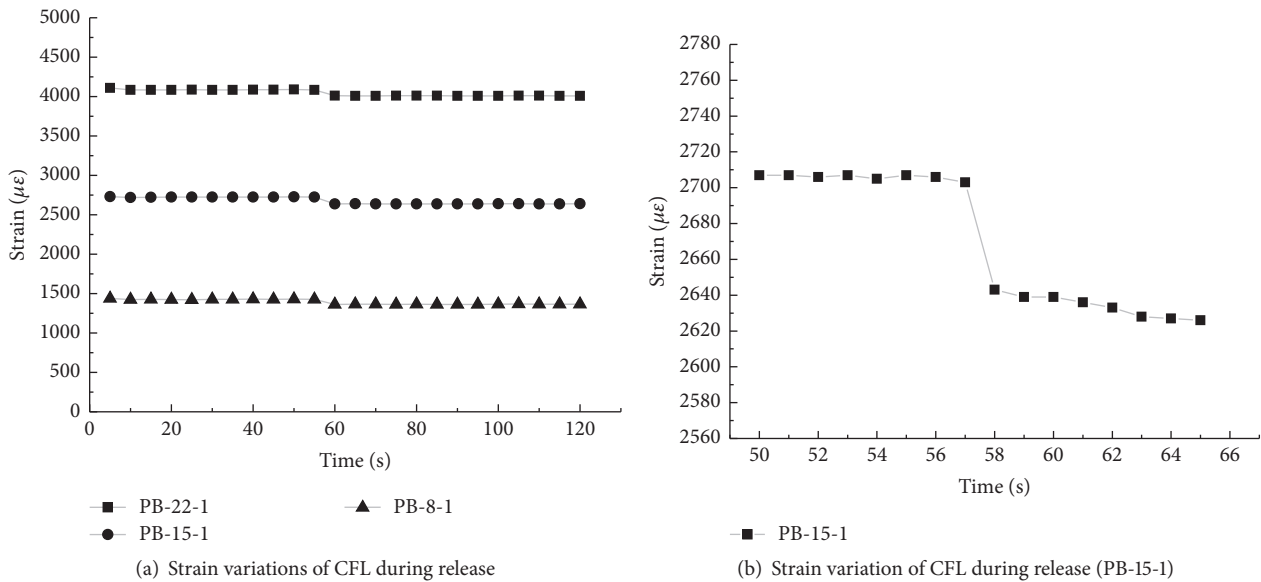


FIGURE 9: Strain variations of CFL during release.

was tensioned with a higher prestress level, but the relative prestress loss decreased as the prestress level increased.

3.5. Long-Term Prestress Loss. After release, the strain gauges on CFL were still connected to the data acquisition system to continue recording the strain. The monitoring periods were 21 and 30 days. The prestress loss in the long term was still due to the elastic shortening of the RC beam, as shown in Figure 10(a), with the three prestress levels (8%, 15%, and 22%). The strain variation of CFL on the specimen PB-15-1 during the first day is plotted in Figure 10(b). As shown in Table 1 and Figure 10, the prestress loss in the long term was

slightly higher when the CFL was tensioned with a higher prestress level and generated during the first 5 days.

3.6. Strains on CFL Wrapping. After releasing the hydraulic jacks and cutting CFL at both ends, the maximum strain on the CFL wrapping was approximately $160 \mu\epsilon$, which was obtained at the end of the CFL in the length direction (Figure 5). The strain on the CFL wrapping gradually decreased when the strain gauge was far from the end of the CFL in the length direction. At a distance of 125 mm from the end of the CFL in the length direction, the strain on the CFL wrapping was zero.

TABLE 2: Prestress loss by predictions and measurements during tension.

| Specimens | Prestress levels/% | $\Delta l_1/\text{mm}$ | Predicted prestress loss/MPa | Measured prestress loss/MPa | Relative errors/% |
|-----------|--------------------|------------------------|------------------------------|-----------------------------|-------------------|
| PB-8 | 8 | 0.4 | 34.28 | 33.17 | 1.033 |
| PB-15 | 15 | 0.6 | 51.43 | 50.16 | 1.025 |
| PB-22 | 22 | 0.8 | 69.57 | 68.66 | 1.013 |

Note. PB-8 are prestressed-CFL-strengthened RC beams with 8% prestress level.

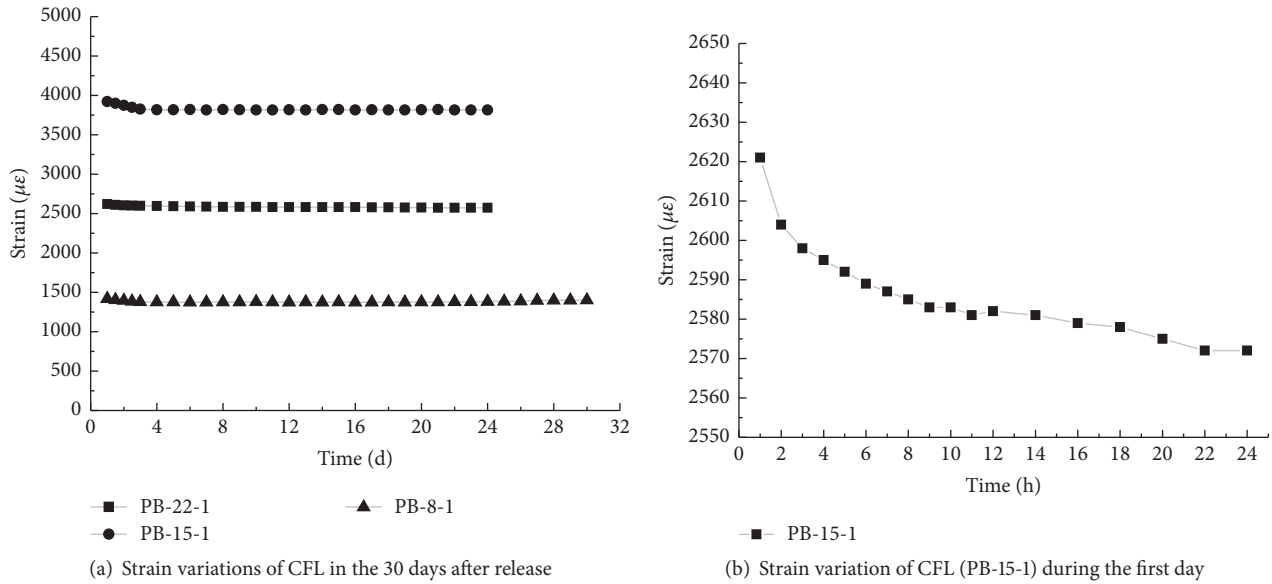


FIGURE 10: Long-term strain variations of CFL after release.

4. Analytical Model of Prestress Loss

As shown in Table 1, during the process of applying prestress to CFL and bonding the prestressed CFL to RC beams, the majority of prestress loss was caused by CFL slipping between the movable wave-shape grip anchors and the elastic shortening of the RC beam. Between these two, the prestress loss caused by the CFL slip was 50–68% of the whole prestress loss, while 20–27% of the whole prestress loss was caused by the elastic shortening of the RC beam. Therefore, it was necessary to calculate the prestress loss caused by the CFL slip during tension and elastic shortening of the RC beam after releasing.

4.1. Calculation of Prestress Loss during Tension. Before loading the prestress force, CFL was wrapped around the roller and sandwiched between the movable anchors. Four bolts were tightened to provide frictional resistance to the anchor. During the tension, CFL slipping was caused by a small amount of deformation of the prestressing bed and the gap between the two anchors.

Considering the above causes, which would lead to prestress loss of CFL, and based on the code of (JTG

D62-2012) [12], the prestress loss during tension, $\sigma_{l\text{slip}}$ (MPa), can be calculated as follows:

$$\sigma_{l\text{slip}} = \frac{\Delta l_1 \cdot E_{\text{cf}}}{l}, \quad (1)$$

where Δl_1 , E_{cf} , and l are the slip deformation during tension, the elastic modulus of CFL, and the distance between the two fixed steel anchors, respectively. The total deformation during tension was a combination of the CFL slip and deformation of the prestressing bed. The CFL slip value was influenced by several factors, such as the friction coefficient between the CFL and the anchor, the bolt pressure on the anchor, and the area between the CFL and the anchor.

The code of (JTG D62-2012) suggests that if the prestressed material is steel, the value of Δl_1 is taken as 1 mm. Because prestressed CFL displays little elongation, the value of Δl_1 was taken as 0.2–1 mm, depending on the prestress level.

In the tests, the distance of two fixed steel anchors l was measured as 2800 mm. The elastic modulus of CFL (E_{cf}) was 230 GPa. Substituting these parameters into formula (1) allows the prestress loss of CFL during tension to be calculated. The comparison of the calculated results to the experimental data is shown in Table 2 and revealed that

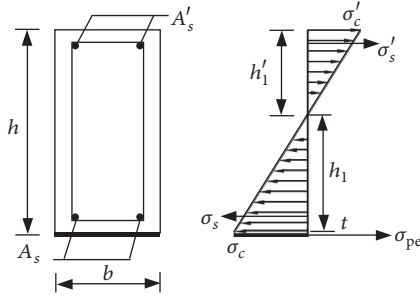


FIGURE 11: Stress distribution on cross-section of the RC beam after releasing.

the predicted values for prestress loss and measured values coincided well. The relative errors were approximately 1%.

To reduce the prestress loss caused by CFL slipping and deformation of the anchor system, some measures should be taken: (1) increasing the friction coefficient between CFL and the anchor; (2) applying pretension to CFL at 2-3% of its strength before loading the prestress force and rotating the loose nut until it locks the movable anchor in place; (3) fastening the bolts on the movable anchor to reduce the gap of the movable anchor and the prestress loss; and (4) increasing the rigidity of the prestressing bed and anchor system.

4.2. Calculation of Prestress Loss after Releasing. The following derivation of the prestress loss caused by elastic shortening of the RC beam was made for a beam with typical rectangular cross-section, but the method of this analysis is also applicable to any beam with arbitrary cross-sections and material properties, providing the same assumption holds.

When prestressed CFL was bonded on a RC beam and the epoxy resin was cured for several days, the prestress force was released and CFL was cut at both ends. After the release, the RC beam was assumed to be linear elastic. Figure 11 shows a stress distribution on a cross-section of an RC beam strengthened with prestressed CFL after release. The equilibrium requires that

$$\begin{aligned} \sigma_{pe} A_{cf} + \int_0^{h'_1} \frac{\sigma'_c}{h'_1} b x dx + \sigma'_s A'_s + \int_{-h_1}^0 \frac{\sigma_c}{h_1} b x dx \\ - \sigma_s A_s = 0 \\ \sigma_{pe} A_{cf} \left(h_1 + \frac{t}{2} \right) - \int_0^{h'_1} \frac{\sigma'_c}{h'_1} b x^2 dx - \sigma'_s (h'_1 - a) A'_s \\ - \int_{-h_1}^0 \frac{\sigma_c}{h_1} b x^2 dx - \sigma_s (h_1 - a) A_s = 0, \end{aligned} \quad (2)$$

where σ_c and σ'_c are the tensile and compressive stress of concrete; σ_s and σ'_s are the tensile and compressive stress of a steel bar; σ_{pe} is the effective stress of CFL after releasing the prestress force; h_1 and h'_1 are the height of the tensile and compressive parts of the beam; t is the computed thickness of CFL; b and h are width and height of the beam; A_s and A'_s are the cross-sectional areas of tensile and compressive steel bars;

a is the thickness of the concrete protective cover, and A_{cf} is the cross-sectional area of CFL.

Considering the compatibility of stress distribution, the normal stress of the steel bar and concrete can be obtained as follows:

$$\begin{aligned} \sigma'_s &= \sigma'_c \frac{h'_1 - a}{h'_1} \frac{E_s}{E_c} \\ \sigma_s &= \sigma_c \frac{h_1 - a}{h_1} \frac{E_s}{E_c} \\ \frac{\sigma'_c}{\sigma_c} &= \frac{h'_1}{h_1} = \beta, \end{aligned} \quad (3)$$

where E_s and E_c are the elastic modulus of the steel bar and concrete, respectively. Let

$$\alpha_E = \frac{E_s}{E_c}. \quad (4)$$

If the thickness of CFL, t , is assumed to be negligible in comparison to the height of the strengthened beam, the effective stress of CFL, σ_{pe} , can be found as follows:

$$\sigma_{pe} = \frac{\sigma_c}{A_{cf}} \left[\frac{bh}{2} (1 - \beta) + \alpha_E A_s \left(1 - \frac{1 + \beta}{h} a \right) \right]. \quad (5)$$

Thus, the prestress loss, σ_{ls} , caused by the elastic shortening of the RC beam was

$$\sigma_{ls} = \sigma_{pf} - \sigma_{pe}, \quad (6)$$

where σ_{pf} is the prestress on CFL before release.

Considering the compatibility of deformation, the reduction strain of CFL, $\Delta \epsilon_{pf}$, is assumed to be

$$\Delta \epsilon_{pf} = \Delta \epsilon_c, \quad (7)$$

where

$$\begin{aligned} \Delta \epsilon &= \frac{\sigma_c}{E_c} \\ \Delta \epsilon_{pf} &= \frac{\sigma_l}{E_{cf}}, \end{aligned} \quad (8)$$

where $\Delta \epsilon_c$ is the strain increment of concrete; E_{cf} is the elastic modulus of CFL; and E'_c is the equivalent elastic moduli of concrete and steel.

$$E'_c = E_s \mu + E_c (1 - \mu), \quad (9)$$

where μ is the reinforcement ratio of the concrete beam.

$$\mu = \frac{A_s + A'_s}{bh}. \quad (10)$$

From (5) to (10), the ratio (σ_l/σ_{pf}) of prestress loss caused by elastic shortening of the RC beam to the prestress on CFL

TABLE 3: Prestress loss by predictions and experiments after releasing.

| Authors | Size of RC beam/mm | E_c /GPa | E_s /GPa | E_{cf} /GPa | t /mm | σ_{pf} /MPa | σ_l/σ_{pf} | |
|----------------------------|--------------------|------------|------------|---------------|---------|--------------------|----------------------------|---------------------|
| | | | | | | | Calculating values by (11) | Experimental values |
| Quantrill and Hollaway [3] | 1000 × 100 × 100 | 34 | 220 | 135 | 1.3 | 221.13 | 8.3% | 7.1% |
| | | | | | | 343.44 | 8.3% | 9.5% |
| This paper | 1850 × 100 × 200 | 35.2 | 206 | 230 | 0.23 | 380.0 | 2.1% | 3.0% |
| | | | | | | 712.5 | 2.1% | 2.8% |
| | | | | | | 1045.0 | 2.1% | 2.9% |

before release can be obtained by the equation

$$\frac{\sigma_l}{\sigma_{pf}} = \frac{t\lambda}{t\lambda + (h/2)(1 - \beta) + (\alpha_E A_s/b)(1 - ((1 + \beta)/h)a) - (\alpha_E A'_s/b)(\beta - ((1 + \beta)/h)a)}, \quad (11)$$

where $\lambda = E_{cf}/E_c$.

To verify the analytical model (11), the experimental data obtained by Quantrill and Hollaway [3] and the experimental results of this paper were analyzed and listed in Table 3.

The comparison between the two showed that the analytical model of prestress loss caused by the elastic shortening of the RC beam after release was in good agreement with the experimental data. However, it should be noted that error may be created by assumptions. In the derivation, the mechanical properties of all materials of the strengthened beam were assumed to be linear elastic. If the initial prestress was higher, then the concrete might show plastic behavior, thus requiring the model derived in this paper to be modified. The error was also influenced by strain measure. The CFL used in this paper was knitted by unidirectional carbon fiber silk and epoxide resin. The force on the CFL was not even absolutely during prestressing procedure. The assumptions and the strain measure were the main causes of the error between the calculating and experimental values.

5. Conclusions

A prestressing system for strengthening RC beams with prestressed CFL was designed. Prestress loss of CFL in the prestressing process of strengthened RC beams was measured. The results of this study were analyzed, and the following conclusions were obtained:

- (1) Prestress loss was measured during the whole prestressing test. The measured results showed that maximum prestress loss of CFL was 14.9% and that the majority of prestress loss was caused by CFL slipping between the movable wave-shape grip anchors and the elastic shortening of the RC beam. The prestress loss caused by the CFL slip between the grip anchors was 50–68% of the whole prestress loss, while 20–27%

of the whole prestress loss was caused by the elastic shortening of the RC beam.

- (2) An analytical model for calculating the prestress loss was established. The results showed that the calculated prestress loss caused by elastic shortening of the RC beam after releasing was in good agreement with the experimental data. The initial prestress was found to have a great effect on the prestress loss caused by the elastic shortening of the RC beam after release, but the ratio (σ_l/σ_{pf}) of prestress loss caused by elastic shortening of the RC beam to the initial prestress was constant.
- (3) A prestressing system and prestress loss measuring method were designed and constructed. Comparing these to other systems and measurement methods of prestress loss of RC members strengthened with CFL showed that the proposed prestressing system and prestress loss measuring method were more effective and convenient.

It should be noted that the RC beam was assumed to be linear elastic and all materials behaved linearly elastically in the analytical model. If the initial prestress was higher, then the concrete would behave plastically, and the model would have to be modified.

Conflicts of Interest

The authors declare that they have no conflicts of interest.

Acknowledgments

The project is supported by the National Natural Science Foundation of China (nos. 11627802, 51678249, 11132004, and 51508202) and Natural Science Foundation of Guangdong Province (no. 2016A030310414).

References

- [1] R. G. Wight, M. F. Green, and M.-A. Erki, "Prestressed FRP sheets for poststrengthening reinforced concrete beams," *Journal of Composites for Construction*, vol. 5, no. 4, pp. 214–220, 2001.
- [2] R. El-Hacha, R. G. Wight, and M. F. Green, "Prestressed fibre-reinforced polymer laminates for strengthening structures," *Progress in Structural Engineering and Materials*, vol. 3, pp. 111–121, 2001.
- [3] R. J. Quantrill and L. C. Hollaway, "The flexural rehabilitation of reinforced concrete beams by the use of prestressed advanced composite plates," *Composites Science and Technology*, vol. 58, no. 8, pp. 1259–1275, 1998.
- [4] R. El-Hacha and M. Y. E. Aly, "Anchorage system to prestress FRP laminates for flexural strengthening of steel-concrete composite girders," *Journal of Composites for Construction*, vol. 17, no. 3, pp. 324–335, 2013.
- [5] Q. Cao, J. Tao, and Z. J. Ma, "Prestress loss in externally FRP reinforced self prestressing concrete beams," *Construction and Building Materials*, vol. 101, pp. 667–674, 2015.
- [6] W.-W. Wang, J.-G. Dai, K. A. Harries, and Q.-H. Bao, "Prestress losses and flexural behavior of reinforced concrete beams strengthened with posttensioned CFRP sheets," *Journal of Composites for Construction*, vol. 16, no. 2, pp. 207–216, 2012.
- [7] I. Costa and J. Barros, "Prestress losses in nsm-cfrp flexurally strengthened rc beams," *Strain*, vol. 51, no. 4, pp. 276–287, 2015.
- [8] H. N. Garden and L. C. Hollaway, "An experimental study of the failure modes of reinforced concrete beams strengthened with prestressed carbon composite plates," *Composites Part B: Engineering*, vol. 29, no. 4, pp. 411–424, 1998.
- [9] H. Diab, Z. Wu, and K. Iwashita, "Short and long-term bond performance of prestressed FRP sheet anchorages," *Engineering Structures*, vol. 31, pp. 1241–1249, 2009.
- [10] A. Abdullah, C. G. Bailey, and Z. J. Wu, "Tests investigating the punching shear of a column-slab connection strengthened with non-prestressed or prestressed FRP plates," *Construction and Building Materials*, vol. 48, pp. 1134–1144, 2013.
- [11] Y. P. Huang and J. C. Zeng, "Carbon fiber laminate and its application," China Patent Administration, 2006.
- [12] JTG D62-2012: Code for design of highway reinforce concrete and prestressed concrete bridges and culverts. Beijing, China, 2012.

Research Article

Bond-Slip Behavior of Basalt Fiber Reinforced Polymer Bar in Concrete Subjected to Simulated Marine Environment: Effects of BFRP Bar Size, Corrosion Age, and Concrete Strength

Yongmin Yang,^{1,2} Zhaoheng Li,^{1,2} Tongsheng Zhang,¹ Jiangxiong Wei,¹ and Qijun Yu¹

¹School of Materials Science and Engineering, South China University of Technology, Guangzhou 510640, China

²Guangdong Research Institute of Water Resources and Hydropower, Guangzhou 510635, China

Correspondence should be addressed to Qijun Yu; concyuq@scut.edu.cn

Received 23 September 2016; Revised 7 January 2017; Accepted 22 February 2017; Published 26 March 2017

Academic Editor: Baolin Wan

Copyright © 2017 Yongmin Yang et al. This is an open access article distributed under the Creative Commons Attribution License, which permits unrestricted use, distribution, and reproduction in any medium, provided the original work is properly cited.

Basalt Fiber Reinforced Polymer (BFRP) bars have bright potential application in concrete structures subjected to marine environment due to their superior corrosion resistance. Available literatures mainly focused on the mechanical properties of BFRP concrete structures, while the bond-slip behavior of BFRP bars, which is a key factor influencing the safety and service life of ocean concrete structures, has not been clarified yet. In this paper, effects of BFRP bars size, corrosion age, and concrete strength on the bond-slip behavior of BFRP bars in concrete cured in artificial seawater were investigated, and then an improved Bertero, Popov, and Eligehausen (BPE) model was employed to describe the bond-slip behavior of BFRP bars in concrete. The results indicated that the maximum bond stress and corresponding slip decreased gradually with the increase of corrosion age and size of BFRP bars, and ultimate slip also decreased sharply. The ascending segment of bond-slip curve tends to be more rigid and the descending segment tends to be softer after corrosion. A horizontal end in bond-slip curve indicates that the friction between BFRP bars and concrete decreased sharply.

1. Introduction

Traditional reinforced concrete (RC) structures often encounter durability problems due to cracks caused by corrosion expansion of steel bar [1]. With respect to steel bar, Basalt Fiber Reinforced Polymer (BFRP) bars present superior corrosion resistance as a kind of novel nonmetallic reinforced bars with high chemical stability [2–5]. Recently, BFRP bars are regarded as a potential alternative material to replace traditional steel bar in reinforced concrete structures subjected to extreme corrosive environment, such as ocean concrete structures [6–10].

Numerous researches have been carried out on mechanical properties and bond durability of BFRP bars or BFRP reinforced concrete [11–14]. The tensile strength loss of BFRP bars was as high as 40% after immersion in 55°C alkaline solution for 63 days [11], and the bond strength of BFRP bars in concrete immersed in artificial seawater for 90 days exhibited a 25% reduction [12]. Tighiouart et al. [13]

confirmed that it was easy bleeding at the interface between BFRP bars and concrete when the large diameter BFRP bars were used, resulting in a decreased bond strength between BFRP bars and concrete. Shen et al. [14] found that the bond strength of the BFRP bars in concrete remained essentially unchanged after exposure to 40°C artificial seawater for 60 days.

The bond-slip behavior, which affects bar anchoring, lap splice strength, concrete-cover requirement, serviceability, and ultimate states, is a key feature for the successful application of BFRP bars as internal reinforcement in concrete structures [15]. It should be noted that the bond-slip behavior of BFRP bars in concrete was different from that of steel bar [16, 17]. Although some achievements about the bond-slip behavior between BFRP bars and concrete have been made [11, 16–24], most of them were focused on small size BFRP bars ($<\Phi$ 10 mm). However, the bond-slip behavior between large size BFRP bars and concrete is different due to larger interfacial transition zone, internal bleeding, and smaller

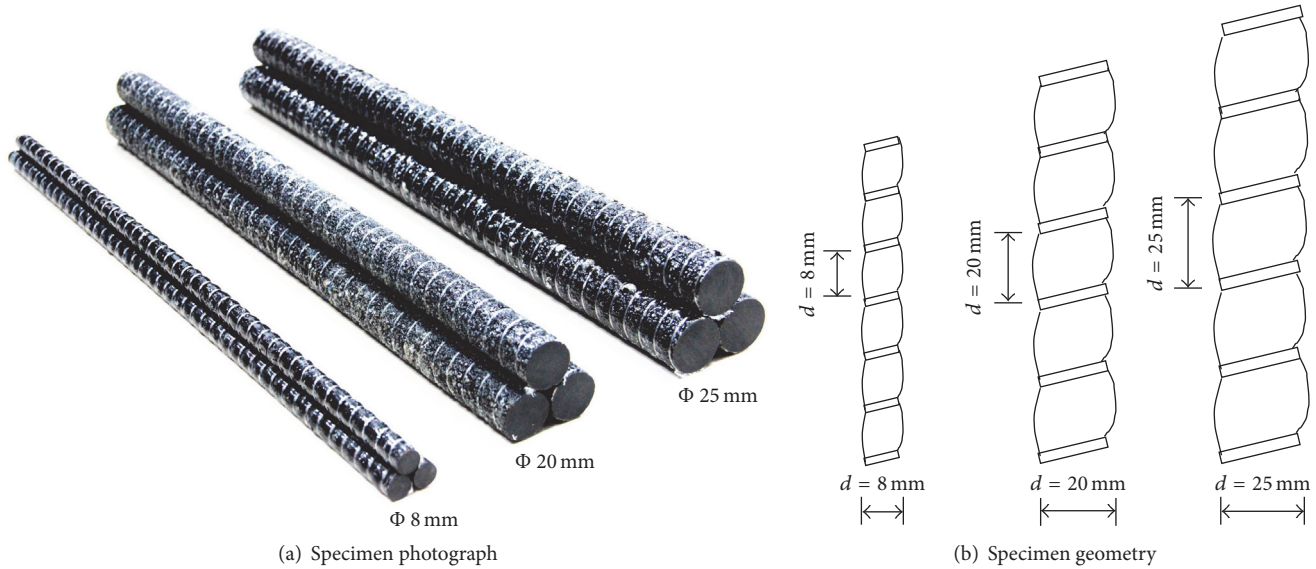


FIGURE 1: The photograph and the size of BFRP bars.

TABLE 1: The mechanical properties of the BFRP bars with different size.

| Size of BFRP bars | Ultimate tensile strength (MPa) | Tensile elastic modulus (GPa) | Ultimate strain (%) |
|-------------------|---------------------------------|-------------------------------|---------------------|
| Φ 8 mm | 1210 | 58.2 | 2.2 |
| Φ 20 mm | 1350 | 62.7 | 2.8 |
| Φ 25 mm | 1180 | 57.4 | 2.6 |

specific perimeter. In addition, long term bond-slip behavior of BFRP bars in concrete exposed to marine environment has not been clarified yet.

Large size BFRP bars ($>\Phi$ 20 mm) are expected to be used as reinforced material in ocean concrete structures, especially for south China coastal area. Therefore, effects of BFRP bars size, corrosion age, and concrete strength on the bond-slip behavior of BFRP bars in concrete subjected to artificial seawater were investigated in the present study, and an improved Bertero, Popov, and Eligehausen (BPE) model was employed to describe the bond-slip behavior of BFRP bars. The results will give a better understanding of bond-slip behavior of BFRP bars in concrete subjected to marine environment and finally provide fundamental data for the design and service life prediction of marine concrete structures.

2. Materials and Methods

2.1. Materials. Basalt filaments were pulled over a roller in the pultrusion process to form bars; then, the bars were coated with epoxy resin and twined with nylon wire (Φ 0.5 mm). The epoxy resin was solidified immediately after adhering a layer of quartz sand on the bars. The obtained BFRP bars are regarded as desirable reinforcement material in corrosion

environment due to their high strength, low weight, corrosion resistance, and cost performance [25]. BFRP bars with size of Φ 8 mm, Φ 20 mm, and Φ 25 mm were used as shown in Figure 1. Their mechanical properties measured according to ASTM D3039 [26] are listed in Table 1.

ASTM type II 42.5 Portland cement, river sand (fineness modulus of 2.7), crushed limestone (particle size of 5.0 mm–31.5 mm), tap water, and polycarboxylate superplasticizer (water reducing ratio of 25%) were used to prepare concrete according to mixture proportions shown in Table 2, and 28-day compressive strength of concrete tested as specified in ASTM C39 [27] is also listed.

2.2. Specimen Preparation. The pullout specimen consisted of 600 mm long BFRP bars embedded centrally in concrete column (Φ 150 mm \times 150 mm) as shown in Figure 2(a). The embedded length was kept constant at 5 times as the diameter of the BFRP bars according to FILEM/FIP recommendation RC6 [28], and PVC tube was used at the loading end of the bar to minimize the stress concentration near the loading plate. Steel pipes were used as anchors at the loading end and were cast with epoxy resin before casting. Fresh concrete was cast into the mould and then vibrated for 30 seconds (Figure 2(b)); demoulding was performed after curing at $20 \pm 1^\circ\text{C}$ and 90% relative humidity chamber for 24 h. The exposed

TABLE 2: The mixture proportions of concrete prepared and their 28 days of compressive strength.

| Sample ID | Cement (kg/m ³) | Sand (kg/m ³) | Stone (kg/m ³) | Water (kg/m ³) | Water-reducing admixture (kg/m ³) | 28 days of compressive strength (MPa) |
|-----------|-----------------------------|---------------------------|----------------------------|----------------------------|---|---------------------------------------|
| C30 | 300 | 766 | 1149 | 165 | 4.5 | 43.8 |
| C40 | 350 | 729 | 1141 | 170 | 5.3 | 52.5 |
| C50 | 400 | 690 | 1127 | 173 | 6.0 | 64.0 |

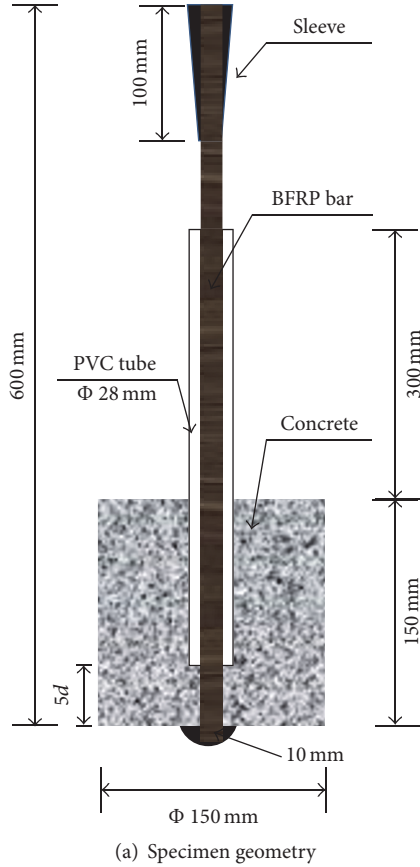


FIGURE 2: The geometry and photograph of pullout specimens.

free end of the bars was sealed by epoxy resin (Φ 10 mm); the specimens were cured in lime-saturated water at $20 \pm 1^\circ\text{C}$ for 27 days and then immersed artificial seawater (NaCl 24.53 g/L, MgCl_2 20 g/L, Na_2SO_4 4.09 g/L, and CaCl_2 1.16 g/L according to ASTM D 1141-98 [29]) under 40°C ; schematic of conditioning container and details are depicted in Figure 3.

2.3. Pullout Test Procedures. Figure 4 depicts the typical details and schematic for pullout test according to ASTM D7913 [30]. The tests were carried out with a MTS testing machine in displacement control mode at a rate of 2 mm/min. The displacements of the free end and loading end of BFRP bar were measured with linear variable displacement transducers (LVDT), and the applied load and displacements were recorded automatically throughout a data-acquisition

system. The slip of the BFRP bars in concrete can be obtained as follows:

$$s = s_L - s_F, \quad (1)$$

where s is the slip of the BFRP bars (mm); s_L is the displacement of the loading end of the BFRP bars (mm); s_F is the displacement of the free end of the BFRP bars (mm).

The bond stress can be calculated assuming a uniform bond stress distribution along the embedded length of the bar in concrete using

$$\tau = \frac{P}{\pi d L_d}, \quad (2)$$

where τ is the bond stress (MPa); P is the pullout force which was measured by pressure sensor (N); d is the diameter of

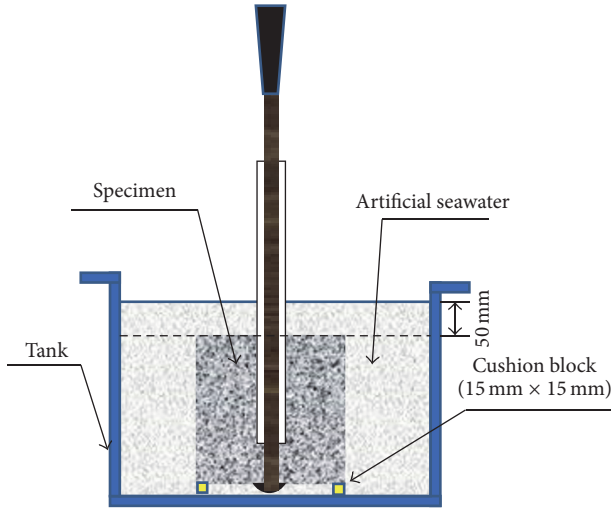


FIGURE 3: Schematic for specimens immersed artificial seawater.

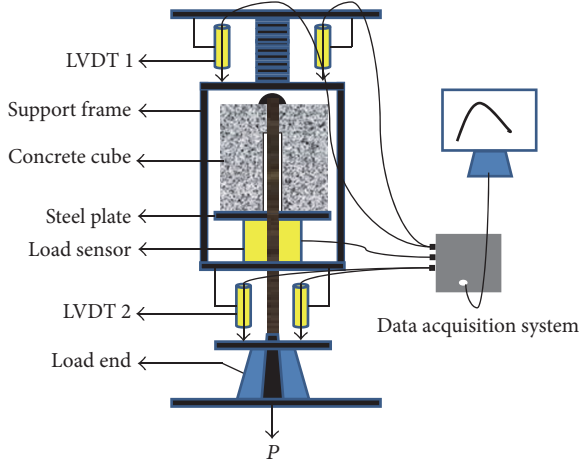


FIGURE 4: Apparatus of pullout test.

BFRP bars (mm); L_d (mm) is bond length of the BFRP bars in concrete.

3. Results and Analysis

3.1. Effect of Corrosion Age on the Bond-Slip Behavior of BFRP Bars in Concrete. The bond-slip behavior of the BFRP bars in concrete shown in Figure 5 can be described by four parameters: τ_1 and s_1 are the maximum bond stress and corresponding slip, while s_2 and τ_2 are ultimate slip and corresponding bond stress. Both τ_1 and s_1 decreased gradually with the increase of corrosion age. For instance, τ_1 and s_1 of BFRP bars (Φ 25 mm) in concrete before corrosion were 21.5 MPa and 3.0 mm and reduced to 17.8 MPa and 1.7 mm after 90-day corrosion in artificial seawater, respectively, indicating that the maximum bond stress decreased with the prolong of corrosion age. τ_2 of BFRP bars (Φ 25 mm) increased from 1.1 MPa to 8.1 MPa after 90 days of corrosion, while s_2 was decreased sharply from 10.0 mm to 5.2 mm. It should be noted that a horizontal end in bond-slip curve was

observed after corrosion, which means significant reduction in ultimate slip after corrosion. Similar tendency was found for BFRP bars with size of Φ 8 mm, and both τ_1 , s_1 and τ_2 , s_2 of BFRP bars with size of Φ 8 mm had higher value than those of BFRP bars with size of Φ 25 mm.

3.2. Effect of Bars Size on Bond-Slip Behavior of BFRP Bars in Concrete. As shown in Figure 6, the maximum bond stress and corresponding slip decreased with the diameter increase of BFRP bars, and ultimate slip also decreased slightly. After 90 days of corrosion, both the maximum bond stress and corresponding slip of the BFRP bars decreased about 8.0%. An obvious horizontal end was observed for all specimens after corrosion, indicating that the friction between BFRP bars and concrete decreased sharply.

3.3. Effect of Concrete Strength on Bond-Slip Behavior of BFRP Bars in Concrete. With the increase of concrete strength, the maximum bond stress increased gradually, while slip corresponds to maximum bond stress and ultimate slip decreased as shown in Figure 7. After 90 days of corrosion, both the maximum bond stress and corresponding slip of the BFRP bars increased with the increase of concrete strength. BFRP bars in high strength concrete had larger ultimate slip. It can be inferred that high strength concrete is benefit to the bond performance between BFRP bars and concrete.

4. Discussion

BPE model [31] is generally used to describe the bond-slip of steel bar in concrete (Figure 8(a)). The ascending segment ($s \leq s_1$) of bond-slip curve can be expressed as follows:

$$\frac{\tau}{\tau_1} = \left(\frac{s}{s_1} \right)^\alpha \quad (s \leq s_1), \quad (3)$$

where τ_1 is the maximum bond stress; s_1 is the corresponding slip; α is a curve-fitting parameter ($\alpha < 1$).

For a second segment with a constant bond ($\tau = \tau_1$) up to a slip ($s = s_2$), a linearly descending segment developed from (s_2, τ_2) to (s_3, τ_3); and a horizontal segment developed for $s > s_3$, with a value of τ due to the development of friction ($\tau = \tau_3$).

Cosenza et al. proposed an improved BPE model to describe the bond-slip curve of FRP bars in concrete by ignoring the second segment (Figure 8(b)) [32]. The ascending segment is coincident with the original BPE model but the slope of descending segment is $p \cdot \tau_1/s_1$, which is given by

$$\frac{\tau}{\tau_1} = 1 - p \left(\frac{s}{s_1} - 1 \right) \quad (s_1 \leq s \leq s_2), \quad (4)$$

where p is parameter accounting for the softening, s_2 is the ultimate slip, and s_3 is friction slip due to bond resistance.

Obviously, the improved BPE model is more suitable to describe the bond-slip behavior of BFRP bars in concrete. The improved BPE model can be further described as A_p , α , and

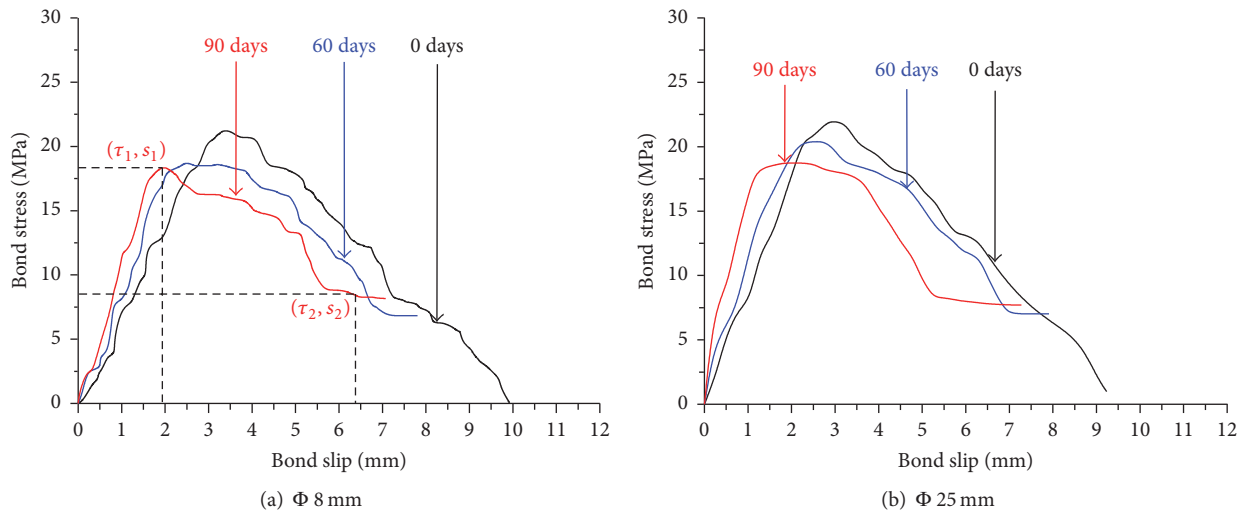


FIGURE 5: Bond-slip behavior of the BFRP bars in concrete specimens after different corrosion ages.

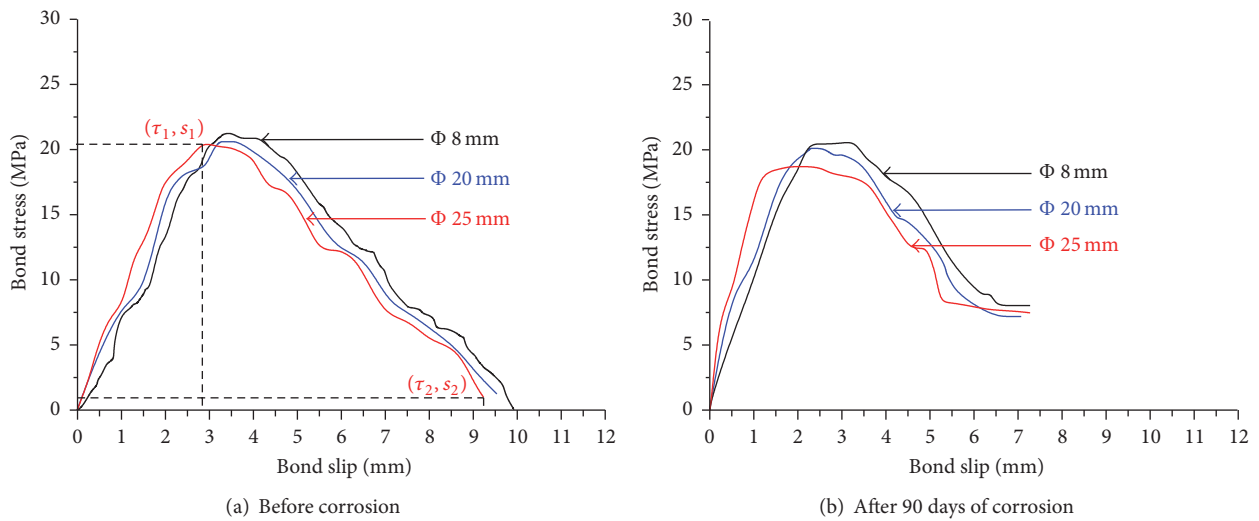


FIGURE 6: Bond-slip behavior of BFRP bars with different size in concrete specimens.

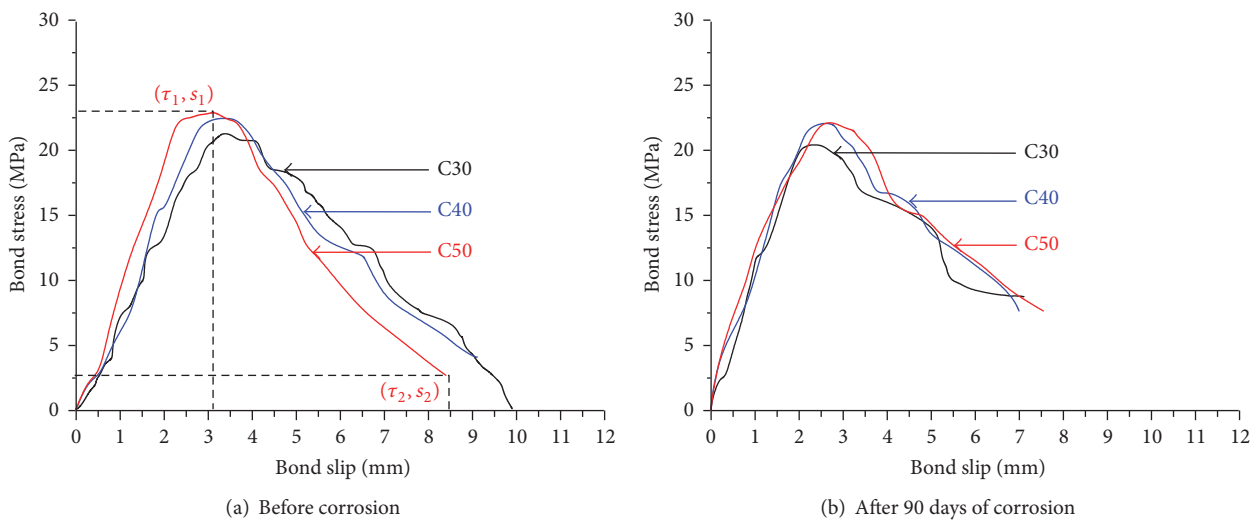


FIGURE 7: Bond-slip behavior of the BFRP bars in concrete with different strength grade.

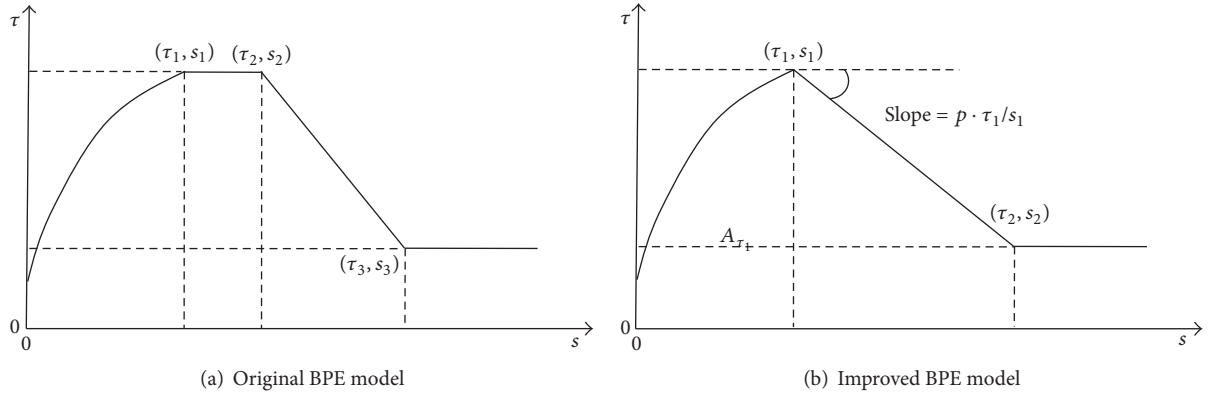


FIGURE 8: Relationship between bond stress and slip in BPE Model.

TABLE 3: The parameters of bond-slip curves of the BFRP bars in concrete specimens after different corrosion ages.

| Size of BFRP bars | Age of corrosion (days) | τ_1 (MPa) | s_1 (mm) | τ_2 (MPa) | s_2 (mm) |
|-------------------|-------------------------|----------------|------------|----------------|------------|
| Φ 8 mm | 0 | 22.5 | 3.5 | 1.2 | 9.2 |
| | 60 | 20.8 | 2.9 | 7.6 | 7.5 |
| | 90 | 20.0 | 2.0 | 11.0 | 5.6 |
| Φ 25 mm | 0 | 21.5 | 3.1 | 1.1 | 10.0 |
| | 60 | 20.0 | 2.5 | 6.4 | 6.7 |
| | 90 | 17.8 | 1.7 | 8.1 | 5.2 |

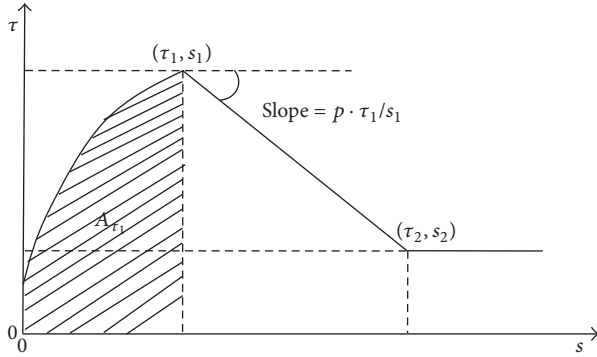


FIGURE 9: Geometrical schematic of improved BEP model.

p , and A_r (area underneath the ascending segment as shown in Figure 9) can be written as follows:

$$A_r = \int_0^{s_1} \tau(s) \cdot ds = \int_0^{s_1} \tau_1 \left(\frac{s}{s_1} \right)^\alpha \cdot ds = \frac{\tau_1 \cdot s_1}{1 + \alpha} \quad (5)$$

Then, α and p in the improved BEP model can be calculated from A_r by

$$\alpha = \frac{\tau_1 \cdot s_1}{A_r} - 1, \quad (6)$$

$$p = \frac{s_2 - s_1}{\tau_1 - \tau_2} \cdot \frac{s_1}{\tau_1}.$$

It can be inferred that a low value of α means bond stress develops without significant slip, and the ascending segment

can be well reproduced using a rigid law. For the descending segment, a low value of p and $p \cdot \tau_1/s_1$ indicates larger slips, and the descending segment can be well fitted using a softening law. Tables 3–6 and Figure 10 showed that the ascending segment tends to be more rigid and the descending segment tends to be softer after corrosion, and the corrosion has much more significant effect on the bond-slip behavior of large size BFRP bars in concrete.

5. Conclusions

Main conclusions that can be drawn from the present study were as follows:

- (1) The maximum bond stress and corresponding slip decreased gradually with the increase of corrosion age, and ultimate slip also decreased sharply from 10.0 mm to 5.2 mm. A horizontal section in bond-slip curve was observed after corrosion, indicating the friction between BFRP bars and concrete decreased sharply.
- (2) The maximum bond stress and corresponding slip decreased with the diameter increase of BFRP bars, and ultimate slip also decreased slightly. Both the maximum bond stress and corresponding slip of the BFRP bars increased with the increase of concrete strength. BFRP bars in high strength concrete possessed larger ultimate slip.
- (3) The ascending segment of bond-slip curve tends to be more rigid and the descending segment tends to

TABLE 4: The parameters of bond-slip behavior of BFRP bars with different size in concrete specimens.

| Size of BFRP bars | Age of corrosion (days) | τ_1 (MPa) | s_1 (mm) | τ_2 (MPa) | s_2 (mm) |
|-------------------|-------------------------|----------------|------------|----------------|------------|
| Φ 8 mm | 0 | 22.5 | 3.5 | 1.2 | 9.2 |
| | 90 | 20.8 | 2.9 | 7.6 | 7.5 |
| Φ 20 mm | 0 | 21.8 | 3.3 | 1.1 | 9.3 |
| | 90 | 20.6 | 2.6 | 7.0 | 6.9 |
| Φ 25 mm | 0 | 21.5 | 3.1 | 1.1 | 10.0 |
| | 90 | 20.0 | 2.5 | 6.4 | 6.7 |

TABLE 5: Parameters of bond-slip behavior of the BFRP bars in concrete with different strength grade.

| Corrosion age | Concrete strength | τ_1 (MPa) | s_1 (mm) | τ_2 (MPa) | s_2 (mm) |
|---------------|-------------------|----------------|------------|----------------|------------|
| 0 days | C30 | 22.5 | 3.5 | 1.2 | 9.2 |
| | C40 | 23.0 | 3.2 | 4.0 | 8.8 |
| | C50 | 23.5 | 2.8 | 3.9 | 8.5 |
| 90 days | C30 | 21.5 | 3.1 | 1.1 | 10.0 |
| | C40 | 22.4 | 2.6 | 3.8 | 8.2 |
| | C50 | 22.6 | 2.2 | 4.4 | 7.9 |

TABLE 6: The geometrical parameters of bond-slip behavior of BFRP bars in concrete according to improved BEP model.

| Size of BFRP bars | Age of corrosion (days) | A_r (mm ²) | α | p | $p \cdot \tau_1 / s_1$ |
|-------------------|-------------------------|--------------------------|----------|-------|------------------------|
| Φ 8 mm | 0 | 37.1 | 1.12 | 0.042 | 3.3 |
| | 60 | 31.5 | 0.91 | 0.049 | 3.2 |
| | 90 | 23.1 | 0.73 | 0.040 | 2.8 |
| Φ 25 mm | 0 | 42.5 | 0.57 | 0.049 | 3.7 |
| | 60 | 28.1 | 0.78 | 0.039 | 2.9 |
| | 90 | 24.7 | 0.23 | 0.034 | 2.5 |

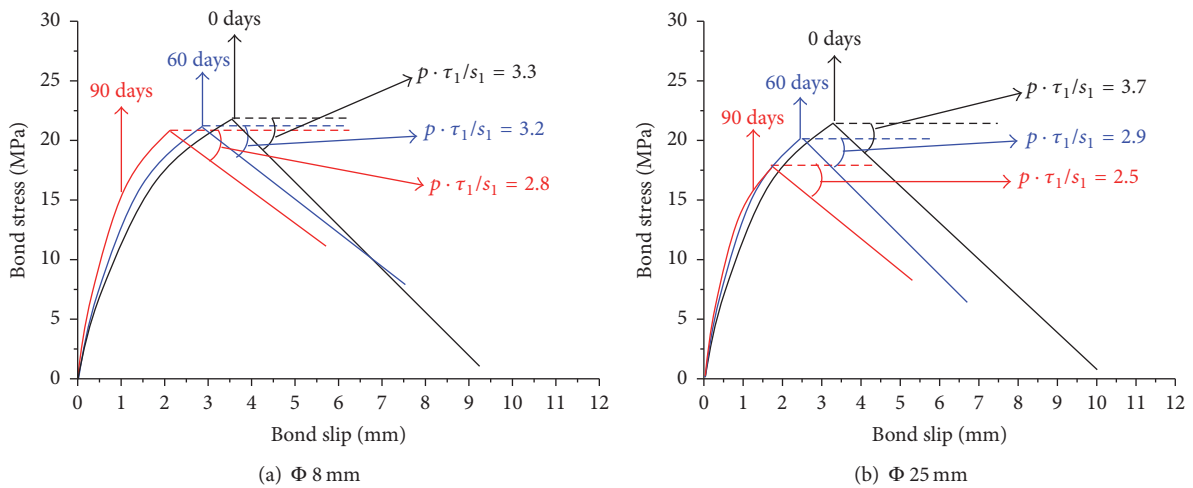


FIGURE 10: Geometry of bond-slip behavior of BFRP bars in concrete according to improved BEP model.

be softer after corrosion, and the corrosion has much more significant effect on the bond-slip behavior of large size BFRP bars in concrete.

Conflicts of Interest

The authors declare that they have no conflicts of interest.

Acknowledgments

This work was funded by National Key Research and Development Program (no. 2016YFB0303502), Water Conservancy Science and Technology of Guangdong Province of China (2015-10 and 2016-23) and the China Postdoctoral Science Foundation (no. 2016M590776). Their financial supports are gratefully acknowledged.

References

- [1] X. Shi, N. Xie, K. Fortune, and J. Gong, "Durability of steel reinforced concrete in chloride environments: an overview," *Construction and Building Materials*, vol. 30, pp. 125–138, 2012.
- [2] F. M. Al-Oqla and S. M. Sapuan, "Natural fiber reinforced polymer composites in industrial applications: feasibility of date palm fibers for sustainable automotive industry," *Journal of Cleaner Production*, vol. 66, pp. 347–354, 2014.
- [3] J. G. Teng, T. Yu, and D. Fernando, "Strengthening of steel structures with fiber-reinforced polymer composites," *Journal of Constructional Steel Research*, vol. 78, pp. 131–143, 2012.
- [4] D. A. Hensher, *Fiber-Reinforced-Plastic (FRP) Reinforcement for Concrete Structures: Properties and Applications*, vol. 42, Elsevier, 2016.
- [5] P. Böer, L. Holliday, and T. H.-K. Kang, "Independent environmental effects on durability of fiber-reinforced polymer wraps in civil applications: a review," *Construction and Building Materials*, vol. 48, pp. 360–370, 2013.
- [6] V. Lopresto, C. Leone, and I. De Iorio, "Mechanical characterisation of basalt fibre reinforced plastic," *Composites Part B: Engineering*, vol. 42, no. 4, pp. 717–723, 2011.
- [7] A. Lapko and M. Urbański, "Experimental and theoretical analysis of deflections of concrete beams reinforced with basalt rebar," *Archives of Civil and Mechanical Engineering*, vol. 15, no. 1, pp. 223–230, 2015.
- [8] X. Wang, G. Wu, Z. Wu, Z. Dong, and Q. Xie, "Evaluation of prestressed basalt fiber and hybrid fiber reinforced polymer tendons under marine environment," *Materials and Design*, vol. 64, pp. 721–728, 2014.
- [9] J. D. Garcia-Espinel, D. Castro-Fresno, P. P. Gayo, and F. Ballester-Muñoz, "Effects of sea water environment on glass fiber reinforced plastic materials used for marine civil engineering constructions," *Materials and Design*, vol. 66, pp. 46–50, 2015.
- [10] D. Borrie, H. B. Liu, X. L. Zhao, R. K. Singh Raman, and Y. Bai, "Bond durability of fatigued CFRP-steel double-lap joints pre-exposed to marine environment," *Composite Structures*, vol. 131, pp. 799–809, 2015.
- [11] G. Wu, X. Wang, Z. Wu, Z. Dong, and Q. Xie, "Degradation of basalt FRP bars in alkaline environment," *Science and Engineering of Composite Materials*, vol. 22, no. 6, pp. 649–657, 2015.
- [12] A. Altalmas, A. El Refai, and F. Abed, "Bond degradation of basalt fiber-reinforced polymer (BFRP) bars exposed to accelerated aging conditions," *Construction and Building Materials*, vol. 81, pp. 162–171, 2015.
- [13] B. Tighiouart, B. Benmokrane, and D. Gao, "Investigation of bond in concrete member with fibre reinforced polymer (FRP) bars," *Construction and Building Materials*, vol. 12, no. 8, pp. 453–462, 1998.
- [14] D. Shen, B. Ojha, X. Shi, H. Zhang, and J. Shen, "Bond stress-slip relationship between basalt fiber-reinforced polymer bars and concrete using a pull-out test," *Journal of Reinforced Plastics and Composites*, vol. 35, no. 9, pp. 747–763, 2016.
- [15] ACI Committee 440, *Guide for the Design and Construction of Structural Concrete Reinforced with FRP Bars*, American Concrete Institute, 2007.
- [16] G. Wu, Z.-Q. Dong, X. Wang, Y. Zhu, and Z.-S. Wu, "Prediction of long-term performance and durability of BFRP bars under the combined effect of sustained load and corrosive solutions," *Journal of Composites for Construction*, vol. 19, no. 3, Article ID 4014058, 2015.
- [17] R. A. Hawileh, H. A. Rasheed, J. A. Abdalla, and A. K. Al-Tamimi, "Behavior of reinforced concrete beams strengthened with externally bonded hybrid fiber reinforced polymer systems," *Materials and Design*, vol. 53, pp. 972–982, 2014.
- [18] A. Serbescu, M. Guadagnini, and K. Pilakoutas, "Mechanical characterization of basalt FRP rebars and long-term strength predictive model," *Journal of Composites for Construction*, vol. 19, no. 2, 2015.
- [19] A. El-Nemr, E. A. Ahmed, and B. Benmokrane, "Flexural behavior and serviceability of normal- and high-strength concrete beams reinforced with glass fiber-reinforced polymer bars," *ACI Structural Journal*, vol. 110, no. 6, pp. 1077–1087, 2013.
- [20] X. Lin and Y. X. Zhang, "Evaluation of bond stress-slip models for FRP reinforcing bars in concrete," *Composite Structures*, vol. 107, no. 1, pp. 131–141, 2014.
- [21] J. Shi, H. Zhu, Z. Wu, R. Seracino, and G. Wu, "Bond behavior between basalt fiber-reinforced polymer sheet and concrete substrate under the coupled effects of freeze-thaw cycling and sustained load," *Journal of Composites for Construction*, vol. 17, no. 4, pp. 530–542, 2013.
- [22] H. Zhu, G. Wu, J. Shi, C. Liu, and X. He, "Digital image correlation measurement of the bond-slip relationship between fiber-reinforced polymer sheets and concrete substrate," *Journal of Reinforced Plastics and Composites*, vol. 33, no. 17, pp. 1590–1603, 2014.
- [23] R. H. Haddad, R. Al-Rousan, and A. Almasry, "Bond-slip behavior between carbon fiber reinforced polymer sheets and heat-damaged concrete," *Composites Part B: Engineering*, vol. 45, no. 1, pp. 1049–1060, 2013.
- [24] A. D'Ambrisi, L. Feo, and F. Focacci, "Experimental analysis on bond between PBO-FRCM strengthening materials and concrete," *Composites Part B: Engineering*, vol. 44, no. 1, pp. 524–532, 2013.
- [25] D. Yeboah, S. Taylor, D. McPolin, and R. Gilfillan, "Pull-out behaviour of axially loaded Basalt Fibre Reinforced Polymer (BFRP) rods bonded perpendicular to the grain of glulam elements," *Construction and Building Materials*, vol. 38, pp. 962–969, 2013.
- [26] ASTM, "Standard test method for tensile properties of polymer matrix composite materials," ASTM D3039/D3039M, ASTM International, West Conshohocken, Pa, USA, 2014.

- [27] ASTM, "Standard test method for compressive strength of cylindrical concrete specimens," ASTM C39/C39M, ASTM International, West Conshohocken, Pa, USA, 2016.
- [28] A. Katz and N. Berman, "Modeling the effect of high temperature on the bond of FRP reinforcing bars to concrete," *Cement and Concrete Composites*, vol. 22, no. 6, pp. 433–443, 2000.
- [29] ASTM, "Standard practice for the preparation of substitute ocean water," ASTM D1141, ASTM International, West Conshohocken, Pa, USA, 2013.
- [30] ASTM, "Standard test method for bond strength of fiber-reinforced polymer matrix composite bars to concrete by pullout testing," ASTM D7913/D7913M, ASTM International, West Conshohocken, Pa, USA, 2014.
- [31] R. Eligehausen, E. P. Popov, and V. V. Bertero, *Local Bond Stress-slip Relationships of Deformed Bars Under Generalized Excitations*, University of California, Berkeley, Calif, USA, 1982.
- [32] E. Cosenza, G. Manfredi, and R. Realfonzo, "Behavior and modeling of bond of FRP rebars to concrete," *Journal of Composites for Construction*, vol. 1, no. 2, pp. 40–51, 1997.

Research Article

Study on Axial Compressive Capacity of FRP-Confined Concrete-Filled Steel Tubes and Its Comparisons with Other Composite Structural Systems

Jun Deng, Yifeng Zheng, Yi Wang, Tonghua Liu, and Hui Li

School of Civil and Transportation Engineering, Guangdong University of Technology, Guangzhou 510006, China

Correspondence should be addressed to Jun Deng; jdeng@gdut.edu.cn

Received 14 September 2016; Revised 15 January 2017; Accepted 23 January 2017; Published 16 February 2017

Academic Editor: Atsushi Sudo

Copyright © 2017 Jun Deng et al. This is an open access article distributed under the Creative Commons Attribution License, which permits unrestricted use, distribution, and reproduction in any medium, provided the original work is properly cited.

Concrete-filled steel tubular (CFST) columns have been widely used for constructions in recent decades because of their high axial strength. In CFSTs, however, steel tubes are susceptible to degradation due to corrosion, which results in the decrease of axial strength of CFSTs. To further improve the axial strength of CFST columns, carbon fiber reinforced polymer (CFRP) sheets and basalt fiber reinforced polymer (BFRP) sheets are applied to wrap the CFSTs. This paper presents an experimental study on the axial compressive capacity of CFRP-confined CFSTs and BFRP-confined CFSTs, which verified the analytical model with considering the effect of concrete self-stressing. CFSTs wrapped with FRP exhibited a higher ductile behavior. Wrapping with CFRP and BFRP improves the axial compressive capacity of CFSTs by 61.4% and 17.7%, respectively. Compared with the previous composite structural systems of concrete-filled FRP tubes (CFFT) and double-skin tubular columns (DSTCs), FRP-confined CFSTs were convenient in reinforcing existing structures because of softness of the FRP sheets. Moreover, axial compressive capacity of CFSTs wrapped with CFRP sheets was higher than CFFT and DSTCs, while the compressive strength of DSTCs was higher than the retrofitted CFSTs.

1. Introduction

In a conventional concrete-filled steel tubular (CFST) column system, concrete was filled in steel tubes, which typically continued throughout several stories or the full-height of a building [1, 2]. After decades of development, CFST columns have been widely used in many buildings.

In CFSTs, however, steel tubes are susceptible to degradation due to corrosion, which results in the reducing of axial strength of CFSTs. To overcome the disadvantages, Xiao [3] proposed the FRP strengthened CFST (FCFST) columns. Both the inward and the outward buckling deformations of the steel tube in the strengthened CFSTs were constrained, thereby substantially enhancing the ductility and strength of the column. Thereafter, many studies were conducted by Xiao et al. [4–6] and other researchers [5, 7–11] on the effectiveness of FRP wrapping in improving the structural behavior of CFST columns. Teng et al. [12] developed a stress-strain model for confined concrete in FCFSTs.

Xue et al. [13] have found that shrinkage of the filled concrete can cause separation between steel tube and concrete, and Ghafari et al. [14] have found that shrinkage can reduce the durability of the structures. Expansive cements, which can increase the volume of concrete due to chemical reactions, can reduce the shrinkage of concrete. Therefore, the self-stressing concrete-filled steel tubes (SSCFSTs) were proposed as they have higher axial strength than CFSTs. A number of experimental studies [15, 16] on SSCFST have been conducted to understand its mechanical performance, and design theory [17] was proposed accordingly. Some models have been developed to predict the load capacity of the FCFST columns [18, 19]; however, the effect of the expansion of the concrete was not considered.

In addition, CFST is not the only system of concrete-filled tubular columns. Ozbakkaloglu et al. [20–22] conducted studies on the axial compressive behavior of concrete-filled FRP tubes (CFFT) and double-skin tubular columns (DSTCs). CFSTs were made of steel tubes, while CFFT were

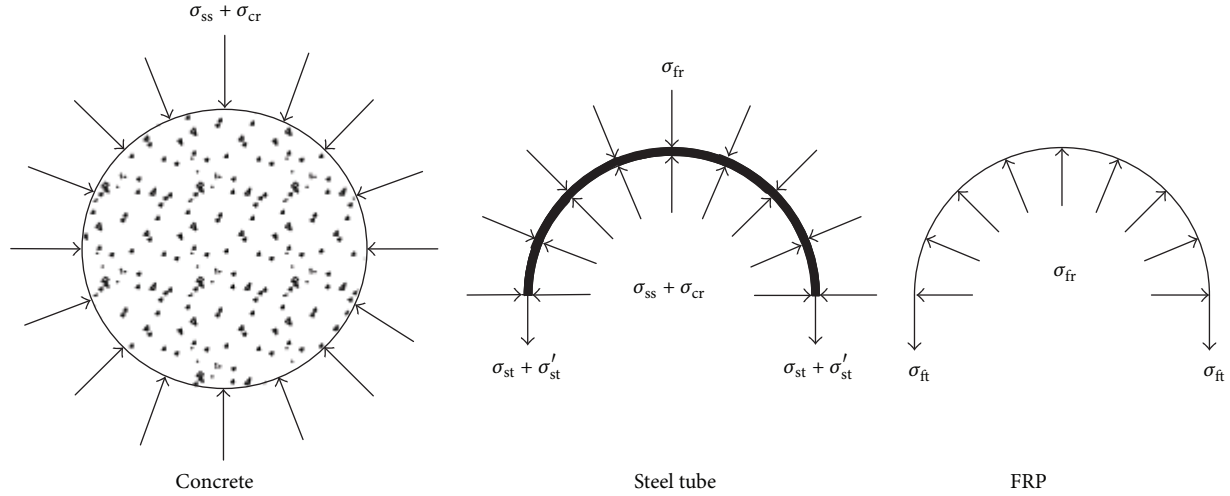


FIGURE 1: Stress distribution in SSCFST.

made of FRP tubes. DSTCs were made of both steel tubes and FRP tubes, including hollow core (DSTC-H) and core-filled (DSTC-F). Since the characteristics and application limitations of each system are still not clear, the comparisons of these four systems are needed.

This paper gives a theoretical model for obtaining the axial compressive capacity of FCFSTs, in which the effect of self-stressing was considered. Besides, experimental study was also conducted to investigate the behavior of CFSTs wrapped with CFRP sheets (CCFSTs) and BFRP sheets (BCFSTs) subjected to axial compression. Finally, our test results were compared with existing test results of CFFT, DSTC-H, and DSTC-F.

2. Analytical Study

2.1. Basic Assumptions. The following assumptions are made in this analytical study:

- (1) The interfaces between the concrete and the steel tube, the steel tube and the FRP sheet are constrained.
- (2) The radial stress in the steel tube is ignored and the steel tube is under biaxial stress.
- (3) The FRP material is linear elastic.
- (4) Only the hoop stress in the FRP sheet is considered; that is, the stress along the fiber direction is considered and the radial stress and the longitudinal stress are ignored.

2.2. Axial Compressive Capacity. Since the concrete in the steel tube is under triaxial compression, the axial compressive strength of concrete σ_{cl} which considered both the self-stressing and axial compression can be expressed as [23]

$$\sigma_{cl} = f_{ck} + k(\sigma_{cr} + \sigma_{ss}), \quad (1)$$

where f_{ck} is the standard compressive strength of the concrete, σ_r the lateral pressure of the concrete, σ_{cr} the lateral stress of the concrete core caused by axial compression, σ_{ss} the

initial lateral stress caused by expansion of the self-stressing concrete, and k the lateral stress coefficient. k is normally between 3 and 5 in accordance with the experimental results [23] and assumed to be 4 in this study.

The critical state of the steel tube is analyzed using the maximum shear stress theory, known as Tresca yield criterion. It can be expressed as

$$\sigma_{st} - \sigma_{sl} + \sigma'_{st} = f_y, \quad (2)$$

where σ_{st} and σ_{sl} are the hoop tensile stress and axial compressive stress of the steel tube, respectively. σ'_{st} is the hoop tensile stress of steel tube that caused by self-stressing and f_y is the yield strength of the steel tube.

According to the basic assumption (1) and the stress-strain relationships of FRP and steel tube, the hoop stress of the FRP σ_{ft} can be expressed as

$$\sigma_{ft} = \frac{E_f}{E_s} [(1 - \mu_s) \sigma_{st} - \mu_s \sigma'_{st} + \mu_s f_y], \quad (3)$$

where E_s , μ_s , and E_f are Poisson's ratio and Young's modulus of the steel tube and the Young's modulus of the FRP sheet, respectively.

Figure 1 shows the stress distribution in SSCFST under axial compression. According to the stress balances in Figure 1, σ_{cr} and σ_{ss} can be expressed as

$$\sigma_{cr} = \sigma_{ft} \frac{A_f}{2A_c} + \sigma_{st} \frac{A_s}{2A_c}, \quad (4)$$

$$\sigma_{ss} = \frac{A_s}{2A_c} \sigma'_{st}, \quad (5)$$

where A_c , A_s , and A_f are the cross-sectional areas of the concrete, the steel tube, and the FRP, respectively.

The axial compressive capacity of the FRP-SSCFST can be described as

$$N_u = A_c \sigma_{cl} + A_s \sigma_{sl}. \quad (6)$$

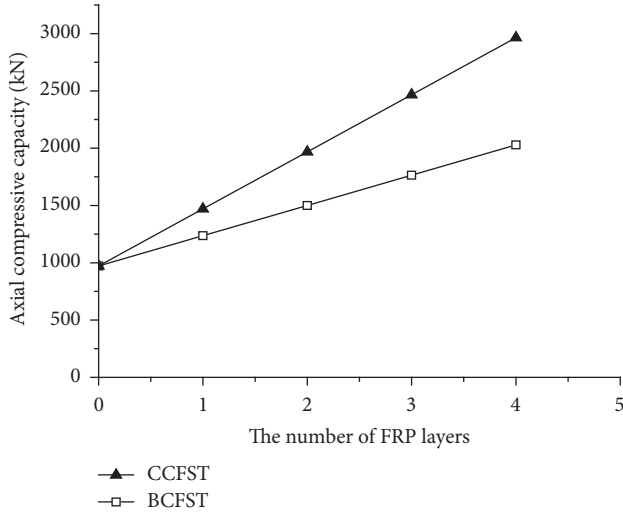


FIGURE 2: Axial compressive capacity with the number of FRP layers.

This study considers the following failure modes of the FRP-SSCFST: steel tube buckling and FRP sheet rupturing.

(1) When the failure mode is steel tube buckling, the hoop tensile stress of the steel tube σ_{st} is the yield stress f_y . Substituting (1), (2), (3), (4), and (5) into (6) gives axial compressive capacity as

$$N_u = A_c f_{ck} \left[1 + 2\xi_s + 2\frac{E_f}{E_s} \xi_f + \left(6 - \frac{4E_f A_f}{E_s A_s} \mu_s \right) \frac{\sigma_{ss}}{f_{ck}} \right], \quad (7)$$

where

$$\xi_s = \frac{A_s f_y}{A_c f_{ck}}, \quad (8)$$

$$\xi_f = \frac{A_f f_f}{A_c f_{ck}}.$$

ξ_s and ξ_f are defined as the coefficients of the constraint effect caused by the steel tube and the FRP sheet, respectively.

(2) When the failure mode is FRP sheet rupturing, the hoop tensile stress of the steel tube σ_{st} is the yield stress f_y and the hoop tensile stress of the FRP σ_{ft} is the ultimate stress f_f . Substituting (1), (2), and (4) into (6) gives axial compressive capacity as

$$N_u = A_c f_{ck} \left(1 + 2\xi_s + 2\xi_f + 6 \frac{\sigma_{ss}}{f_{ck}} \right). \quad (9)$$

2.3. Parametric Analysis. Parametric analysis was performed to investigate the effects of the number of FRP layers and the self-stressing on the axial compressive capacity. The less one between the results calculated by (7) and (9) was the axial compressive capacity of the retrofitted CFSTs.

Figure 2 plots the axial compressive capacity versus the number of layers of FRP sheets. It shows that the axial compressive capacity increased with the number of FRP

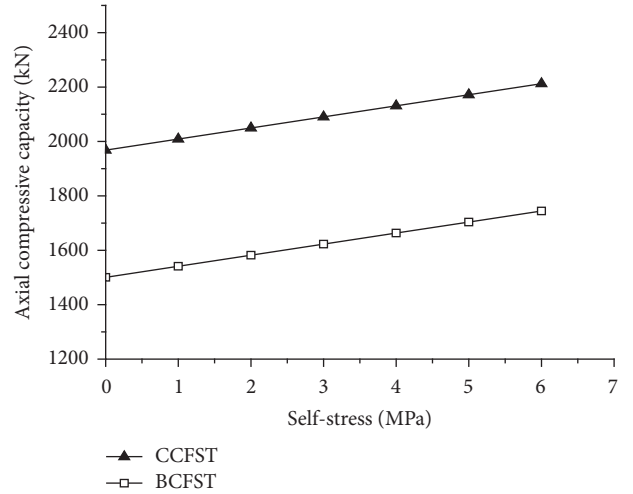


FIGURE 3: Axial compressive capacity with the self-stress.

TABLE 1: Material parameters of CFST.

| Materials | Yield strength (MPa) | 28-day compressive strength (MPa) | Young's modulus (GPa) |
|-----------|----------------------|-----------------------------------|-----------------------|
| steel | 275 | — | 201 |
| concrete | — | 31.2 | 3.35×10^{-5} |

Note. The mix proportions of the concrete were 190:400:786:1065:8 (water : cement : sand : aggregate : water reducer).

TABLE 2: Material parameters of FRP.

| FRP types | Slice thickness (mm) | Tensile strength (MPa) | Young's modulus (GPa) |
|-----------|----------------------|------------------------|-----------------------|
| CFRP | 0.167 | 2878 | 244 |
| BFRP | 0.167 | 1526 | 71 |

layers and the axial strength of CCFSTs is higher than that of BCFSTs. This is because the lateral restraint can be effectively enhanced with the thickness and ultimate tensile strength of FRP, thereby increasing the axial compressive capacity.

Figure 3 plots the axial compressive capacity versus self-stressing level of the filled concrete. It shows that the axial compressive capacity increased with the self-stress. This is because that the lateral restraint increased with the self-stress, thereby increasing the axial compressive capacity.

3. Experimental Study

In total, 11 specimens were prepared, including 3 CFSTs, 4 CCFSTs, and 4 BCFSTs.

Table 1 shows the parameters of steel and concrete of CFSTs. Table 2 shows the parameters of CFRP and BFRP.

After cutting the steel tubes into the desired dimensions, specimens were cast. Then two layers of FRP were wrapped in the hoop direction covering the whole steel tube after 28 days curing.

The tests were carried out in a servohydraulic test machine with a maximum capacity of 10000 kN. The load was

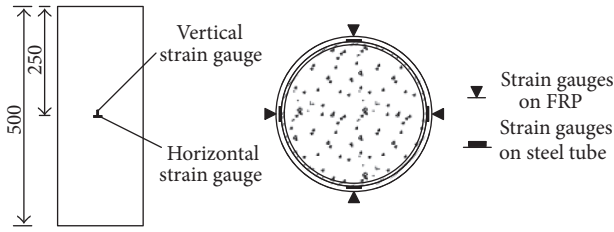


FIGURE 4: Strain gauges arrangement for specimens.

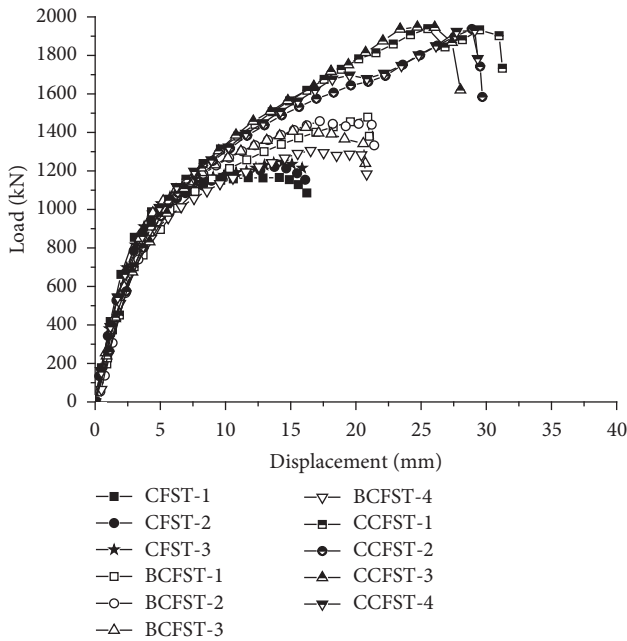


FIGURE 5: Load-displacement curves.

applied at a constant rate of 0.5 kN/s during the elastic stage and at a constant rate of 0.25 mm/min during the plastic stage until the specimens reached its ultimate axial compressive capacity. Four pairs of 3 mm long strain gauges were mounted on both the exterior of the steel tubes and FRP at the mid-height of the specimens to capture the longitudinal and hoop strains. All data was automatically recorded by a data logging system (TDS-530). The strain gauges' arrangement was shown in Figure 4.

4. Experimental Results and Discussions

4.1. Strength and Stiffness of the Specimens. The load versus displacement of the specimens is shown in Figure 5. All specimens have the same loading steps, which can be classified into four stages: elastic stage, elastic-plastic stage, plastic stage, and failure stage. During the elastic stage, the load is apportioned according to the proportion of stiffness between FRP, steel, and concrete. Therefore, after calculation, it can be seen that the load steel suffered is more than 80% of the whole load, which is much greater than FRP and concrete. The stiffness of steel plays a leading role in this stage, which results in the stiffness of FCFST specimens closed to that of the CFST

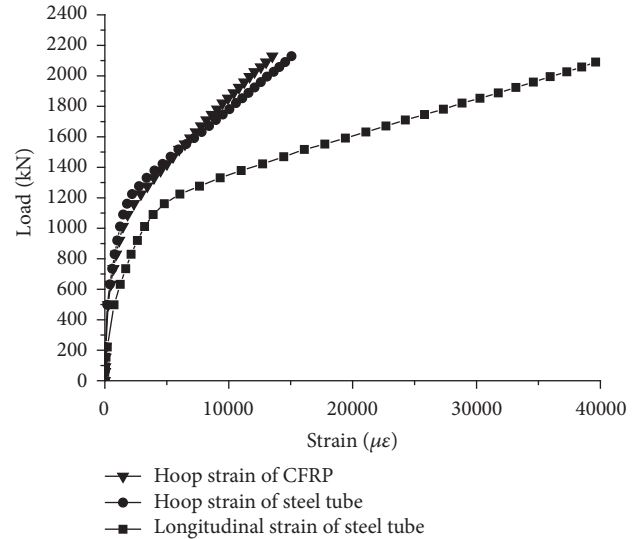


FIGURE 6: Load-strain curves of CCFST-3.

specimens. During the elastic-plastic stage, the stiffness of the strengthened specimens, especially the CCFST specimens, was significantly higher than the CFST specimens. Because outward buckling deformation of the steel tube was constrained by FRP wrapping, the CFRP has more effective confinement than BFRP because of its higher Young's modulus.

The average axial compressive capacity of CFSTs, CCFSTs, and BCFSTs was 1207 kN, 1949 kN and 1421 kN, respectively. The CFRP and BFRP strengthening enhanced the axial compressive capacity of CFSTs by 61.4% and 17.7%, respectively. The average ultimate displacement of CFSTs, CCFSTs, and BCFSTs was 16 mm, 30 mm, and 20 mm, respectively. Besides, CFRP and BFRP strengthening enhanced the ductility by 87.5% and 25%, respectively. It indicates that the strength and ductility of the CFSTs can be significantly improved by FRP wrapping, especially CFRP wrapping.

4.2. Strains of the Specimens. The hoop strain of CFRP and hoop and longitudinal strain of steel tube recorded during the tests of CCFST-3 and BCFST-1 are shown in Figures 6 and 7, respectively. It can be seen that the hoop strains of both CFRP and steel tube were very small during the elastic stage. This is because that the steel tube and the concrete carried on the axial load and the confinement of the steel tube and FRP sheets was not pronounced. The longitudinal strains of the steel tubes developed as elastic-perfectly plastic body. Comparing Figures 6 and 7, the ultimate longitudinal strain of the steel tubes in the CCFST is larger than that in the BCFST, which shows that the confinement of CFRP wrapping is more effective. The load-strain curves of the FRP developed consistently with those of the steel tubes, which indicates that the FRP wraps and steel tube can work together well. Similar results were obtained from the other strengthened specimens.

4.3. Failure Modes. All specimens were loaded to failure to understand the effect of the FRP on the axial strength of CFSTs. The failure modes of typical specimens were shown

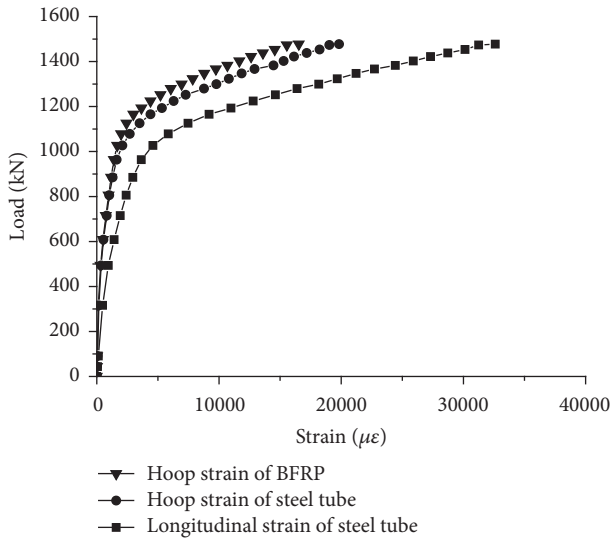


FIGURE 7: Load-strain curves of BCFST-1.

TABLE 3: Comparisons of axial compressive capacity from experiment and analytical results.

| Specimens | Axial compressive capacity (kN) | | Deviations (%) |
|-----------|---------------------------------|--------------------|----------------|
| | Average experimental results | Analytical results | |
| CFSTs | 1207.3 | 1198 | -4.01 |
| CCFSTs | 1948.8 | 2037 | 4.53 |
| BCFSTs | 1420.5 | 1247 | -12.21 |

in Figure 8. As shown in Figure 8(a), the outward buckling of CFSTs was observed in the middle of the steel tube at failure load. In the case of FRP strengthened specimens, snapping sound of fiber was observed after steel tube yielded. The reason could be that FRP wrapping provided significant restraint against the lateral deformations of concrete core and steel tube and the FRP was subjected to tension in the hoop direction. When the FRP reached its ultimate strain, rupture of FRP occurred followed by the outward buckling of steel tube in the middle of the specimens, as shown in Figures 8(b) and 8(c).

4.4. *Validating Analytical Analysis.* The axial compressive capacity of the specimens obtained from tests was compared to the corresponding analytical results calculated by (7) or (9), as presented in Table 3. The agreement between the experimental and analytical results of CFSTs was reached. The deviations of experimental and analytical results of CCFSTs and BCFSTs are 4.53% and -12.21%, respectively, which is considered acceptable.

5. Comparisons of CFST, CFFT, DSTC-H, and DSTC-F

Over the past five years, significant numbers of studies have been reported on the composite columns such as CFFT, DSTC, and FCFST, in which Ozbakkaloglu et al. [20–22]



(a) CFST



(b) CCFST



(c) BCFST

FIGURE 8: Failure modes of specimens.

conducted studies on axial compressive behavior of CFFT, DSTC-H, and DSTC-F made of normal-strength and high-strength concrete, making great contribution to the new composite structure systems. To date, there are few literatures on the contrasted analysis of axial compressive strength and capacity of the different composite columns. The schematics of the four types of columns in literatures [20, 21] and this study were shown in Figure 9.

Table 4 shows the axial compressive capacity (N_u) and axial compressive strength (f_{cc}) obtained from the experimental results of the four types of columns made of CFRP. It demonstrates that the axial compressive capacity (N_u) of

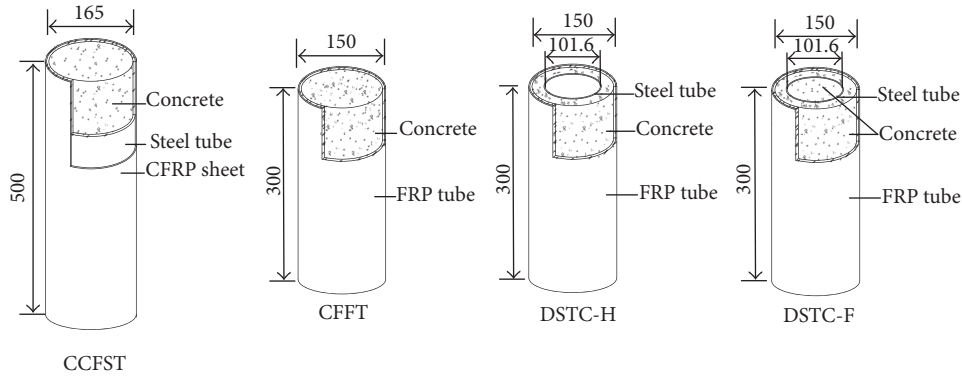


FIGURE 9: The schematics of four columns.

TABLE 4: Comparisons of CCFST, CFFT, DSTC-H, and DSTC-F.

| Type | Specimen | t_f (mm) | t_s (mm) | f_c (MPa) | f_y (MPa) | f_t (MPa) | N_u (kN) | f_{cc} (MPa) |
|-------------|------------|------------|------------|-------------|-------------|-------------|------------|----------------|
| CCFST | average | 0.334 | 2.0 | 31.2 | 275 | 2878 | 1948.8 | 91.2 |
| CFFT [20] | N-150C2L-2 | 0.234 | — | 34.6 | — | 3626 | 1104.5 | 60.9 |
| DSTC-H [21] | DSTC-2 | 0.234 | 3.2 | 37.0 | 302 | 3626 | 955.0 | 99.9 |
| DSTC-F [21] | DSTC-4 | 0.234 | 3.2 | 36.7 | 302 | 3626 | 1322.0 | 74.9 |

Note. f_c = the 28-day compressive strength of concrete; t_f = the total nominal thickness of CFRP; t_s = the thickness of steel tube; CFRP tubes of CFFT, DSTC-H, and DSTC-F were made of two layers of CFRP (nominal thickness is 0.117 mm/ply), while CCFSTs were wrapped with two layers of CFRP sheets (nominal thickness is 0.167 mm/ply).

CCFSTs is higher than those of CFFT, DSTC-H, and DSTC-F. However, the cross-sectional area of CCFSTs is the largest in the four types of columns. The axial compressive strength (f_{cc}) of DSTC-H is greater than CCFSTs and CFFT. Overall, the four types of columns have their own advantages: (a) CFFTs do not need steel and DSTC-H can cost less concrete; (b) DSTC-H is lighter than CCFST and CFFT; (c) CFFT, DSTC-H, and DSTC-F are used as new structures, while CCFST is generally applied to reinforce existing structures; (d) as the novel structures, CFFT and DSTC are applied by well-shaped columns in present; (e) CCFST is conveniently utilized in the structures of the steel tube columns reinforced in active service, which benefits from softness of the FRP sheets.

6. Conclusions

This paper investigated the axial compressive capacity and strength of FCFSTs. Theoretical study was presented to predict the nominal axial compressive strength of FCFSTs, in which the effect of self-stressing concrete was considered. In addition, the experimental study was also conducted to verify the model and investigate the behavior of CCFSTs and BCFSTs subjected to axial compression. As discussed, the following conclusions can be reached.

(1) The axial compressive capacity of the CFSTs wrapped with CFRP and BFRP was improved by 61.4% and 17.7%, respectively. Besides, the ductility of the CFSTs was improved as well.

(2) The good agreement between the experimental axial strength and the analytical results confirmed the validity of the theoretical model.

(3) CCFST can be conveniently and effectively utilized in the existing structure strengthening, while CFFT, DSTC-H, and DSTC-F are applied by well-shaped column as novel structures. Among the four types of columns, DSTC-H has the highest compressive strength.

Competing Interests

The authors declare that there is no conflict of interests regarding the publication of this paper.

Acknowledgments

This work is supported by the National Natural Science Foundation of China through Grant 51278131, Program for New Century Excellent Talents in University through Grant NCET-13-0739, and Fok Ying Tong Education Foundation through Grant 131073.

References

- [1] W. P. Moore and N. K. Gosain, "Mixed systems, past practices, recent experience and future direction," in *Proceedings of the Composite and Mixed Construction*, ASCE, pp. 138–149, 1985.
- [2] I. M. Viest, J. P. Colaco, R. W. Furlong, L. G. Griffis, R. T. Leon, and L. A. Wyllie, *Composite Construction: Design for Buildings*, John Wiley & Sons, New York, NY, USA, 1997.
- [3] Y. Xiao, "Applications of FRP composites in concrete columns," *Advances in Structural Engineering*, vol. 7, no. 4, pp. 335–343, 2004.

- [4] X. Y. Mao and Y. Xiao, "Seismic behavior of confined square CFT columns," *Engineering Structures*, vol. 28, no. 10, pp. 1378–1386, 2006.
- [5] J. H. Shan, R. Chen, W. X. Zhang, Y. Xiao, W. J. Yi, and F. Y. Lu, "Behavior of concrete filled tubes and confined concrete filled tubes under high speed impact," *Advances in Structural Engineering*, vol. 10, no. 2, pp. 209–218, 2007.
- [6] Y. Xiao, W. He, and K.-K. Choi, "Confined concrete-filled tubular columns," *Journal of Structural Engineering*, vol. 131, no. 3, pp. 488–497, 2005.
- [7] W. Gu, C. W. Guan, Y. H. Zhao, and H. Cao, "Experimental study on concentrically compressed circular concrete filled CFRP-steel composite tubular short columns," *Journal of Shenyang Archit Engineering University (Natural Science)*, vol. 20, no. 2, pp. 118–120, 2004.
- [8] Z. Tao, L.-H. Han, and J.-P. Zhuang, "Axial loading behavior of CFRP strengthened concrete-filled steel tubular stub columns," *Advances in Structural Engineering*, vol. 10, no. 1, pp. 37–46, 2007.
- [9] Z.-B. Wang, Z. Tao, and L.-H. Han, "Performance of CFRP-strengthened concrete filled steel tubes under axial compression," in *Proceedings of the 10th International Symposium on Structural Engineering for Young Experts (ISSEYE '08)*, pp. 689–694, Changsha, China, October 2008.
- [10] L. Liu and Y. Y. Lu, "Axial bearing capacity of short FRP confined concrete-filled steel tubular columns," *Journal Wuhan University of Technology—Materials Science Edition*, vol. 25, no. 3, pp. 454–458, 2010.
- [11] J. W. Park, Y. K. Hong, and S. M. Choi, "Behaviors of concrete filled square steel tubes confined by carbon fiber sheets (CFS) under compression and cyclic loads," *Steel and Composite Structures*, vol. 10, no. 2, pp. 187–205, 2010.
- [12] J. G. Teng, Y. M. Hu, and T. Yu, "Stress-strain model for concrete in FRP-confined steel tubular columns," *Engineering Structures*, vol. 49, pp. 156–167, 2013.
- [13] J.-Q. Xue, B. Briseghella, and B.-C. Chen, "Effects of debonding on circular CFST stub columns," *Journal of Constructional Steel Research*, vol. 69, no. 1, pp. 64–76, 2012.
- [14] E. Ghafari, S. A. Ghahari, H. Costa, E. Júlio, A. Portugal, and L. Durães, "Effect of supplementary cementitious materials on autogenous shrinkage of ultra-high performance concrete," *Construction and Building Materials*, vol. 127, pp. 43–48, 2016.
- [15] C. Maltese, C. Pistolesi, A. Lolli, A. Bravo, T. Cerulli, and D. Salvioni, "Combined effect of expansive and shrinkage reducing admixtures to obtain stable and durable mortars," *Cement and Concrete Research*, vol. 35, no. 12, pp. 2244–2251, 2005.
- [16] L. Xu, *Research on the design theory for self-stressing and self-compacting concrete filled steel tube column under axial load [Ph.D. thesis]*, Dalian University of Technology, Dalian, China, 2005.
- [17] Z. Q. Shang, *Research on mechanical behavior of self-stressing and self-compacting concrete filled steel tube columns [Ph.D. thesis]*, Dalian University of Technology, Dalian, China, 2007.
- [18] Y. Lu, N. Li, and S. Li, "Behavior of FRP-confined concrete-filled steel tube columns," *Polymers*, vol. 6, no. 5, pp. 1333–1349, 2014.
- [19] Z.-B. Wang, Q. Yu, and Z. Tao, "Behaviour of CFRP externally-reinforced circular CFST members under combined tension and bending," *Journal of Constructional Steel Research*, vol. 106, pp. 122–137, 2015.
- [20] T. Ozbakkaloglu and T. Vincent, "Axial compressive behavior of circular high-strength concrete-filled FRP tubes," *Journal of Composites for Construction*, vol. 18, no. 2, Article ID 04013037, 2014.
- [21] T. Ozbakkaloglu and B. L. Fanggi, "Axial compressive behavior of FRP-concrete-steel double-skin tubular columns made of normal- and high-strength concrete," *Journal of Composites for Construction*, vol. 18, no. 1, Article ID 04013027, 2014.
- [22] B. A. L. Fanggi and T. Ozbakkaloglu, "Behavior of hollow and concrete-filled FRP-HSC and FRP-HSC-steel composite columns subjected to concentric compression," *Advances in Structural Engineering*, vol. 18, no. 5, pp. 715–738, 2015.
- [23] S. H. Cai, *Modern Concrete Filled Steel Tubular Structures*, Communications Press, Beijing, China, 2003.

Research Article

Combined Effects of Curing Temperatures and Alkaline Concrete on Tensile Properties of GFRP Bars

Wen-ruì Yang,¹ Xiong-jun He,¹ Kai Zhang,² Yang Yang,¹ and Li Dai¹

¹School of Transportation, Wuhan University of Technology, Wuhan 430063, China

²Department of Road and Material, Jiangxi Transportation Institute, Nanchang 330025, China

Correspondence should be addressed to Xiong-jun He; hxjwhut@163.com

Received 13 October 2016; Revised 29 November 2016; Accepted 20 December 2016; Published 19 January 2017

Academic Editor: Ulrich Maschke

Copyright © 2017 Wen-ruì Yang et al. This is an open access article distributed under the Creative Commons Attribution License, which permits unrestricted use, distribution, and reproduction in any medium, provided the original work is properly cited.

A significant number of studies have been conducted on the tensile properties of GFRP bars embedded in concrete under different environments. However, most of these studies have been experimentally based on the environmental immersion test after standard-curing and the lack of influence on the tensile properties of GFRP bars embedded in concrete during the curing process of concrete. This paper presents the results of the microscopic structures through scanning electron microscopy (SEM), Fourier transform infrared spectroscopy (FTIR), differential scanning calorimetry (DSC), and tensile properties of GFRP bars, which were employed to investigate the combined effects of curing temperatures and alkaline concrete on tensile properties of GFRP bars. The results showed that the higher curing temperature aggravated the influence of the alkaline concrete environment on GFRP bars but did not change the mechanisms of mechanical degradation of the GFRP bars. The influence of different curing temperatures on the tensile strength of GFRP bars was different between the bare bar and bars in concrete. Finally, the exponential correlation equation of two different test methods was established, and the attenuation ratio of the tensile strength of GFRP bars embedded in concrete under different curing temperatures was predicted by the bare test.

1. Introduction

Decades of researches and practical applications have proved that the use of GFRP bars embedded in concrete has been an effective method to solve the reinforce corrosion in concrete structures [1–8]. A number of investigations have been conducted to evaluate the effects of temperature, moisture, chemical erosion, loading, and different harsh environments on the properties of GFRP bars. These studies indicated that the influence of GFRP bars in alkaline environment was more obvious especially under the same load. He et al. [6–8] explored the long-term tensile strength and flexural behavior of GFRP bars embedded in concrete beams with initial cracks. The experimental results showed that the beams with crack will accelerate the degradation of the flexural properties, shear properties, and tensile strength of GFRP bars. The durability of GFRP bars will be significantly affected under high temperature and humidity [9, 10].

Many researchers revealed that the alkaline concrete will increase the additional stress, surface crack, and porosity

under the steam-curing of high temperature and humidity [11–15]. Therefore, the influence of the curing system on GFRP bars embedded in concrete cannot be neglected. The lack of investigations about the effect of different curing systems on the performance of GFRP bars embedded in concrete is a vital problem.

In order to evaluate combined effects of curing temperatures and alkaline concrete tensile properties of GFRP bars, the scanning electron microscopy (SEM), Fourier transform infrared spectroscopy (FTIR), differential scanning calorimetry (DSC), and pull-out test of GFRP bars have been conducted. Based on the test data, the exponential correlation equation was established to provide a theoretical basis for the tensile property design of GFRP bars under different curing systems.

2. Experimental

Sun et al. [16] revealed that the performance degradation of GFRP bars embedded in concrete was significantly lower

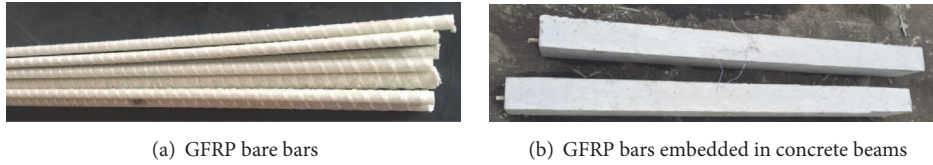


FIGURE 1: Specimens.

TABLE 1: Test specimens.

| Environment | Curing system | Curing temperature | Working condition |
|--------------------------------|-----------------|--------------------|-------------------|
| GFRP bare bars | Reference | — | RE |
| | Standard-curing | 20°C | B-Sta |
| | | 40°C | B-Ste40 |
| | | 60°C | B-Ste60 |
| | Steam-curing | 80°C | B-Ste80 |
| GFRP bars embedded in concrete | Standard-curing | 20°C | C-Sta |
| | | 40°C | C-Ste40 |
| | Steam-curing | 60°C | C-Ste60 |
| | | 80°C | C-Ste80 |

than that of GFRP bars conditioned in an alkaline solution. The practical application and experimental studies showed that the traditional accelerated test results cannot reflect the long-term performance of FRP in concrete [17]. In ACI440.1R-15, it points out that the relationships between data on bare bars and data on bars embedded in concrete are affected by additional variables, such as the degree of protection offered to the bars by the concrete [18]. These reports indicated that the data on GFRP bars embedded in concrete were more accurate in the prediction and design guidance of GFRP bars reinforced concrete. The exponential correlation equation of two different test methods is established to extend previous researches and provide a more reliable basis for the tensile properties degradation of GFRP bars. Therefore, the specimens used in experiments included GFRP bars embedded in concrete and the GFRP bare bars to highlight the influence of alkaline concrete on the tensile properties of GFRP bars.

2.1. Materials

2.1.1. GFRP Bars. The GFRP bars used in the study were provided by Fenghui Composite Materials Co., Ltd., Nanjing, China. This type of bars is made up of unidirectional roving of E-glass and epoxy vinyl ester resin. The bars appear as milky spiral sandblasting, and each screw is 14 mm in length and 0.325 mm in height.

2.1.2. Specimen Preparation. The specimens used in experiments included GFRP bars embedded in concrete beams and the GFRP bare bars (Figure 1). The concrete beams were cast in accordance with typical concrete mix design procedures with a cure time of 28 days to obtain a target strength of 42.5 MPa [19, 20]. The concrete was provided by a local ready-mix plant and had a water-to-cement ratio of 0.59. The GFRP reinforced concrete beams specimens were

rectangular plain concrete beams with a length of 1100 mm, width of 80 mm, and depth of 110 mm, with a single longitudinal GFRP bar centered at 30 mm from the bottom of the section.

2.2. Curing Systems. Two types of curing systems for GFRP bare bars and GFRP bars embedded in concrete beams were used in this study: (1) for standard-curing system, the specimens were treated under a standard-curing with the temperature of $(20 \pm 5)^\circ\text{C}$; subsequently, the specimens were conditioned with a temperature of $(20 \pm 2)^\circ\text{C}$ and a relative humidity more than 95% for 28 d, and (2) steam-curing system, in which the concrete is exposed to elevated temperature, shows an accelerated hydration and nonuniform distribution of hydration products resulting in a rapid increase of the compressive strength in early age. The faster hardening and the changes of porosity may be more obvious when the temperature is higher. The temperatures of steam-curing are 40°C, 60°C, and 80°C, respectively, with the treatment duration of 8 h. The heating rate and cooling rate are controlled as 10°C/h [21]. After the process of steam-curing, the specimens were placed in the standard-curing room for 28. The related parameters of the specimens are shown in Table 1.

2.3. Method

2.3.1. Tensile Test. All tensile specimens were tested under tension according to ACI 440.3R-04 [22]. Tensile specimen for testing was prepared by anchoring two ends of the bar in steel plugs filled with epoxy resin. The free length between the steel plugs was about 300 mm to ensure the anchor bonding strength is higher than the tensile stress according to the guidelines as specified in ACI 440.3R-04 [22]. The test was carried out with a universal testing machine (SHT4106-G) and an extensometer of 50 mm gauge length was mounted with clips at the center of test specimen. The applied load

TABLE 2: Tensile test results of GFRP bars.

| Environment | Curing system | Working condition | Average (MPa) | Ultimate tensile strength (UTS) | |
|--------------------------------|-----------------|-------------------|---------------|---------------------------------|--------------------------|
| | | | | Tensile strength retention (%) | Variable coefficient (%) |
| GFRP bare bars | Reference | RE | 1320 | 100 | 1.67 |
| | Standard-curing | B-Sta | 1300 | 98 | 2.48 |
| | | B-Ste40 | 1271 | 96.3 | 3.31 |
| | Steam-curing | B-Ste60 | 1214 | 92 | 5.11 |
| | | B-Ste80 | 1122 | 85 | 3.69 |
| GFRP bars embedded in concrete | Standard-curing | C-Sta | 1287 | 97.5 | 2.67 |
| | | C-Ste40 | 1273 | 96.42 | 3.28 |
| | Steam-curing | C-Ste60 | 1252 | 94.85 | 3.57 |
| | | C-Ste80 | 1192 | 90.34 | 2.96 |

was recorded during the test with a data-acquisition system monitored by a computer.

2.3.2. Microstructural Observations. Scanning electron microscopy (SEM) observations and image analysis were performed to examine the microstructure of specimens in steam-curing with 60°C. All specimens were first cut, polished, and coated with a thin layer of gold palladium by a vapor deposition process. Once the surfaces were coated, the transversal and longitudinal surfaces were examined using a JSM-5610LV SEM. Before the observation, the surface of the specimen should be cleaned to avoid the influence of the surface residue.

2.3.3. Differential Scanning Calorimetry (DSC). Differential scanning calorimetry (DSC) can be used to characterize information on the thermal behavior and characteristics of polymer materials and composites. The glass transition temperature (T_g) is one of the key parameters in analyzing the durability behavior of GFRP bars. Specimens weighing 10–13 mg were cut from unconditioned GFRP bars, GFRP bars embedded in standard-curing concrete and steam-curing concrete. Subsequently, they were analyzed using a PYRISI differential scanning calorimeter (DSC).

2.3.4. Fourier Transform Infrared Spectroscopy (FTIR). FTIR spectra were recorded using a Nicolet 6700 spectrometer equipped with an attenuated total reflectance (ATR) device. Fourier transform infrared spectroscopy (FTIR) analysis of GFRP bars embedded in standard-curing concrete and steam-curing concrete were conducted to determine if hydrolysis reactions occurred in the polymer resin, which can lead to an important loss of mechanical properties.

3. Results and Discussion

3.1. Tensile Strength Retention of GFRP Bars. Some researchers [4, 6] found that the tensile strength of the GFRP bar was not only related to its diameter, but also had a great relationship with the environmental factors, such as temperature, humidity, and alkaline solution. The degeneration of GFRP bars tensile strength is a function of the relevant

time during long-term service process, which is mainly due to the presence of moisture or corrosion solution leading to corrosion of glass fiber as well as the corrosion rate increases with temperature increase [23]. In the same external environment, the corrosion rate will increase with time. When GFRP bars are in a humid environment, water diffuses into the polymer matrix and even reaches the glass fibers by the matrix to reduce the tensile strength [24]. It can be seen that the difficulty from the external media into the GFRP bar and the variation of tensile properties of the GFRP bar are different under different temperature curing systems.

Table 2 shows the degradation of the tensile strength of GFRP bars under different curing systems. Table 2 indicates that the tensile strength of GFRP bars embedded in concrete is lower than that of GFRP bare bars under standard-curing system, which can prove that the strong alkaline concrete has impact on GFRP bars. However, the tensile strength retention of GFRP bars embedded in steam-curing concrete is 97.5% of that of GFRP bars in the standard-curing concrete, and the minor damage is mainly due to the lower temperature of standard-curing environment and shorter curing period (28 d). Therefore, the effect on the tensile strength degradation of GFRP bars is relatively insignificant, which is consistent with the conclusion that the degradation of GFRP bars does not appear by the Canada A Mufti research team's study for a period of 5 years to 8 years [25].

The degradation of tensile strength of GFRP bars embedded in steam-curing concrete is significantly lower than that of GFRP bars embedded in standard-curing concrete, and the tensile strength retention ratio declines with the rise of curing temperature. But the difference is very small between standard-curing system and steam-curing system, which is mainly due to the steam-curing age of 28 days leading to relatively small impact on GFRP bars. If the steam-curing time is extended or the steam-curing temperature is elevated, the deterioration degree of tensile strength of GFRP bars will increase. Therefore, it is necessary to study the influence of curing temperature and curing period on the performance of GFRP bars.

The variation of tensile strength of GFRP bare bars and GFRP bars embedded in concrete is different with different curing temperatures. It did not demonstrate a consistent

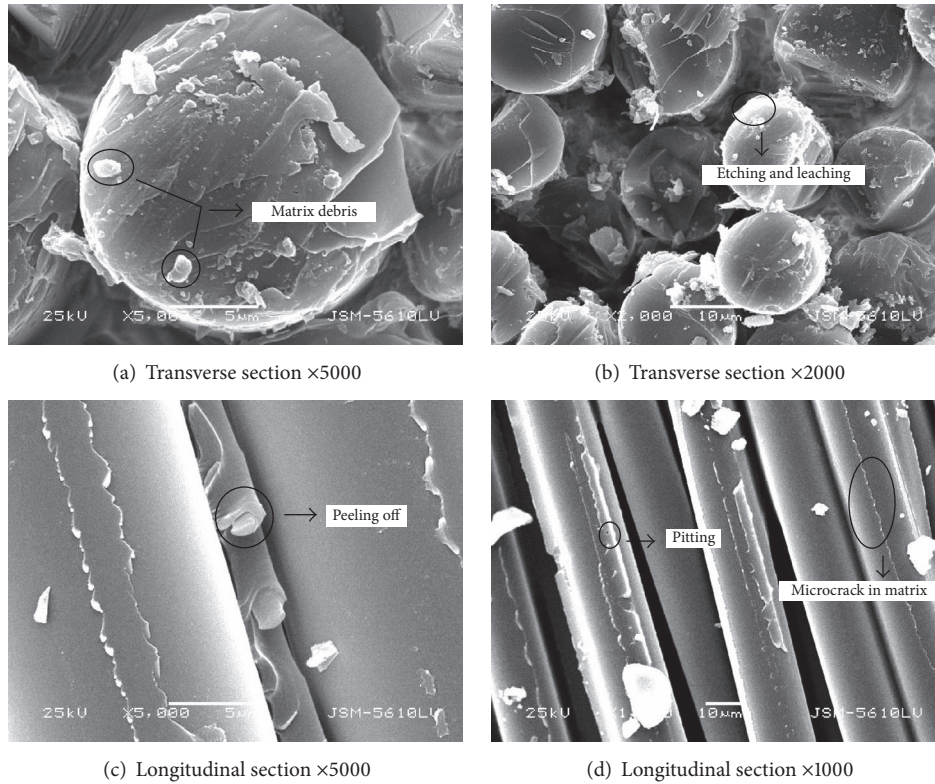


FIGURE 2: Microstructure morphology of GFRP bars in the standard-curing environment.

change trend in Table 2. The tensile strength retention of GFRP bare bars is higher than the GFRP bars embedded in concrete with the lower curing temperature (below 40°C). The effects of high curing temperature and alkaline concrete on GFRP bare bars are gradually significant. The deterioration degree of GFRP bare bars is higher than which were embedded in concrete with the increase of curing temperature. It is necessary to analyze the correlation of two test methods for the design of GFRP bars embedded in concrete because the variation of tensile properties of GFRP bars is not the same as the GFRP bars embedded in concrete.

3.2. Microanalysis of GFRP Bars. Figures 2 and 3 illustrate the effect of the micromorphology of GFRP bare bars and GFRP bars embedded in concrete with the standard-curing. Figures 3(a) and 3(b) show that the transverse section of GFRP bars is loose, and the longitudinal section of GFRP bars presents scattered fragments of resin as shown in Figures 3(c) and 3(d). The same phenomenon existed for the GFRP bare bars, but the transverse and longitudinal of fibers are relatively smooth. It is obvious that the damage degree of GFRP bars embedded in concrete is greater than the GFRP bare bars with standard-curing system. The main reason is that alkali ions destroy the backbone of glass molecules by breaking the Si-O-Si network to form dissolvable products. The reaction between the glass fiber and alkali will lead to degradation of the mechanical properties of glass fiber and hence to reduction in the fracture properties of the GFRP bars embedded in concrete beams.

Figure 5 shows that the steam-curing system with 60°C temperature aggravates the influence of the alkaline concrete environment on GFRP bars. However, the curing temperature (60°C) certainly has the impact on degradation of GFRP bars compared with Figures 2 and 4. Figures 4 and 5 show that there is no significant difference between GFRP bare bars and GFRP bars embedded in concrete under steam-curing system.

3.3. Glass Transition Temperature. Glass fibers are the most susceptible to degradation without the absence of moisture and alkalinity [13]. The reaction of GFRP composite with the alkali in concrete is a major durability concern. Typically, steam-curing concrete environments have high alkalinity [12]. Sun et al. [16] reported that glass fibers were known to degrade in the presence of water, and the moisture can decrease the glass transition temperature (T_g) of the resin, which potentially had a significant effect on the tensile strength of GFRP bars. High temperature environment will make the GFRP bar of the resin and glass fiber soft as well as cause a weakening or even loss of bond performance between the two, leading to a decline in tensile properties of GFRP bars.

Table 3 presents the glass transition temperature (T_g) for the first and second heating scans of GFRP bars. The T_g values of the second scan for all tested samples are higher than of the first scan. This result illustrates that the GFRP bars were not completely cured, as postcure reactions were shown in the process of the second heating scan. Compared with RE specimens, the cure ratio of C-Sta specimens decreases

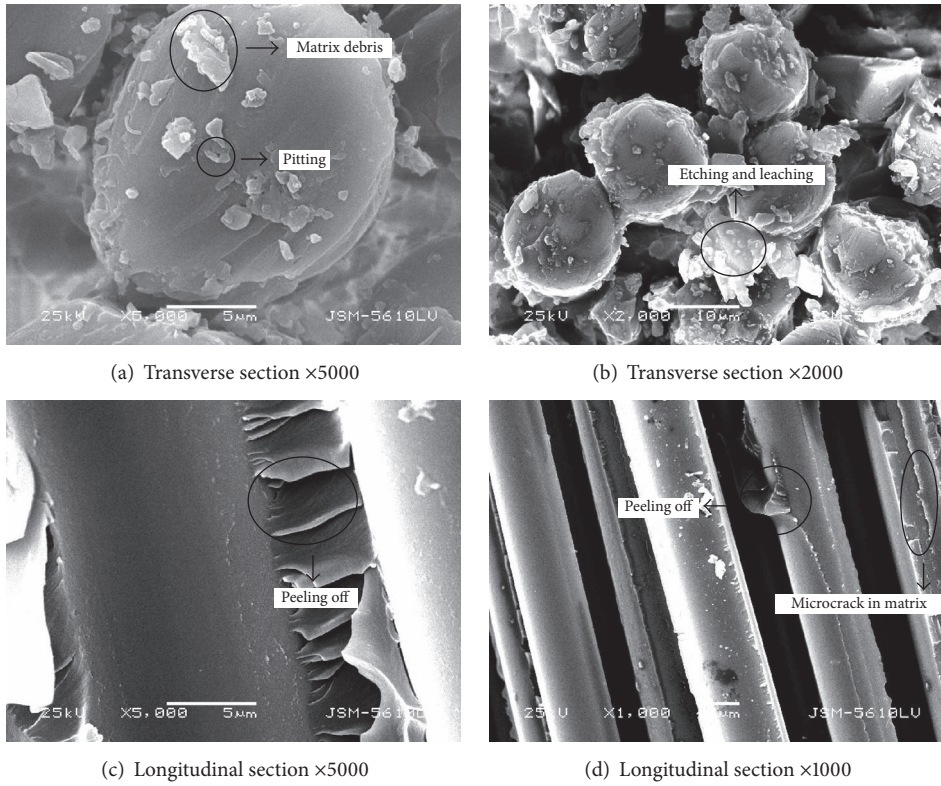


FIGURE 3: Microstructure morphology of GFRP bars embedded in concrete in the standard-curing environment.

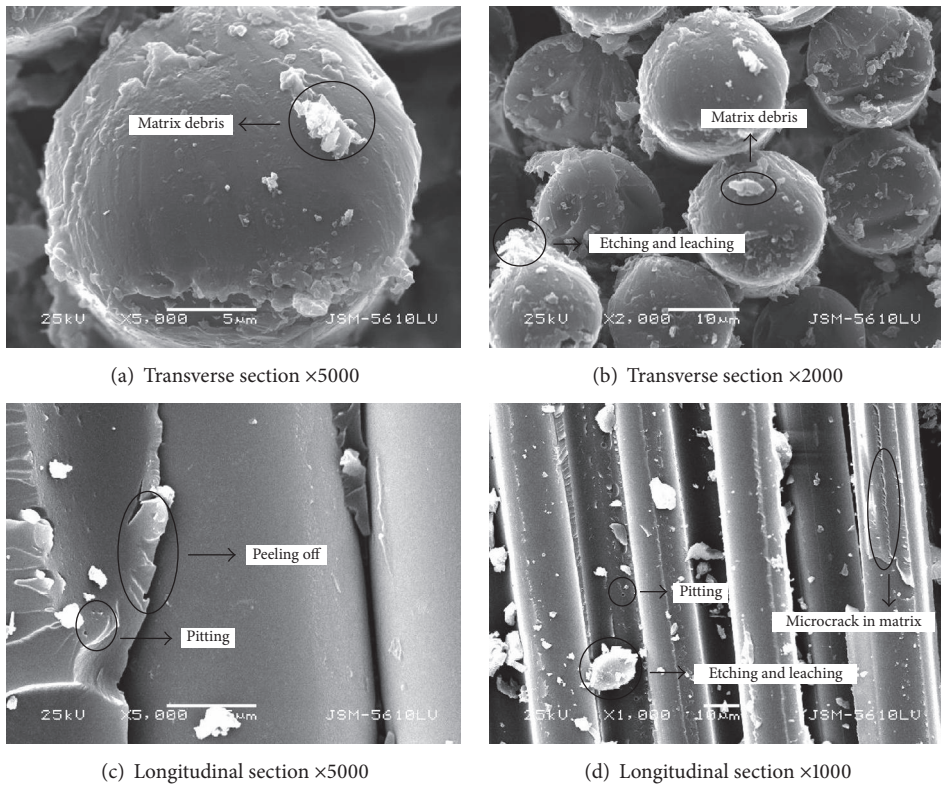


FIGURE 4: Microstructure morphology of GFRP bars in the steam-curing environment.

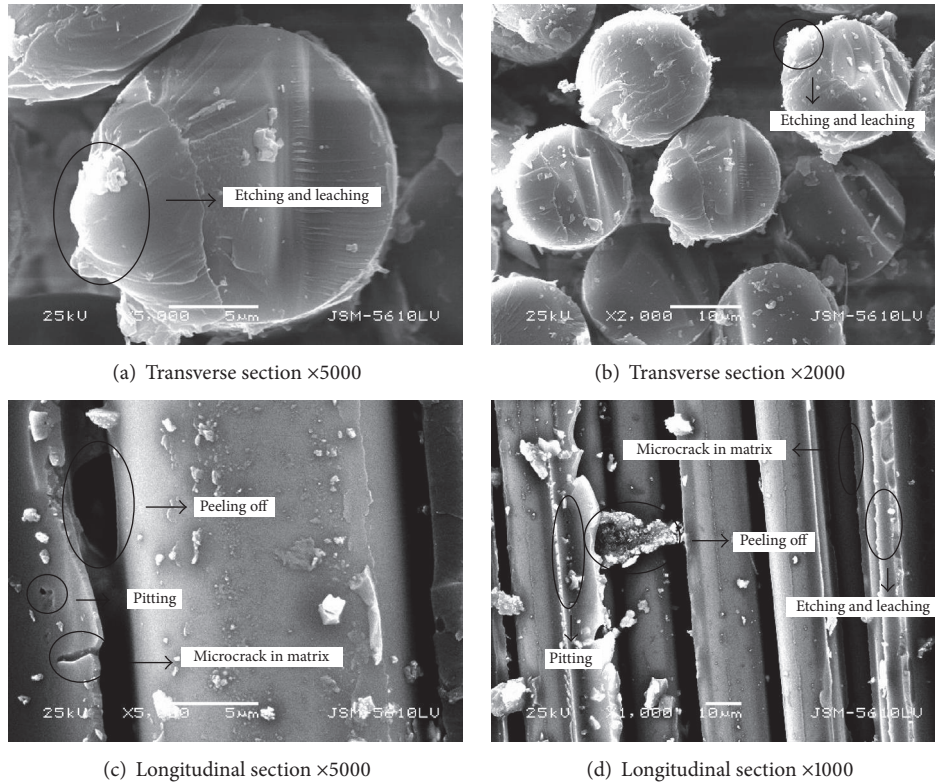


FIGURE 5: Microstructure morphology of GFRP bars embedded in concrete in the steam-curing environment.

TABLE 3: The glass transition temperature of GFRP bars under different curing systems.

| Name | Temperature/°C | Duration/m | T_g run 1/°C | T_g run 2/°C | Cure ratio/% |
|---------|----------------|------------|----------------|----------------|--------------|
| RE | — | — | 123 | 125 | 98.4 |
| C-Sta | 60 | 9 | 122 | 125 | 97.6 |
| C-Ste60 | 60 | 9 | 119 | 124 | 96.0 |

by 0.8%. It is indicated that the irreversible alkaline chemical reactions of the matrix resin have occurred. The glass transition temperature values of C-Ste specimens compared with C-Sta specimens decrease by 0.4%. This result could be explained by the fact that the high temperature curing process accelerated the chemical reaction rate of resin matrix. However, no matter under the standard-curing or steamed-curing concrete environment, no major degradation occurred at the polymer level and that the loss of tensile properties was not related to the degradation of the material.

3.4. Chemical Changes. Figure 6 shows the FTIR analysis of GFRP bars extracted from the standard-curing concrete beams and the steam-curing concrete beams. The curves of the different wavelengths are characterized by different wavelengths. Different vibration frequencies are characteristic of particular types of chemical groups, and the strong absorption band of hydroxyl is located between 3300 cm^{-1} and 3650 cm^{-1} . It can be seen from Figure 6 that the hydroxyl peak did not reveal any significant changes and the experimental spectra did not show any new characteristic absorption peaks in different curing environment. It

indicated that the matrix resins of GFRP bars embedded in standard-curing concrete beams and steam-curing concrete beams did not produce a new group after resin ester bond rupture.

4. Correlation Analysis on the GFRP Bare Bars and GFRP Bars Embedded in Concrete under Different Curing Systems

The relationship between the GFRP bare bars and GFRP bars embedded in concrete under different curing systems is established to obtain the tensile properties of GFRP bars embedded in concrete from the data of GFRP bare bars, which greatly reduced the difficulty of GFRP concrete structural design, prediction, and detection.

Table 2 shows that the influence of different curing temperatures on the tensile strength of GFRP bars embedded in concrete is different from the bare bars. When curing temperature is low (below 40°C), the influence of the curing process on bare bars is less than GFRP bars embedded in concrete; the influence on bare bars is greater than GFRP bars embedded in concrete with higher curing temperature

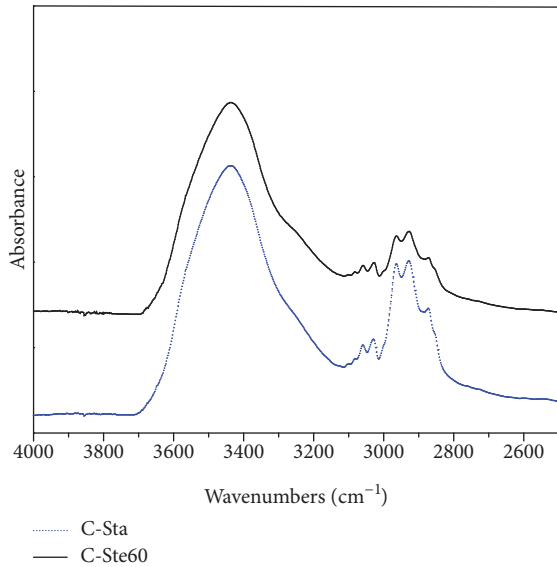


FIGURE 6: FTIR spectra for C-Sta and C-Ste60 samples.

(higher than 40°C), and the ratio of difference increases with the increase of curing temperature.

Figure 7 shows the relationship between the GFRP bare bars and GFRP bars embedded in concrete which can be expressed by exponential function:

$$K_B = 1.037 \exp(0.033T), \quad (1)$$

$$K_C = 1.275 \exp(0.025T), \quad (2)$$

where K_B , K_C are the attenuation ratio of tensile strength of GFRP bare bars and GFRP bars embedded in concrete and T is curing temperature.

The fitting square difference is 0.97 and 0.99 about the two exponential functions, which can be considered to be in accordance with the actual test results. Therefore, the formula (2)/(1) can be used to express the attenuation ratio relationship of tensile strength between the two methods:

$$\delta = 1.23 \exp(-0.008T). \quad (3)$$

The retention rate of tensile strength of GFRP bars embedded in concrete under different curing systems (Y_C) can be calculated by the attenuation ratio K_B and the correlation coefficient δ :

$$Y_C = 100 - \delta K_B. \quad (4)$$

It indicated that the design tensile strength, fracture reduction coefficient, and bond length determined are needed to fully consider the influence of microstructure and tensile properties of GFRP bars under the curing systems when GFRP bars in concrete component are used in high temperature curing process.

5. Conclusions

In this paper, a unique set of experimental data of the GFRP bare bars and the GFRP bars embedded in concrete

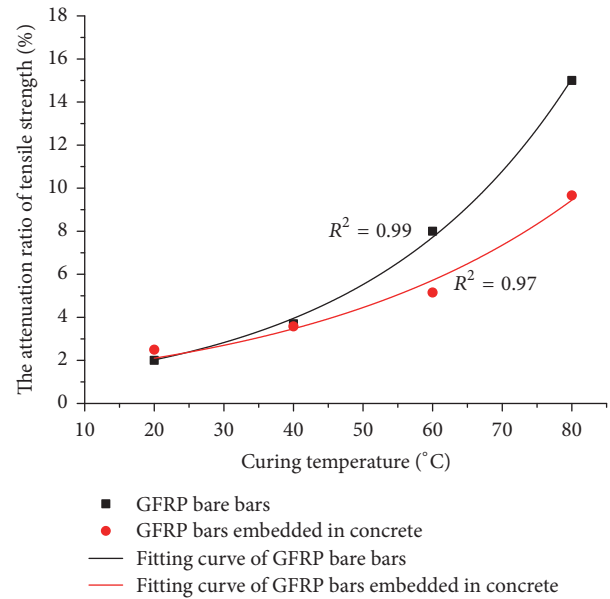


FIGURE 7: The change of tensile strength with curing temperature.

under standard-curing system (20°C) and steam-curing system (40°C, 60°C, and 80°C) was reported to characterize the combined effects of curing temperatures and alkaline concrete on tensile properties of GFRP bars. Based on the results of this study, the following conclusions may be drawn:

- (i) The tensile strength of GFRP bars as studied in this work showed that the combined effect of high curing temperature and alkaline concrete on GFRP bars was gradually significant, and the deterioration degree of tensile strength increased with the increase of curing temperature.
- (ii) The influence of different curing temperatures on the tensile strength of GFRP bars embedded in concrete was different from the bare bars; when curing temperature was low (below 40°C), the influence on bare bars was less than GFRP bars embedded in concrete; when the curing temperature was high (higher than 40°C), the influence of the curing process of bare bars was greater, and the ratio of difference increased with the increase of curing temperature.
- (iii) The microanalysis of GFRP bar was conducted. It was shown that the alkaline concrete environment and the steam-curing temperature of 60°C will cause some damage to the GFRP bars, without a significant difference between GFRP bare bars and GFRP bars embedded in concrete under steam-curing system.
- (iv) Based on the test data of different curing systems, the exponential correlation equation of two different test methods was established. The attenuation ratio of the tensile strength of GFRP bars embedded in concrete under different curing systems was predicted through the bare test, resulting in reliable results and high R^2 values. The conclusions of this paper not only can extend previous research results, but also reduce the

difficulty of the tensile strength test of GFRP bars embedded in concrete.

Competing Interests

The authors declare that they have no competing interests.

Acknowledgments

This research was supported by the National Natural Science Foundation of China (Grant no. 51178361).

References

- [1] B. Benmokrane, P. Wang, T. M. Ton-That, H. Rahman, and J.-F. Robert, "Durability of glass fiber-reinforced polymer reinforcing bars in concrete environment," *Journal of Composites for Construction*, vol. 6, no. 3, pp. 143–153, 2002.
- [2] Q. Khan, M. Sheikh, and M. Hadi, "Axial-flexural interactions of GFRP-CFFT columns with and without reinforcing GFRP bars," *Journal of Composites for Construction*, 2016.
- [3] Hughes Brothers, *Glass Fiber Reinforced Polymer (GFRP) Rebar—Aslan™ 100 Series FIBERGLASS REBAR*, Hughes Brothers, Seward, Neb, USA, 2011, <http://www.aslanfrp.com>.
- [4] W. Wang, *Experimental and Theoretical Studies on Durability of GFRP Rebars Exposed to Alkaline Environment*, Tongji University, 2011, (Chinese).
- [5] W. R. Yang, X. J. He, and L. Dai, "Damage behaviour of concrete beams reinforced with GFRP bars," *Composite Structures*, vol. 161, pp. 173–186, 2017.
- [6] X. J. He, J. N. Yang, and C. E. Bakis, "Tensile strength characteristics of GFRP bars in concrete beams with work cracks under sustained loading and severe environments," *Journal of Wuhan University of Technology-Materials Science Edition*, vol. 28, no. 5, pp. 934–937, 2013.
- [7] W. R. Yang, X. J. He, and L. Dai, "Shear performance of GFRP bars embedded in concrete beams with crack in different environments," in *Proceedings of the 12th International Symposium on Fiber Reinforced Polymers for Reinforced Concrete Structures (FRPRCS-12 '15)*, Nanjing, China, December 2015.
- [8] W. R. Yang, X. J. He, L. Dai, X. Zhao, and F. Shen, "Fracture performance of GFRP bars embedded in concrete beams with cracks in an alkaline environment," *Journal of Composites for Construction*, vol. 20, no. 6, Article ID 04016040, 2016.
- [9] A. Katz and N. Berman, "Modeling the effect of high temperature on the bond of FRP reinforcing bars to concrete," *Cement and Concrete Composites*, vol. 22, no. 6, pp. 433–443, 2000.
- [10] A. Abbasi and P. J. Hogg, "Temperature and environmental effects on glass fibre rebar: modulus, strength and interfacial bond strength with concrete," *Composites Part B: Engineering*, vol. 36, no. 5, pp. 394–404, 2005.
- [11] K. O. Kjellsen, R. J. Detwiler, and O. E. Gjrv, "Development of microstructures in plain cement pastes hydrated at different temperatures," *Cement and Concrete Research*, vol. 21, no. 1, pp. 179–189, 1991.
- [12] G. M. Campbell and R. J. Detwiler, "Development of mix designs for strength and durability of steam-cured concrete," *Concrete International*, vol. 15, no. 7, pp. 37–39, 1993.
- [13] H. H. Patel, C. H. Bland, and A. B. Poole, "The microstructure of concrete cured at elevated temperatures," *Cement and Concrete Research*, vol. 25, no. 3, pp. 485–490, 1995.
- [14] M.-F. Ba, C.-X. Qian, X.-J. Guo, and X.-Y. Han, "Effects of steam curing on strength and porous structure of concrete with low water/binder ratio," *Construction and Building Materials*, vol. 25, no. 1, pp. 123–128, 2011.
- [15] Z. M. He, *Heat Damage Effects of Steam on Concrete and Corresponding Improvement Measures*, Central South University, 2012 (Chinese).
- [16] C. Sun, W. H. Qiu, X. B. Zeng et al., "Contrast research on mechanical properties experimental of GFRP bars for a long time under different environmental conditions," *Fiber Reinforced Plastics/Composites*, no. 8, pp. 88–91, 2014 (Chinese).
- [17] V. Dejke, *Durability of FRP Reinforcement in Concrete*, Chalmers University of Technology, Gothenburg, Sweden, 2001.
- [18] ACI, "Guide for the design and construction of structural concrete reinforced with fiber-reinforced polymer (FRP) bars," ACI 440.1R-15, American Concrete Institute, Farmington Hills, Mich, USA, 2015.
- [19] JGJ55-2011, *Concrete Mix Design Procedures*, China Building Industry Press, Beijing, China, 2011.
- [20] China Building Industry Press, "Ordinary concrete mechanics performance test method standard," Tech. Rep. GB/T50081-2002, China Building Industry Press, 2003.
- [21] TB10752-2010, *High Speed Railway Bridge Engineering Construction Quality Acceptance Standards*, China Railway Press, Beijing, China, 2011.
- [22] ACI 440.3R-04, *Guide Test Methods for Fiber-Reinforced Polymers (FRPs) for Reinforcing or Strengthening Concrete Structures*, American Concrete Institute Farmington Hills, Farmington Hills, Mich, USA, 2004.
- [23] J. M. Sousa, J. R. Correia, S. Cabral-Fonseca, and A. C. Diogo, "Effects of thermal cycles on the mechanical response of pultruded GFRP profiles used in civil engineering applications," *Composite Structures*, vol. 116, no. 1, pp. 720–731, 2014.
- [24] M. Robert and B. Benmokrane, "Combined effects of saline solution and moist concrete on long-term durability of GFRP reinforcing bars," *Construction and Building Materials*, vol. 38, no. 1, pp. 274–284, 2013.
- [25] A. Mufti, M. Onofrei, B. Benmokrane et al., "Durability of GFRP reinforced concrete in field structures," *ACI Structure Journal*, vol. 230, pp. 1361–1378, 2005.

Research Article

Bond-Slip Models for FRP-Concrete Interfaces Subjected to Moisture Conditions

Justin Shrestha,¹ Dawei Zhang,² and Tamon Ueda³

¹Engineering Development Department, Takenaka Civil Engineering & Construction Co., Ltd., Shinsuna, Koto-ku, Tokyo 136-8570, Japan

²Department of Civil Engineering, College of Civil Engineering and Architecture, Zhejiang University, Hangzhou 310058, China

³Division of Engineering and Policy for Sustainable Environment, Faculty of Engineering, Hokkaido University, Kita 13 Jo Nishi 8 Chome Kita-ku, Sapporo 060-8628, Japan

Correspondence should be addressed to Dawei Zhang; dwzhang@zju.edu.cn

Received 22 September 2016; Accepted 14 December 2016; Published 18 January 2017

Academic Editor: Baolin Wan

Copyright © 2017 Justin Shrestha et al. This is an open access article distributed under the Creative Commons Attribution License, which permits unrestricted use, distribution, and reproduction in any medium, provided the original work is properly cited.

Environmental related durability issues have been of great concerns in the structures strengthened with the fiber reinforced polymers (FRPs). In marine environment, moisture is one of the dominant factors that adversely affect the material properties and the bond interfaces. Several short-term and long-term laboratory experimental investigations have been conducted to study such behaviors but, still, there are insufficient constitutive bond models which could incorporate moisture exposure conditions. This paper proposed a very simple approach in determining the nonlinear bond-slip models for the FRP-concrete interface considering the effect of moisture conditions. The proposed models are based on the strain results of the experimental investigation conducted by the authors using 6 different commercial FRP systems exposed to the moisture conditions for the maximum period of 18 months. The exposure effect in the moisture conditions seems to have great dependency on the FRP system. Based on the contrasting differences in the results under moisture conditions, separate bond-slip models have been proposed for the wet-layup FRP and prefabricated FRP systems. As for the verification of the proposed model under moisture conditions, predicted pull-out load was compared with the experimental pull-out load. The results showed good agreement for all the FRP systems under investigation.

1. Introduction

The use of fiber reinforced polymer (FRP) is extensive in strengthening and rehabilitation of infrastructures. However, there are great concerns regarding the environment-related durability problems. To precisely predict the service life of the strengthened/rehabilitated structures, it is necessary to take account of the environmental durability related deteriorations. In the marine environment, the moisture is considered as one of the dominant factors which could affect both the material and the bond properties of the FRP strengthened/rehabilitated concrete structures. Various existing design guidelines for FRP strengthening reinforced concrete members recommended deterioration coefficient for FRP materials to reflect the effect of exposure environment. The coefficient was usually applied to the material properties of FRP itself, while the effect of environment on

the bond-slip relation of FRP-concrete interfaces was not considered. Meanwhile, there are quite a number of studies trying to simulate the marine environmental conditions by altering the materials, immersion solutions, exposure durations, environmental conditions, testing methods, and so forth [1–5]. Among them, most of the studies have pointed out that the moisture conditions severely deteriorated bond interfaces between FRP and substrate concrete while the degree of effect varied. Generally, the moisture affects the interface between FRP and the concrete resulting in the reduction of the bond capacity. Such effects are usually reflected by transition in failure mode from concrete cohesion to the mixed or adhesion failures [1]. The extensive experimental investigation conducted by the authors found that the effect of moisture was largely dependent on the selection of the materials. Among 6 of the commercial FRP systems investigated for the maximum moisture immersion

period of 18 months, two of the cases suffered significant deterioration in the bond properties compared to the rest of the systems [6]. These experimental findings should be accounted properly into the bond interface properties by incorporating the moisture effects in the bond-slip models.

In order to evaluate the interfacial bond mechanism between FRP and concrete and to simulate the interfacial behavior of FRP strengthened members under moisture condition, there is a necessity to develop related bond stress-slip models [7]. Dai et al. [8] proposed a simple analytical method of determining the nonlinear bond stress-slip models, which was proved to predict the bond behavior of the FRP-concrete interface with fairly good accuracy. However, the model was only meant to predict for the cases without the influence of environmental actions that a structure usually experiences during its service life. Some of the available literatures considering such environmental effects in the bond-slip models are briefly summarized hereafter. Dai et al. [9] developed nonlinear bond-slip model for FRP laminates externally bonded to concrete at elevated temperature considering the existing test data of FRP-concrete bonded interfaces at temperatures ranging from 40 to 180°C. They modified the two-parameter bond-slip model to consider the influences of both temperature induced thermal stress and temperature induced bond degradation. The interfacial fracture energy decreased after approaching the glass transition temperature of the bonding adhesive. The proposed temperature dependent bond-slip model was able to provide reasonably close prediction despite the large scatter of the data. Yun [10] developed an analytical model for bond-slip relationship considering the effect of freeze-thaw cycles. Yun used the measured slip distribution to propose the bond-slip relation. According to the model, if the bond length is sufficient then the bond-slip relation for that region does not vary along the bonded area, whereas if the bond length is not sufficient then the bond-slip relation varies with the location.

In a study on effect of moist environment, Ouyang and Wan [11] identified the interface region relative humidity (IRRH) as the primary factor that affected the bond fracture energy of FRP-concrete interface in moist environment and the ultimate bond performance. A deterioration model was developed to describe the local relation between the interfacial fracture energy and the IRRH in moist environment [12]. Similarly, Silva et al. [13] investigated the effect of moisture, salt fog, and temperature cycles on the CFRP/GFRP-to-concrete interfaces for the maximum period of 10,000 hours. The authors compared several components such as maximum bond stresses, ultimate slip, fracture energies, and effective bond length and proposed bond stress-slip laws taking into account those effects.

All the above literatures point out that the bond-slip models incorporating the effects of long-term environmental conditions are extremely scarce and the findings are based on a certain FRP system. But as the environmental durability is greatly dependent on the materials, it is crucial to consider many FRP systems while deriving the interfacial bond models. Therefore, the objective of this paper is to propose interface bond-slip models considering the long-term effect of moisture exposure up to 18 months in 6 commercially

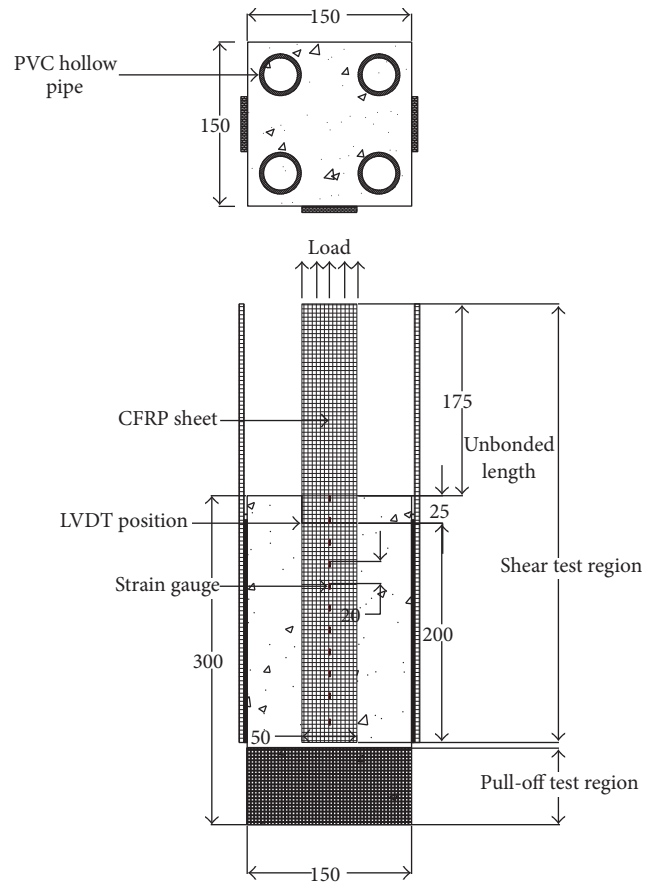


FIGURE 1: Details of bond specimen (unit: mm) for single lap shear test.

available FRP systems in the world. Brief experimental information required in the paper is presented hereafter.

2. Experimental Details

The experimental program consisted of single lap shear bond specimens prepared by using 6 commercial FRP systems from well-known Japanese, European, and US based manufacturers. This included 4 FRP sheet bonding instances, one plate bonding, and one strand sheet bonding along with the suggested epoxy resins. The 6 systems are identified as SB-A, SB-B, SB-C, SB-D, SB-E, and SB-F, respectively. The epoxy resins were two component room curing type resin with base and hardener. The base was a bisphenol-A type epoxy resin, whereas the hardener was modified polyamines. Prior to the bonding of the FRP, primer layer was applied on the concrete for the systems SB-A and SB-B based on the suggestion of the manufacturers.

Altogether 126 concrete prisms were prepared with the dimensions of 150 × 150 × 300 mm as shown in Figure 1. The compressive strength of the concrete cylinders tested after 28 days of curing was 29.50 MPa. For the preparation of the bond specimens, the concrete surface was treated uniformly with a disk grinder till the coarse aggregates were

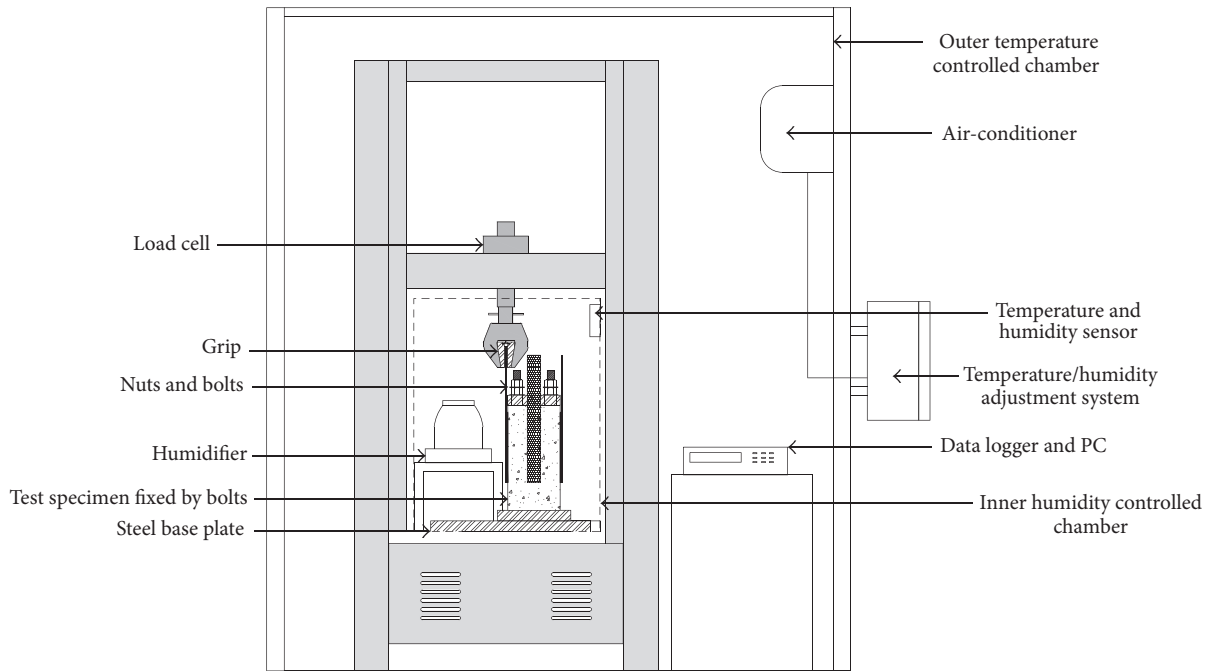


FIGURE 2: Test arrangement schematic for the bond specimen inside the environmental testing chamber.

exposed and cleaned properly. Then FRPs were attached on 3 sides of the concrete following the application procedure of each manufacturer. For the shear bond test, FRP strip of 50 mm width was attached on the concrete blocks with the bonding length of 200 mm. As for the tensile test, FRP strip of 50 mm width and 150 mm length was bonded at the bottom of the specimen to conduct the direct pull-off test. All the specimens were left for curing in the laboratory environmental conditions for more than a month. The nonimmersion specimens, which are also referred to as the 0-month case, were kept at ambient condition inside the laboratory until the test. As for the moisture exposure conditions, the specimens were completely immersed in a water pool maintained at a constant temperature of 20°C for the maximum period up to 18 months. The immersed specimens were taken out from the water every 3-month interval and immediately transferred into the environmental chamber (Figure 2) for the bond tests. Inside the environmental chamber, the humidity of over 85% and temperature of $20 \pm 3^\circ\text{C}$ were maintained throughout the test period. Three samples were tested for each exposure condition to validate the results. However, the strain information was measured only in one of the three cases during the shear bond test at 0-, 6-, 12-, and 18-month duration of exposure. The strain gauges were placed at spacing of 20 mm from the loaded end to 160 mm. The strain gauge arrangements and the moisture chamber are shown in Figure 3.

3. Experimental Results and Discussions

The detailed experimental results are reported in Shrestha et al. [14]. Thus, only a brief summary is presented in this paper. According to the results of 18-month exposure, the



FIGURE 3: Specimen during the test under moisture condition.

moisture effect varied greatly depending on the FRP systems. Overall, the wet-layup FRP systems performed poorly in comparison with the prefabricated FRP systems after moisture exposure. All the wet-layup FRP systems showed certain deteriorations due to moisture exposure and the effects were quite significant in two of the systems. The average bond strength was reduced by 25% and 16%, respectively, for SB-C and SB-D after the exposure, whereas the reduction in systems SB-A and SB-B was less than 5%. As indicated by the observation of the failure modes, the reductions were mainly due to local deterioration of the bonds at the interfaces as a result of moisture exposure. Such deterioration of the bond was most serious when the adhesion failures occurred as observed in systems SB-C and SB-D, while transition of

TABLE 1: Verification of Dai's approach using different FRP bonding systems.

| Fiber material | System | A | B | R ² | E _f (N/mm ²) | t _f (mm) | (P _{pre.}) | (P _{exp.}) | P _{pre./P_{exp.}} |
|---|--------|--------|-------|----------------|-------------------------------------|---------------------|----------------------|----------------------|------------------------------------|
| CFS | SB-A-0 | 0.0077 | 10.96 | 0.948 | 230000 | 0.111 | 9.78 | 11.57 | 0.84 |
| CFS | SB-B-0 | 0.0065 | 14.46 | 0.954 | 230000 | 0.111 | 8.33 | 9.82 | 0.85 |
| CFS | SB-C-0 | 0.007 | 10.73 | 0.967 | 230000 | 0.218 | 17.52 | 15.81 | 1.11 |
| CFS | SB-D-0 | 0.006 | 11.81 | 0.952 | 240000 | 0.176 | 12.65 | 11.77 | 1.07 |
| CFSS | SB-E-0 | 0.0034 | 14.4 | 0.968 | 245000 | 0.333 | 13.71 | 12.49 | 1.1 |
| CFRP | SB-F-0 | 0.002 | 17.44 | 0.969 | 210000 | 1.4 | 29.55 | 26.06 | 1.13 |
| Average of the ratio of the predicted to experimental ultimate load | | | | | | | | | 1.02 |

failure modes from concrete cohesion to the mixed mode resulted in a mere reduction in the bond strength. In contrast, prefabricated FRP systems SB-E and SB-F showed either no effect or some positive effect of moisture exposure conditions. No correlation was found with the evolution of the material properties to explain such phenomenon. However, it is well-known that the prefabricated FRPs have better and consistent quality than the wet-layup FRPs which is due to the process of resin impregnation and curing of the fibers in the factory. It could be one of the reasons for the overall better performance. But the obvious distinction in the behavior was mainly observed in the failure modes after the moisture exposure. For the wet-layup, it was either mixed or interface failure for most of the cases. In contrast, failure modes for the prefabricated cases were mostly concrete or mixed failure suggesting stronger adhesion bonds at the interface [14].

Finally, the FRP strain results obtained from the experiments were used to develop the bond-slip relations for moisture exposure conditions which is discussed hereafter.

4. Analytical Approach

4.1. Review of Dai's Methodology. Dai et al. [8] developed a simple method to determine the local bond stress-slip relationships of FRP sheet-concrete interfaces which required pull-out force and loaded end slip. Based on the method, a simple interfacial shear stress-slip (τ - s) relationship was proposed with only two parameters; interfacial fracture energy, G_f , and interfacial material constant B . The applicability of the method has already been verified with the experimental results. Brief background of the model is presented hereafter.

Dai et al. [8] used a simple mathematical function as given in (1) which was proved to represent the strain-slip (ε - s) relationship with a good accuracy when compared with the experimental results.

$$\varepsilon = f(s) = A(1 - e^{(-Bs)}), \quad (1)$$

where A and B are experimental parameters obtained from the nonlinear regression between the plots of strain-slip relationship. The physical meaning of A corresponds to the maximum strain in the FRP provided the bond length is sufficient and B can be regarded as the ductility index which controls the shape of the bond-slip curve [9].

Then the expression for the τ - s is given by

$$\tau = A^2 B E_f t_f e^{(-Bs)} (1 - e^{(-Bs)}). \quad (2)$$

E_f and t_f are Young's modulus in MPa and thickness of FRP in mm, respectively.

By integrating τ - s function, the interfacial fracture energy G_f can be obtained as

$$G_f = \frac{1}{2} A^2 E_f t_f. \quad (3)$$

The final expression of τ - s in terms of G_f and B is as follows:

$$\tau = 2B G_f (e^{(-Bs)} - e^{(-2Bs)}). \quad (4)$$

The relationship for the ultimate pull-out load is given by

$$P_{\max} = b_f \sqrt{2E_f t_f G_f}. \quad (5)$$

Even though the above approach is not dependent on the FRP reinforcement type, the validity of the above approach has not been tested for the strand sheet and plate bonding cases. Therefore, applicability of Dai's methodology was first confirmed in case of all the six CFRP systems in ambient conditions. As for the evaluation of the accuracy of the model, integral absolute error (IAE) was calculated as given by (6). This IAE factor which is the cumulative error value is sensitive to the deviation of test results in the model. Previous researchers have used this factor to evaluate the accuracy of the model [15, 16].

$$\text{IAE} = \sum \frac{\sqrt{(\text{Expe.} - \text{Theo.})^2}}{\sum |\text{Expe.}|} \quad (6)$$

Table 1 shows fairly good ratio of predicted ultimate load and experimental ultimate load with the average ratio of close to 1 with an IAE of 11.55%. The predicted ultimate loads were calculated using (5) where the parameter A was determined by regression analysis of the experimental strain-slip relationship given by (3) for each individual case.

It is known that Dai's methodology was only developed and confirmed for the ambient environment conditions; however, the applicability of the method in the case of other environmental exposures is still unknown. Therefore, the experimental data obtained from the shear test conducted at different moisture conditions were used to predict the ultimate load to check its applicability other than ambient condition. Figure 4 shows the comparison of predicted and experimental ultimate loads, the former of which were

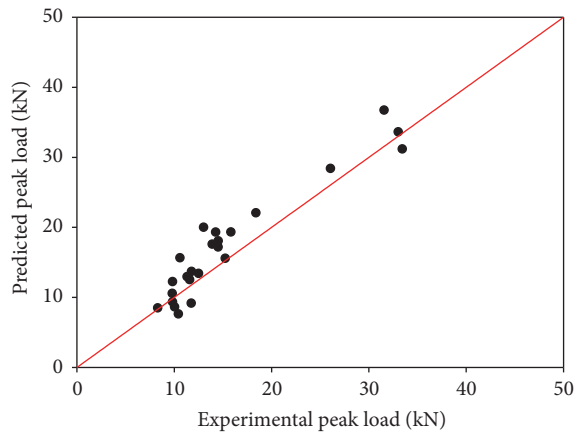


FIGURE 4: Comparison of predicted and experimental ultimate loads using Dai's method. Average ratio of predicted to experimental ultimate load = 1.12.

calculated by (5) with the regressed value of A for the case at ambient condition. The figure shows slight overestimation of the ultimate load by the predicted model, signifying that the moisture affected cases cannot be predicted precisely with it. The average ratio of predicted to the experimental ultimate load is 1.12 with IAE of 16.43%, which is higher than that for the case without the environmental effects (as shown in Table 1). This could be possibly due to the fact that the strain-slip (ϵ - s) relationship in case of the ambient exposure is different from that of the moisture exposure. The local deteriorations caused by the moisture at the interfacial region affects the debonding process. Therefore, to incorporate such local effects in the model, Dai's methodology of determining the bond-slip relation should be modified accordingly.

4.2. Analytical Approach to Nonlinear Bond Stress-Slip Model for Moisture Exposure. The brief steps to determine the bond-slip relationships in moisture condition are shown in Figure 5. According to Dai et al.'s [8] concept, when there is a sufficient bond length, the pull-out forces and the slips at the loaded end can be measured accurately through which the relationship between the strain in the FRP sheets and the slips can be determined easily. Based on that, a single ϵ - s at the loaded end of the FRP was used to determine the values of A and B by nonlinear regression analysis as shown in (1). However, in this study, the local responses along the bond length were measured by strain gauges attached at the regular interval. The corresponding slips at those locations were calculated by integration of strain. The obtained ϵ - s relationships at such different locations were regressed using a common mathematical function as given in (1), to determine a single regressed curve that would represent the average response of ϵ - s distribution throughout the bonded length. For the regression purpose, only those locations were selected in which the bond lengths were greater than the effective bond length estimated from the strain distribution. In Figure 6, typical measured strain-slip data at 0, 6, 12, and 18 months and their corresponding regressed curve fittings are shown for SB-B system. Similarly, the regressed ϵ - s curves were determined

in all the 6 FRP systems at different exposure durations which are shown in Figure 7. The regression coefficients in all the cases with their correlation factors are given in Table 2. The values of correlation factor lie within the range of 0.92 to 0.97, showing a very good agreement between the proposed shape function (see (1)) and the experimental data. For all the FRP systems shown in Figure 7, ϵ - s curves show distinct responses to the moisture exposure durations. The moisture at the interface region seems to influence the load transfer mechanism between FRP composite and concrete, affecting the ultimate strains on the FRPs. Specimens SB-C and SB-D show the greatest reduction in the peak strain values and increase in interfacial slip after exposure, whereas specimens SB-E and SB-F show increase in peak strain after exposure. Such effect is unclear in SB-A case, but SB-B case shows a small reduction in the peak strain after exposure.

Using the obtained regression coefficient values of A for each individual FRP systems at each exposure duration, the fracture energies were calculated using (3). As for the stiffness of the FRP composites, it is assumed to be unaffected by the moisture conditions; thus, the same values provided by the manufacturers were used for the calculations. This assumption seems to be fair in case of CFRP composites, as the carbon fibers are the major component in the composite, which are highly durable material against environmental degradations. However, it cannot be denied that some degradations could occur in epoxy resin binding those fibers or resin-fiber interfaces, but its overall contribution towards the ultimate strength and stiffness would be small for the CFRPs. Both Nguyen et al. [17] and Sciolti et al. [18] have found similar negligible effect of immersion in water on the tensile modulus of the CFRP, when exposed for 1 year and 30 weeks, respectively.

All the calculated fracture energies and the regressed values A and B are presented in Table 2. For the comparison purpose, the table also shows the normalized fracture energy values, which were calculated by (3). For each system, it is the ratio between the fracture energy for a particular exposure duration to the fracture energy for the nonimmersion case (0 months). For systems SB-A, SB-B, SB-C, and SB-D, the normalized fracture energies are mostly less than 1 after exposure indicating the reduction in the bond capacity in presence of moisture. In contrast, SB-E and SB-F show higher fracture energies after exposure indicating improved bond properties after moisture exposure. As the fracture energy and the bond strength are closely correlated (also shown by (5)), their behaviors towards the moisture exposure duration have similar trends in all the FRP systems. The loss/gain in the bond strengths after immersion can be explained by reduction/increment in fracture energy due to degradation/improvement in the bond properties from moisture exposure. Even though many of the previous studies have observed more severe degradation in bond properties with the increase in exposure duration, it was not the case in the present study. Two different sets of responses were obtained based on the FRP systems. Thus, all the systems cannot be generalized into a single common framework. Nevertheless, to visualize the effect of exposure, the immersion cases were simply grouped as one by taking the average of all the values,

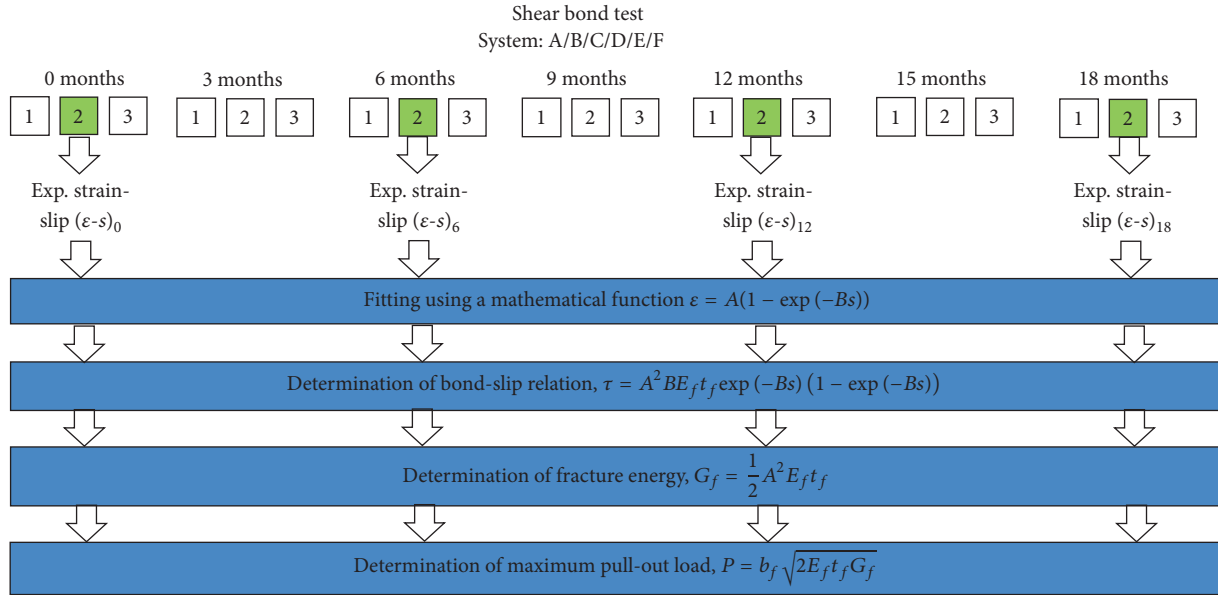


FIGURE 5: Brief procedure to determine bond-slip relations in moisture conditions.

TABLE 2: Regression coefficients and fracture energies of all the specimens.

| Specimens | Exposure duration (months) | E_f (N/mm ²) | t_f (mm) | A | B | R^2 | G_f (N/mm) | Normalized G_f |
|-----------|----------------------------|----------------------------|------------|---------|-------|-------|--------------|------------------|
| SB-A-0 | 0 | 230000 | 0.111 | 0.00766 | 10.96 | 0.95 | 0.749 | 1.00 |
| SB-A-6 | 6 | 230000 | 0.111 | 0.01066 | 6.08 | 0.93 | 1.451 | 1.94 |
| SB-A-12 | 12 | 230000 | 0.111 | 0.00693 | 12.62 | 0.95 | 0.614 | 0.82 |
| SB-A-18 | 18 | 230000 | 0.111 | 0.00733 | 9.79 | 0.97 | 0.686 | 0.92 |
| SB-B-0 | 0 | 230000 | 0.111 | 0.00652 | 14.46 | 0.95 | 0.543 | 1.00 |
| SB-B-6 | 6 | 230000 | 0.111 | 0.00622 | 13.02 | 0.97 | 0.494 | 0.91 |
| SB-B-12 | 12 | 230000 | 0.111 | 0.00621 | 11.74 | 0.94 | 0.493 | 0.91 |
| SB-B-18 | 18 | 230000 | 0.111 | 0.00591 | 12.06 | 0.96 | 0.446 | 0.82 |
| SB-C-0 | 0 | 230000 | 0.218 | 0.00699 | 10.73 | 0.97 | 1.225 | 1.00 |
| SB-C-6 | 6 | 230000 | 0.218 | 0.00616 | 10.88 | 0.93 | 0.952 | 0.78 |
| SB-C-12 | 12 | 230000 | 0.218 | 0.00561 | 12.12 | 0.95 | 0.790 | 0.64 |
| SB-C-18 | 18 | 230000 | 0.218 | 0.00664 | 10.19 | 0.95 | 1.106 | 0.90 |
| SB-D-0 | 0 | 240000 | 0.176 | 0.00599 | 11.81 | 0.95 | 0.758 | 1.00 |
| SB-D-6 | 6 | 240000 | 0.176 | 0.00549 | 13.93 | 0.92 | 0.637 | 0.84 |
| SB-D-12 | 12 | 240000 | 0.176 | 0.00451 | 16.81 | 0.96 | 0.430 | 0.57 |
| SB-D-18 | 18 | 240000 | 0.176 | 0.00542 | 14.99 | 0.97 | 0.621 | 0.82 |
| SB-E-0 | 0 | 245000 | 0.333 | 0.00336 | 14.40 | 0.97 | 0.461 | 1.00 |
| SB-E-6 | 6 | 245000 | 0.333 | 0.00399 | 13.72 | 0.92 | 0.650 | 1.41 |
| SB-E-12 | 12 | 245000 | 0.333 | 0.00389 | 10.98 | 0.93 | 0.618 | 1.34 |
| SB-E-18 | 18 | 245000 | 0.333 | 0.00432 | 13.99 | 0.95 | 0.762 | 1.65 |
| SB-F-0 | 0 | 210000 | 1.4 | 0.00201 | 17.44 | 0.97 | 0.594 | 1.00 |
| SB-F-6 | 6 | 210000 | 1.4 | 0.00238 | 15.72 | 0.96 | 0.833 | 1.40 |
| SB-F-12 | 12 | 210000 | 1.4 | 0.00240 | 13.36 | 0.96 | 0.847 | 1.43 |
| SB-F-18 | 18 | 210000 | 1.4 | 0.00241 | 15.50 | 0.95 | 0.854 | 1.44 |

irrespective of the exposure duration, and then compared with the reference or nonimmersion condition. Figure 8 shows such relative changes in both bond strengths and fracture energies. From the figure, significant reductions are evident in SB-C and SB-D cases, with small changes in SB-A

and SB-B cases. Nevertheless, such losses in bond strengths and fracture energies could be attributed to degradation of the interfaces caused by moisture conditions. In contrast to such behaviors, specimens SB-E and SB-F showed significant gain in performance after exposure.

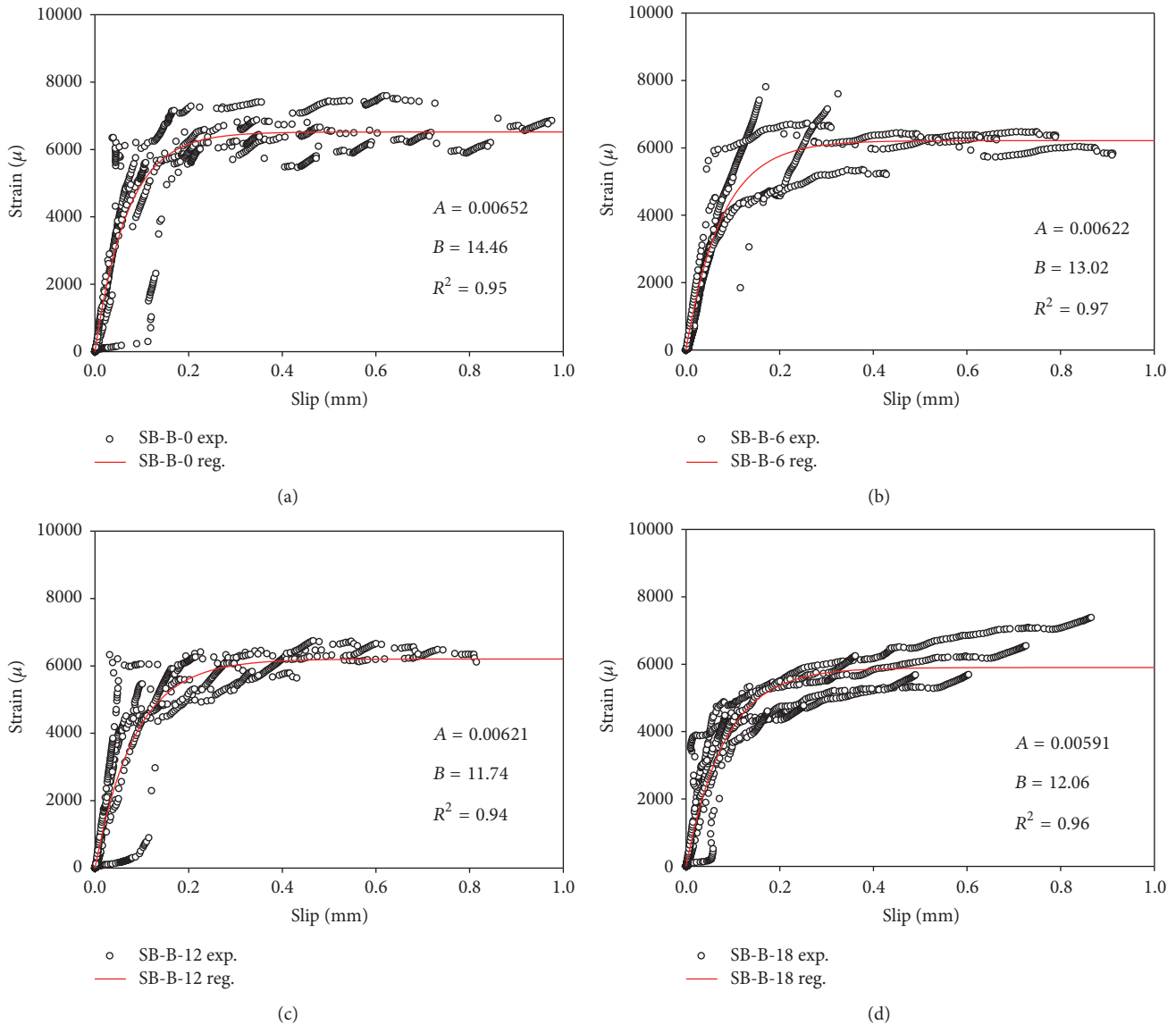
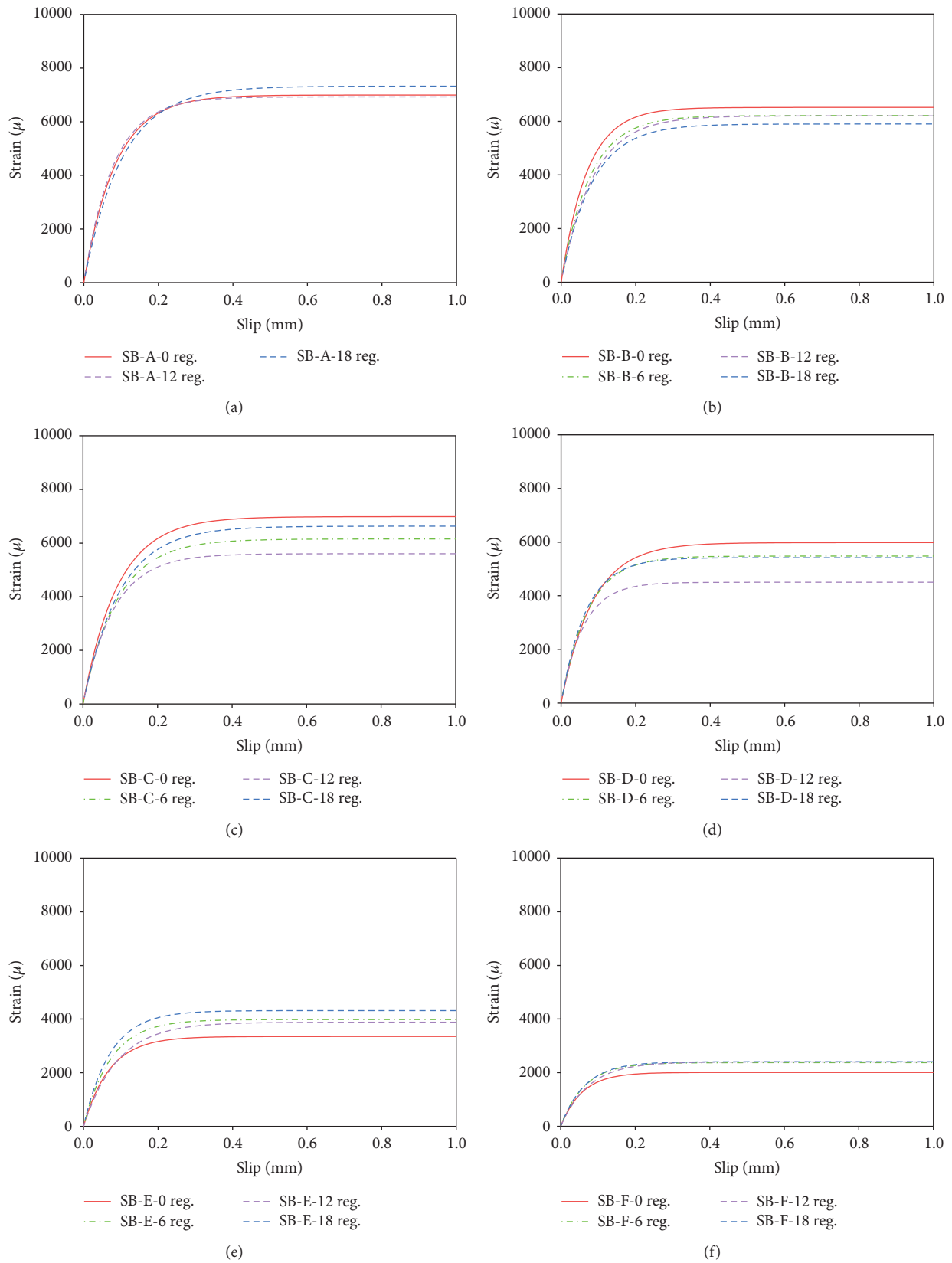


FIGURE 6: Regressed ε - s curve from the experimental results for specimen SB-B.

The proposed bond-slip models from (4) using two known parameters, A and B , were compared with the experimentally obtained local bond-slip curves at different locations as shown in Figure 9. As for the nature of the experimental local bond-slip relationship, there are some variations on the bond-slip curves at different locations even for the same specimen. This means that one cannot choose any one local bond-slip relationship as the representative one. Thus, it is common to take the average response of such local phenomenon. In this regard, the predicted models showed fair agreement showing average response of the experimental data.

4.2.1. Influence of Moisture Exposure on the Parameters G_f and B . The interfacial fracture energy (G_f), which was calculated from A based on (3), and the ductility index (B) are two of the

key parameters in the bond-slip models. While introducing the moisture effect, it is necessary to know the influence of the moisture exposure on those two parameters. The changes in the material or the interfacial properties due to the moisture exposure will be reflected by changes in these parameters. Since each FRP system has its own set of G_f and B , which are dependent on the FRP material properties, concrete properties, surface roughness, and so forth, they are normalized by the reference/nonimmersion cases, to know the influence of moisture exposure conditions and to make a comparison among different FRP systems. Based on the trend of the experimental results, FRP systems were divided into two categories. The first category includes all the wet-layup FRP systems SB-A, SB-B, SB-C, and SB-D that showed some form of reductions in the bond strength and the fracture energy after the exposure to moisture, whereas the second category consisted of prefabricated FRP systems SB-E and

FIGURE 7: Regressed ϵ - s curves for all the specimens.

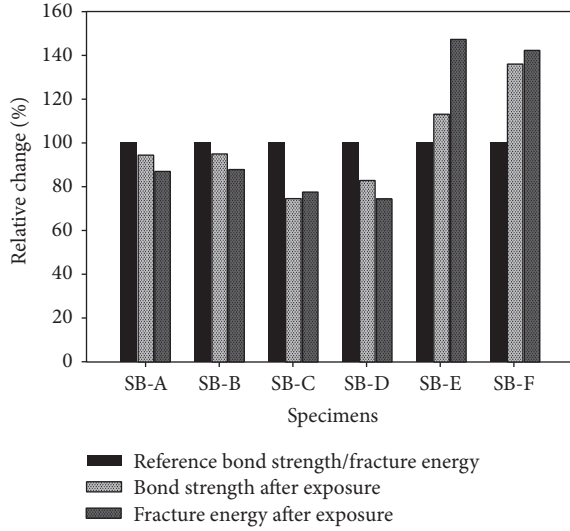


FIGURE 8: Relative change in bond strength and fracture energy after immersion.

SB-F that showed improvement in the bond strength and the fracture energy after the exposure to moisture.

To evaluate such effect of moisture, the parameters B and G_f at any exposure duration (t , in months) was normalized by the nonimmersion case (0 months). $B_t^{\text{Env.}}$ and $G_{f_t}^{\text{Env.}}$ are the ductility parameter and the interfacial fracture energy, respectively, for immersion case, whereas B_0 and G_{f_0} are for the nonimmersion case. The effect of moisture exposure duration on the normalized parameters $B_t^{\text{Env.}}/B_0$ for the wet-layup FRP systems and the prefabricated FRP systems were fitted into an exponential relation which are shown in Figures 10(a) and 10(b), respectively. Similarly, the effect of moisture exposure duration (t , in months) on the normalized parameters $G_{f_t}^{\text{Env.}}/G_{f_0}$ for the wet-layup FRP systems and the prefabricated FRP systems were also best fitted in an exponential relation which are shown in Figures 11(a) and 11(b), respectively. Those figures clearly indicate larger effect of exposure durations until the first 6 months and then remained almost unchanged until the 18 months. The following expressions were obtained from a simple regression analysis which best described the nature of the parameters' dependency on the exposure duration.

In case of the wet-layup FRP systems,

$$(B_t^{\text{Env.}})_w = B_0 (1.05 - 0.05e^{-0.40t}) \quad (7)$$

$$(G_{f_t}^{\text{Env.}})_w = G_{f_0} (0.8 + 0.2e^{(-0.38t)}). \quad (8)$$

In case of the prefabricated FRP systems,

$$(B_t^{\text{Env.}})_p = B_0 (0.85 + 0.15e^{-0.25t}) \quad (9)$$

$$(G_{f_t}^{\text{Env.}})_p = G_{f_0} (1 + 0.45(1 - e^{(-0.20t)})). \quad (10)$$

Based on the above expressions from (7)–(10), the effect of moisture conditions is incorporated in the parameters $B_t^{\text{Env.}}$

TABLE 3: Calculated values for $B_t^{\text{Env.}}$ and $G_{f_t}^{\text{Env.}}$.

| (a) | | | | |
|----------|----------------------------|-------------------------|-----------------------------|--|
| Specimen | Exposure duration (months) | $(B_t^{\text{Env.}})_w$ | $(G_{f_t}^{\text{Env.}})_w$ | |
| SB-A-0 | 0 | 10.96 | 0.75 | |
| SB-A-3 | 3 | 11.34 | 0.65 | |
| SB-A-6 | 6 | 11.46 | 0.61 | |
| SB-A-18 | 18 | 11.51 | 0.60 | |
| SB-A-24 | 24 | 11.51 | 0.60 | |
| SB-B-0 | 0 | 14.46 | 0.54 | |
| SB-B-3 | 3 | 14.97 | 0.47 | |
| SB-B-6 | 6 | 15.12 | 0.45 | |
| SB-B-18 | 18 | 15.18 | 0.43 | |
| SB-B-24 | 24 | 15.18 | 0.43 | |
| SB-C-0 | 0 | 10.73 | 1.23 | |
| SB-C-3 | 3 | 11.10 | 1.06 | |
| SB-C-6 | 6 | 11.22 | 1.01 | |
| SB-C-18 | 18 | 11.27 | 0.98 | |
| SB-C-24 | 24 | 11.27 | 0.98 | |
| SB-D-0 | 0 | 11.81 | 0.76 | |
| SB-D-3 | 3 | 12.22 | 0.65 | |
| SB-D-6 | 6 | 12.35 | 0.62 | |
| SB-D-18 | 18 | 12.40 | 0.61 | |
| SB-D-24 | 24 | 12.40 | 0.61 | |
| (b) | | | | |
| Specimen | Exposure duration (months) | $(B_t^{\text{Env.}})_p$ | $(G_{f_t}^{\text{Env.}})_p$ | |
| SB-E-0 | 0 | 14.40 | 0.46 | |
| SB-E-3 | 3 | 13.26 | 0.56 | |
| SB-E-6 | 6 | 12.72 | 0.61 | |
| SB-E-18 | 18 | 12.26 | 0.67 | |
| SB-E-24 | 24 | 12.25 | 0.67 | |
| SB-F-0 | 0 | 17.44 | 0.59 | |
| SB-F-3 | 3 | 16.06 | 0.72 | |
| SB-F-6 | 6 | 15.41 | 0.78 | |
| SB-F-18 | 18 | 14.85 | 0.86 | |
| SB-F-24 | 24 | 14.83 | 0.86 | |

and $G_{f_t}^{\text{Env.}}$ and it can be determined for any specific period of exposure duration just by knowing the values of B_0 and G_{f_0} for nonimmersion case. For simplicity, B_0 and G_{f_0} can be obtained from the original Dai model. The new calculated values of the parameters for all the specimens considering the moisture effects are shown in Table 3.

Thus, the two-parameter bond-slip relationship given in (4) can be rewritten incorporating the effect of moisture exposure duration as

$$\tau_t^{\text{Env.}} = 2B_t^{\text{Env.}}G_{f_t}^{\text{Env.}} \left(e^{(-B_t^{\text{Env.}}s_t^{\text{Env.}})} - e^{(-2B_t^{\text{Env.}}s_t^{\text{Env.}})} \right), \quad (11)$$

where t is the duration in months.

Using (11), the bond-slip models for all the systems were prepared for different exposure durations as shown in Figure 12.

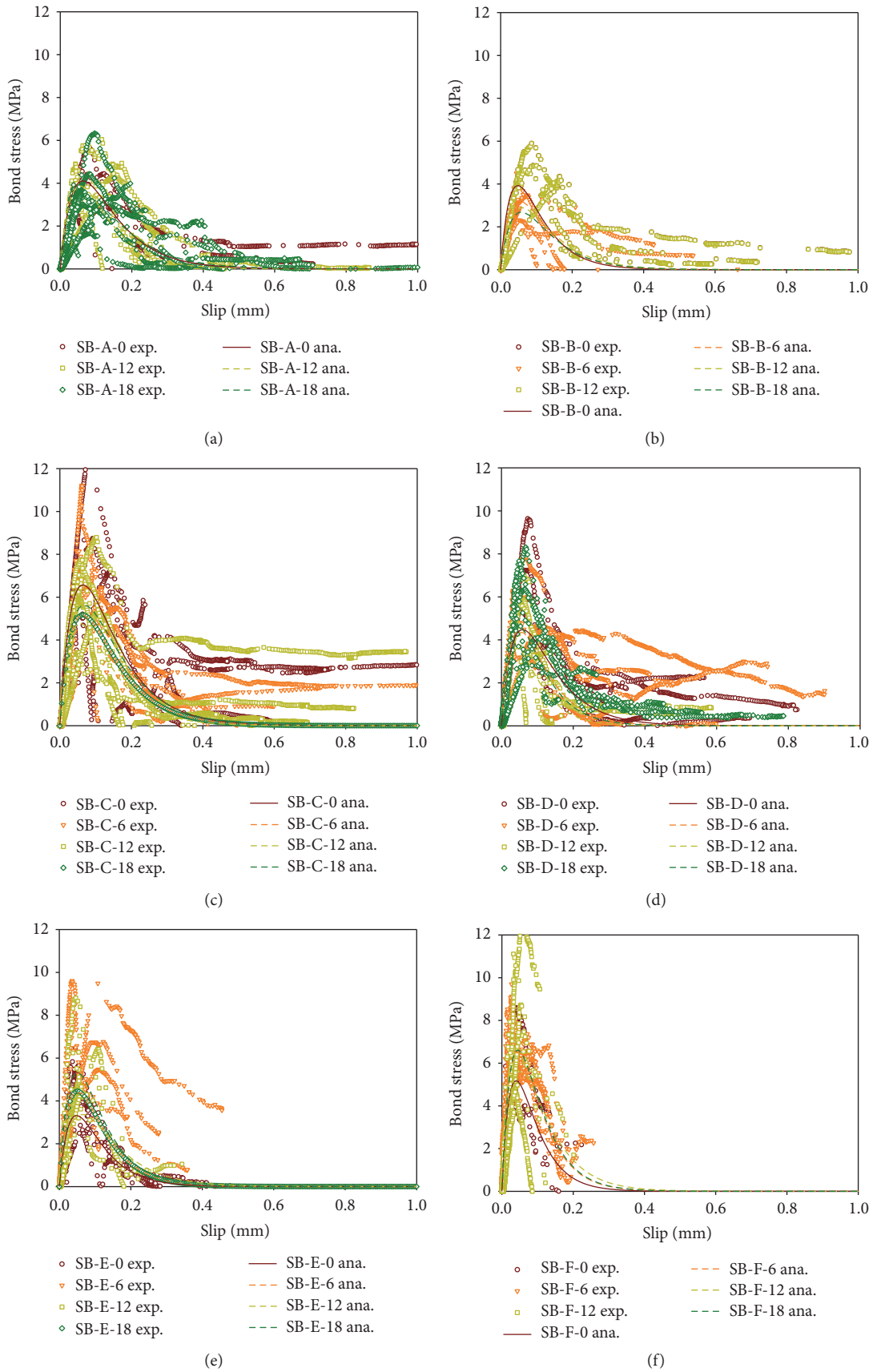


FIGURE 9: Comparison of predicted bond-slip models with the experimental data.

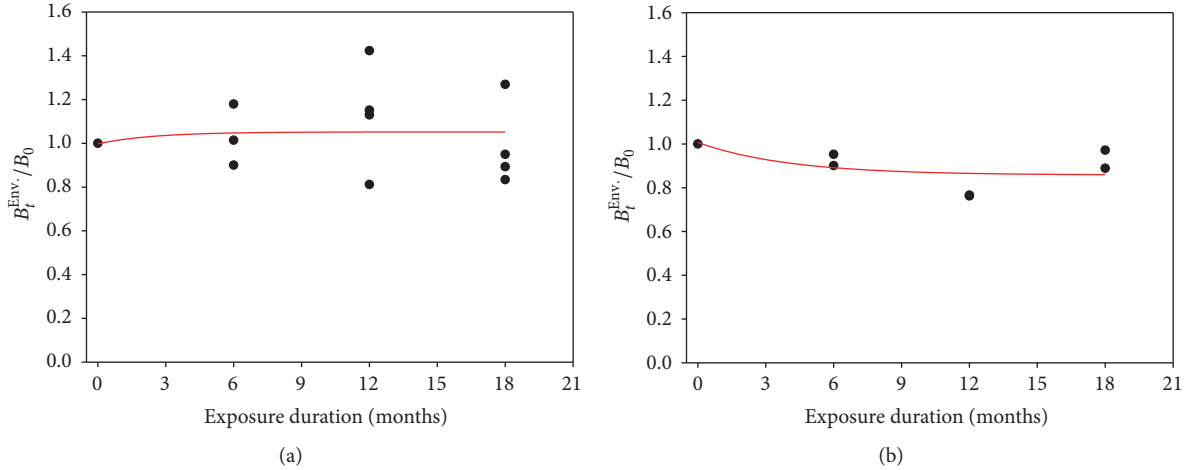


FIGURE 10: (a) Effect of exposure duration on the normalized B for wet-layup FRP system. $B_t^{\text{Env.}} = B_0(1.05 - 0.05e^{-0.40t})$. (b) Effect of exposure duration on the normalized B for prefabricated FRP system. $B_t^{\text{Env.}} = B_0(0.85 + 0.15e^{-0.25t})$.

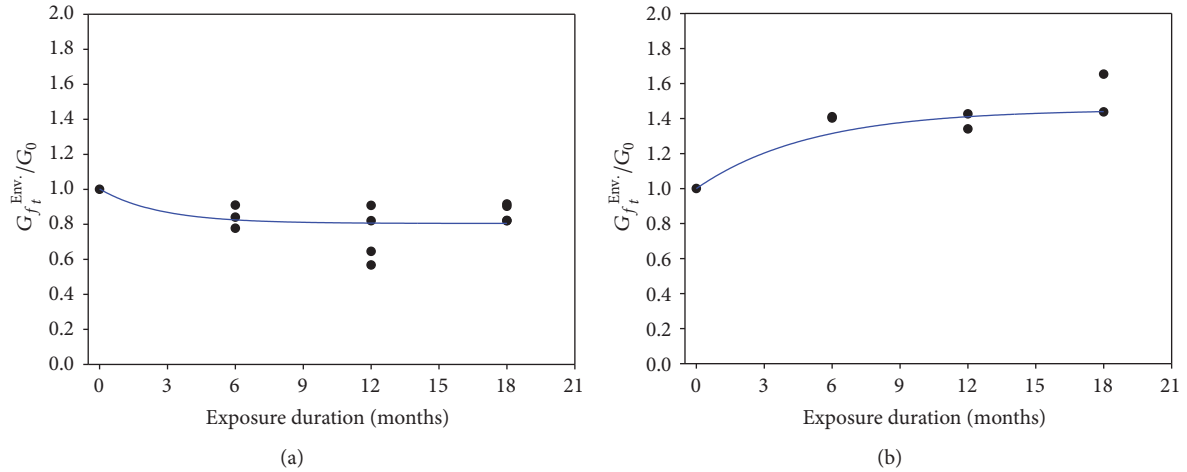


FIGURE 11: (a) Effect of exposure duration on the normalized G_f for wet-layup FRP system. $G_{f_t}^{\text{Env.}}/G_f = 0.8 + 0.2e^{(-0.35t)}$. (b) Effect of exposure duration on the normalized G_f for prefabricated FRP system. $G_{f_t}^{\text{Env.}}/G_f = 1.45 - 0.45e^{(-0.20t)}$.

4.2.2. *Verification of the Model.* As for the verification of the proposed model for the moisture conditions, the ultimate pull-out loads from the experiment were compared with that of the predicted load. The expression for ultimate predicted load for the case of moisture exposure condition is given by

$$P_t^{\text{Env.}} = b_f \sqrt{2E_f t_f G_{f_t}^{\text{Env.}}}. \quad (12)$$

In the above equation, calculated fracture energies given in Table 3 were used for the exposed cases to determine the ultimate pull-out loads. Figure 13 shows good agreement of the predicted and experimental ultimate loads at 0, 6, 12, and 18 months for all the 6 FRP systems investigated in this paper. The average ratio of the predicted to the experimental ultimate load was around 0.99 with an IAE of 12.84%.

5. Conclusions

The effects of moisture conditions on the 6 different FRP-concrete bonded systems were investigated for the maximum period of 18 months. Based on the experimental results, Dai's approach of determining the nonlinear bond-slip model was modified to propose the new bond-slip models incorporating the moisture effects at the normal temperature. Some of the main points are briefly summarized below:

- (1) The effect of moisture on the FRP systems can be categorized into two different cases based on the observation of average interfacial fracture energies and bond strength after exposure. In general, wet-layup FRP systems showed reduction in the interfacial fracture energy and the ultimate bond strength after exposure, whereas the prefabricated FRP systems

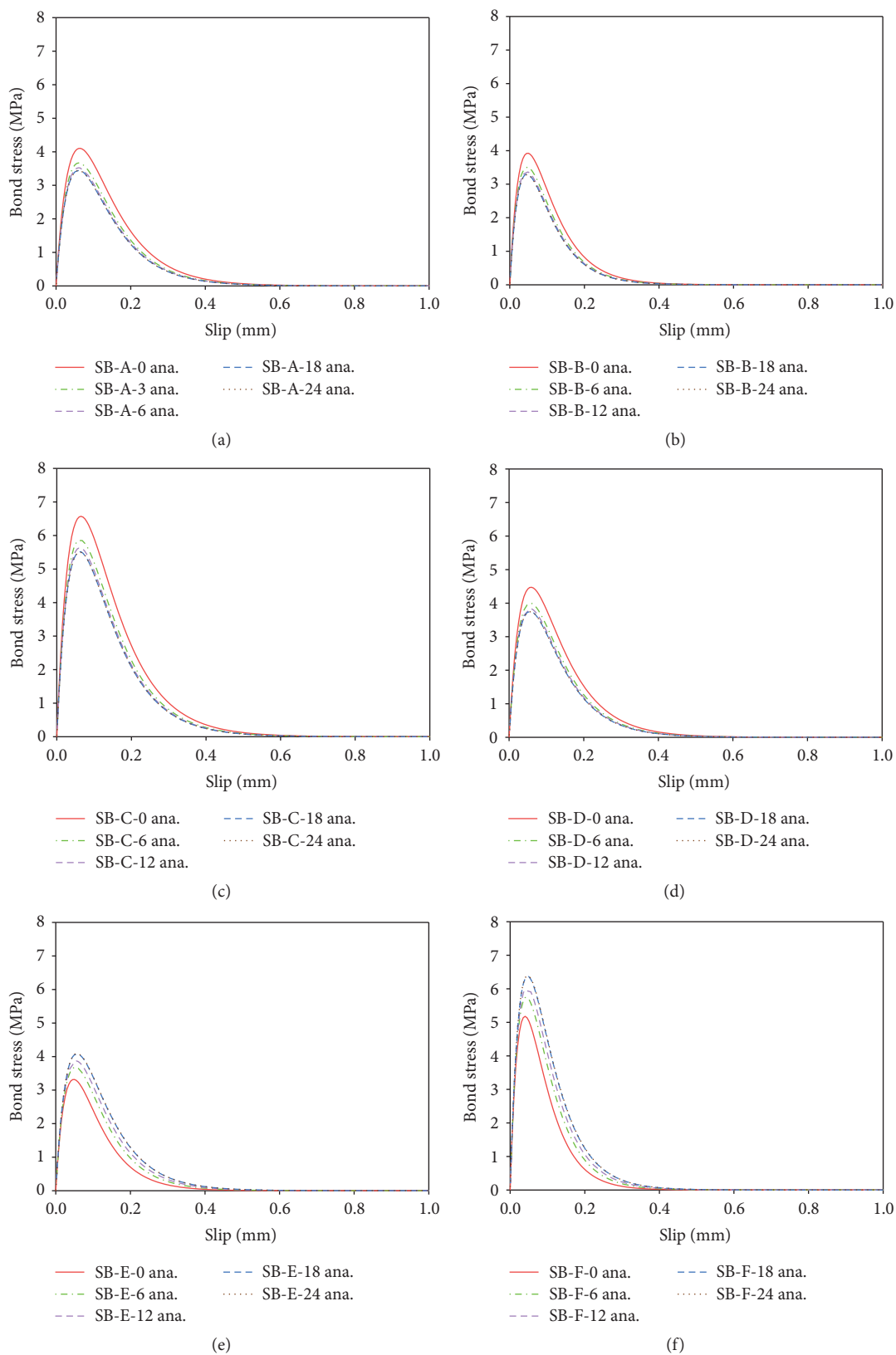


FIGURE 12: Modified bond-slip models incorporating moisture effect.

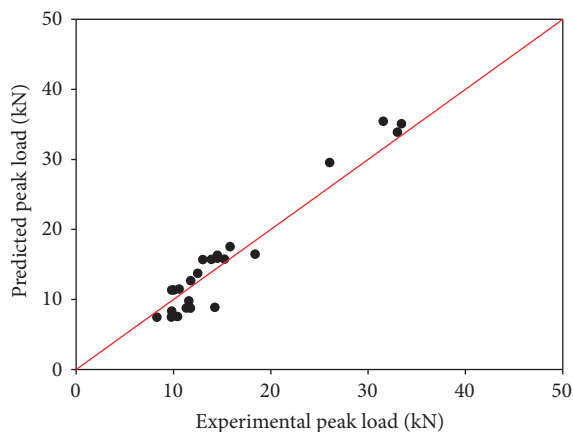


FIGURE 13: Comparison between predicted and experimental ultimate pull-out loads at 0, 6, 12, and 18 months taking all the 6 FRP systems.

showed improvement. Separate bond-slip relationships have been proposed to mark such contrasting behavior.

- (2) The effect of exposure duration was related to the two parameters: interfacial fracture energy (G_f) and ductility index (B) separately for the two systems. In both of the cases, the effect of moisture seems to primarily affect the bond properties until the period of the first 6 months, after which further exposure does not affect much.
- (3) Bond-slip models are determined with modified fracture energy $G_{f_t}^{Env.}$ and ductility index $B_t^{Env.}$ to incorporate the effect of moisture condition and duration of exposure.
- (4) The predicted ultimate loads were compared with the experimental loads at different exposure durations for all the 6 FRP systems. The results show fair agreement between the predicted and experimental values.

Competing Interests

The authors declare that they have no competing interests.

Acknowledgments

The authors acknowledge the support of Nippon Steel and Sumikin Materials Co., Ltd.; Mitsubishi Plastics Infracore Co., Ltd.; FYFE Japan Co., Ltd.; Simpson Strong-Tie Asia Ltd.; and Sika Ltd. for providing necessary materials to conduct this research work. The financial support from the Research Fund of Ministry of Transport Construction Technology (2014318494020) and Grant-in-Aid for Scientific Research (A) of Japan Society of Promotion of Science (no. 26249064) and NEXCO Group Companies' Support Fund to Disaster Prevention Measures on Expressways is greatly appreciated. The authors also highly appreciate the support of

Mr. Tsutomu Kimura for his technical assistance during the experiments.

References

- [1] J. Shrestha, T. Ueda, and D. Zhang, "Durability of FRP concrete bonds and its constituent properties under the influence of moisture conditions," *Journal of Materials in Civil Engineering*, vol. 27, no. 2, Article ID A4014009, 2015.
- [2] S. Choi, A. L. Gartner, N. V. Etten, H. R. Hamilton, and E. P. Douglas, "Durability of concrete beams externally reinforced with CFRP composites exposed to various environments," *Journal of Composites for Construction*, vol. 16, no. 1, pp. 10–20, 2012.
- [3] K. Benzarti, S. Chataigner, M. Quiertant, C. Marty, and C. Aubagnac, "Accelerated ageing behaviour of the adhesive bond between concrete specimens and CFRP overlays," *Construction and Building Materials*, vol. 25, no. 2, pp. 523–538, 2011.
- [4] C. Tuakta and O. Büyüköztürk, "Deterioration of FRP/concrete bond system under variable moisture conditions quantified by fracture mechanics," *Composites Part B: Engineering*, vol. 42, no. 2, pp. 145–154, 2011.
- [5] J. G. Dai, H. Yokota, M. Iwanami, and E. Kato, "Experimental investigation of the influence of moisture on the bond behavior of FRP to concrete interfaces," *Journal of Composites for Construction*, vol. 14, no. 6, pp. 834–844, 2010.
- [6] J. Shrestha, T. Ueda, D. Zhang, A. Kitami, and A. Komori, "Investigation on moisture behavior for different FRP-concrete bonded systems," in *Proceedings of the JCI Annual Convention*, pp. 1135–1140, Chiba, Japan, 2015.
- [7] T. Ueda and J. G. Dai, "Interface bond between FRP sheets and concrete substrates: properties, numerical modeling and roles in member behaviour," *Progress in Structural Engineering and Materials*, vol. 7, no. 1, pp. 27–43, 2005.
- [8] J. Dai, T. Ueda, and Y. Sato, "Development of the nonlinear bond stress-slip model of fiber reinforced plastics sheet-concrete interfaces with a simple method," *Journal of Composites for Construction*, vol. 9, no. 1, 2005.
- [9] J. G. Dai, W. Y. Gao, and J. G. Teng, "Bond-slip model for FRP laminates externally bonded to concrete at elevated temperature," *Journal of Composites for Construction*, vol. 17, no. 2, 2013.
- [10] Y. Yun, *Durability of FRP-concrete interface [Ph.D. thesis]*, City University of Hong Kong, 2011.
- [11] Z. Ouyang and B. Wan, "Experimental and numerical study of moisture effects on the bond fracture energy of FRP/concrete joints," *Journal of Reinforced Plastics and Composites*, vol. 27, no. 2, pp. 205–223, 2008.
- [12] Z. Ouyang and B. Wan, "Nonlinear deterioration model for bond interfacial fracture energy of FRP-concrete joints in moist environments," *Journal of Composites for Construction*, vol. 13, no. 1, pp. 53–63, 2009.
- [13] M. A. G. Silva, H. C. Biscaia, and R. Marreiros, "Bond-slip on CFRP/GFRP-to-concrete joints subjected to moisture, salt fog and temperature cycles," *Composites Part B: Engineering*, vol. 55, pp. 374–385, 2013.
- [14] J. Shrestha, D. Zhang, and T. Ueda, "Durability performances of carbon fiber-reinforced polymer and concrete-bonded systems under moisture conditions," *Journal of Composites for Construction*, vol. 20, no. 5, Article ID 04016023, 2016.

- [15] Z. C. Girgin, N. Arioglu, and E. Arioglu, "Evaluation of strength criteria for very-high-strength concretes under triaxial compression," *ACI Structural Journal*, vol. 104, no. 3, pp. 278–284, 2007.
- [16] Y.-F. Wu and C. Jiang, "Quantification of bond-slip relationship for externally bonded FRP-to-concrete joints," *Journal of Composites for Construction*, vol. 17, no. 5, pp. 673–686, 2013.
- [17] T.-C. Nguyen, Y. Bai, X.-L. Zhao, and R. Al-Mahaidi, "Durability of steel/CFRP double strap joints exposed to sea water, cyclic temperature and humidity," *Composite Structures*, vol. 94, no. 5, pp. 1834–1845, 2012.
- [18] M. S. Sciolti, M. Frigione, and M. A. Aiello, "Wet lay-up manufactured FRPs for concrete and masonry repair: influence of water on the properties of composites and on their epoxy components," *Journal of Composites for Construction*, vol. 14, no. 6, pp. 823–833, 2010.

Research Article

Fatigue Crack Propagation Behavior of RC Beams Strengthened with CFRP under High Temperature and High Humidity Environment

Dongyang Li,¹ Peiyan Huang,^{1,2} Guang Qin,¹ Xiaohong Zheng,¹ and Xinyan Guo¹

¹School of Civil Engineering and Transportation, South China University of Technology, Guangzhou 510640, China

²State Key Laboratory of Building Science, South China University of Technology, Guangzhou 510640, China

Correspondence should be addressed to Peiyan Huang; pyhuang@scut.edu.cn

Received 13 September 2016; Accepted 21 December 2016; Published 15 January 2017

Academic Editor: Giuseppina Amato

Copyright © 2017 Dongyang Li et al. This is an open access article distributed under the Creative Commons Attribution License, which permits unrestricted use, distribution, and reproduction in any medium, provided the original work is properly cited.

Numerical and experimental methods were applied to investigate fatigue crack propagation behavior of reinforced concrete (RC) beams strengthened with a new type carbon fiber reinforced polymer (CFRP) named as carbon fiber laminate (CFL) subjected to hot-wet environment. J -integral of a central crack in the strengthened beam under three-point bending load was calculated by ABAQUS. In finite element model, simulation of CFL-concrete interface was based on the bilinear cohesive zone model under hot-wet environment and indoor atmosphere. And, then, fatigue crack propagation tests were carried out under high temperature and high humidity (50°C, 95% R · H) environment pretreatment and indoor atmosphere (23°C, 78% R · H) to obtain a - N curves and crack propagation rate, da/dN , of the strengthened beams. Paris-Erdogan formula was developed based on the numerical analysis and environmental fatigue tests.

1. Introduction

External bonding of carbon fiber reinforced polymer (CFRP) composites has become more and more widely used for strengthening RC structures all over the world in the past two decades [1, 2] due to its lightweight, high strength, and good erosion resistance. Many researchers have demonstrated that external bonding of CFRP can obviously improve the fatigue performance of RC structures [3–5]. In subtropical regions, hot-wet environment has a marked effect on fatigue performance and durability of the RC bridge components strengthened with CFRP and even leads to the components being not able to meet the safety, reliability, and durability requirements in the whole life cycle [6]. Therefore, study on fatigue crack propagation behavior of RC structures strengthened with CFRP in hot-wet environment has important scientific significance. However, the effect mechanism of hot-wet environment on the fatigue crack propagation behavior of strengthened RC structures remains unclear.

Previous studies of our research group [7, 8] show that Paris-Erdogan law [9] was an effective method to study

fatigue crack propagation behavior in RC structures strengthened with CFRP. However, considering the quasi-brittle and nonlinear characteristic of concrete, stress intensity factor (SIF) has limitations to explain crack initiation and propagation in concrete [10]. J -integral is more sufficient to describe the crack propagation behavior in concrete [11]. According to the J -integral approach, the fatigue crack propagation rate, da/dN , is put in relation to the cyclic J -integral amplitude, ΔJ .

In the calculation of J -integral, concrete damage plastic (CDP) model uses concepts of isotropic damage in combination with tensile and compressive plasticity to represent the nonlinear-elastic behavior of concrete. Also, concrete materials show different response under fatigue load compared with static load. Petryna et al. [12] developed a fatigue damage model of reinforced concrete, which was capable of simulating arbitrary damage states under cyclic loading. Sain and Chandra Kishen [13] and Zanuy et al. [14] illustrated tensile and compressive behavior of concrete under fatigue loading, respectively. J.-S. Zhu and X.-C. Zhu [15] proposed a numerical simulation method of the full-range fatigue

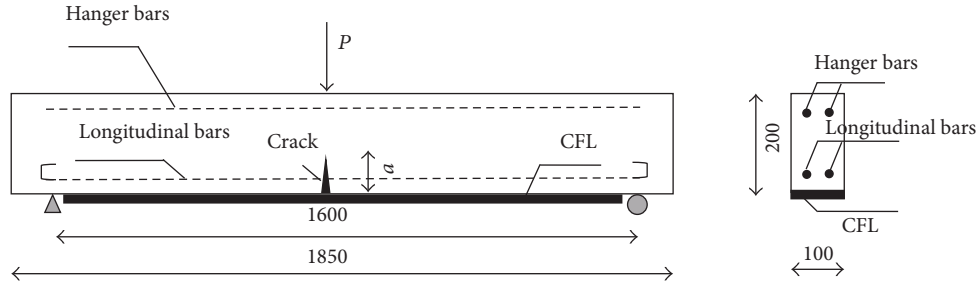


FIGURE 1: CFL-strengthened RC beam with a crack (unit: mm).

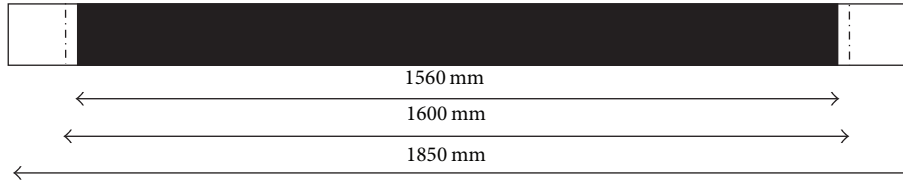


FIGURE 2: Size of CFL pasted at the bottom of RC beam.

damage accumulation failure of RC bridges, based on the CDP model in ABAQUS [16].

As many studies [16, 17] show, interface debonding is the main failure mode of the RC beams strengthened with FRP under static and cyclic loading. Moreover, hot-wet environment has a significant influence on bonding behavior of the CFRP-concrete interface [6, 18]. Qin et al. [19] found that hot-wet environment has a harsh influence on fatigue durability of RC structure strengthened with FRP. Therefore, the constitutive relation of the CFRP-concrete interface under hot-wet environment would be applied to discuss the fatigue crack propagation behavior. Zheng et al. [6, 18] investigated the behavior of FRP-concrete interface under hot-wet environment through double-shear tests, which provided significantly guidance for the simulation of FRP-concrete interface in detail later in this paper.

Against the above background, the present paper is divided into two main sections. Firstly, a finite element model of RC beam strengthened with CFRP was established for determination of J -integral of main crack based on nonlinear fracture mechanics, considering CFRP-concrete interface behavior under different environment. Secondly, several fatigue crack propagation tests were carried out for RC beams strengthened with CFL under high temperature and high humidity (50°C, 95% R · H) and indoor atmosphere (23°C, 78% R · H) to obtain fatigue crack propagation rate, da/dN . Then, Paris law with J -integral was developed to describe the fatigue crack propagation behavior, which can be applied to predict the fatigue lives of the RC beams strengthened with CFRP.

2. FEM for Calculation of J -Integral

A finite element model of CFL-strengthened RC beam was built to calculate J -integral using the commercial finite element (FE) software ABAQUS in this paper. Geometry, material properties, and mesh division of the strengthened beam

were introduced in detail later. Moreover, nonlinear and fatigue behavior of concrete and effect of hot-wet environment were considered.

2.1. Geometry of Specimen. Three-dimensional FE model of the simply supported RC beam strengthened with carbon fiber laminate (CFL) [20] was shown in Figure 1. CFL-strengthened RC beam was subjected to three-point bending (3PB) load with a crack at midspan. The size of RC beam was 1850 mm length \times 100 mm width \times 200 mm height. Distance between the supports was 1600 mm and height of crack was a . The internal steel bar consisted of two $\phi 10$ mm longitudinal bars and two $\phi 8$ mm hanger bars. CFL with a cross section of 100 mm (width) \times 0.23 mm (computing thickness) and a total length of 1560 mm was bonded to the bottom of RC beams (Figure 2).

2.2. Material Properties and Constitutive Models

(1) Nonlinear Behavior of Concrete. The compressive and tensile behaviors of concrete with nonlinear properties were described by the stress-strain curve (provided by the standard GB50010-2010 [21]) as shown in Figure 3. The stress-strain curve of the concrete was described as

$$\sigma = (1 - d_c) E_c \varepsilon, \quad (1)$$

where E_c is the initial elastic modulus. For the compressive behavior, $d_c = 1 - \rho_c / [\alpha_c (x - 1)^2 + x]$, $\rho_c = f_c / E_c \varepsilon_c$, $n = E_c \varepsilon_c / (E_c \varepsilon_c - f_c)$, $x = \varepsilon / \varepsilon_c$, and $\alpha_c = 0.74 \sim 3.99$ (when $f_c = 20 \sim 80$ MPa); f_c is the uniaxial compressive strength; ε_c is the strain values when σ reaches f_c ; d_c is the damage evolution parameter of concrete under uniaxial compression loading. For the tensile behavior, $d_c = 1 - \rho_t / [\alpha_t (x - 1)^{1.7} + x]$, $\rho_t = f_t / E_c \varepsilon_t$, $x = \varepsilon / \varepsilon_t$, $\alpha_t = 0.31 \sim 5$ (when $f_t = 1 \sim 4$ MPa); f_t is uniaxial tensile strength; ε_t are strain values when σ reaches f_t .

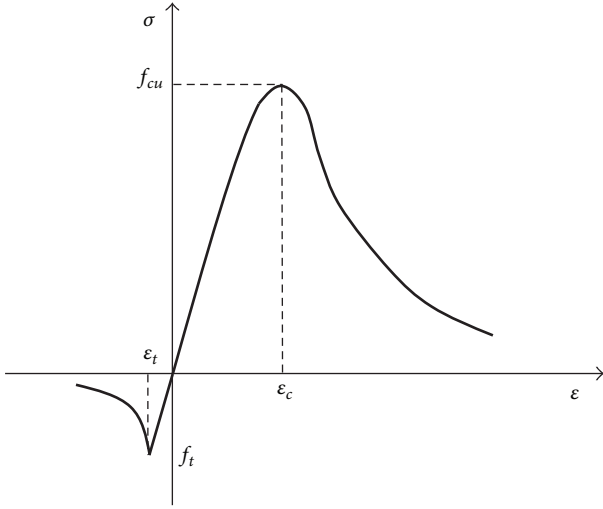


FIGURE 3: Uniaxial stress-strain curve of concrete.

The constitutive model, which is called concrete damage plasticity (CDP) model, was used for the numerical calculations in ABAQUS. CDP model was implemented for modeling tensile cracking and compressive crushing behavior of concrete, which was shown in Figure 3.

The elastic modulus, Poisson's ratio, tensile strength, and compressive strength of the concrete were $E_c = 35.2$ GPa, $\nu_c = 0.193$, $f_t = 4.45$ MPa, $f_c = 37.3$ MPa, and $\varepsilon_c = 0.00175$, $\varepsilon_t = 0.000095$.

(2) *Elastic Modulus Degradation of Concrete.* Steel bar in RC beams strengthened with CFRP remains linear-elastic

before yielding in fatigue test. Also, due to excellent fatigue resistance, CFRP keep linear-elastic in most of fatigue life [22]. Thus, this paper placed emphasis on fatigue damage evolution of concrete instead of steel bar and CFRP, including consideration of the effective elastic modulus and residual strength of concrete.

Based on test results, Holmen [23] proposed a formula about effective elastic modulus of concrete under fatigue loading:

$$E_N = \left(1 - 0.33 \frac{N}{N_f}\right) E_c, \quad (2)$$

where E_N is the effective elastic modulus of concrete at N loading cycles; E_c is initial elastic modulus of concrete; N_f is the number of loading cycles to failure (fatigue life).

(3) *Strength Degradation of Concrete.* Many researchers [14] applied envelope concept to describe the degradation process of concrete strength. Fatigue residual strength envelope was defined as the relation curve between residual strength and loading cycles. Through the analysis of hysteretic stress-strain curves of concrete under fatigue loading, J.-S. Zhu and X.-C. Zhu [15] found that the shape of residual strength envelope was similar to the descending branch of uniaxial stress-strain curve (Figure 3) and established residual compressive and tensile strength envelope (shown in Figure 4).

Fatigue residual strength envelope equations based on Figure 4 and the descending branch of (1) can be given as follows:

$$f_{i=c,t}(N) = f_{i=c,t} \cdot \frac{(\log N / \log N_f) [x(N_f) - x(1)]}{\alpha_{i=c,t} \left[(\log N / \log N_f) [x(N_f) - x(1)] - x(1) \right]^n + (\log N / \log N_f) [x(N_f) - x(1)]}, \quad (3)$$

where relative life ratio is defined as $r(N) = [x(N) - x(1)] / [x(N_f) - x(1)] = \log N / \log N_f$. Therefore, $x(1) = 1$, $x(N_f) = \log N / \log N_f [x(N_f) - 1] + 1$; α_c and α_t are the same as (1); $n = 2$ when $i = c$, and $n = 1.7$ when $i = t$.

As shown in Figures 3 and 4, compressive and tensile constitutive model of concrete under fatigue loading shared the same shape of the stress-strain curve under static loading. Therefore, fatigue constitutive model of concrete at any loading cycle N was obtained through replacing the initial elastic modulus E_c , the uniaxial compressive strength f_c , and tensile strength f_t in (1) with effective elastic modulus E_N , residual compressive strength $f_c(N)$, and residual tensile strength $f_t(N)$.

(4) *Steel Bar.* The steel bar was assumed to be an elastic-perfectly plastic material. The elastic modulus $E_s = 206$ GPa, Poisson's ratio $\nu_s = 0.3$, and yield stress $f_y = 307$ MPa. The bond between steel bar and concrete was assumed as a

perfect bond, which was simulated by embedded constraint in ABAQUS.

(5) *CFL.* CFL is a linear-elastic composite material. Though it is obvious that CFL is orthotropic, primarily stress is in the fiber direction under three points bending load which makes the isotropic assumption suitable [24, 25]. The elastic modulus $E_f = 230$ GPa; Poisson's ratio $\nu_f = 0.25$.

(6) *CFL-Concrete Interface.* Cohesive zone model (CZM) [26] was applied to model CFL-concrete interface. The CZM method was commonly used to simulate bond-slip relationship between CFRP and concrete. There were several shapes of bond-slip curve such as bilinear, linear-parabolic, exponential, and trapezoidal. Obaidat et al. [24] investigated the influence of the shape of bond-slip curve, and they concluded that the shape of curve had a minor effect. Alfano [27] found that bilinear law represented the best compromise between computational cost and approximation. Therefore,

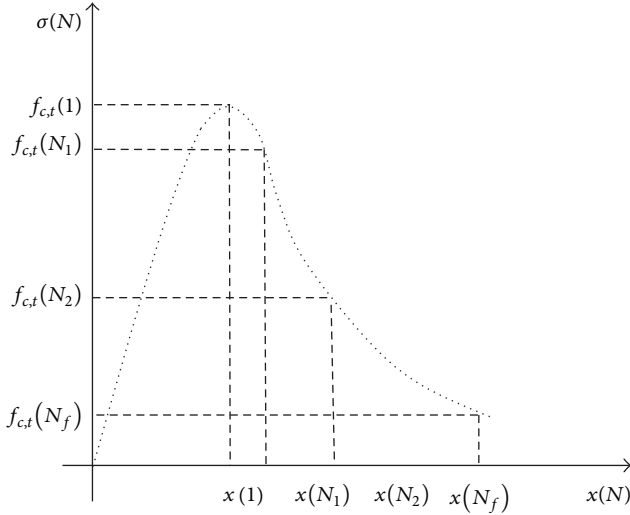


FIGURE 4: Residual strength envelope of concrete under cyclic loading.

bilinear bond-slip law was applied in this paper, which was shown in Figure 5.

Surface-based cohesive behavior in ABAQUS 6.14, which was defined as a surface interaction property based on CZM, was used to model the bond-slip behavior of CFL-concrete interface. The bilinear constitutive relation of the cohesive behavior includes the following parameters: peak value of the shear stress τ_{\max} , peak value of slip δ_0 , and initial elastic stiffness $EI = \tau_{\max}/\delta_0$. The damage initiation was determined by the slip value δ_0 when the shear stress τ reached the peak value, τ_{\max} . The linear damage evolution was described by a damage variable, D , which was defined by the following expression:

$$D = \frac{\delta_f (\delta - \delta_0)}{\delta (\delta_f - \delta_0)}, \quad (4)$$

where $\delta_f = 2G_f/\tau_{\max}$ and G_f is the critical fracture energy required to cause failure. δ refers to the value of slip attained during the loading history.

In the computation, different CZM parameters were used to model the bond-slip behavior of CFL-concrete interface under high temperature and high humidity (50°C, 95% R · H) and indoor atmosphere (23°C, 78% R · H) environment. The parameters are based on the experimental research on bond-slip behavior of CFL-concrete interface proposed by this research group [6, 18], including τ_{\max} , δ_0 , δ_f , and G_f listed in Table 1.

2.3. Finite Element Mesh and Computing Procedure. To model the crack at midspan of CFL-strengthened RC beam, a seam was assigned through crack module as shown in Figure 6. Three-dimensional, 4-node quadrilateral shell elements (S4) were used for the CFL. Two-dimensional, 3-node truss elements (T3D2) were used for the steel bars. Three-dimensional, 8-node, fully integrated hexahedral elements (C3D8) and 6-node, wedge elements (C3D6) were used for

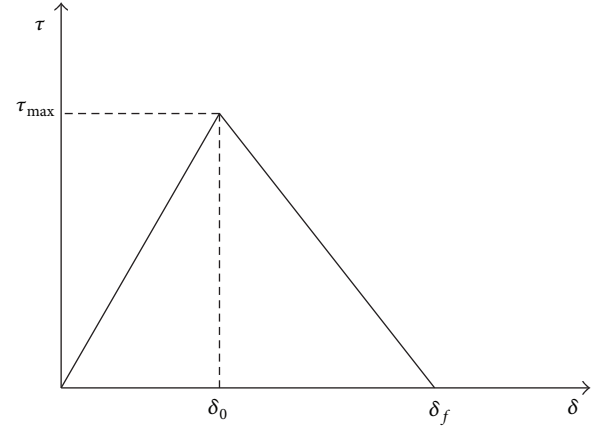


FIGURE 5: Bilinear bond-slip law.

the concrete. C3D6 elements were assigned at crack tip and C3D8 elements were assigned in other parts of concrete. Region around the crack tip was modeled using multiple rings of elements in a swept mesh which uses C3D8 elements, while C3D6 elements were assigned in the innermost rings as shown in Figure 8. Each ring provided an evaluation of the contour integral. The J -integral was calculated using a domain integral method [28].

To calculate J -integral amplitude $\Delta J = J_{\max} - J_{\min}$ (J_{\max} and J_{\min} are J -integral under maximum stress S_{\max} and minimum stress S_{\min} , resp.) of main crack at a certain cycle of fatigue life, the whole fatigue process was divided into multiple steps under static loading. In order to model the load process at target cycle N , the finite element analysis jumped over $N-1$ cycles before N . Fatigue degradation of the strength and elastic modulus caused by $N-1$ loading cycles were considered in the constitutive model of concrete. Two analysis steps under static load were established: (1) step (1), to calculate J_{\min} , load added from 0 to S_{\min} , in which fatigue constitutive model of concrete was considered; (2) step (2), to calculate J_{\max} , load added from S_{\min} to S_{\max} following fatigue loading curve. Thus, J -integral amplitude $\Delta J = J_{\max} - J_{\min}$ at a certain cycle N was obtained. Complicated simulation of full-range fatigue process was simplified as multiple steps under static loading, which gave a simple and effective method to extract J -integral of the RC beam strengthened with CFL under fatigue loading.

2.4. Calculation and Analysis of J -Integral

(1) Effect of Fatigue Performance Degradation of Concrete. The FE model of RC beam strengthened with CFL based on above FE analysis procedure was applied to study the effect of fatigue performance degradation of concrete on J -integral. Figure 7 shows J - a/h curves under different relative fatigue lives ($N/N_f = 0, 0.2, 0.4, 0.6, 0.8$) when load level $P = 27.5$ kN, where $N/N_f = 0$ means no fatigue degradation of concrete was considered. As shown in Figure 7, J - a/h curves exhibit a three-stage tendency: (1) rapid increase stage: When relative crack height $a/h \leq 0.15$, the value of J -integral increases rapidly and almost linearly as crack height

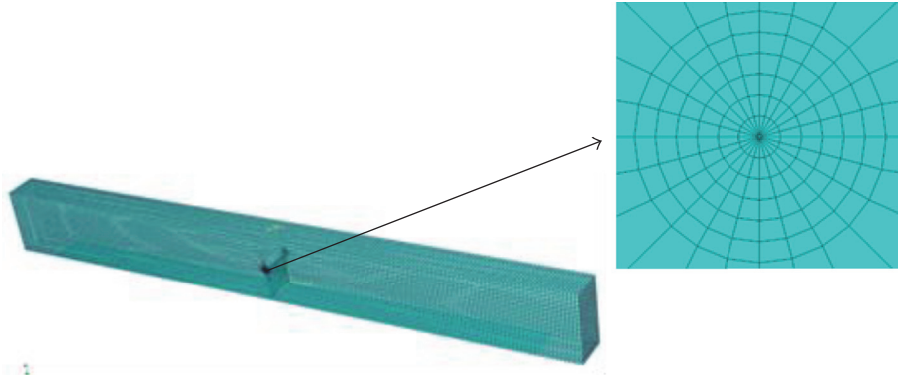
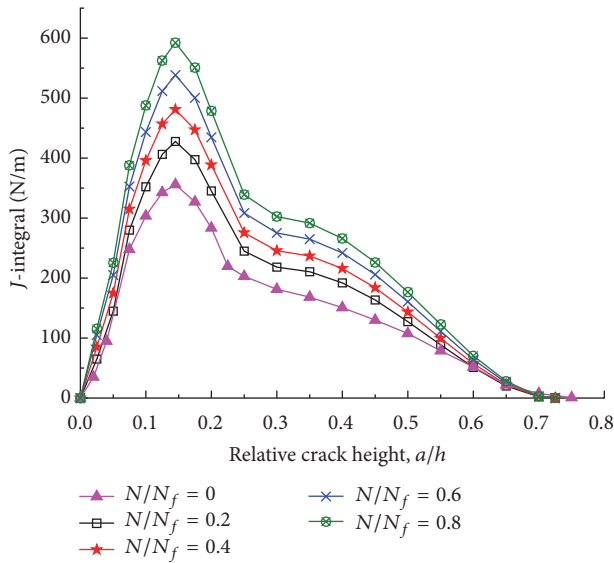


FIGURE 6: Finite element mesh of CFL-RC beam.

TABLE 1: CZM parameters.

| Environment | | Parameters | | | |
|------------------------------------|--------------------|---------------------|-----------------|-----------------|-------------|
| Temperature ($^{\circ}\text{C}$) | Humidity (% R · H) | τ_{\max} (MPa) | δ_0 (mm) | δ_f (mm) | G_f (N/m) |
| 50 | 95 | 3.0 | 0.03 | 0.068 | 103 |
| 23 | 78 | 6.0 | 0.06 | 0.194 | 583 |

FIGURE 7: Effect of fatigue performance degradation on J -integral.

increases, and the value of J -integral reaches the highest point at $a/h = 0.15$; (2) rapid decrease stage: when relative crack height $0.15 \leq a/h \leq 0.25$, the value of J -integral decreases rapidly and almost linearly, and an inflection point appears at $a/h = 0.25$; (3) slow decrease stage: when relative crack height $a/h > 0.25$, the value of J -integral begins to decrease slowly and nonlinearly. When relative crack height $a/h > 0.7$, the value of J -integral tends to be zero. The three-stage tendency coincides with our previous research [7] and achieves good agreements with fatigue crack propagation behavior observed from fatigue test in chapter 3.

It can be seen from Figure 7 that the value of J -integral considering fatigue performance degradation is always higher than the one without consideration of degradation ($N/N_f = 0$). Also, at the same crack length, the value

of J -integral increases with the increase of fatigue life. When $N/N_f = 0.8$, the value of J -integral is 70% higher than the one without consideration of degradation ($N/N_f = 0$). It indicates that as fatigue life increases, the cracking resistance of concrete around the crack tip is significantly weakened.

(2) *Effect of Hot-Wet Environment.* In order to study the effect of hot-wet environment on J -integral, two kinds of FE model were established considering bond-slip relation under hot-wet environment and indoor atmosphere, respectively. Bond-slip parameters of CFL-concrete interface were shown in Table 1. For simplicity, fatigue performance degradation of concrete was not considered in this section. When load level $P = 27.5$ kN, J - a/h curves were obtained and shown in Figure 8. As shown in Figure 8, the J - a/h curves were divided into two zones. In zone 1 ($a/h \leq 0.45$), the values of J -integral are the same whether under hot-wet environment or indoor atmosphere, because damage did not appear in the interface when $a/h \leq 0.45$ and the initial stiffness values of interface $T = \tau_{\max}/\delta_0$ are the same under both environments (seen in Table 1). In zone 2 ($a/h > 0.45$), the value of J -integral under hot-wet environment is higher than that under indoor atmosphere, because damage appeared earlier under hot-wet environment (smaller fracture energy, seen in Table 1) than that under indoor atmosphere. Debonding was firstly found at midspan when $a/h = 0.45$ under hot-wet environment. It can be concluded that hot-wet environment leads to the degradation of CFRP-concrete interface. It made cracking resistance of concrete around the crack tip weakened, which resulted in increase of J -integral under hot-wet environment.

3. Fatigue Crack Propagation Tests

A series of fatigue crack propagation tests were carried out for the RC beams strengthened with CFL under high temperatures and high humidity (50°C , 95% R · H) and

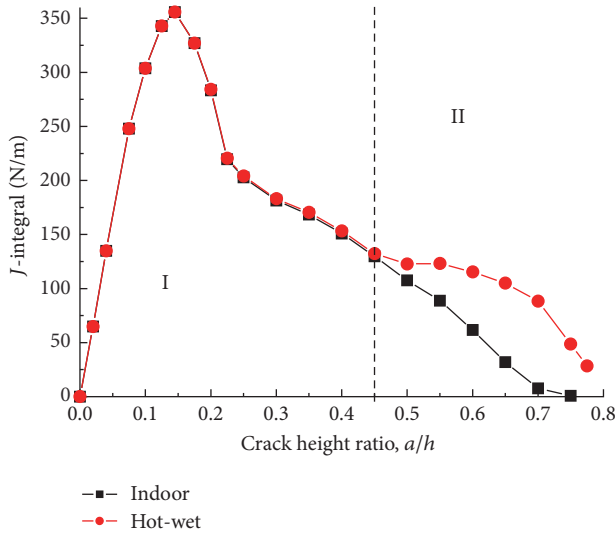


FIGURE 8: Effect of environment on J -integral.

indoor atmosphere (23°C, 78% R · H) environment to obtain fatigue crack propagation curves (a - N curves). The strengthened beams were placed in hot-wet environment pretreatment and then removed to fatigue testing machine for crack propagation tests under indoor atmosphere. As the contrast experiments, the other group of the strengthened beams were tested without hot-wet environment pretreatment. Experimental materials and methods were introduced as follows.

3.1. Experimental Materials and Specimens. As stated in [29, 30], the new CFRP called carbon fiber laminate (CFL) [20] invented by this research group possesses universal applicability in bridge engineering and comprehensive advantages of carbon fiber plates and sheets. In this paper, the RC beams strengthened with CFL were used as specimens. Four specimens for fatigue crack propagation tests were three-point bending beam. The size of the beam was shown in Figure 1.

The specimens were composed of three parts: concrete, steel bars, and CFL. Composition proportion of concrete was $m_c:m_w:m_s:m_a = 1.0:0.5:2.06:3.66$ (cement:water:sand:gravel). The main steel bars were Grade II $\Phi 10$ and other steel bars were Grade I $\Phi 8$; the reinforcement ratio was 0.981%, shown in Figure 9. CFL (preimmersion laminate) was 1560 mm long, 100 mm wide, and 0.23 mm thick and was fabricated of T700-12k carbon fiber silk made in Tolei Corporation, Japan. CFL was made of laminate immersed with epoxy resin. Adhesive used between concrete and CFL was A and B epoxy adhesive produced in Shenliling Company, China. The thickness of A and B epoxy adhesive was totally 0.2 mm, and most of the adhesive was penetrated into the concrete. CFLs were then bonded to the bottom of RC beams. The shear strength of A and B epoxy adhesive was 14 MPa, and its working temperature was $-30\sim+100^\circ\text{C}$. Physical and mechanical properties of the main materials used were listed in Tables 1 and 2 of [30].

It should be noted that dimensions of the specimens above were referenced to the recommendations of the Japanese Society of Civil Engineering and determined according to test conditions of this research team. Reinforcement ratio of RC beams and concrete mix design were determined according to C25 concrete in Code for Design of Highway Reinforced Concrete and Prestressed Concrete Bridges and Culverts (JTG D62-2004). The method to determine the size and thickness of CFL is important. The size and thickness of CFL were optimally designed based on static mechanical behaviors and failure modes of RC beams strengthened with CFL. The failure modes include yielding of main steel bars, debonding of CFL, and crush of concrete.

3.2. Experimental Devices. In order to simulate real service conditions of bridge structures in subtropical area, hot-wet environment simulation and control device [31] combined with MTS810 fatigue machine was developed as shown in Figure 10. This system was used to simulate the actual bridge environment in hot-wet condition. The main performance indexes were as follows: (1) temperature: $-40^\circ\text{C}\sim+100^\circ\text{C}$; temperature fluctuation degree: $\pm 1^\circ\text{C}$; (2) the rate of heating-cooling $\geq 3^\circ\text{C}/\text{min}$ (in $0^\circ\text{C}\sim 100^\circ\text{C}$); (3) humidity: 65% R · H \sim 98% R · H; humidity fluctuation: $\pm 2\%$ R · H; (4) humidity change rate: 0.5% R · H/min.

The environmental simulation and control system was composed of four parts: simulation cabin, temperature and humidity regulator, electrical control cabinet, and compressor room. On each side of the simulation cabin, observation window was set with the size of 500 mm \times 200 mm, which was frost prevention and insulated.

3.3. Experimental Method. To study the effect of hot-wet environment on fatigue crack propagation of RC beam strengthened with CFL, nine specimens were divided into two groups: Group A was set as hot-wet environmental group and Group B was set as control group. The hot-wet environment setting was based on measured data of bridge servicing environment in subtropical area such as south China [32]. The pretreatment environment was set as the worst servicing environment of bridge: temperature is 50°C and humidity is 95% R · H. The specimens in Group A was first placed in simulation cabin for hot-wet environmental pretreatment for 6 days, which refers to the standard of test method for aging properties of glass fiber reinforced plastics [33]. Then, the specimens were removed into laboratory indoor environment for another two days to ensure that the specimens were dry before fatigue test.

The fatigue crack propagation tests were carried out with MTS810 hydraulic test system using a three-point bending setup. The span of the specimen was 1600 mm and the loading point was in the middle. Loading was applied sinusoidally with a frequency of 10 Hz and a stress ratio of 0.2. Based on the previous testing result for ultimate load-bearing capacity P_u of the RC beam strengthened with CFL ($P_u = 41.6$ kN), three loading levels were set, the peak load P_{\max} of which separately was 30 kN, 27.5 kN, and 25 kN. The experimental conditions were shown in Table 2.

TABLE 2: Fatigue crack propagation test conditions and results.

| Group | Specimen no. | Temperature ($^{\circ}\text{C}$) | Humidity (% R · H) | Peak load P_{\max} (kN) | Stress ratio R | Fatigue lives N_f (cycles) |
|-------|--------------|------------------------------------|--------------------|---------------------------|------------------|------------------------------|
| A | A1 | 50 | 95 | 30.0 | 0.2 | 600001 |
| | A2 | | | 27.5 | | 654546 |
| | A3 | | | 27.5 | | 1190748 |
| | A4 | | | 25.0 | | 874760 |
| | A5 | | | 22.5 | | 5892062 |
| B | B1 | 23 | 78 | 30.0 | 0.2 | 1010371 |
| | B2 | | | 27.5 | | 1405703 |
| | B3 | | | 27.5 | | 1073814 |
| | B4 | | | 25.0 | | 1750067 |

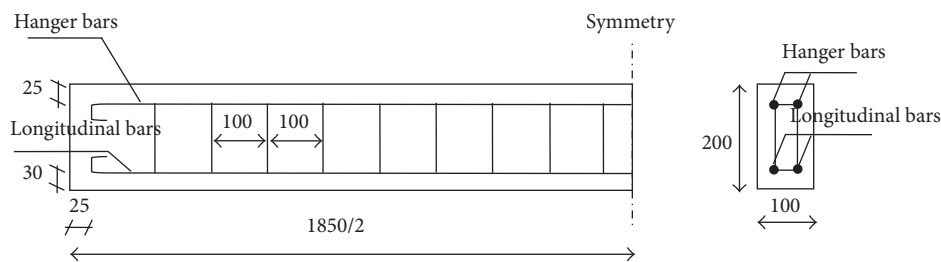


FIGURE 9: Size of steel bars used in RC beam.



FIGURE 10: Hot-wet environment simulation and control system.

The width and length of the main fatigue crack were measured using a microscope and crack width gauge. According to the research of our research group [7], the main crack on the strengthened beam grew rapidly in fast propagation stage. Macrocrack was observed every one or two cycles under the above loading levels. Therefore, at the beginning of the tests, fatigue machine would temporarily stop every dozen cycles for observation of fatigue crack propagation. Average loading level was applied during the stop for about five minutes. In steady propagation stage (generally $N > 15000$), main crack was observed every ten thousand or one hundred thousand cycles until complete failure of the specimens. The maximum and minimum loads and midspan displacements

of the specimens were recorded by MTS810. 8~10 sets of data were recorded in one loading cycle.

4. Fatigue Crack Propagation Behavior

4.1. Fatigue Crack Propagation Law of Main Crack. Fatigue crack propagation experiments with 5 specimens (Group A) pretreated in hot-wet environment and 4 specimens (Group B) in indoor atmosphere were carried out by using the testing method presented in Section 3. The testing results and crack propagation curve (a - N curve) of each specimen were obtained as shown in Table 2 and Figure 11, among which, crack height, a , was the crack projection length under the

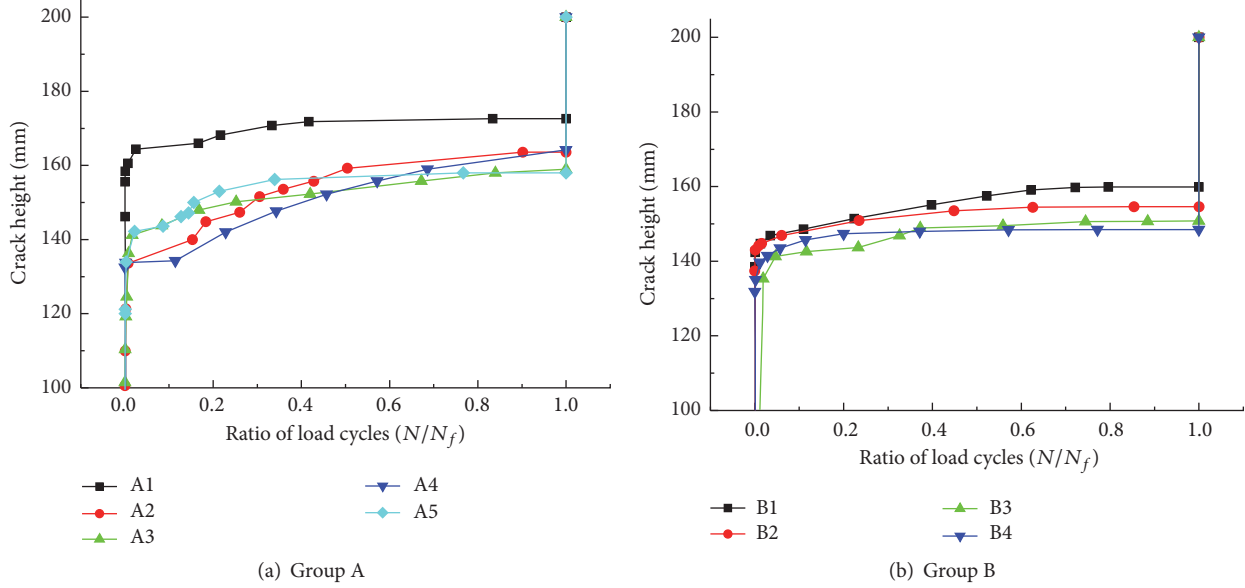
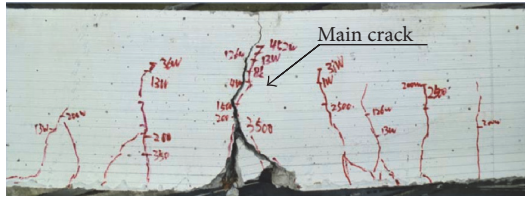
FIGURE 11: Experimental a - N curves.

FIGURE 12: Morphology and distribution of cracks (A4).

direction along the beam height. From the previous work done by our research group [7] and from Figure 12, the main crack propagation behavior on the strengthened beam can be summarized into three stages: (1) fast propagation stage; (2) steady propagation and arrest stage; (3) unstable propagation stage.

4.2. Effect of Hot-Wet Environment on Failure Mode. Failure mode of all the specimens is CFL debonding. In indoor atmosphere environment, lots of concrete fragment were bonded on CFL when specimens failed as shown in Figure 13(a). In hot-wet environment, it is different that less concrete fragment bonded on CFL in hot wet environment compared to indoor atmosphere when specimens failed as shown in Figure 13(b). The reason is that, in indoor atmosphere, the damage of concrete nearby CFL preceded the adhesive layer between CFL and concrete because shear strength of adhesive layer (14 MPa) is much higher than that of concrete (6 MPa). It is obvious that adhesive layer is sensitive to hot-wet environment. After pretreatment of hot-wet environment, shear strength of adhesive layer reduced, which causes fewer concrete fragments to be bonded on CFL compared to those under indoor atmosphere environment.

4.3. Fatigue Crack Propagation Rate. Extensive experimental studies had shown that Paris-Erdogan law was also applicable to quasibrittle materials such as rock [34] and concrete [35] if the structure size was kept constant. According to the J -integral approach, the fatigue crack propagation rate, da/dN , was put in relation to the cyclic J -integral amplitude [11]:

$$\frac{da}{dN} = C_J (\Delta J)^{m_J}, \quad (5)$$

where da is crack growth increment; dN is loading cycle increment; C and m are material constants; $\Delta J = J_{\max} - J_{\min}$ is J -integral amplitude, which can be obtained through finite element method shown in Section 2.

da/dN can be calculated based on a - N curves obtained by fatigue crack propagation tests of five specimens (A1, A2, A5, B1, and B2). The FE model of the strengthened RC beam was established to calculate ΔJ considering nonlinear material properties and fatigue performance degradation introduced in Section 2. However, the test results of specimens (A3, A4, B3, and B4) were not considered in the fitting of Paris law, which were used for verification of the fitting in next section.

Taking $\log(da/dN)$ and $\log(\Delta J)$ as the vertical and horizontal coordinates, respectively, the calculated results under indoor atmosphere and hot-wet environment are shown in Figure 14. As shown in Figure 14, a good linear relation existed between the two variables. Regression equations were established with the least square method (with correlation coefficients $R^2 = 0.96$ and 0.80) and the testing data from five specimens (A1, A2, A5, B1, and B2) as follows:

$$\frac{da}{dN} = 13.19 (\Delta J)^{2.87}, \quad (\text{indoor atmosphere}) \quad (6)$$

$$\frac{da}{dN} = 10.51 (\Delta J)^{1.97}, \quad (\text{hot-wet environment}). \quad (7)$$

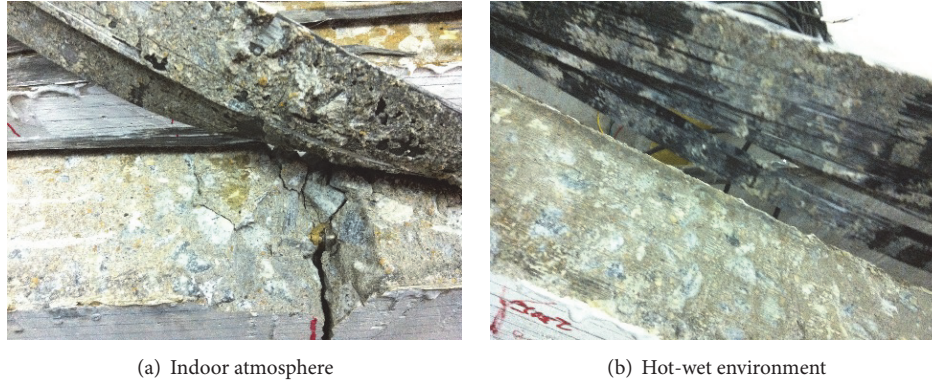


FIGURE 13: The sketch of debonded CFL at different environment.

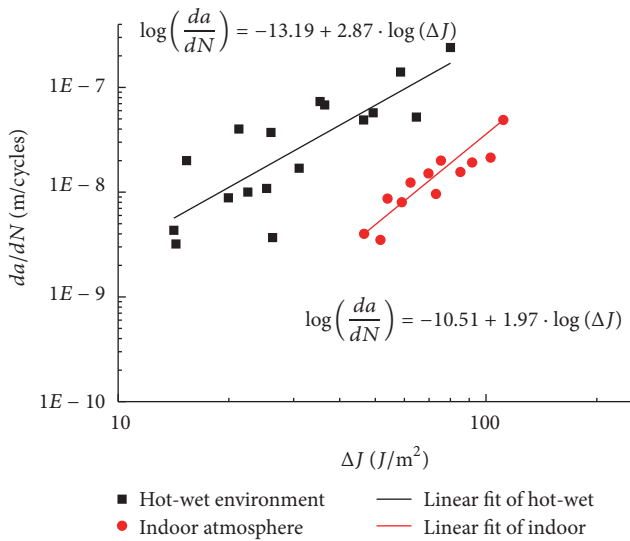


FIGURE 14: $da/dN \sim \Delta J$ curves for the main crack.

It was observed that the slopes of the fatigue crack propagation curve of all the specimens were similar as shown in Figure 14. The fatigue crack propagation rate of the RC beams strengthened with CFL by hot-wet pretreatment was higher than that without pretreatment across all the ΔJ ranges, which indicated that the specimens with hot-wet pretreatment exhibited the lower resistance to fatigue crack propagation.

5. Fatigue Life Prediction of the Strengthened Beams

As shown in Figure 11, fatigue lives of steady propagation stage occupied for 95% of full fatigue lives of RC beams strengthened with CFL. Therefore, in engineering practice, fatigue lives in crack steady propagation stage can be approximately used for prediction of full fatigue lives of the strengthened beams. It can be expected that the predicting results will be conservative.

The fatigue lives in crack steady propagation stage can be computed by the following, which was transformed from (5):

$$\int_{N_0}^{N_c} dN = \int_{a_0}^{a_c} \frac{da}{C(\Delta J)^m} = \sum_i \frac{\Delta a_i}{C(\Delta J_i)^m}, \quad (8)$$

where N_0 is initial loading cyclic number at the beginning of crack steady propagation stage. As period of fast propagation stage is very short, it would not lead to big error if taking $N_0 = 0$; N_c is the loading cyclic number at the end of crack steady propagation stage; a_0 is crack height at the beginning of crack steady propagation stage and a_c is that at the end of this stage; $\Delta a_i = a_i - a_{i-1}$ is crack increment in one calculation step. In this paper, Δa_i was chosen to be 0.2 mm according to total crack increment in steady propagation stage and calculation accuracy. Accumulated calculation of N_c began from $a_{i-1} = a_0$ to $a_i = a_c$ and ΔJ_i was calculated using the FE model which was established to calculate ΔJ considering nonlinear material properties and fatigue performance degradation introduced in Section 2.

Substituting (6) and (7) into (8), respectively, the prediction results for fatigue lives of the specimens under three-point bending loads with $P_{\max} = 30, 27.5, 25$ kN were obtained as shown in Table 3. The experimental data of four specimens (A3, A4, B3, and B4) were taken to compare with the prediction results, which were shown in Table 3. As shown in this table, the average relative error of prediction results is about -10.0%. The predicted values are always smaller than experimental data and conform to the practical facts. Therefore, fatigue lives of the RC beams strengthened with CFL can be predicted accurately using (6) and (7) under different environment. The prediction results could be conservative and consistent with the experimental data.

6. Conclusions

Finite element analyses on J -integral for main crack of RC beam strengthened with CFRP under three-point bending load were completed based on nonlinear fracture mechanics and cohesive zone model under hot-wet environment, and the fatigue crack propagation tests of the RC beams strengthened with CFL under hot-wet environment were carried out, and the following conclusions were obtained:

TABLE 3: Predicting and experimental results of fatigue lives.

| Specimen number | Predicting N_f (cycles) | Experimental N_f (cycles) | Relative error (%) |
|-----------------|---------------------------|-----------------------------|--------------------|
| A3 | 1050014 | 1190748 | -11.8 |
| A4 | 781455 | 874760 | -10.7 |
| B3 | 1006696 | 1073814 | -6.25 |
| B4 | 1595176 | 1750067 | -11.3 |

- (1) J -integral of main crack on RC beam strengthened with CFRP can be calculated accurately with the FE method based on nonlinear fracture mechanics. In the FE model of J -integral, Cohesive Zone Model under hot-wet environment and indoor atmosphere environment was applied to model the bond-slip relation of interface between CFRP and concrete, and Concrete Plastic Damage Model was also used with consideration of fatigue strength degradation.
- (2) Fatigue crack propagation process on RC beams strengthened with CFRP can be summarized into three stages: fast propagation stage, steady propagation stage, and unstable propagation stage. Fatigue lives of the specimen in the steady propagation stage of the main crack account for 95% of full fatigue lives. Therefore, in engineering practice, fatigue lives of the specimen in steady propagation stage of the main crack can be approximately used for predicting the full fatigue lives.
- (3) Semiempirical formula of fatigue crack propagation rate on RC beam strengthened with CFRP was proposed based on the above finite element calculation and fatigue crack propagation tests under high temperature and high humidity (50°C, 95% R · H) environment pretreatment and indoor atmosphere environment (23°C, 78% R · H). Fatigue lives of the strengthened RC beams can be predicted accurately using the semiempirical formula. The prediction results were conservative compared with the experimental data.

Competing Interests

The authors declare that they have no competing interests.

Acknowledgments

The project is supported by National Natural Science Foundation of China (nos. 11627802, 51678249, 11132004, and 51508202), China Scholarship Council (no. 201606155018), and Open Project for Key Laboratory Construction of Mountainous Bridges and Tunnels in Chongqing Jiaotong University (no. CQSLBF-Y16-9).

References

- [1] J. F. Dong, Q. Y. Wang, and Z. W. Guan, "Structural behaviour of RC beams externally strengthened with FRP sheets under

- fatigue and monotonic loading," *Engineering Structures*, vol. 41, pp. 24–33, 2012.
- [2] Y. J. Kim and P. J. Heffernan, "Fatigue behavior of externally strengthened concrete beams with fiber-reinforced polymers: state of the art," *Journal of Composites for Construction*, vol. 12, no. 3, pp. 246–256, 2008.
- [3] L. C. Meneghetti, M. R. Garcez, L. C. P. Da Silva Filho, F. D. P. S. L. Gastal, and T. N. Bittencourt, "Fatigue life of RC beams strengthened with FRP systems," *Structural Concrete*, vol. 15, no. 2, pp. 219–228, 2014.
- [4] F. Oudah and R. El-Hacha, "Research progress on the fatigue performance of RC beams strengthened in flexure using Fiber Reinforced Polymers," *Composites Part B: Engineering*, vol. 47, pp. 82–95, 2013.
- [5] G. El-Saikaly and O. Chaallal, "Fatigue behavior of RC T-beams strengthened in shear with EB CFRP L-shaped laminates," *Composites Part B: Engineering*, vol. 68, pp. 100–112, 2015.
- [6] X. H. Zheng, P. Y. Huang, G. M. Chen, and X. M. Tan, "Fatigue behavior of FRP-concrete bond under hygrothermal environment," *Construction and Building Materials*, vol. 95, pp. 898–909, 2015.
- [7] J. Deng and P. Huang, "Main crack propagation behaviour of RC beams strengthened with CFRP under fatigue load," *Key Engineering Materials*, vol. 462-463, pp. 791–795, 2011.
- [8] P. Huang, G. Liu, X. Guo et al., "Experimental study on fatigue crack propagation rate of RC beam strengthened with carbon fiber laminate," in *Proceedings of the International Conference on Experimental Mechanics (ICEM '08)*, vol. 7375 of *Proceedings of SPIE*, Nanjing, China, November 2008.
- [9] P. Paris and F. Erdogan, "A critical analysis of crack propagation laws," *Journal of Basic Engineering*, vol. 85, no. 4, pp. 528–534, 1963.
- [10] G. C. Sih and A. DiTommaso, *Fracture Mechanics of Concrete: Structural Application and Numerical Calculation*, Springer, Dordrecht, Netherlands, 1985.
- [11] C. L. Chow and T. J. Lu, "On the cyclic J -integral applied to fatigue cracking," *International Journal of Fracture*, vol. 40, no. 3, pp. R53–R59, 1989.
- [12] Y. S. Petryna, D. Pfanner, F. Stangenberg, and W. B. Krätzig, "Reliability of reinforced concrete structures under fatigue," *Reliability Engineering and System Safety*, vol. 77, no. 3, pp. 253–261, 2002.
- [13] T. Sain and J. M. Chandra Kishen, "Residual fatigue strength assessment of concrete considering tension softening behavior," *International Journal of Fatigue*, vol. 29, no. 12, pp. 2138–2148, 2007.
- [14] C. Zanuy, P. de la Fuente, and L. Albajar, "Effect of fatigue degradation of the compression zone of concrete in reinforced concrete sections," *Engineering Structures*, vol. 29, no. 11, pp. 2908–2920, 2007.
- [15] J.-S. Zhu and X.-C. Zhu, "Study on simplified method for the analysis of fatigue failure process of RC bridges," *Engineering Mechanics*, vol. 29, no. 5, pp. 107–121, 2012.
- [16] Z. B. Haber, K. R. MacKie, and L. Zhao, "Mechanical and environmental loading of concrete beams strengthened with epoxy and polyurethane matrix carbon fiber laminates," *Construction and Building Materials*, vol. 26, no. 1, pp. 604–612, 2012.
- [17] J. Deng, A. Liu, Z. Ma, P. Huang, and R. Zhou, "Interfacial behavior of RC beams strengthened with FRP under fatigue loading," *Advances in Structural Engineering*, vol. 18, no. 2, pp. 283–293, 2015.

- [18] X. H. Zheng, *Study on the Bond-Slip Mechanism of CFL-Concrete Interface under Hot-Wet Environment*, South China University of Technology, Guangzhou, China, 2014.
- [19] G. Qin, P. Huang, H. Zhou, X. Guo, and X. Zheng, "Fatigue and durability behavior of RC beams strengthened with CFRP under hot-wet environment," *Construction and Building Materials*, vol. 111, pp. 735–742, 2016.
- [20] P. Y. Huang and J. C. Zeng, Carbon Fiber Laminate and its application, China: The invention patent authorization number: ZL200410026742.8, Date of authorization proclamation, 2006.
- [21] Code for Design of Concrete Structure (GB50010-2010), China, 2011.
- [22] H. Saadatmanesh and F. E. Tannous, "Relaxation, creep, and fatigue behavior of carbon fiber reinforced plastic tendons," *ACI Materials Journal*, vol. 96, no. 2, pp. 143–153, 1999.
- [23] J. O. Holmen, *Fatigue of Concrete by Constant and Variable Amplitude Loading*, Division on Concrete Structures, Norwegian Institute of Technology, University of Trondheim, 1979.
- [24] Y. T. Obaidat, S. Heyden, and O. Dahlblom, "Evaluation of parameters of bond action between FRP and concrete," *Journal of Composites for Construction*, vol. 17, no. 5, pp. 626–635, 2013.
- [25] Y. T. Obaidat, S. Heyden, and O. Dahlblom, "The effect of CFRP and CFRP/concrete interface models when modelling retrofitted RC beams with FEM," *Composite Structures*, vol. 92, no. 6, pp. 1391–1398, 2010.
- [26] D. S. Dugdale, "Yielding of steel sheets containing slits," *Journal of the Mechanics and Physics of Solids*, vol. 8, no. 2, pp. 100–104, 1960.
- [27] G. Alfano, "On the influence of the shape of the interface law on the application of cohesive-zone models," *Composites Science and Technology*, vol. 66, no. 6, pp. 723–730, 2006.
- [28] N. Bouklas, C. M. Landis, and R. Huang, "Effect of solvent diffusion on crack-tip fields and driving force for fracture of hydrogels," *Journal of Applied Mechanics, Transactions ASME*, vol. 82, no. 8, Article ID 081007, 2015.
- [29] P. Y. Huang, C. Zhao, and X. Y. Guo, *Fatigue Performance of RC Members Strengthened with FRP*, Science Press, Beijing, China, 2009.
- [30] P.-Y. Huang, H. Zhou, H.-Y. Wang, and X.-Y. Guo, "Fatigue lives of RC beams strengthened with CFRP at different temperatures under cyclic bending loads," *Fatigue & Fracture of Engineering Materials and Structures*, vol. 34, no. 9, pp. 708–716, 2011.
- [31] H. Zhou, *Study on Durability Experimental Methods of RC Beams Strengthened with FRP in Hot-wet Environments*, South China University of Technology, Guangzhou, China, 2012.
- [32] H. Zhou, P. Y. Huang, G. Qin, and D. M. Wei, "Durability experimental method of RC components strengthened with FRP in hot-wet environment," *Applied Mechanics and Materials*, vol. 782, pp. 183–196, 2015.
- [33] China National Technology Standard, "Test method for aging properties of glass fiber reinforced plastics," GB/T 2573-2008, 2008.
- [34] J.-L. Le, J. Manning, and J. F. Labuz, "Scaling of fatigue crack growth in rock," *International Journal of Rock Mechanics and Mining Sciences*, vol. 72, pp. 71–79, 2014.
- [35] Z. P. Bazant and M. H. Hubler, "Theory of cyclic creep of concrete based on Paris law for fatigue growth of subcritical microcracks," *Journal of the Mechanics and Physics of Solids*, vol. 63, no. 1, pp. 187–200, 2014.

Research Article

Mechanical Properties of Steel-FRP Composite Bars under Tensile and Compressive Loading

Zeyang Sun,¹ Yu Tang,² Yunbiao Luo,³ Gang Wu,^{1,2} and Xiaoyuan He²

¹*Southeast University, Key Laboratory of Concrete and Prestressed Concrete Structures of the Ministry of Education, Nanjing 210096, China*

²*School of Civil Engineering, Southeast University, Nanjing 210096, China*

³*Department of Civil Engineering, Tianjin University, Tianjin 300072, China*

Correspondence should be addressed to Gang Wu; g.wu@seu.edu.cn

Received 20 October 2016; Accepted 4 December 2016; Published 3 January 2017

Academic Editor: Jun Deng

Copyright © 2017 Zeyang Sun et al. This is an open access article distributed under the Creative Commons Attribution License, which permits unrestricted use, distribution, and reproduction in any medium, provided the original work is properly cited.

The factory-produced steel-fiber reinforced polymer composite bar (SFCB) is a new kind of reinforcement for concrete structures. The manufacturing technology of SFCB is presented based on a large number of handmade specimens. The calculated stress-strain curves of ordinary steel bar and SFCB under repeated tensile loading agree well with the corresponding experimental results. The energy-dissipation capacity and residual strain of both steel bar and SFCB were analyzed. Based on the good simulation results of ordinary steel bar and FRP bar under compressive loading, the compressive behavior of SFCB under monotonic loading was studied using the principle of equivalent flexural rigidity. There are three failure modes of SFCB under compressive loading: elastic buckling, postyield buckling, and no buckling (ultimate compressive strength is reached). The increase in the postyield stiffness of SFCB (r_{sf}) can delay the postyield buckling of SFCB with a large length-to-diameter ratio, and an empirical equation for the relationship between the postbuckling stress and r_{sf} is suggested, which can be used for the design of concrete structures reinforced by SFCB to consider the effect of reinforcement buckling.

1. Introduction

Fiber Reinforced Composites (FRP) have been widely used in the aerospace, shipbuilding, automobile, and mechanical industries since the 1940s. In recent years, FRP has become a new type of reinforcement for civil engineering with high strength, light weight, and anticorrosion performance [1, 2]. The design guidelines for the FRP bar for prestressing concrete structures were proposed by an ACI committee [3]. With the development of research and application, the shortcomings of different types of FRP include the following: (1) the ultimate tensile strain of FRP is generally not more than 3%, which cannot meet the ductility demand for concrete structures located in a region of high seismic hazard; (2) the price of carbon FRP (CFRP) cannot meet the low-cost requirements for use in civil engineering; (3) the shear strength of FRP is approximately 5% of its tensile strength, and the brittle FRP may be broken during the construction process (concrete vibration, anchoring, or bending); (4) the

elastic modulus of glass FRP (GFRP) or basalt FRP (BFRP) is low, which cannot guarantee the stiffness of the corresponding concrete structures. Studies on concrete beams reinforced by hybrid FRP were conducted to enhance the stiffness or ductility [4]; however, the ductility was achieved as a result of the partial fracture of fibers with low elongation rates. Steel bar has the characteristics of low strength, high elastic modulus, high ductility, poor durability, and large density, while FRP has the opposite characteristics. By combining steel and FRP, a composite bar with optimized performance can be obtained, and the hybrid reinforced concrete beams were studied by research from the perspective of corrosion control and improvement in stiffness [5, 6].

As shown in Figure 1, the stable postyield stiffness (E_2) of a steel-FRP composite bar (SFCB) [7] can be achieved by combining the linear elastic FRP and the elastic-plastic steel bar. Compared with steel bars, the weight of SFCB is comparatively reduced, and the anticorrosion performance is enhanced. Compared with a pure FRP bar, the stiffness of

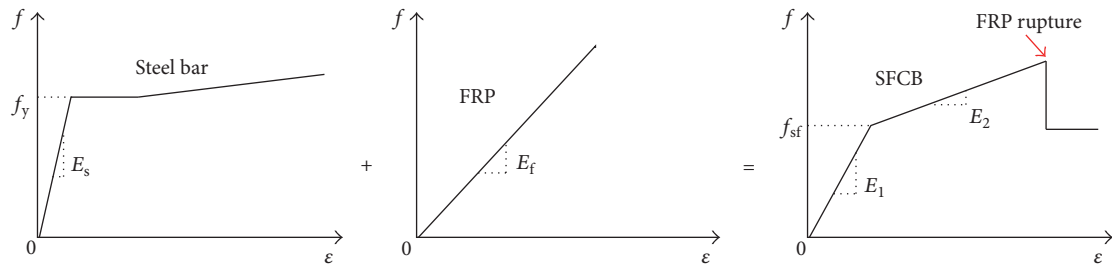


FIGURE 1: Schematic view of the mechanical property of an SFCB.

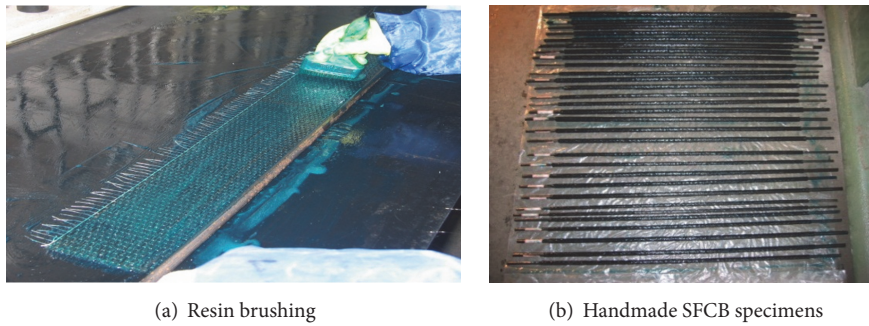


FIGURE 2: Exploratory handmade SFCB specimens.

the composite bar is greatly improved, especially for a GFRP or BFRP bar [8], and the cost is much lower. Compared to a GFRP bar, a BFRP bar can have a relatively higher stiffness and strength with the same cost [9], and the fatigue behavior and the degradation mechanism of BFRP under different stress levels of cyclic loadings were conducted [10] by Zhao et al. in Southeast University. BFRP was adopted to produce the composite bar (steel-BFRP composite bar) in this study.

The mechanical behavior of SFCB [11], the static behavior of concrete beams reinforced by SFCB [12], and concrete beams strengthened by near-surface-mounted (NSM) SFCB [13] were conducted by our research group. These studies demonstrated that the effective postyield stiffness of SFCB can improve the corresponding reinforced concrete structures. To improve the seismic performance of concrete structures, SFCB can be used as the longitudinal reinforcement to form a controllable postyield stiffness [14, 15]. In addition, the bond strength between SFCB and concrete can be optimized to enhance the seismic performance of the structure [16]. This paper mainly introduces the technology of factory-produced SFCB and its mechanical properties under tensile/repeated tensile loading. Based on the experimental results for ordinary steel bars and FRP bar under compressive loading, the effects of postyield stiffness and equivalent length-to-diameter ratio (ELDR) of the SFCB on compressive behavior were analyzed.

2. Factory Production of SFCB

SFCB has several key interfaces that include the fiber/resin matrix, steel/FRP, and SFCB/environmental media. The shear

performance of the interfaces directly reflects the mechanical property of SFCB. The debonding of FRP at the interface between the fiber and resin matrix can effectively adjust the stress distribution inside the FRP, and the ultimate strength of fiber can be fully utilized. The key production technology and the basic mechanical properties of the SFCB were carried out based on numerous exploratory trials (Figure 2) using parameters including inner steel type (round or ribbed rebar), inner steel bar diameter, FRP sheet type, steel/FRP interface treatment, and so on.

When using a round bar as the inner core, a uniform distribution of the outer longitudinal fiber can be ensured. In such a case, the strength of the FRP can be fully utilized. However, the tensile test of the corresponding SFCB shows that the relative slip between the round inner steel bar and outer FRP happened. The anchorage test demonstrated that the bonding performance between round steel bar and the outer FRP was difficult to guarantee. As a result, ribbed rebar with winding roving was selected as the inner core of the SFCB (Figure 3(a)). The winding roving could fill in the gaps between the ribs of the steel bar to protect the longitudinal FRP from being hurt. Meanwhile, an enhanced interface was achieved between steel bar and FRP. The factory production of SFCB was proposed by modifying the current FRP pultrusion equipment (Figure 3(b)), and the surface rib was formed by winding a plastic tape with a specific width during the pultrusion process. The modified pultrusion equipment can also be used to produce steel wire-FRP composite bar or steel-hybrid FRP composite bar for different structural needs.

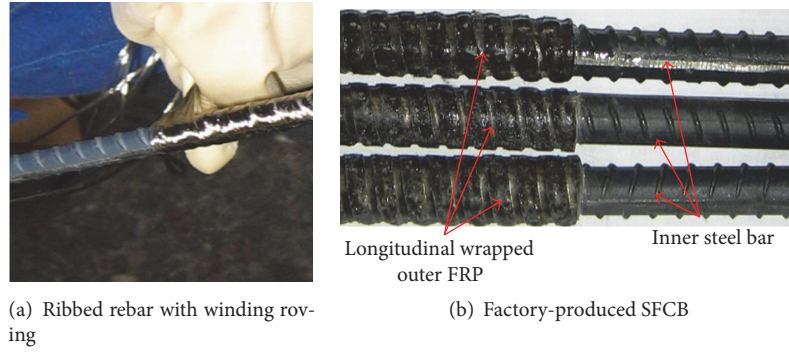


FIGURE 3: Factory-produced SFCB and its interface treatment.

TABLE 1: Mechanical properties of steel bar, basalt fibers, and SFCBs.

| Material type | Elastic modulus GPa | Yield strength MPa | Ultimate strength MPa | Elongation rate (%) |
|----------------------------|------------------------|-----------------------|--------------------------|------------------------|
| Steel bar (HRB400) | 200 | 420 | 580 | 15 |
| S10-B20 | 140.03 | 309.6 | 541.8 | 2.5 |
| S10-B30 | 138.10 | 302.35 | 573.45 | 2.3 |
| 20 bundles of basalt fiber | 60 | — | 1670 | 2.5 |
| 30 bundles of basalt fiber | 60 | — | 1500 | 2.3 |

3. Mechanical Properties of SFCB under Tensile and Repeated Tensile Loading

The mechanical properties of SFCB can be expressed based on the composite law [11], and the tensile postyield stiffness ratio of SFCB (r_{sf}) can be calculated by

$$r_{sf} = \frac{E_f A_f}{(E_s A_s + E_f A_f)}, \quad (1)$$

where E_f and A_f are the elastic modulus and cross-sectional area of the outer FRP of the SFCB, respectively, and E_s and A_s are the elastic modulus and cross-sectional area of the inner steel bar, respectively.

The mechanical properties of the steel bar, basalt fiber, and SFCBs obtained experimentally are shown in Table 1, in which S10-B20 represents the SFCB made of 10 mm diameter inner steel bar longitudinally wrapped by 20 bundles of 2400 tex basalt fiber. The unit “tex” represents the weight in grams of each bundle fiber 1000 meters long. It can be seen from Table 1 that the strength of the basalt fiber with 20 bundles in S10-B20 was approximately 65.7% of the original fiber strength. Moreover, the effective strength of the basalt fiber will be further decreased by the increasing amount of basalt fiber. For example, the average strength of 30 bundles of basalt fiber in S10-B30 was approximately 57.3% of the original fiber. The reason for this strength reduction could be due to the fact of the inevitable nonuniformity of the outer fiber during the SFCB pultrusion process, which would result in an initial bending and partial fracture of the outer fiber.

The numerical models for the inner steel bar and the outer FRP of the SFCB were separately established in OpenSees ([17]), and *ReinforcingSteel* was adopted for the steel bar by defining the yield point (f_y, ϵ_y), hardening point (f_{sh}, ϵ_{sh}), tangent at initial strain hardening (E_2), and the peak stress-strain point (f_u, ϵ_u). The mechanical behavior of FRP in SFCB was set according to the test results; the interface of steel/FRP was assumed to be perfect bonding. The load-strain curves of inner steel bar and S10-B20 under repeated tensile loading are presented in Figure 4. It can be found that the calculated values were basically in agreement with the experimental curves. Compared with an ordinary steel bar, an SFCB can achieve less residual strain under the same unloading strain and therefore reduce the unloading residual strain of an SFCB reinforced concrete structure. There are two reasons for this advantage: (1) the unloading stress level of an SFCB is higher than an ordinary steel bar with the same unloading strain and unloading stiffness; (2) when the inner steel bar of an SFCB reaches “0” stress with the plastic residual strain, the corresponding FRP still remains in “tension” due to the residual tensile strain of inner steel bar. Therefore, the FRP will further compress the inner steel bar and then decrease the residual strain of the SFCB. After S10-B20 reached a relatively large strain ($>13500 \mu\epsilon$), the tested residual strain was slightly larger than the calculated value, which indicated that the compression effect of the linear elastic FRP on the inner steel bar was reduced.

The energy-dissipation capacity of a steel bar and an SFCB that achieve the same unloading strain was shown in Figure 5(a), which can be calculated by the integration of the

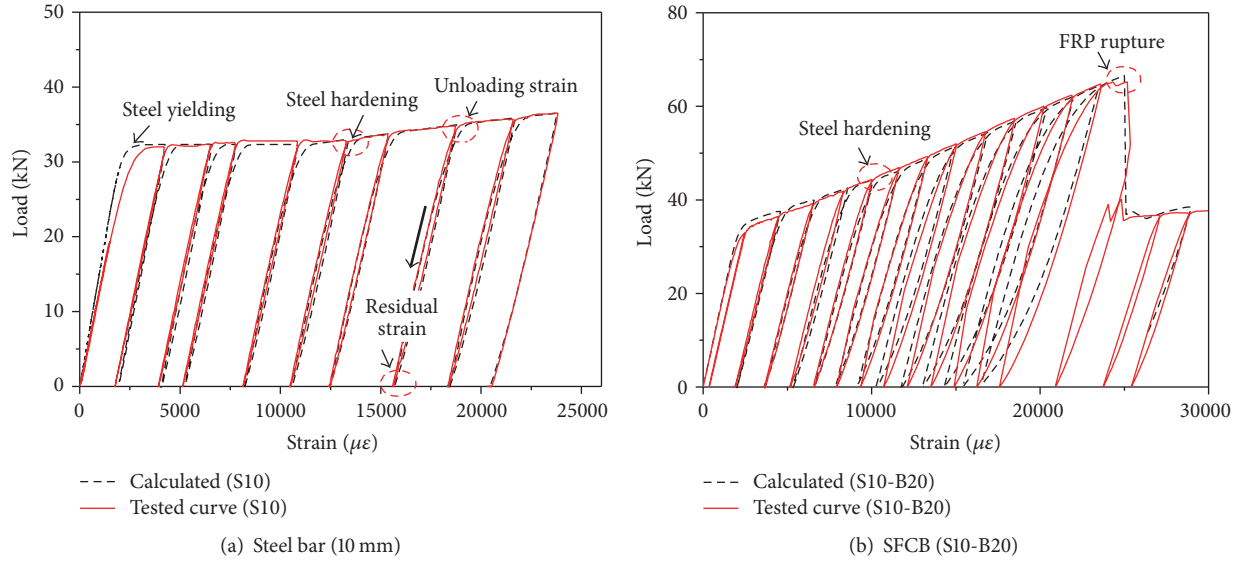


FIGURE 4: Typical performance of a steel bar and an SFCB under repeated tensile loading.

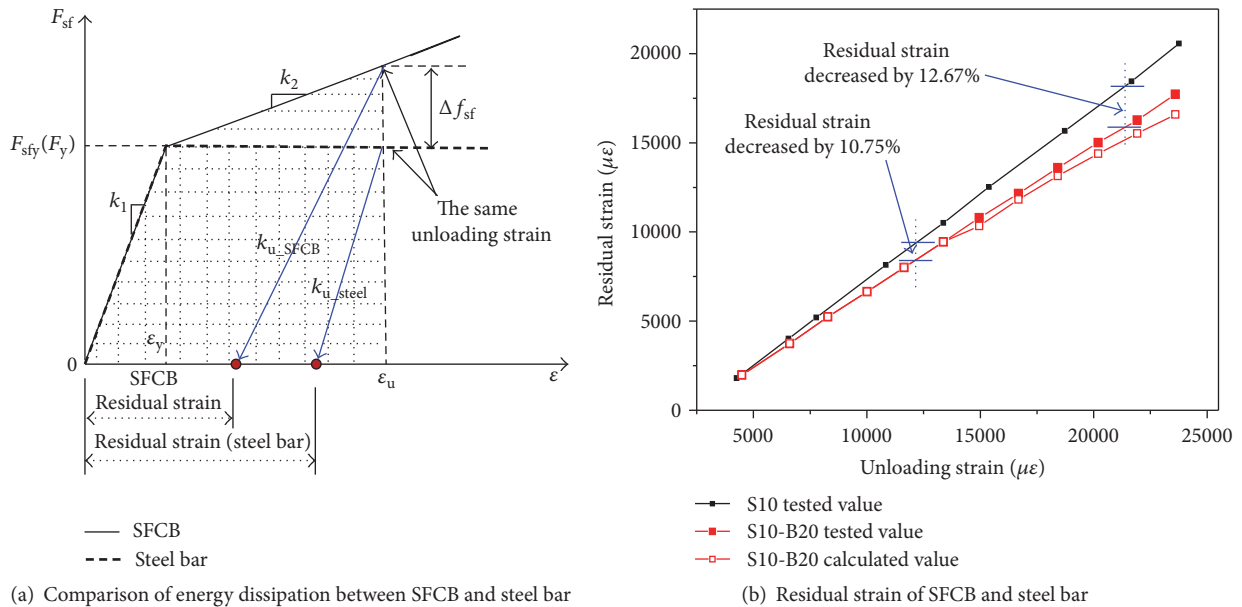


FIGURE 5: Energy-dissipation capacity and residual strain of SFCB and steel bar.

load-strain curve. The hardening of the steel bar is very small before the FRP fractures; therefore, the ratio of the dissipated energy of the inner steel bar (S_{steel}) to the SFCB (S_{SFCB}) can be calculated as follows:

$$\frac{S_{SFCB}}{S_{steel}} = \frac{r_{sf} (\epsilon_u - \epsilon_y)^2}{2\epsilon_y \epsilon_u - \epsilon_y^2}, \quad (2)$$

where ϵ_y and ϵ_u are the yield strain and ultimate strain, respectively. It can be seen that with the increase of r_{sf} the SFCB has a larger energy-dissipation capacity at the same peak strain.

The experimental and calculated residual strains of S10-B20 are shown in Figure 5(b). Only the experimental values of the steel bar (S10) were listed because the calculated values were basically consistent with the experimental values. It can be found that the residual strain of S10-B20 was reduced by approximately 10% compared with the corresponding steel bar, and the reduction of the residual strain slightly increased when the strain approached the ultimate stage (Figure 5(b)). The tested residual strain of S10-B20 was slightly larger than that of the calculated value. The reasons for this are mainly as follows: (1) FRP is assumed to be completely straight in the calculation and the steel bar had no initial bending, while in the experiment the surface of the SFCB was formed by

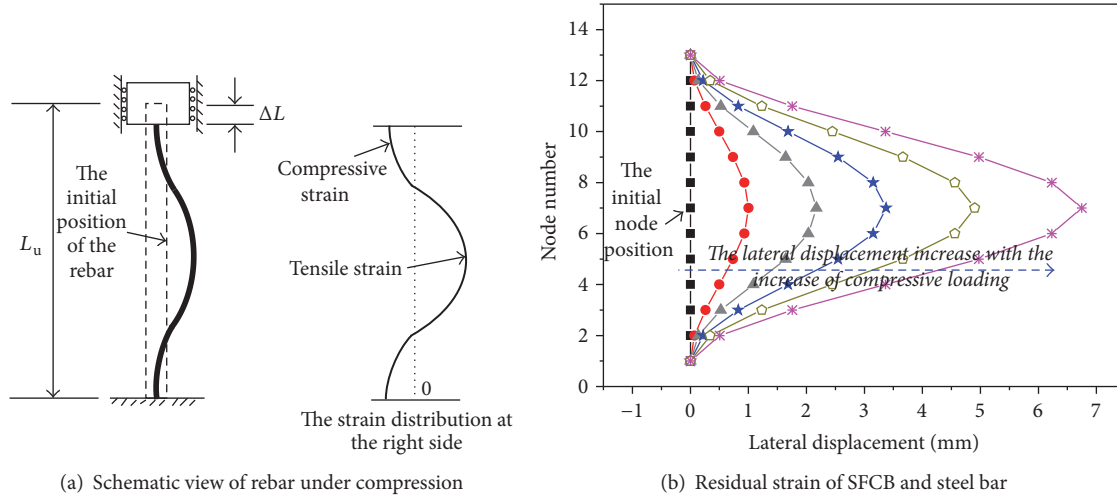


FIGURE 6: The mechanics of a steel bar under compressive loading.

a plastic band; that is, the longitudinal fibers were partially curved, resulting in an FRP strain slightly behind that of the inner steel bar; (2) the inner steel bar was assumed to work together with the outer FRP, while in reality a relative slip occurred at the steel/FRP interface after the inner steel bar yielded.

4. The Compressive Behavior of SFCB

4.1. The Compressive Behavior of Ordinary Steel Bar. When partial spalling of the concrete cover of a concrete column occurs, the longitudinal rebar would be exposed to the environment with the stirrup [18], and the mechanical model in the laboratory can be regarded as having both ends fixed (Figure 6(a)). With the development of the compression force, the left side of the middle part was in compression while the right side was in tension. The lateral deformation of the middle section increased with the development of compressive loading (Figure 6(b)).

A great amount of experimental and theoretical research on the compressive behavior of steel bars has been conducted [19–21]. The main parameters were the geometric shape of the rebar, yield strength (ordinary steel bar, high-strength steel bar), hardening degree, and loading pattern (unidirectional compression, cyclic tensile, and compressive loading). The ratio between the tested length and diameter of the steel bar (r_{LD}) was defined as follows:

$$r_{LD} = \frac{L_u}{d_b}, \quad (3)$$

where L_u and d_b are the calculated length of longitudinal reinforcement and rebar diameter, respectively.

An experimental study on the hysteretic behavior of the steel bars subjected to tensile, repeated tensile and cyclic tensile, and compressive loading was conducted by Zheng [22]. The comparison between the test results and the corresponding calculated curves is shown in Figure 7, in which the elastic modulus of the rebar was $E_s = 200$ GPa, yield strength $f_y = 568$ MPa, hardening strain $\varepsilon_{sh} = 0.1505$, and ultimate

strength $f_u = 1.286 f_y$. It is found that the tensile skeleton curve agrees well with the experimental results (Figure 7(a)). Figures 7(b)–7(d) illustrated the simulation results of the compressive behavior of the rebar with r_{LD} of 10 and 20. The initial lateral drift of the middle node was set to be 1/1000 of the diameter to achieve a uniform buckling mode. It was found that the calculated backbone curves under compressive loading with r_{LD} of 10 and 20 agree well with the experimental data.

The comparison of the stress-strain relationships of the steel bar under cyclic loading ($r_{LD} = 20$) is presented in Figure 7(d). The calculated curve cannot exactly agree with the tested result due to the convergence problem. To avoid the influence of the effect of the loading path on the compressive behavior of SFCB, the performance of SFCB under monotonous compressive loading is presented.

4.2. The Compressive Behavior of SFCB. FRP is wrapped on the outside of the SFCB, so it is necessary to analyze the compressive behavior of an FRP bar. There is a large difference between the tensile and compressive behavior of an FRP bar [23]. The difference can be caused by the fiber type, fiber volume fraction, and resin type. The failure modes of an FRP bar under compression include horizontal tensile failure, local fiber buckling, or shear failure. The compressive strength values of GFRP bar, CFRP bar, and AFRP bar are generally considered to be 55%, 78%, and 20% of their tensile strengths, respectively [24].

The stress-strain relationship of SFCB under compressive loading (see (4)) can be obtained according to the constitutive relation under tensile loading [7]:

$$f_{sf}^- = \begin{cases} \varepsilon_{sf}^- (E_s A_s + E_f^- A_f), & 0 < |\varepsilon_{sf}^-| \leq |\varepsilon_{sfy}^-| \\ f_{sfy}^- + \frac{(\varepsilon_{sf}^- - \varepsilon_{sfy}^-) E_f^- A_f}{A}, & |\varepsilon_{sfy}^-| < |\varepsilon_{sf}^-| \leq |\varepsilon_{sfu}^-| \\ \frac{f_y^- A_s}{A}, & |\varepsilon_{sfu}^-| < |\varepsilon_{sf}^-|, \end{cases} \quad (4)$$

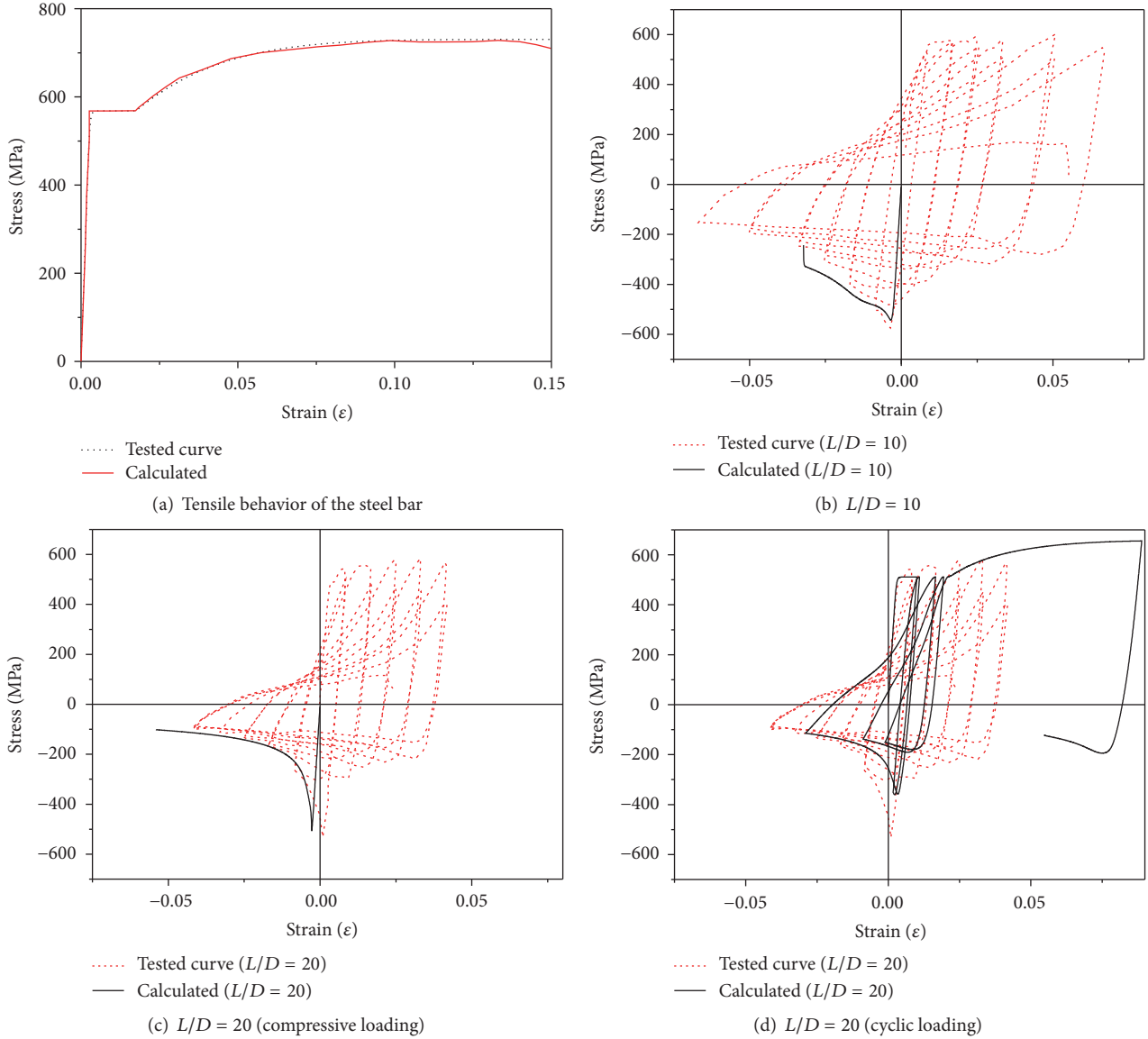


FIGURE 7: Comparison of the tested and calculated results of a steel bar.

where “-” means that the SFCB is under compressive loading. The corresponding postyield stiffness ratio of SFCB under compressive loading (r_{sf}^-) can be calculated as follows:

$$r_{sf}^- = r_{sf} \frac{E_f^- (E_s A_s + E_f A_f)}{E_f (E_s A_s + E_f^- A_f)}. \quad (5)$$

It can be found that r_{sf}^- of an SFCB is 0 when the tensile postyield stiffness ratio r_{sf} is 0, and the r_{sf}^- of a pure FRP bar is 1 when the corresponding r_{sf} is 1.

Since there is a large difference between the compressive modulus of a steel bar and an FRP bar, the equivalent flexural rigidity of an SFCB is defined as $E_s I_{sf,Is}^e = E_s I_s + E_f I_f$ (Figure 8), and the corresponding equivalent diameter

($d_{sf,Is}^e$) and equivalent compressive strength ($f_{sf,Is}^e$) of SFCB can be calculated using (6) and (7), respectively:

$$d_{sf,Is}^e = \sqrt[4]{\frac{E_f}{E_s} (d_{sf}^4 - d_s^4) + d_s^4}, \quad (6)$$

$$f_{sf,Is}^e = \frac{P_{sf}^-}{\sqrt{(E_f/E_s) (A_f^2 + 2A_s A_f) + A_s^2}}, \quad (7)$$

where d_s and d_{sf} are the diameter of the inner steel bar and the diameter of the SFCB, respectively. P_{sf}^- is the compressive load. The critical load $P_{cr,sf}$ of SFCB with two fixed ends can be calculated based on

$$P_{cr,sf} = \frac{\pi^2 (E_s I_s + E_f I_f)}{(\mu_b L_u)^2}, \quad (8)$$

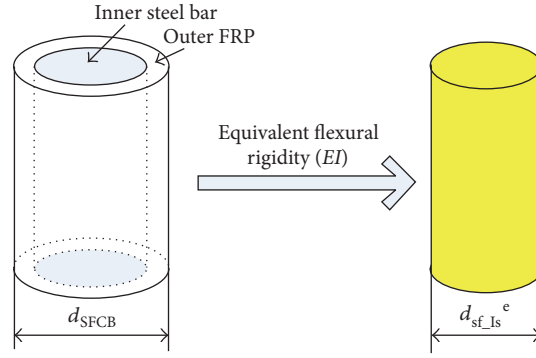
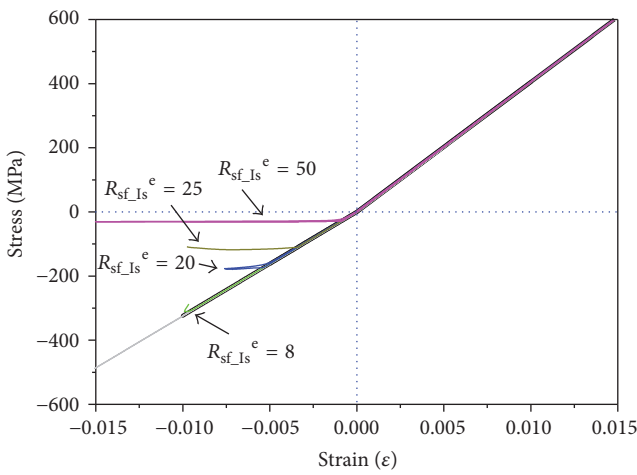
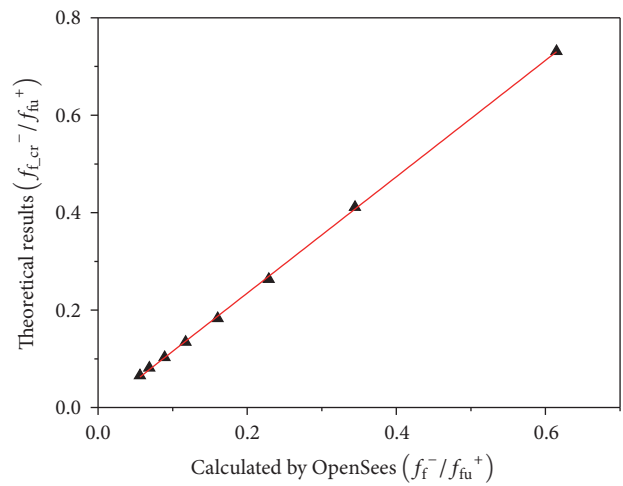


FIGURE 8: Equivalent diameter of SFCB based on equivalent flexural rigidity.



(a) BFRP bar under tensile and compressive loading



(b) The comparison between the calculated results and the theoretical results

FIGURE 9: The simulation results of a BFRP bar under cyclic loading.

where I_s and I_f are the area moments of inertia of steel bar and FRP, respectively. μ_b is the coefficient considering the end constraints. The corresponding ELDR of SFCB is defined as $R_{sf_Is}^e = L_u/d_{sf_Is}^e$.

4.3. Parametric Analysis of SFCB. The experimental study of the compressive behavior of BFRP bar under monotonic compressive loading has been conducted by Zhou [25], who found that the compressive elastic modulus of a BFRP bar is approximately 80% of the tensile elastic modulus, and the compressive strength is approximately 50% of the tensile strength. Based on the test results, the stress-strain behavior of the BFRP bar under tensile and compressive loading was illustrated in Figure 9(a). With an increase in $R_{sf_Is}^e$, the maximum average stress of FRP bar gradually decreases due to bar buckling. The comparison between the

calculated dimensionless critical compressive load and the corresponding theoretical value is presented in Figure 9(b), and the former was approximately 14.2% less than the latter, which was caused by the initial offset (1/1000 of the diameter) in the OpenSees model. The development trends of critical stress with the increase in $R_{sf_Is}^e$ are still in good agreement with each other; therefore, this calculation method can be used to analyze the compressive properties of SFCB.

The load-strain curves and equivalent stress-strain curves of SFCB, with the same $L_u/d_{sf_Is}^e$ and different postyield stiffness ratios, are shown in Figure 10. The load-strain curve shows that the initial compressive stiffness of SFCB is kept constant (Figure 10(a)), while the initial compressive elastic modulus of SFCB decreases with the increase of r_{sf}^- (Figure 10(b)). The equation of initial compressive elastic modulus (E^-) of SFCB could be presented as follows:

$$E^- = \frac{E_{sf}^- A_{sf}}{\sqrt{(E_s/E_f^-) (A_s (r_{sf}^- / (1 - r_{sf}^-)))^2 + 2A_s (r_{sf}^- / (1 - r_{sf}^-)) + A_s^2}} \quad (9)$$

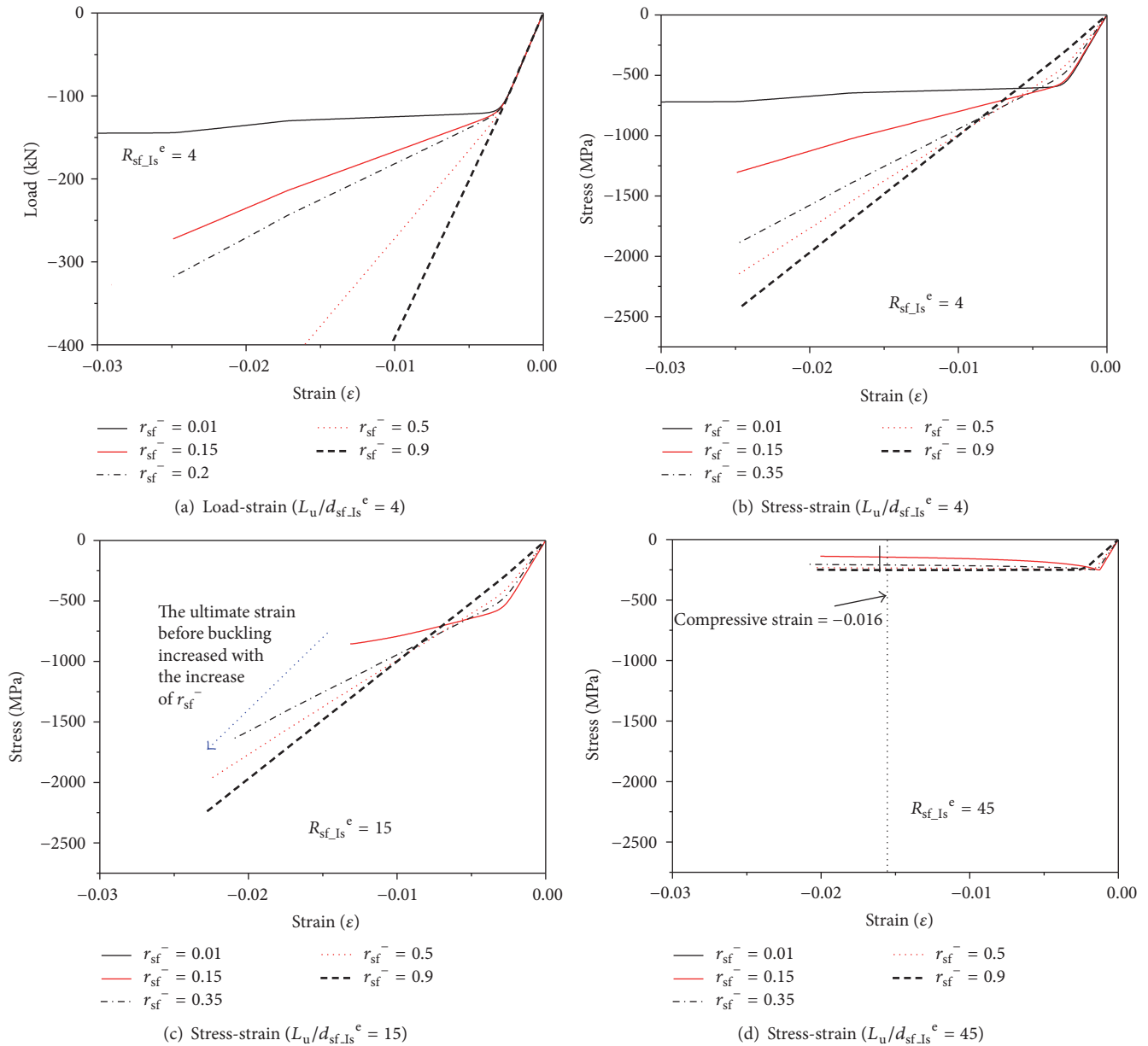


FIGURE 10: The compressive behavior of SFCB.

When r_{sf}^- is relatively small, the stiffness degradation increases significantly with the increase of $L_u/d_{sf.ls}^e$ after the average stress reaches the peak stress. When the value of $L_u/d_{sf.ls}^e$ is between 4 and 15, the yield occurred first, and then a stable postyield stiffness was obtained (Figure 10(b)), which is similar to the tension behavior. With an increase in $L_u/d_{sf.ls}^e$, the SFCB with a lower r_{sf}^- value buckled earlier. In contrast, the SFCB with a higher r_{sf}^- shows a better compression postyield stiffness. After the compressive yield of SFCB occurred, the ultimate stable strain increased with the increase of r_{sf}^- (Figure 10(c)). For example, when the values of $L_u/d_{sf.ls}^e$ for SFCB were 15, 20, and 25, the corresponding r_{sf}^- to maintain a stable compressive postyield stiffness were 0.15, 0.35, and 0.50, respectively. When the $L_u/d_{sf.ls}^e$ is between

30 and 45, elastic buckling occurred in all of the SFCBs. However, the slope of the compressive postbuckling curves varies from negative stiffness to zero stiffness as the r_{sf}^- value increases (Figure 10(d)). For example, the postbuckling stress of an ordinary steel bar decreased dramatically with the development of compressive loading, while for SFCB, when $r_{sf}^- = 0.35$, the postbuckling stress-strain curve could maintain a horizontal line, which indicates a stable postbuckling capacity can be realized. This phenomenon is similar to that of the elastic FRP bars after elastic buckling.

The relationship between the compressive postyield stiffness ratio and tensile postyield stiffness ratio is illustrated in Figure 11, where the compression postyield stiffness ratio is fitted by using compressive strain values between -0.0054

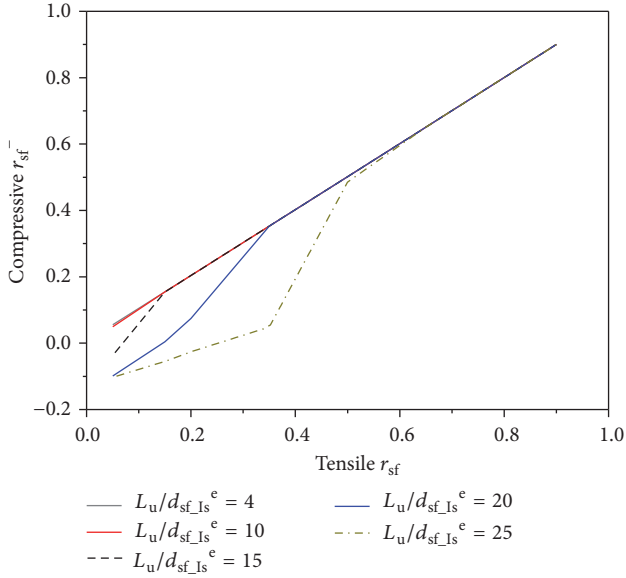


FIGURE 11: The relationship between the values of tensile r_{sf} and compressive r_{sf} .

and -0.0064 . It can be found that, with an increase in $L_u/d_{sf,Is}^e$, the demands on r_{sf}^- to maintain a stable compressive postyield stiffness increase.

With an increase of r_{sf}^- , the buckling loads of SFCBs with the same initial stiffness gradually increase, while the equivalent stresses remained constant. The stress in the descending part of elastic buckling also increases with an increase of r_{sf}^- , until the buckling stress is reached. By comparing the stress values of the two sets of elastic buckling specimens ($L_u/d_{sf,Is}^e$ equal to 45 and 50), the average compression stress was a function of r_{sf}^- (when the compressive strain was -0.016) and basically independent of $L_u/d_{sf,Is}^e$. When r_{sf}^- was between 0 and 0.8, (10) can be obtained with a coefficient of determination R^2 equal to 0.998 (Figure 12). After the value of r_{sf}^- reached 0.8 for the SFCB, the compressive stress was approximately equal to the peak buckling stress

$$\frac{f_{cr,-0.016}^e}{f_{cr,sf}^e} = -1.437 (r_{sf}^-)^2 + 2.004 (r_{sf}^-) + 0.3024 \quad (10)$$

$$r_{sf} \leq 0.8.$$

4.4. Compression Failure Modes of SFCB. Based on the above parametric analysis, it can be found that there are three compression failure modes of SFCB (Figure 13): (a) elastic buckling before the yield of the inner steel bar; (b) buckling failure after the yield of the inner steel of the SFCB; and (c) the SFCB reaching its ultimate strength. When the failure mode is elastic buckling, the postpeak stress carrying capacity increases with the increase in r_{sf}^- , until it reaches the peak buckling stress.

The determination methods of different failure modes are as follows:

- (1) When $P_{cr} < P_{sfy}$, elastic buckling occurred, the peak buckling stress can be calculated using (8), and the postpeak stress is expressed by (10).

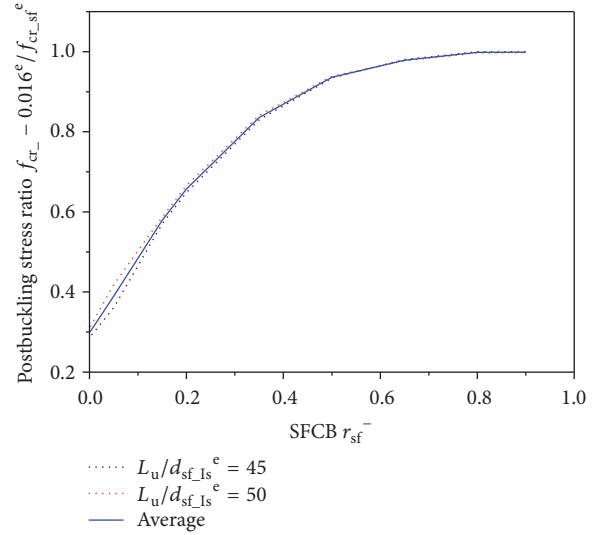


FIGURE 12: The postpeak stress of SFCB with elastic buckling.

- (2) When the critical load is between the yield load of the SFCB ($P_{sfy} \leq P_{cr}$) and the ultimate load, the elastic buckling equation is no longer applicable. In this case the load increase after yield is defined as $P_{cr,sf,part2} = P_{cr,sf,f} - P_{sfy,f}$. This is a load equal to the critical buckling load of the FRP minus the yield load carried by the FRP ($P_{cr,sf,part2} + P_{sfy} < P_{sfu}$). The failure mode is SFCB buckling after the yield of the inner steel bar.
- (3) When the critical load reaches the ultimate compressive strength of the SFCB, no buckling occurred.

5. Conclusions

Based on the factory-produced SFCB, the mechanical properties of SFCB under tensile, repeated tensile, and compressive loading are analyzed, and the following conclusions can be drawn:

- (1) The interface of an SFCB manufactured by round rebar and FRP cannot be guaranteed, and roving should be placed between the inner ribbed steel bar and outer longitudinal fibers to ensure the interface performance.
- (2) The mechanical behavior of SFCB under repeated tensile loading can be well simulated in OpenSees. Similar to a pure FRP bar, the ultimate strength of SFCB slightly decreases with an increase in FRP content. Due to the elastic property of FRP, the residual strain of SFCB (S10-B20) can be reduced by more than 10% after the unloading strain reached $13500 \mu\epsilon$.
- (3) The elastic buckling stress of SFCB with different postyield stiffness ratios can be unified by the corresponding equivalent length-to-diameter ratio of the SFCB based on the equivalent flexural rigidity. When the buckling of SFCB occurred after yield of the inner steel bar, the postyield buckling load of SFCB

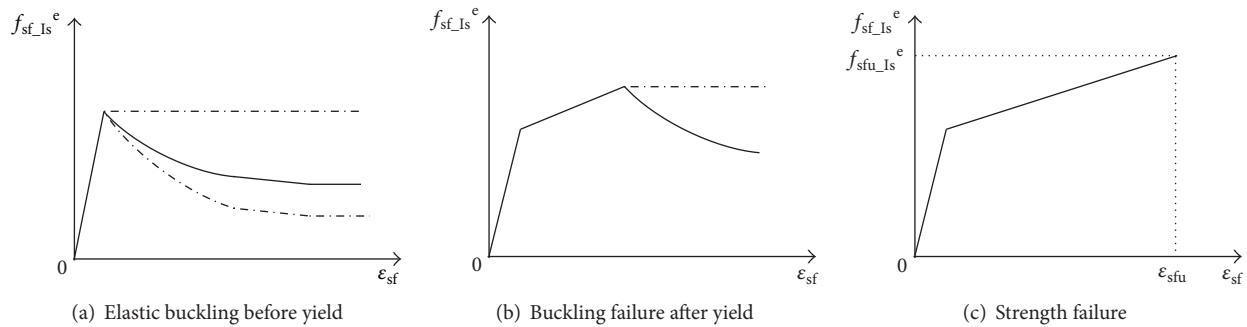


FIGURE 13: Schematic compression failure modes of SFCB.

increases with the increase in the postyield stiffness, and the contribution of the FRP bar to the buckling load should be considered. An empirical equation for the postbuckling stress considering the effect of r_{sf}^- was proposed.

Competing Interests

The authors declare that there is no conflict of interests regarding the publication of this paper.

Acknowledgments

The authors acknowledge the financial support from the National Key Technology Support Program of China (2014BAK11B04), the National Natural Science Foundation of China (nos. 51408126, 51528802), the Natural Science Foundation of Jiangsu Province, China (no. BK20140631), and the project funding from the Priority Academic Program Development of Jiangsu Higher Education Institutions (CE01-2-3).

References

- [1] L. Lam and J. G. Teng, "Strength models for fiber-reinforced plastic-confined concrete," *Journal of Structural Engineering*, vol. 128, no. 5, pp. 612–623, 2002.
- [2] J. Deng, T. Liu, W. Xie, and W. Lu, "Study on repaired earthquake-damaged bridge piers under seismic load," *Advances in Materials Science and Engineering*, vol. 2015, Article ID 295392, 10 pages, 2015.
- [3] "Prestressing concrete structures with FRP tendons," ACI 440.4R-04, 2004.
- [4] D. Lau and H. J. Pam, "Experimental study of hybrid FRP reinforced concrete beams," *Engineering Structures*, vol. 32, no. 12, pp. 3857–3865, 2010.
- [5] A. Nanni, M. J. Henneke, and T. Okamoto, "Tensile properties of hybrid rods for concrete reinforcement," *Construction and Building Materials*, vol. 8, no. 1, pp. 27–34, 1994.
- [6] B. Saikia, J. Thomas, A. Ramaswamy, and K. S. N. Rao, "Performance of hybrid rebars as longitudinal reinforcement in normal strength concrete," *Materials and Structures*, vol. 38, no. 10, pp. 857–864, 2005.
- [7] G. Wu, Z. S. Wu, Y. B. Luo, and H. C. Wei, "A new reinforcement material of steel fiber composite bar (SFCB) and its mechanics properties," in *Proceedings of the 9th International Symposium on "Fiber Reinforced Polymer (FRP) Reinforcement for Concrete Structures" (FRPRCS-9)*, University of Adelaide, Adelaide, Australia, July 2009.
- [8] J. Sim, C. Park, and D. Y. Moon, "Characteristics of basalt fiber as a strengthening material for concrete structures," *Composites Part B: Engineering*, vol. 36, no. 6-7, pp. 504–512, 2005.
- [9] X. Wang, Z. Wu, G. Wu, H. Zhu, and F. Zen, "Enhancement of basalt FRP by hybridization for long-span cable-stayed bridge," *Composites Part B: Engineering*, vol. 44, no. 1, pp. 184–192, 2013.
- [10] X. Zhao, X. Wang, Z. Wu, and Z. Zhu, "Fatigue behavior and failure mechanism of basalt FRP composites under long-term cyclic loads," *International Journal of Fatigue*, vol. 88, pp. 58–67, 2016.
- [11] G. Wu, Z.-S. Wu, Y.-B. Luo, Z.-Y. Sun, and X.-Q. Hu, "Mechanical properties of steel-frp composite bar under uniaxial and cyclic tensile loads," *Journal of Materials in Civil Engineering*, vol. 22, no. 10, pp. 1056–1066, 2010.
- [12] Z. Y. Sun, Y. Yang, W. H. Qin, S. T. Ren, and G. Wu, "Experimental study on flexural behavior of concrete beams reinforced by steel-fiber reinforced polymer composite bars," *Journal of Reinforced Plastics and Composites*, vol. 31, no. 24, pp. 1737–1745, 2012.
- [13] Z. Y. Sun, G. Wu, Z. S. Wu, and Y. B. Luo, "Flexural strengthening of concrete beams with near-surface mounted steel-fiber-reinforced polymer composite bars," *Journal of Reinforced Plastics and Composites*, vol. 30, no. 18, pp. 1529–1537, 2011.
- [14] A. I. Ibrahim, G. Wu, and Z. Sun, "Experimental study of cyclic behavior of concrete bridge columns reinforced by steel basalt-fiber composite bars and hybrid stirrups," *Journal of Composites for Construction*, 2016.
- [15] Z.-Y. Sun, G. Wu, Z.-S. Wu, and M. Zhang, "Seismic behavior of concrete columns reinforced by steel-FRP composite bars," *Journal of Composites for Construction*, ASCE, vol. 15, no. 5, pp. 696–706, 2011.
- [16] G. R. Pandey, H. Mutsuyoshi, and T. Maki, "Seismic performance of bond controlled RC columns," *Engineering Structures*, vol. 30, no. 9, pp. 2538–2547, 2008.
- [17] S. Mazzoni, F. McKenne, M. H. Scott, and G. L. Fenves, *Open System for Earthquake Engineering Simulation User Manual Version 2.0*, Pacific Earthquake Engineering Center, University of California, Berkeley, Calif, USA, 2009, <http://opensees.berkeley.edu/OpenSees/manuals/usermanual/index.html>.
- [18] M. M. Kashani, A. J. Crewe, and N. A. Alexander, "Nonlinear stress-strain behaviour of corrosion-damaged reinforcing bars including inelastic buckling," *Engineering Structures*, vol. 48, pp. 417–429, 2013.

- [19] S. Bae, A. M. Miseses, and O. Bayrak, "Inelastic buckling of reinforcing bars," *Journal of Structural Engineering*, vol. 131, no. 2, pp. 314–321, 2005.
- [20] J. B. Mander, F. D. Panthaki, and A. Kasalanati, "Low-cycle fatigue behavior of reinforcing steel," *Journal of Materials in Civil Engineering*, vol. 6, no. 4, pp. 453–468, 1994.
- [21] R. Hawileh, A. Rahman, and H. Tabatabai, "Evaluation of the low-cycle fatigue life in ASTM A706 and A615 grade 60 steel reinforcing bars," *Journal of Materials in Civil Engineering*, vol. 22, no. 1, pp. 65–76, 2010.
- [22] J. Zheng, *Experimental studies on cyclic behavior of reinforcing bars including buckling [M.S. thesis]*, Chongqing University, 2012 (Chinese).
- [23] "Guide for the design and construction of concrete reinforced with FRP bars," ACI 440.1R-06, 2006.
- [24] W. P. Wu, *Thermomechanical properties of Fiber Reinforced Plastic (FRP) bars [Ph.D. dissertation]*, West Virginia University, Morgantown, WV, USA, 1992.
- [25] S. Zhou, *Study on the basic mechanical performance of concrete members with BFRP bars [M.S. thesis]*, Southeast University, 2012 (Chinese).

Research Article

Experimental Study on Bond Behavior of FRP-Concrete Interface in Hygrothermal Environment

X. H. Zheng,¹ P. Y. Huang,¹ X. Y. Guo,¹ and J. L. Huang²

¹School of Civil Engineering and Transportation, South China University of Technology, Guangzhou 510640, China

²College of Water Conservancy and Civil Engineering, South China Agriculture University, Guangzhou 510642, China

Correspondence should be addressed to P. Y. Huang; pyhuang@scut.edu.cn

Received 23 September 2016; Accepted 13 November 2016

Academic Editor: Baolin Wan

Copyright © 2016 X. H. Zheng et al. This is an open access article distributed under the Creative Commons Attribution License, which permits unrestricted use, distribution, and reproduction in any medium, provided the original work is properly cited.

As the technique of fiber-reinforced polymer (FRP) composite material strengthened reinforced concrete structures is widely used in the field of civil engineering, durability of the strengthened structures has attracted more attention in recent years. Hygrothermal environment has an adverse effect on the bond behavior of the interface between FRP and concrete. This paper focuses on the bond durability of carbon fiber laminate- (CFL-) concrete interface in hygrothermal condition which simulates the climate characteristic in South China. Twenty 100 mm × 100 mm × 720 mm specimens were divided into 6 groups based on different temperature and humidity. After pretreatment in hygrothermal environment, the specimens were tested using double shear method. Strain gauges bonded along the CFL surface and linear variation displacement transducers (LVDTs) were used to measure longitudinal strains and slip of the interface. Failure mode, ultimate capacity, load-deflection relationship, and relative slip were analyzed. The bond behavior of FRP-concrete interface under hygrothermal environment was studied. Results show that the ultimate bearing capacity of the interface reduced after exposure to hygrothermal environments. The decreasing ranges were up to 27.9% after exposure at high temperature and humidity (60°C, 95% RH). The maximum strains (ϵ_{\max}) of the specimens pretreated decreased obviously which indicated decay of the bond behavior after exposure to the hygrothermal environment.

1. Introduction

External bonding of fiber-reinforced polymer (EB-FRP) composite material is a popular technique for strengthening concrete structures [1–3]. In this method, the adhesively bonded joint plays a crucial role which provides effective stress transferring from concrete to FRP to secure the integrity and durability of the strengthened structures [4–6]. In recent years, the durability of FRP-concrete bond interface attracted more attention, and a number of experimental programs have been conducted to examine the behavior of FRP-concrete interface exposed to aggressive conditions [7–11]. Temperature and moisture, the two dominant conditions, have significant impacts on a variety of mechanical and durability issues. Exposure to high temperature and humidity can result in adhesive bond degradation [12–21] which causes a rapid decrease in efficiency of the entire strengthened system.

Wan et al. [12] studied the moisture effects on the durability of FRP/concrete bond. After 8 weeks of immersion in the water, the energy release rate of bonded interface was found soundly reduced by 85%. Benzarti et al. [13] designed 4 different composite systems to study the CFRP-to-concrete bond durability under constant hydrothermal ageing conditions (40°C and 95% relative humidity). The research included two parts of experiments by using pull-off tests and single shear test. The periods of exposure were 20 and 13 months, respectively. It was found that hydrothermal ageing caused a significant reduction in the capacity strength of the bonded interfaces for specimens strengthened with CFS and CFRP compared to the unstrengthened concrete slabs. Moreover, the failure mode changed from a substrate failure to a compound or interfacial failure. The chemical compositions reports explained that moisture diffusion from the superficial layer of concrete towards the adhesive joint is possibly the key reason causing the degradation process during hydrothermal

ageing. As for the two methods, the shear test was more sensitive than the pull-off test and should be used to evaluate the adhesive bond strength. Gamage et al. [14] studied the bond characteristics of CFRP plated concrete members under elevated temperatures through experimental and numerical analysis. Eleven single shear specimens made of noninsulated CFRP-strengthened concrete blocks were conducted to verify the temperature distributions. Two insulated single shear specimens were tested to determine the effects of insulation on the heat transfer behavior of the concrete bonded with CFRP. On the other hand, finite element analysis program was used to analyze heat transfer. Both experimental and finite element results show that epoxy adhesive being used in the construction industry is very sensitive to temperature variations. The epoxy working temperature should not exceed 70°C in order to maintain the integrity between the CFRP and concrete. Silva and Biscaia [15] investigated FRP-concrete bond degradation considering salt fog cycles, temperature, moisture, and immersion in salt water through bending tests. The concrete specimens were externally bonded with GFRP or CFRP. The results showed that failure surfaces differed under different ageing environmental conditions. Temperature cycles (−10°C; 10°C) and moisture cycles were found with failure in the concrete substrate, while salt fog cycles failure happened at the interface concrete-adhesive. The temperature cycles caused significant loss of capacity of beams. As for beams bonded with GFRP and CFRP, the corresponding maximum loss of load capacity is 31% and 20%. Immersion in salt water and salt fog caused considerable degradation of bond between the GFRP strips and concrete. In the literature of Lai et al. [16], a method combining the use of destructive (pull-out) and nondestructive (pulsed IRT) tests was introduced to study the full field debonding process of CFRP-strengthened concrete beam specimens exposed to 45°C with different humidity (RH 45%, 90%, and water bath) conditions. The exposure durations were 3, 5, 7, and 9 months. Four unexposed control specimens (room temperature at about 23°C and 65% RH) and 48 exposed specimens were tested using modified pull-out test. The bonding between the CFRP strips and concrete was found weakened significantly after the specimens were exposed to humid conditions (RH > 90%) for several months. Blackburn et al. [17] investigated the effects of hygrothermal environmental conditions on the curing kinetics of epoxy used in FRP composites. Results showed that all clear epoxies experienced a significant decrease in T_g , ranging from approximately 9 to 25°C, from their theoretical values due to the exposure to hygrothermal conditions which caused the degradation of the bond interface. Shrestha et al. [18] studied the durability of the FRP-concrete bond and its constituent properties under moisture conditions for duration up to 24 months. The results show that the bond strength decreased up to 32%, and the failure mode changed from concrete cohesion to primer-concrete mixed failure for normal-strength concrete and from mixed failure to complete adhesion failure in case of high-strength concrete. The author explained that shifts in failure patterns were mainly due to destruction of the adhesion bond caused by water molecules at the interface. Mikami et al. [19] examined the effects of

hot temperature (100 and 180°C) on the deterioration of bond strength and the changes in failure modes. The combination of high temperature and low humidity (at 180°C and 0% humidity) was the most detrimental to bond strength, and the adhesive strength was reduced to 0.5 MPa which was 6.0 MPa at the room environment. Kabir et al. [20] investigated the time dependent behavior of CFRP-concrete bond subjected to temperature cycles, wet-dry cycles, and outdoor environment separately by using single shear tests. The maximum reduction of pull-out strength of CFRP-concrete bond was 15.2% compared to that for the corresponding unexposed specimens due to degraded epoxy properties. Failure modes changed from thick concrete to very thin concrete layer attached to the FRP except the specimens subjected to temperature cycles. Effective bond length increased due to exposed condition.

In general, humidity and water exposure will cause significant reduction in bond stress of the FRP-concrete interface. However, the research above mostly focused on the bond strength and global durability of the FRP-strengthened concrete specimens. These tests serve to provide strength data in the final state, but limited data are available to explain the load history and the actual failure mechanism before failure. Also the hygrothermal environmental effects on the bond during loading progress were seldom reported. In addition, the studies focusing on the durability of the system in tropical climate are very limited. Information on the effect of aggressive environments on bond durability is still lacking which links to the service life of strengthened structures. Therefore, the long-term performance of FRP-concrete interface needs further research and more data.

This paper reports the study of FRP-strengthened concrete specimens subjected to accelerated hygrothermal (coupled temperature and moisture) attack. Double shear tests were used to test the bond degradation in the specimens. The objectives of this study are twofold: (i) experimentally studying the effects of high temperature and humidity on EB-FRP specimens, mainly on bond between the composite and concrete, and (ii) explaining the hygrothermal environmental effects on bond interface behavior during the loading progress.

2. Experimental Program

2.1. Specimens. Twenty specimens were tested by using double shear method in this research. Each specimen consisted of two concrete prisms, with dimensions 100 mm × 100 mm × 250 mm, as shown in Figure 1. A $\phi 20$ mm ribbed steel bar was inserted at the center location of every prism before cast, by which the tensile force was applied with an electronic machine. To avoid loading eccentricity, a set of steel mold was designed as shown in Figure 2(a). A pair of concrete blocks were casted together in the mold and marked. The three holes where the steel bar passed through were center aligned. The two steel bars were separate at the middle of the mold. All concrete blocks were cast in laboratory conditions and cured in a water bath for 28 days at standard conditions

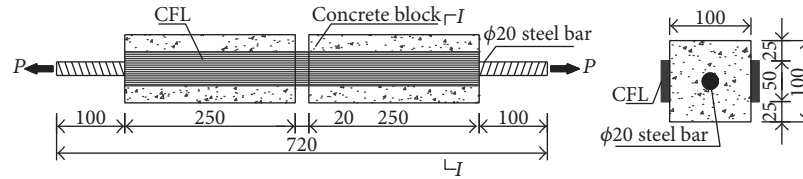
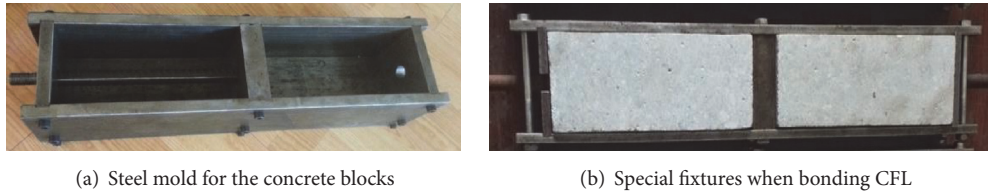


FIGURE 1: Schematic diagram of a double shear specimen (unit: mm).



(a) Steel mold for the concrete blocks

(b) Special fixtures when bonding CFL

FIGURE 2: Molds and fixtures used to make the specimens.

[21]. Then they were removed from the water bath and dried for a week in laboratory.

One pair of concrete blocks were bonded together by FRP to make a specimen. The two concrete prisms were connected only through two carbon fiber laminates (CFL [22]), externally bonded to two opposite sides of the concrete prisms by a wet layup process. Between the two concrete blocks there was a space of 20 mm (Figure 1). In order to ensure the alignment, special fixture as shown in Figure 2(b) was used when bonding FRP. The bonding process mainly included 3 steps. First, the concrete surface was ground with a stone wheel in order to remove the weak layer of mortar, just until the aggregate was visible. Then the dust on the surface was properly cleaned with air jet. Finally, carbon fiber laminates (CFL [22]) with a width of 50 mm and a thickness of 0.23 mm were bonded to the two opposite surfaces of the concrete blocks, respectively, using epoxy resin by wet layup method.

2.2. Material Properties. In this study, the mix proportions of the main ingredients in the concrete by weight were cement (1.0) : water (0.5) : sand (2.06) : gravel (3.66). Chinese standard Portland cement (P.O42.5R) was adopted; river sand with fineness modulus of 2.74 and granite aggregate with diameter of 5–20 mm were used in the experiment. The mean 28-day cubic (150 mm × 150 mm × 150 mm) compressive strength of the concrete was 35.4 MPa according to the standard for test method of mechanical properties on ordinary concrete (GB/T 50081-2002 [23]).

The carbon fiber laminates (CFL [22]) used in this test were one kind of FRP invented by our research group, and presaturated laminates were fabricated using T700-12k carbon fibers. The tensile strength, tensile modulus, and elongation of the carbon fibers reported by the manufacturer were 5040 MPa, 232 GPa, and 2.1%, respectively. The measured values of the tensile strength, tensile modulus,

and Poisson's ration for CFL were 4030 MPa, 220 GPa, and 0.25, respectively. The adhesive used for bonding CFL to concrete surface was a two-component epoxy adhesive. The manufacturer reported properties of the epoxy resin were the Young modulus of 2.5 GPa, the tensile strength of 40 MPa, the ultimate strain of 5.0%, and the vitreous transition temperature of 85°C. The material properties are summarized in Table 1.

2.3. Hygrothermal Environmental Conditions. In this test, the specimens were moved to pretreatment in an environmental chamber in which temperature and relative humidity (RH) conditions can be preset. The characteristic values of temperature and humidity were chosen according to the measured data of a number of bridges in service in the coastal provinces of South China combined with some relevant codes [24]. The curves of monthly temperature and humidity throughout one year are shown in Figure 3. It indicates that the temperature was from 5°C to 50°C in service and that for humidity is from 70% RH to 95% RH. According to the Chinese guidelines (GB/T1446-2005 [25] and GB/T2573-2008 [26]), the accelerated condition for hygrothermal environment is $60 \pm 2^\circ\text{C}$, $93 \pm 3\%$. The prescribed temperature and RH conditions in this test were chosen as 5°C, 25°C, and 60°C and 60% RH, 75% RH, and 95% RH, respectively.

The temperature and humidity conditions for different groups of specimens are listed in Table 2. The specimens were kept in the environmental chamber as shown in Figure 4 for 14 days in accordance with the Chinese guidelines (GB/T1446-2005 [25] and GB/T2573-2008 [26]). After exposure to the simulated environment, the specimens were taken out from the chamber and dried at air environment in laboratory at an average temperature of 25°C with 80% RH before testing.

2.4. Test Setup. Double shear tests were carried out to study the bond performance of the FRP-concrete bonded interface

TABLE 1: Summary of material properties.

| Materials | Index of material properties | Values |
|-----------------------|---|--------|
| Concrete | 28-day cubic compressive strength (MPa) | 35.4 |
| | Guaranteed tensile strength (MPa) | 4030 |
| Carbon fiber laminate | Nominal modulus of elasticity (GPa) | 220 |
| | Poisson's ration | 0.25 |
| | Shear strength (MPa) | 14.0 |
| Epoxy adhesive | Vitreous transition temperature (°C) | 85 |
| | Young modulus (GPa) | 2.5 |
| | Tensile strength (MPa) | 40 |
| | Poisson's ration | 0.33 |

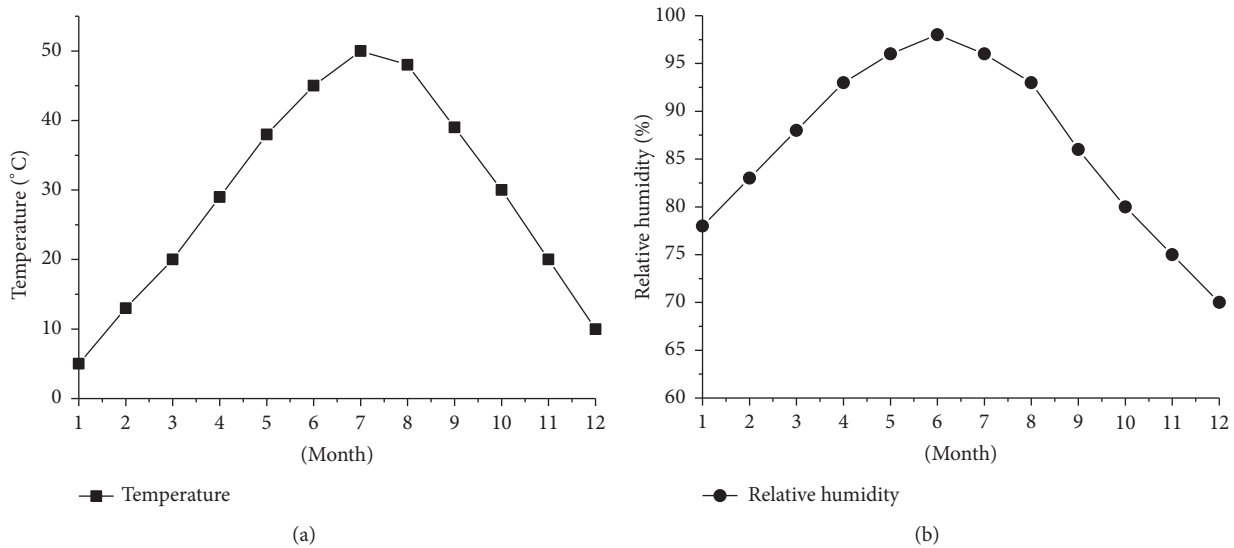


FIGURE 3: Monthly temperature and humidity curves over one year on the bridges in South China.

using a modified setup. A steel bar was embedded within each concrete block, centered, and aligned with the concrete faces. And the bars extended 100 mm from the outer ends of each block to be applied tension load (P , as shown in Figure 1). The two steel bars were unconnected, which means that the connection of the two concrete blocks was ensured only through the CFL sheet. Special care was taken during the installation of the formwork to position the internal steel reinforcement perfectly aligned. Additional strain gauges were bonded at the same location on opposite face of the specimen to check the coaxial condition before test.

All specimens were tested on an electronic universal testing machine (CMT5105) with 100 kN capacity as shown in Figure 5. Loading was controlled in displacement mode at a rate of 0.005 mm/s. Strain gauges were externally bonded on the CFL to measure the strains in CFL. A total of 13 strain gauges were distributed along the bonded length of CFL with a center-to-center spacing of 20 mm as shown in Figure 6(a). During the test, strains were automatically recorded by a data-acquisition system (TMR-211) at 10 Hz

as shown in Figure 6(b). The relative slip ($\Delta\omega$) between two concrete blocks was measured by a linear displacement sensor fixed on the surface of concrete block near the middle of the specimens as shown in Figure 7.

2.5. Test Program. In the experiment 20 specimens were divided into 6 groups, namely, A-1, B-1~3, and C-1~3, according to different temperature and humidity conditions. Group A-1 was used as reference specimens which were maintained at laboratory condition without pretreatment. Groups B and C were pretreated in the environmental chamber for 14 days with different temperature and humidity conditions. Group B tested the influence of temperature with the same humidity 95% RH. Three different test temperatures were used: 25°C, 50°C, and 60°C corresponding to B-1, B-2, and B-3, respectively. Group C tested the influence of humidity with the same temperature 60°C. Three different test humidity conditions were used: 60% RH, 75% RH, and 95% RH corresponding to C-1, C-2, and C-3, respectively. Conditions for B-3 were the same as C-3, so only one group of specimens

TABLE 2: Details of the double shear tests.

| Group number | Hygrothermal conditions | Specimens number | Ultimate load (P_u /kN) |
|--------------|---------------------------|------------------|----------------------------|
| A-1 | Air environment untreated | A-1-1 | 23.2 |
| | | A-1-2 | 20.0 |
| | | A-1-3 | 24.1 |
| B-1 | 5°C, 95% RH, 14 days | B-1-1 | 18.3 |
| | | B-1-2 | 20.5 |
| | | B-1-3 | 17.9 |
| B-2 | 25°C, 95% RH, 14 days | B-2-1 | 16.8 |
| | | B-2-2 | 17.3 |
| | | B-2-3 | 17.6 |
| | | B-2-4 | 16.8 |
| B-3 (C-3) | 60°C, 95% RH, 14 days | B-3-1 | 17.2 |
| | | B-3-2 | 16.0 |
| | | B-3-3 | 15.3 |
| | | B-3-4 | 16.4 |
| C-1 | 60°C, 60% RH, 14 days | C-1-1 | 17.9 |
| | | C-1-2 | 19.2 |
| | | C-1-3 | 20.0 |
| C-2 | 60°C, 75% RH, 14 days | C-2-1 | 20.4 |
| | | C-2-2 | 17.5 |
| | | C-2-3 | 17.1 |



FIGURE 4: Programmable environmental chamber (HP-800U) and specimens.

TABLE 3: Influence of hygrothermal environment on the ultimate load.

| Group | Conditions | Avg. P_u /kN | ΔP_u /(reference P_u) |
|-------|------------------|----------------|----------------------------------|
| A-1 | Lab. environment | 22.5 | Reference |
| B-1 | 5°C, 95% RH | 18.9 | -16.0 |
| B-2 | 25°C, 95% RH | 17.1 | -23.9 |
| B-3 | 60°C, 95% RH | 16.2 | -27.9 |
| C-1 | 60°C, 60% RH | 19.1 | -15.2 |
| C-2 | 60°C, 75% RH | 18.3 | -18.4 |



FIGURE 5: Electronic testing machine (type: CMT5105).

was tested for them. Details of the specimens are listed in Table 2.

3. Results and Discussion

3.1. Failure Mode. Only one typical debonding failure mode was observed in all specimens. As shown in Figure 8, a thin concrete layer attached to the surface of the debonded CFL shows that the debonding failure happened in the substrate concrete. Such failure mode is also widely reported in other resources [17, 18, 20].

3.2. Hygrothermal Environment Effect on the Ultimate Load (P_u). Table 3 summarizes the statistics of the ultimate loads for each group of specimens. Hygrothermal environment influence on the ultimate load was obtained by comparing the ultimate loads of the aged specimens with those of reference specimens as shown in Figure 9. In Figure 9(a), results for the reference specimens (A-1, without ageing) and those of group B subjected to different temperature with the same humidity are compared to analyze the temperature effect on

the ultimate load. In Figure 9(b), results for the specimens under different humidity are compared.

A clear decrease of the ultimate load for the specimens exposed in hygrothermal environment can be observed except C-2-1. In general, higher temperature and humidity cause higher reduction in ultimate load.

The degree of influence of hygrothermal environment on the ultimate load is also presented in Table 3.

Comparing to the reference specimen group A-1, decreases of 16.0%, 23.9%, and 27.9% are found for group B corresponding to 5°C, 25°C, and 60°C, respectively, with the same high humidity (95%). For group C, the decreases are 15.2%, 18.4%, and 27.9% corresponding to 60% RH, 75%, and 90% relative humidity, respectively, with the same high temperature (60°C). In particular, P_u has a maximum decrease of 27.9% at 60°C and 95% RH.

3.3. Load-Deflection Curves. Figure 10 shows the total load versus deflection graphs for all the specimens tested. The curves of all the specimens in each group are similar to each other. Load-deflection data for C-1-2 were lost in the test.

The slope of the load-deflection curves reflects the total stiffness of the bond interface. It is steeper at the initial loading stage indicating good bond stiffness and then decreases with the increase of loading. The fluctuations in the curves indicate that local debonding happened on the bond face before the sudden failure.

The load-deflection curves of the reference specimens (without ageing) and group B specimens subjected to different temperatures (5°C, 25°C, and 60°C) with the same humidity (95%) are compared in Figure 11(a) to analyze the temperature effect. The comparison between the reference specimens (without ageing) and group C specimens subject to different humidity (60%, 75%, and 95%) with the same temperature (60°C) is shown in Figure 11(b).

The results presented in Figure 11 clearly reveal that noticeable deterioration was caused by exposure in hygrothermal environment. Compared to the reference specimens, the smaller slopes of the curves for the aged specimens mean bond degradation and this becomes more obvious with increasing temperature and humidity.

4. Influence of the Hygrothermal Environment on the Bond Behavior

The results reported in this section indicate that the bond performance is significantly influenced by service temperature

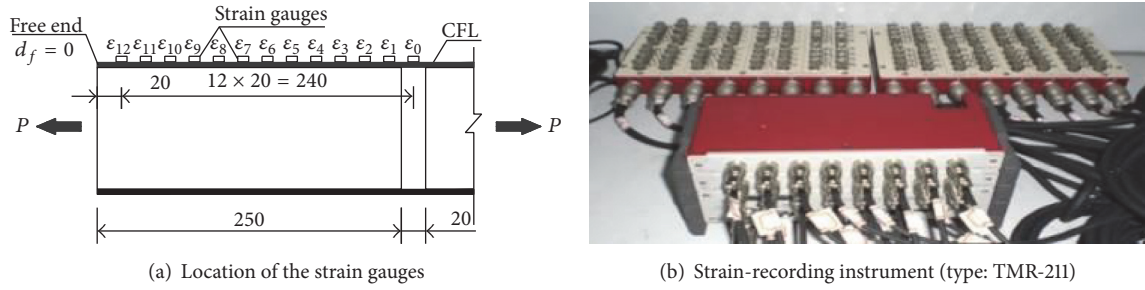


FIGURE 6: Measurement of strain.

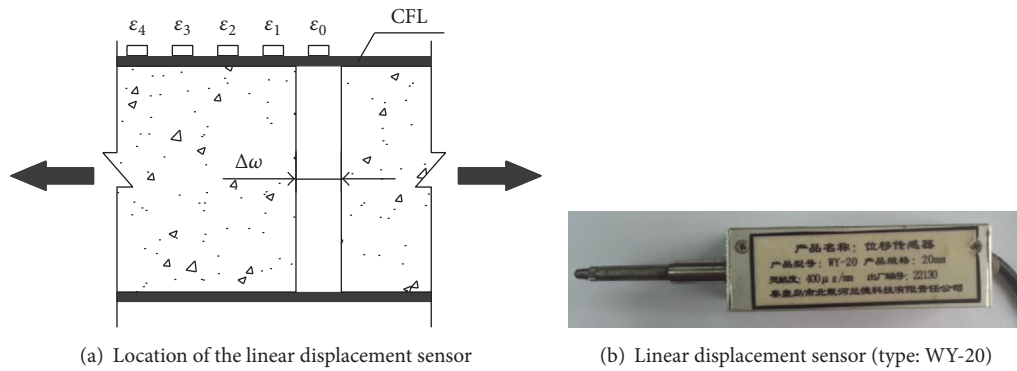


FIGURE 7: Measurement of relative slip between the concrete blocks.



FIGURE 8: Typical bond failure mode.

and humidity. As a result, hygrothermal environment effects must be properly taken into account from the design point of view.

4.1. Relative Slips between the Two Concrete Blocks. The relative slips ($\Delta\omega$) at different load levels between the two concrete blocks were obtained by the linear displacement sensor fixed on the concrete blocks which reflected the total bond stiffness indirectly. In this test, the slip measurements for some specimens such as A-1-1 and A-1-3 and C-1 and C-2 failed because of the difficulty of fixing the displacement sensor

effectively. Figure 12 shows some relative displacement-load curves for specimens with different temperatures. The typical experimental relative slip-load response has a 3-stage characteristic containing an initial linear growth stage, a rapid growth stage, and an instable growth stage. Compared to the reference specimens in group A, the slopes of the relative slip-load curves of group B specimens were higher which indicated faster degradation of the bond behavior. As for group B aged with different temperatures under the same high humidity (95% RH), the higher the ageing temperature was, the faster the speed rate grew. However, the ultimate relative slips of all specimens were not sensitive to temperature and humidity and all were in the range of 0.7 mm and 0.8 mm.

4.2. Strain Distribution in the CFL. These strains were read from the strain gauges mounted on the upper surface of the CFL as shown in Figure 6. Longitudinal strains in the CFL at various load levels for each specimen are shown in Figure 13, where the horizontal axis d_f is the distance from the free end of the CFL shown in Figure 6, and the vertical axis is the measured strains of the CFL.

In general, the external loads were transferred through the concrete blocks into the CFL over a range of 100 mm to

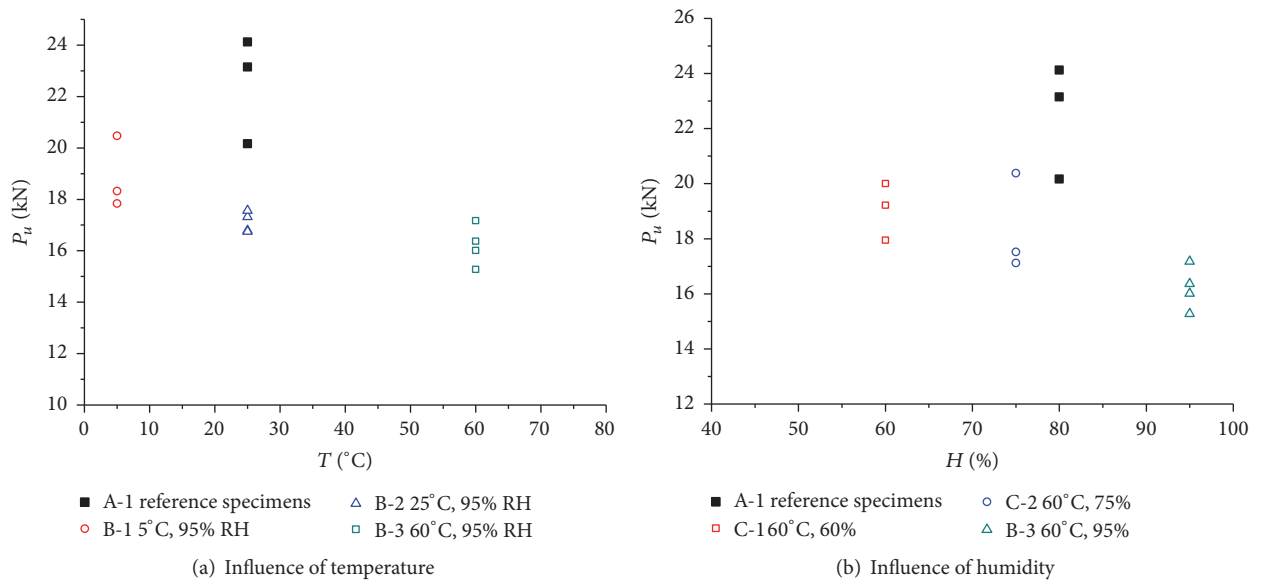


FIGURE 9: Influence of the hygrothermal environment on the ultimate load.

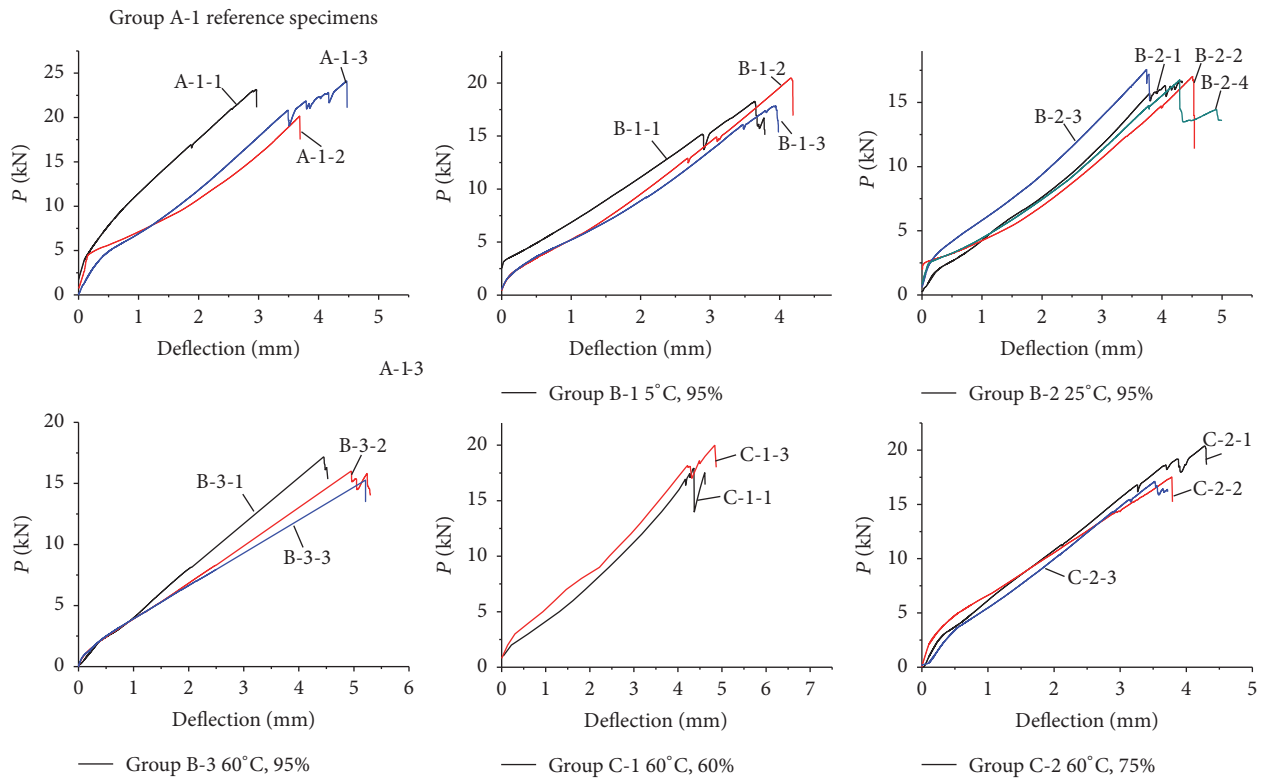


FIGURE 10: Load-deflection curves of all the specimens.

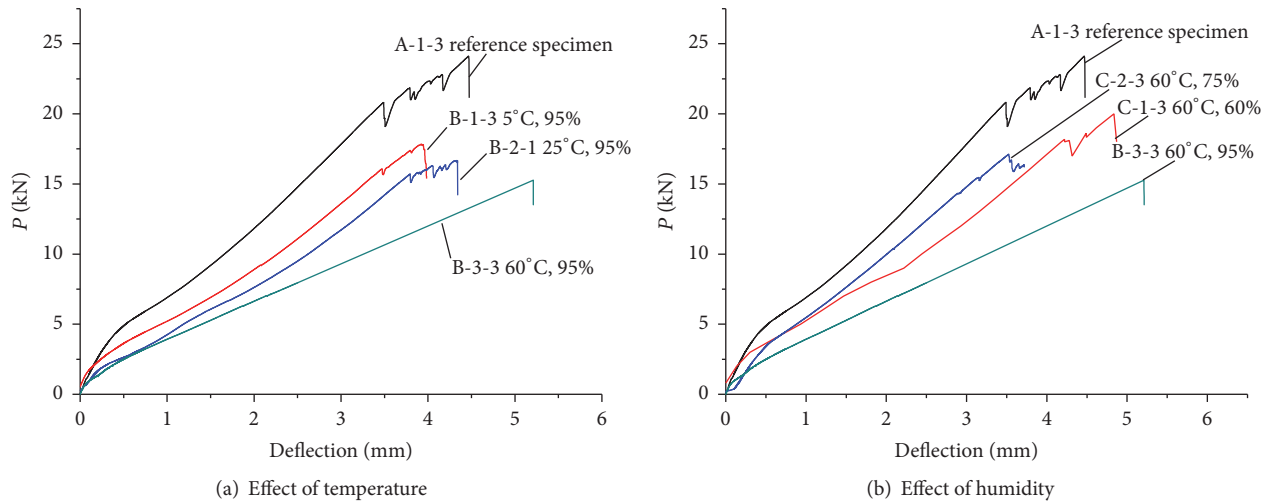


FIGURE 11: Effect of hot-wet environment on the load-deflection curves.

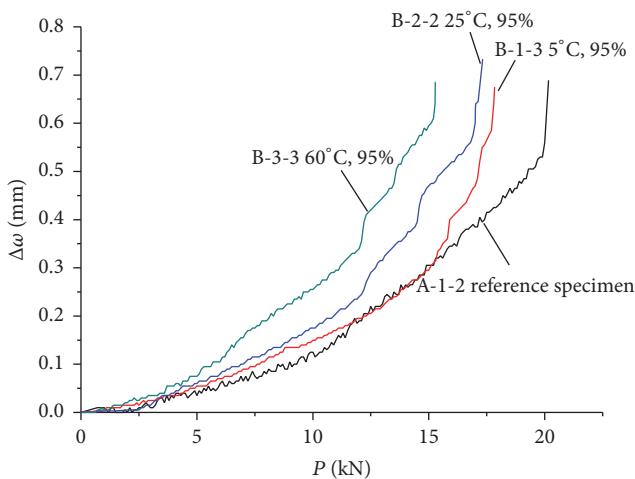


FIGURE 12: Hot-wet pretreatments effect on the relative slips ($\Delta\omega$).

150 mm at each side of the gap. The strain of the CFL was at maximum at the gap location and reduced at the locations away from the gap. The strains also increased with external loading. It needs to be noted that the strain distribution across the width of the CFL was not uniform due to the imperfection in loading and/or geometry.

Compared with the reference specimens (group A-1), the maximum strains (ϵ_{\max}) of the specimens in groups B and C decreased obviously which indicated decay of the bond behavior after exposure to the hygrothermal environment. The maximum strains were 5500~6000 $\mu\epsilon$, 3500~4500 $\mu\epsilon$, and 3500~5000 $\mu\epsilon$ for groups A-1, B-2~3, and C-2, respectively. This means that the aggressive environment caused premature debonding failure along the interface.

5. Conclusions

This study experimentally investigated the bond-slip behavior of the CFL-concrete bond subjected to static load after hygrothermal environment exposure. The failure modes, load-deflection, relative slip, and strain distributions in CFL were measured and analyzed in detail.

The following conclusions can be drawn based on the experimental data:

- (1) Hygrothermal environment adversely affected the bond behavior of the CFL-concrete interface. Compared to the reference specimen, the ultimate load decreased as much as 27.9% when the specimens exposed to the hygrothermal environment of 60°C and 95% RH.
- (2) Hygrothermal environment exposure caused noticeable deterioration of the bond stiffness shown in the load-deflection curves and relative slips curves. As temperature and humidity increased, the slopes of the curves for the aged specimens decreased.
- (3) Compared with the reference specimens, the maximum strains (ϵ_{\max}) of the specimens subjected to hygrothermal environment pretreatment decreased from 5500~6000 $\mu\epsilon$ to 3500~5000 $\mu\epsilon$. Furthermore, the effective bond length increased from about 100 mm to near 150 mm, which indicated bond behavior degradation.

Competing Interests

The authors declare that there is no conflict of interests regarding the publication of this paper.

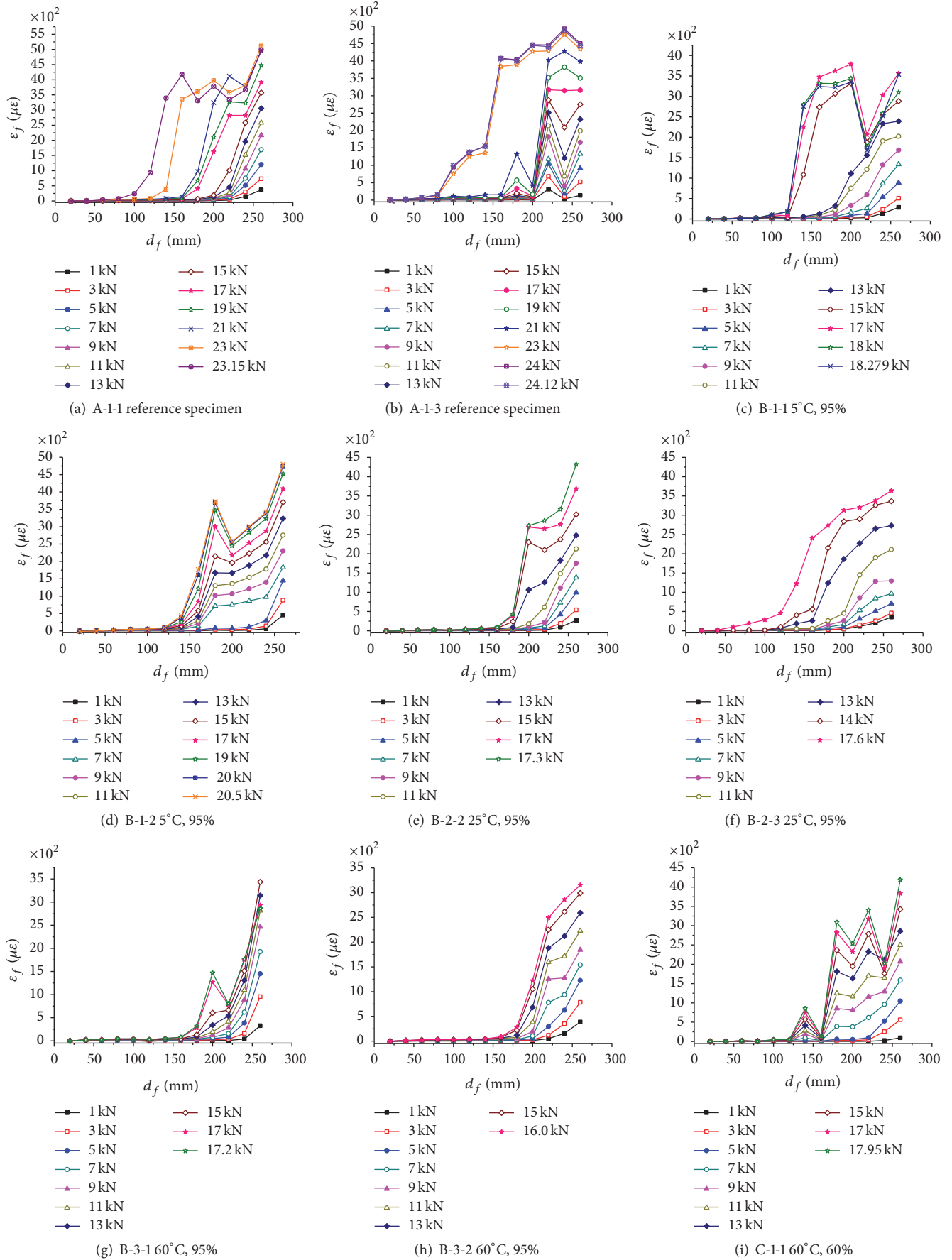


FIGURE 13: Continued.

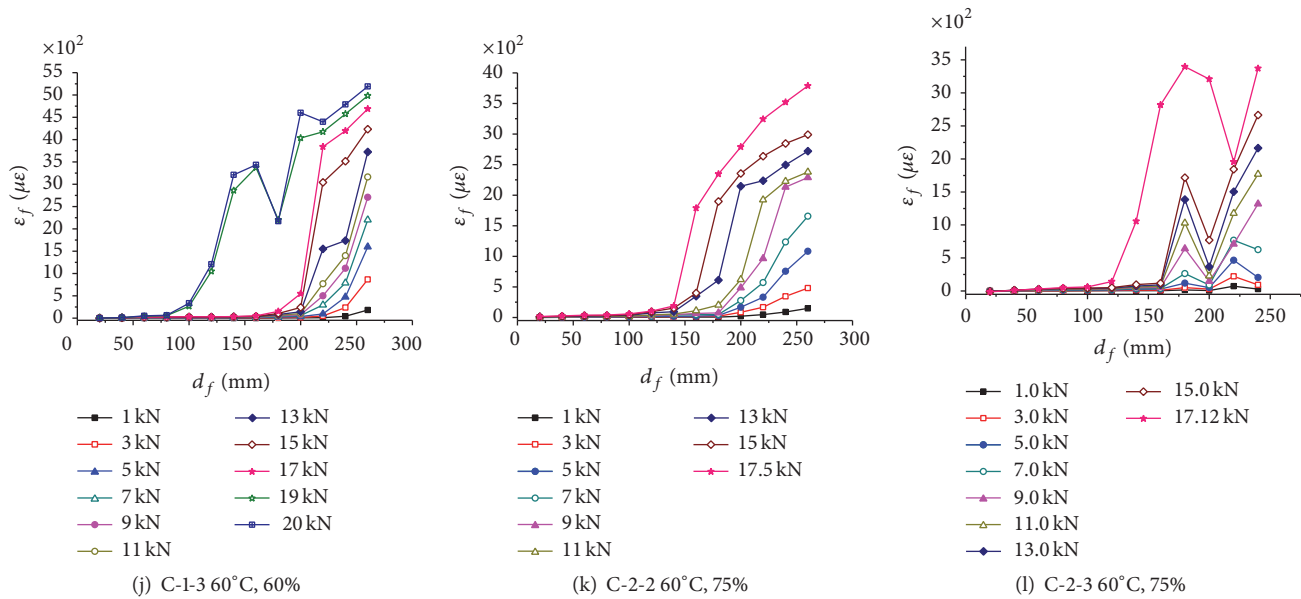


FIGURE 13: Strain distributions for groups A to C specimens.

Acknowledgments

The project was supported by the National Natural Science Foundation of China (nos. 11132004, 11627802, 51678249, and 51508202), China Scholarship Council (no. 201606155018), Guangdong Province Natural Science Foundation of China (no. 2016A030310414), and Open Project for Key Laboratory Construction of Mountainous Bridges and Tunnels in Chongqing Jiaotong University (no. CQSLBF-Y16-9).

References

- [1] V. M. Karbhari, F. Seible, R. Burgueño, A. Davol, M. Wernli, and L. Zhao, "Structural characterization of fiber-reinforced composite short- and medium-span bridge systems," *Applied Composite Materials*, vol. 7, no. 2, pp. 151–182, 2000.
- [2] J. G. Teng, J. F. Chen, S. T. Smith, and L. Lam, *FRP-Strengthened RC Structures*, John Wiley and Sons, Chichester, UK, 2002.
- [3] D. J. Oehlers and R. Seracino, *Design of FRP and Steel Plated RC Structures: Retrofitting Beams and Slabs for Strength, Stiffness and Ductility*, Elsevier, London, UK, 2004.
- [4] J. G. Teng and J. F. Chen, "Mechanics of debonding in FRP-plated RC beams," *Proceedings of the Institution of Civil Engineers: Structures and Buildings*, vol. 162, no. 5, pp. 335–345, 2009.
- [5] Y.-F. Wu and C. Jiang, "Quantification of bond-slip relationship for externally bonded FRP-to-concrete joints," *Journal of Composites for Construction*, vol. 17, no. 5, pp. 673–686, 2013.
- [6] Y.-F. Wu, X.-S. Xu, J.-B. Sun, and C. Jiang, "Analytical solution for the bond strength of externally bonded reinforcement," *Composite Structures*, vol. 94, no. 11, pp. 3232–3239, 2012.
- [7] P. Mukhopadhyaya, R. N. Swamy, and C. J. Lynsdale, "Influence of aggressive exposure conditions on the behaviour of adhesive bonded concrete-GFRP joints," *Construction and Building Materials*, vol. 12, no. 8, pp. 427–446, 1998.
- [8] R. Sen, "Developments in the durability of FRP-concrete bond," *Construction and Building Materials*, vol. 78, pp. 112–125, 2015.
- [9] H. C. Biscaia, M. A. G. Silva, and C. Chastre, "An experimental study of GFRP-to-concrete interfaces submitted to humidity cycles," *Composite Structures*, vol. 110, pp. 354–368, 2014.
- [10] J. F. Davalos, S. S. Kodkani, I. Ray, and Chunfu Lin, "Fracture evaluation of GFRP-concrete interfaces for freeze-thaw and wet-dry cycling," *Journal of Composite Materials*, vol. 42, no. 14, pp. 1439–1466, 2008.
- [11] J. Lyons, D. Laub, V. Giurgiutiu, M. Petrou, and H. Salem, "Effect of hygrothermal aging on the fracture of composite overlays on concrete," *Journal of Reinforced Plastics and Composites*, vol. 21, no. 4, 2002.
- [12] B. L. Wan, M. F. Petrou, and K. A. Harries, "The effect of the presence of water on the durability of bond between CFRP and concrete," *Journal of Reinforced Plastics and Composites*, vol. 25, no. 8, pp. 875–890, 2006.
- [13] K. Benzarti, S. Chataigner, M. Quiertant, C. Marty, and C. Aubagnac, "Accelerated ageing behaviour of the adhesive bond between concrete specimens and CFRP overlays," *Construction and Building Materials*, vol. 25, no. 2, pp. 523–538, 2011.
- [14] J. C. P. H. Gamage, R. Al-Mahaidi, and M. B. Wong, "Bond characteristics of CFRP plated concrete members under elevated temperatures," *Composite Structures*, vol. 75, no. 1-4, pp. 199–205, 2006.
- [15] M. A. G. Silva and H. Biscaia, "Degradation of bond between FRP and RC beams," *Composite Structures*, vol. 85, no. 2, pp. 164–174, 2008.
- [16] W. L. Lai, S. C. Kou, C. S. Poon, W. F. Tsang, and K. K. Lee, "A durability study of externally bonded FRP-concrete beams via full-field infrared thermography (IRT) and quasi-static shear test," *Construction and Building Materials*, vol. 40, pp. 481–491, 2013.
- [17] B. P. Blackburn, J. Tatar, E. P. Douglas, and H. R. Hamilton, "Effects of hygrothermal conditioning on epoxy adhesives used in FRP composites," *Construction and Building Materials*, vol. 96, pp. 679–689, 2015.
- [18] J. Shrestha, T. Ueda, and D. Zhang, "Durability of FRP concrete bonds and its constituent properties under the influence of

- moisture conditions,” *Journal of Materials in Civil Engineering*, vol. 27, no. 2, Article ID A4014009, 2015.
- [19] C. Mikami, H.-C. Wu, and A. Elarbi, “Effect of hot temperature on pull-off strength of FRP bonded concrete,” *Construction and Building Materials*, vol. 91, pp. 180–186, 2015.
- [20] M. I. Kabir, R. Shrestha, and B. Samali, “Effects of applied environmental conditions on the pull-out strengths of CFRP-concrete bond,” *Construction and Building Materials*, vol. 114, pp. 817–830, 2016.
- [21] “Standard for test method of mechanical properties on ordinary concrete,” GB/T 50081-2002, Ministry of Construction P. R. China, 2002.
- [22] P. Y. Huang and J. C. Zeng, “Carbon fiber laminate and application,” ZL200410026742.8, 2006.
- [23] “Standard for test method of mechanical properties on ordinary concrete,” Tech. Rep. GB/T 50081-2002, Ministry of Construction P. R. China, 2002.
- [24] P. Y. Huang, H. Zhou, X. H. Zheng, and X. Y. Guo, “On the experimental method for durability measurement of RC members strengthened with FRP served in hot and humid environments,” *Journal of Experimental Mechanics*, vol. 26, no. 5, pp. 603–610, 2011.
- [25] GB/T1446-2005, “Fiber-reinforced plastics composites-the generals for determination of properties,” Ministry of Communications of the People’s Republic of China, 2005.
- [26] GB/T2573-2008, *Test Method for Aging Properties of Glass Fiber Reinforced Plastics*, Ministry of Communications of the People’s Republic of China, 2008.

Research Article

Effect of Chloride on Tensile and Bending Capacities of Basalt FRP Mesh Reinforced Cementitious Thin Plates under Indoor and Marine Environments

Yan Xie, Kunhua Guan, and Lin Lai

School of Civil and Transportation Engineering, Guangdong University of Technology, Guangzhou 510006, China

Correspondence should be addressed to Yan Xie; xieyan@gdut.edu.cn

Received 23 September 2016; Accepted 9 November 2016

Academic Editor: Baolin Wan

Copyright © 2016 Yan Xie et al. This is an open access article distributed under the Creative Commons Attribution License, which permits unrestricted use, distribution, and reproduction in any medium, provided the original work is properly cited.

This paper presented a durability experimental study for thin basalt fiber reinforced polymer (BFRP) mesh reinforced cementitious plates under indoor and marine environment. The marine environment was simulated by wetting/drying cycles (wetting in salt water and drying in hot air). After 12 months of exposure, the effects of the chloride on the tensile and bending behaviors of the thin plate were investigated. In addition to the penetration of salt water, the chloride in the thin plate could be also from the sea sand since it is a component of the plate. Experimental results showed that the effect of the indoor exposure on the tensile capacity of the plate is not pronounced, while the marine exposure reduced the tensile capacity significantly. The bending capacity of the thin plates was remarkably reduced by both indoor and marine environmental exposure, in which the effect of the marine environment is more severe. The tensile capacity of the meshes extracted from the thin plates was tested, as well as the meshes immersed in salt solution for 30, 60, and 90 days. The test results confirmed that the chloride is the reason of the BFRP mesh deterioration. Moreover, as a comparison, the steel mesh reinforced thin plate was also tested and it has a similar durability performance.

1. Introduction

Basalt fiber reinforced polymer (BFRP) is a new type of composite material with high performance and relatively low cost. It has good durability and chemical stability as well as excellent electrical insulation, fire resistance, and thermal resistance [1–3]. Recently, BFRP has been developed for some applications in civil engineering [4, 5]. As a nonmetallic material, furthermore, BFRP has become an attractive alternative to steel in the structures subjected to marine environment [6–8]. The BFRP tendons showed superior resistance to salt corrosion [9], while the bond strength of the BFRP bars embedded in concrete exposed to a long-term chloride environment decreased remarkably. In addition, some studies had shown that the concrete pore alkaline solution can affect the durability of BFRP, which can reduce the bonding strength between the BFRP bar and concrete [10, 11].

Because of the reduction in available river sand and development of ocean engineering, the exploration and utilization of sea sand resources have been gaining increased attention.

The chloride present in sea sand threatens the durability of concrete structures containing it, thereby limiting its application [12]. Currently, there are two main approaches to maximize the utilization of sea sand: after washing and direct usage. Because of the high cost and low efficiency of the former approach, direct usage will be the predominant approach in the future. Yin et al. [13] indicated that longer curing times, less water consumption per cubic meter, and a smaller water/cement ratio can effectively reduce the chloride ion penetration and improve the durability of the concrete. To avoid steel corrosion by the chloride, nevertheless, many studies had considered using FRP materials to replace steel [14–16]. Dong et al. [17] investigated the durability performance of steel-BFRP composite bars in sea sand concrete.

Deng and Lee [18] reported a steel mesh reinforced cementitious thin plate. Based on the study, the authors [19] further presented an innovative thin plate with BFRP mesh and sea sand instead of steel mesh and river sand, respectively. The initial flexural toughness and flexural bearing capacity were better than those of the steel mesh thin plate. Although

the BFRP sheet and bar exhibited high resistance to chloride corrosion, the degradation of BFRP mesh needs to be investigated. Because of the differences among the mesh, sheet, and bar in production technology, the matrix types and fiber volume fraction can affect the durability performance of BFRP [9].

To date, no particular study on the effect of the chloride on the mechanical properties of the BFRP mesh as well as its reinforced thin plate can be found. This paper conducted an experimental study on the durability of the BFRP mesh reinforced sea sand cementitious thin plates under indoor and marine environments. Mechanical behaviors of the thin plates as well as the BFRP mesh were tested after environmental exposure. In addition, for comparison, the specimens of steel mesh reinforced thin plate were tested in the same procedures.

2. Experimental Study

2.1. Materials. The mix proportions of sea sand mortar were 1 : 2.23 : 0.012 : 0.45 (cement : sea sand : superplasticizer : water). The particles of the sea sand were filtered in the range of 0.063–0.355 mm. Portland cement used was P-O 42.5. The superplasticizer had a water reduction rate of $\geq 38\%$. The sea sand mortar has the advantages of high density, low water absorption, and high compressive and flexural strengths.

For comparison, two types of mesh, BFRP mesh and steel mesh with a grid size of 10 mm \times 10 mm, were used. The test procedures of the fiber and steel were carried out according to Chinese standard (GB/T3362-2005) [20]. The linear density and the density of fiber bundle of BFRP mesh were 800 g/km and 2.65 g/cm³, respectively. Therefore, the section area of the fiber bundle was 0.3 mm². The ultimate tensile capacity and ultimate elongation of fiber were 291.5 N and 1.8%, respectively. The ultimate strength and elastic modulus of BFRP bundle were 970 MPa and 100 GPa, respectively. The diameter and section area of the steel wire were 0.7 mm and 0.38 mm², respectively. The yield strength and elastic modulus of wire were 300 MPa and 200 GPa, respectively.

2.2. Environmental Conditions. Three environmental conditions were considered. Condition (I) represents no environmental exposure, under which the control specimens were tested just after 28-day curing. Condition (II) represents exposure to natural indoor environment for 12 months. Condition (III) represents exposure to the marine environment for 12 months. The marine environment was produced by placing specimens in a salt solution under wetting/drying cycles. Each wetting/drying cycle was 24 h. The specimens were immersed in a 3.5% NaCl solution for 10 h, following by drying at 40°C for 14 h. The temperature control accuracy is $\pm 1^\circ\text{C}$.

2.3. Specimens of Thin Plate. The thin plates were fabricated in the wooden molds with the dimensions of 800 mm \times 150 mm \times 8 mm, as shown in Figure 1. Two layers of BFRP or steel meshes were placed in the mold and fixed. After

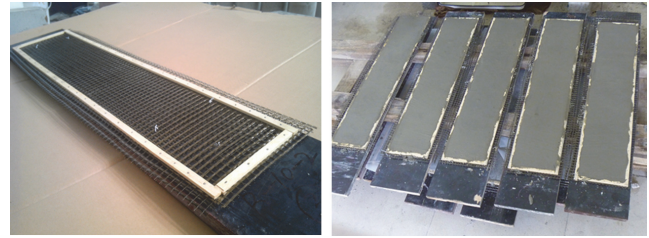


FIGURE 1: Molds of thin plates.

TABLE 1: Details of specimens.

| Specimens of tensile test | Specimens of bending test | Reinforced mesh | Environmental condition |
|---------------------------|---------------------------|-----------------|-------------------------|
| T-B(I) | M-B(I) | BFRP mesh | Without exposure |
| T-B(II) | M-B(II) | BFRP mesh | Indoor for 12 months |
| T-B(III) | M-B(III) | BFRP mesh | Marine for 12 months |
| T-S(I) | M-S(I) | Steel mesh | Without exposure |
| T-S(II) | M-S(II) | Steel mesh | Indoor for 12 months |
| T-S(III) | M-S(III) | Steel mesh | Marine for 12 months |

being cast with mixed mortar, the specimens were vibrated and then the surfaces were smoothed. The specimens were cured at 20°C and RH > 95% for 28 days. Specimens for tensile test were cut into the dimensions of 150 mm \times 50 mm [18], containing ten bundles or wires in longitudinal direction. Specimens for bending test were cut into the dimensions of 700 mm \times 150 mm according to Chinese standard (GB/T19631-2005) [21].

Table 1 summarizes all the thin plate specimens. The references “T” and “M” indicate tensile test and bending test, respectively. “B” and “S” mean BFRP mesh and steel mesh, respectively. The Roman numerals (I), (II), and (III) represent the environmental conditions.

2.4. Tensile and Bending Tests. The tensile and bending tests were carried out in a DDL100 electronic universal testing machine. The two ends of the tensile specimens treated with epoxy resin were fixed in two clamps at 60 mm spacing, respectively, as shown in Figure 2. The load was applied at a constant rate of 0.2 mm/min during the tensile tests. As shown in Figure 3, the ends of bending specimens were fixed in a G-type clamping device to simulate the fixed ends in the bending test. Three-point bending with a clear span of 500 mm was carried out at a constant rate of 2 mm/min. The data of the load and displacement was automatically recorded by the testing machine.

2.5. Tensile Test of Mesh. Two series of meshes were tested. (1) BFRP bundles or steel wires were obtained from the meshes in the thin plates exposed to the indoor and marine

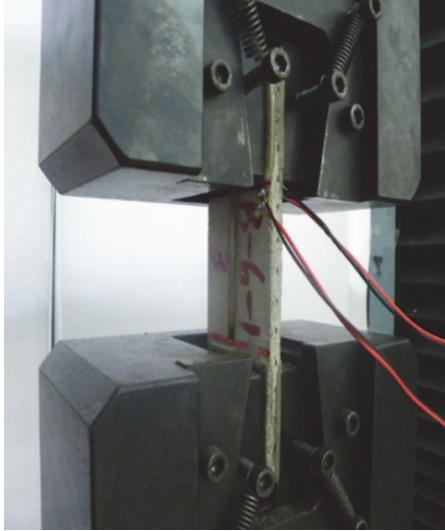


FIGURE 2: Tensile test of thin plate.



FIGURE 3: Bending test of thin plate.

environments; (2) BFRP bundles or steel wires obtained from the sound meshes were immersed in saturated NaCl solution for 30 d, 60 d, and 90 d and thereafter were vacuum-dried after washing by distilled water. After measuring the mass loss, the BFRP bundles and steel wires were tensile-tested according to Chinese standard (GB/T 3362-2005) [20]. The clear length of the specimens is 150 mm, as shown in Figure 4.

3. Results

3.1. Tensile Capacity of Thin Plates. The load-displacement curves obtained from the tensile tests of the thin plates were shown in Figures 5 and 6. The curves can be divided into three stages. The first stage is the linear ascent segment, during which the tensile force was mainly carried by the mortar and no crack was observed on the thin plates. During the second stage, the cracks continually developed and the tensile force carried by the bundles or wires increased gradually. During the third stage, the bundles or wires carried the tensile force individually until the specimens failed.

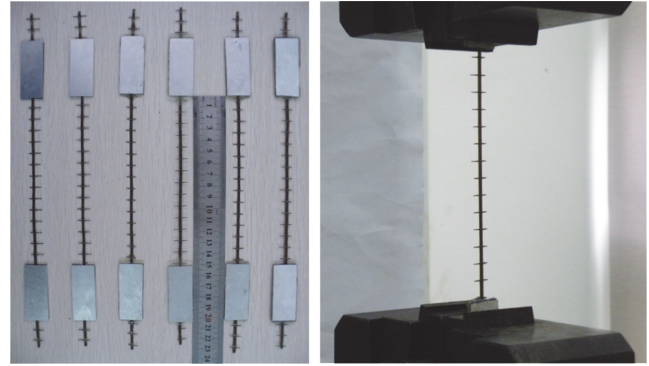


FIGURE 4: Specimens and tensile test of BFRP bundle.

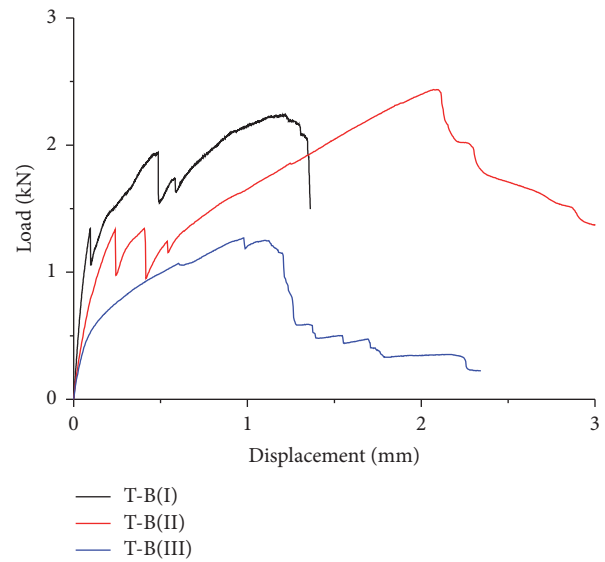


FIGURE 5: Load-displacement curves of specimens T-B.

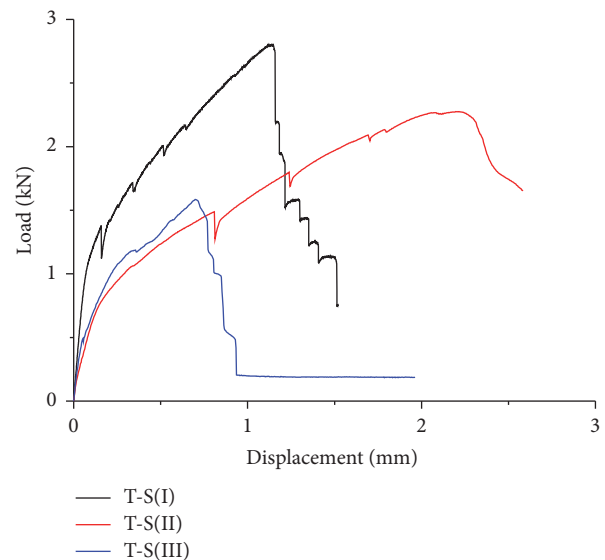


FIGURE 6: Load-displacement curves of specimens T-S.

TABLE 2: The results of tensile tests.

| Specimen | Cracking load F_r (kN) | Failure load F_u (kN) |
|----------|--------------------------|-------------------------|
| T-B(I) | 1.34 | 2.24 |
| T-B(II) | 1.34 | 2.43 |
| T-B(III) | 0.47 | 1.26 |
| T-S(I) | 1.38 | 2.80 |
| T-S(II) | 1.47 | 2.27 |
| T-S(III) | 0.50 | 1.58 |

Because the load was mainly borne by the mortar in the first stage of the tensile test, the first cracking loads of B(II) and B(I) were almost the same. However, the BFRP was corroded by the high alkalinity of cement, which deteriorated the interface and affected the integrity of the fiber bundles. Because of this, relative slip occurred between the fibers during the tensile and bending tests, which led to larger ultimate displacement of B(II) and B(I) as shown in Figure 5.

As shown in Figures 5 and 6, the ultimate displacement of specimens T-B(II) and T-S(II) under indoor condition was larger than of the specimens under two other environmental conditions. Meanwhile, the ultimate displacement of specimens T-B(III) and T-S(III) was the minimum, which showed that the marine environment has an extensive effect on the ductility of the thin plate. In addition, BFRP thin plates showed better ductility than steel thin plates under the same conditions.

The cracking loads and failure loads of the tensile tests were recorded in Table 2. As shown in the table, the cracking loads between specimens T-B(I) and T-B(II) as well as T-S(I) and T-S(II) were close. Meanwhile, the differences of the failure loads obtained from the specimens under conditions (I) and (II) were not pronounced. However, the cracking load and failure load of specimen T-B(III) showed significant decline of 53% and 43.8%, respectively. The cracking load and failure load of specimen T-s(III) showed significant decline of 63.8% and 58%, respectively.

3.2. Bending Capacity of Thin Plate. The bending load-deflection curves were shown in Figures 7 and 8. In terms of the testing process, the curves can be divided into three stages. The first one was the elastic stage until crack initiated. During the second stage, the microcracks developed in the thin plate until a macrocrack appeared. During the third stage, the bending loading was gradually carried by the meshes until the plate failed.

The cracking loads, failure loads, and ultimate deflections of the bending tests were recorded in Table 3. Compared with B(I), the cracking and failure loads of B(II) declined by 33.8% and 44%, whereas those of B(III) decreased by 49.6% and 79%, respectively. Compared with S(I), the cracking and failure loads of S(II) decreased by 42% and 21.5%, whereas those of S(III) decreased by 56.1% and 44.2%, respectively. The environmental exposure clearly had a more significant effect on the failure load of the BFRP thin plates than the steel mesh thin plates. The ultimate deflections were affected by the conditions as well. The ultimate deflections of both

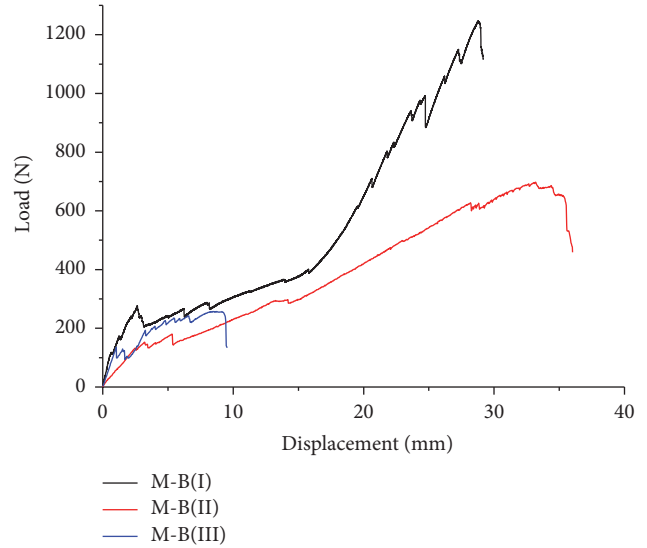


FIGURE 7: Load-displacement curves of specimens M-B.

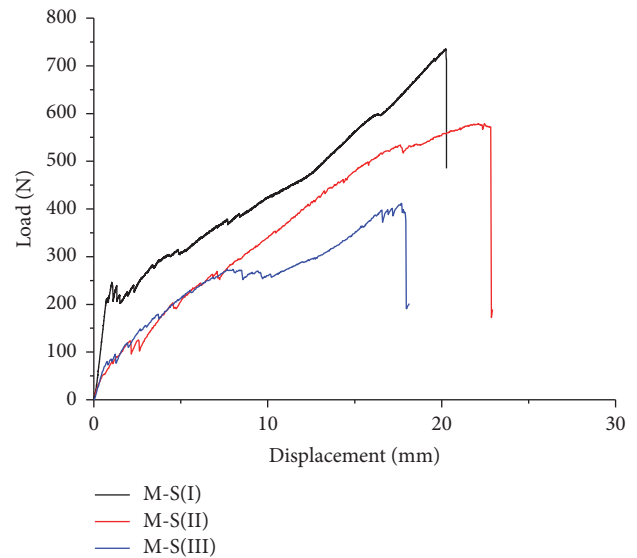


FIGURE 8: Load-displacement curves of specimens M-S.

the BFRP and the steel mesh thin plates increased slightly under condition (II), while they decreased remarkably under condition (III). In particular, the ultimate deflection of B(III) was only 9 mm.

The fracture surfaces of the thin plates failed by bending tests were shown in Figure 9. Small pores were observed on the interfaces between the mortar and BFRP bundles in Figures 9(a) and 9(b), where the small pores were more significant under marine environment (Figure 9(b)) than under indoor environment (Figure 9(a)). In Figure 9(d), corrosion of the steel meshes was obvious, while the pores were not pronounced. This demonstrated that the reduction of the failure load of M-S(III) was lower than that of M-B(III).

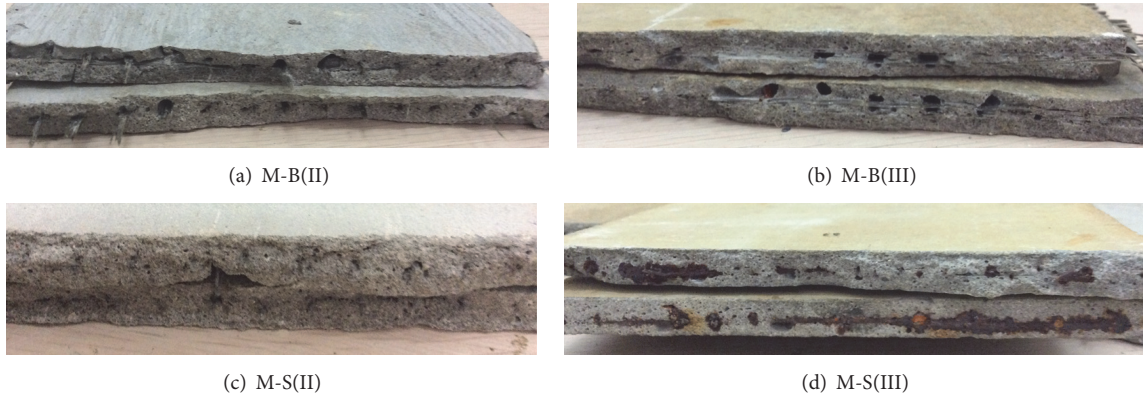


FIGURE 9: Fracture surfaces of the thin plates failed by bending tests.

TABLE 3: The results of bending test.

| Specimen | Cracking load P_r (N) | Failure load P_u (N) | Ultimate deflection D (mm) |
|----------|-------------------------|------------------------|------------------------------|
| M-B(I) | 272 | 1249 | 28.7 |
| M-B(II) | 180 | 697 | 33.1 |
| M-B(III) | 137 | 257 | 9.0 |
| M-S(I) | 212 | 734 | 20.3 |
| M-S(II) | 123 | 576 | 22.8 |
| M-S(III) | 93 | 409 | 17.7 |

TABLE 4: Tensile capacity of the bundles and wires.

| Specimens | Failure load P (kN) | Ultimate elongation (%) |
|--------------|-----------------------|-------------------------|
| BFRP-C | 0.34 | 7.3 |
| BFRP-B(II) | 0.26 | 4.2 |
| BFRP-B(III) | 0.14 | 1.9 |
| Steel-C | 0.35 | 5.1 |
| Steel-S(II) | 0.22 | 2.4 |
| Steel-S(III) | 0.15 | 1.6 |

Note. References “BFRP-C” and “Steel-C” indicate the BFRP bundle and steel wires directly obtained from sound meshes, respectively, while the others indicate the BFRP bundle or steel wires extracted from thin plates after environmental exposure.

3.3. Tensile Test Results of the Mesh from Thin Plates. The tensile capacities of the mesh extracted from the thin plates were recorded in Table 4. Compared with the control specimen “BFRP-C,” the failure load and ultimate elongation of BFRP-B(II) decreased by 25% and 42.5%, whereas those of BFRP-B(III) declined by 58.3% and 73.9%. This indicated that BFRP meshes were seriously corroded after the environmental exposure, especially the marine environmental exposure. Besides, the steel wires had similar durability performance. These results demonstrated that the chloride from the sea sand in the plates as well as that penetrated from the outside salt water has a significant effect on BFRP bundles and steel wires.

Since only meshes carried the tensile load when the thin plate failed, the theoretical tensile failure load of the plates

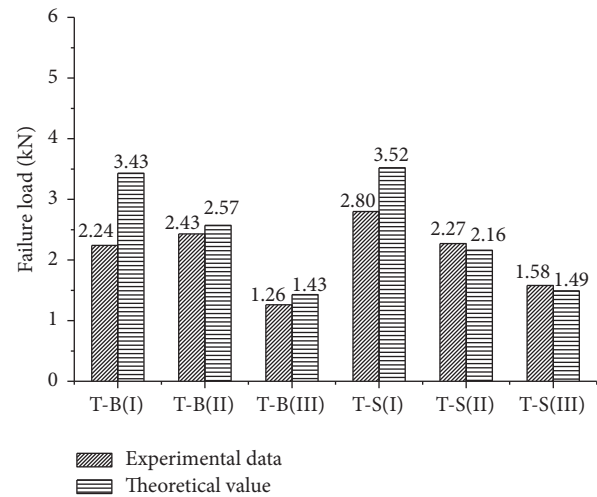


FIGURE 10: Comparisons of the tensile failure loads of the thin plates.

can be evaluated by the tensile capacity of the bundles or wires. The thin plate specimens had 10 bundles or wires in the longitudinal direction; therefore, the theoretical tensile failure loads of the plates were equal to 10 times the tensile capacity of the bundles or wires, which were compared with experimental results in Figure 10. The experimental and theoretical results of the thin plates exposed to environmental conditions, T-B(II), T-B(III), T-S(II), and T-S(III), were very close, which confirmed that the meshes carried most of the failure loads. The experimental results of T-B(I) and T-S(I) were obviously lower than those of theoretical results. This is because the specimens BFRP-C and Steel-C were obtained from the sound meshes and not from the meshes extracted from the plates. This indicated that the chloride contained in sea sand can corrode both BFRP and steel even just after 28 days of curing [22].

3.4. Influence of Chloride on BFRP and Steel Wire. The mass loss rates and failure loads of the bundles and wires were recorded in Table 5. As shown in the table, the mass loss rate of both BFRP and steel increased with the days of immersing

TABLE 5: Mass loss rate and failure load of bundles after being placed in NaCl solution.

| Time (day) | Mass loss rate (%) | | Failure load (kN) | |
|------------|--------------------|------------|-------------------|------------|
| | BFRP bundle | Steel wire | BFRP bundle | Steel wire |
| 0 | 0 | 0 | 0.29 | 0.52 |
| 30 | 2 | 0.08 | 0.29 | 0.26 |
| 60 | 3 | 9 | 0.24 | 0.15 |
| 90 | 11 | 40 | 0.1 | 0.07 |

in the NaCl solution, while the tensile capacity decreased. Particularly, the tensile capacity of the BFRP bundles reduced by 65.5% after being immersed in NaCl solution for 90 days; this indicated that chloride causes BFRP deterioration significantly. In addition, both the mass loss rates and the failure loads of the BFRP bundles varied slightly during a period of 0–60 days, while they decreased significantly during a period of 60–90 days. This indicated that the degradation of mechanical property is consistent with the mass loss. Fe element existing in the former with mainly Fe^{2+} in BFRP [23] can react with Cl^- . The final product of this chemical reaction was $\text{Fe}_2\text{O}_3 \cdot n\text{H}_2\text{O}$ which can absorb H_2O and expand the matrix of BFRP. As a result, microcracks initiated in BFRP fibers and weakened their mechanical performance. Meanwhile, some components in BFRP, such as Ca, Mg, Al, and K, dissolved in the solution, resulting in mass loss.

4. Conclusions

This paper studied the durability of the BFRP mesh reinforced sea sand cementitious thin plates under indoor and marine environments for 12 months. Mechanical behaviors of the thin plates and the BFRP mesh were tested. As a comparison, steel mesh reinforced thin plate was investigated as well. The following conclusions can be drawn from the experimental results:

- (1) The indoor exposure on the tensile capacity of the BFRP mesh reinforced cementitious thin plate is not pronounced, while the marine exposure reduced the tensile capacity by 43.8%.
- (2) After exposure to the indoor and marine environments, the bending capacity of the BFRP thin plates was reduced by 49.6% and 79.0%, respectively.
- (3) The tensile capacity of the BFRP bundle extracted from thin plate under indoor and marine environments for 12 months decreased by 25.0% and 58.3%.
- (4) The tensile strength of the BFRP bundles reduced by 65.5% after being immersed in NaCl solution for 90 days, which confirmed that the chloride is the main cause of the BFRP mesh deterioration.
- (5) The steel mesh reinforced cementitious thin plates have similar durability performance to the BFRP thin plates.

Competing Interests

The authors declare that there are no competing interests regarding the publication of this paper.

Acknowledgments

The authors thank the following groups for their financial support: the National Natural Science Foundation of China (nos. 51278131 and 51202036), New Century Outstanding Talent Support Program Project of China (NCET-13-0739), and Guangdong Provincial Education Department Project of China (2012LYM_0056).

References

- [1] T. Zych and K. Wojciech, "Study on the properties of cement mortars with basalt fibres," *Brittle Matrix Composites*, vol. 10, pp. 155–166, 2012.
- [2] V. A. Rybin, A. V. Utkin, and N. I. Baklanova, "Alkali resistance, microstructural and mechanical performance of zirconia-coated basalt fibers," *Cement and Concrete Research*, vol. 53, pp. 1–8, 2013.
- [3] C. Jiang, K. Fan, F. Wu, and D. Chen, "Experimental study on the mechanical properties and microstructure of chopped basalt fibre reinforced concrete," *Materials & Design*, vol. 58, no. 6, pp. 187–193, 2014.
- [4] J. Sim, C. Park, and D. Y. Moon, "Characteristics of basalt fiber as a strengthening material for concrete structures," *Composites Part B: Engineering*, vol. 36, no. 6–7, pp. 504–512, 2005.
- [5] J. Deng, T. Liu, W. Xie, and W. Lu, "Study on repaired earthquake-damaged bridge piers under seismic load," *Advances in Materials Science and Engineering*, vol. 2015, Article ID 295392, 10 pages, 2015.
- [6] Z. Dong, G. Wu, B. Xu, X. Wang, and L. Taerwe, "Bond durability of BFRP bars embedded in concrete under seawater conditions and the long-term bond strength prediction," *Materials & Design*, vol. 92, pp. 552–562, 2016.
- [7] X. Wang, G. Wu, Z. Wu, Z. Dong, and Q. Xie, "Evaluation of prestressed basalt fiber and hybrid fiber reinforced polymer tendons under marine environment," *Materials & Design*, vol. 64, pp. 721–728, 2014.
- [8] G. Wu, Z.-Q. Dong, X. Wang, Y. Zhu, and Z.-S. Wu, "Prediction of long-term performance and durability of BFRP bars under the combined effect of sustained load and corrosive solutions," *Journal of Composites for Construction*, vol. 19, no. 3, Article ID 4014058, 2015.
- [9] X. Wang, G. Wu, Z. Wu, Z. Dong, and Q. Xie, "Evaluation of prestressed basalt fiber and hybrid fiber reinforced polymer tendons under marine environment," *Materials and Design*, vol. 64, pp. 721–728, 2014.
- [10] Y. Chen, J. F. Davalos, I. Ray, and H.-Y. Kim, "Accelerated aging tests for evaluations of durability performance of FRP reinforcing bars for concrete structures," *Composite Structures*, vol. 78, no. 1, pp. 101–111, 2007.
- [11] A. Altalmas, A. E. Refai, and F. Abed, "Bond degradation of basalt fiber-reinforced polymer (BFRP) bars exposed to accelerated aging conditions," *Construction and Building Materials*, vol. 81, pp. 162–171, 2015.
- [12] S. L. Amey, D. A. Johnson, M. A. Miltenberger, and H. Farzam, "Predicting the service life of concrete marine structures: an

- environmental methodology," *ACI Structural Journal*, vol. 95, no. 2, pp. 205–214, 1998.
- [13] H. Yin, Y. Li, H. Lv, and Q. Gao, "Durability of sea-sand containing concrete: effects of chloride ion penetration," *Mining Science and Technology*, vol. 21, no. 1, pp. 123–127, 2011.
- [14] R. Hempel, "Thin textile-reinforced concrete thin-walled panel material," *Betonwerk and Fertigteil-Technik/Concrete Precasting Plant and Technology*, vol. 63, no. 3, pp. 144–146, 1998.
- [15] H. W. Reinhardt, M. Krüger, and C. U. Große, "Concrete prestressed with textile fabric," *Journal of Advanced Concrete Technology*, vol. 1, no. 3, pp. 231–239, 2003.
- [16] M. Butler, V. Mechtcherine, and S. Hempel, "Durability of textile reinforced concrete made with AR glass fibre: effect of the matrix composition," *Materials and Structures*, vol. 43, no. 10, pp. 1351–1368, 2010.
- [17] Z. Dong, G. Wu, and Y. Xu, "Experimental study on the bond durability between steel-FRP composite bars (SFCBs) and sea sand concrete in ocean environment," *Construction and Building Materials*, vol. 115, pp. 277–284, 2016.
- [18] J. Deng and M. M. K. Lee, "A study on an innovative composite panellised wall with steel wire mesh," *New Building Materials*, vol. 34, no. 1, pp. 26–28, 2007 (Chinese).
- [19] Y. Xie, J. Deng, and L. G. Huang, "Research on mechanical properties of basalt fiber net reinforced sea sand cementitious thin plate," in *Fiber Reinforced Plastics/Composites*, pp. 19–22, 2014 (Chinese).
- [20] Chinese Standard, "Test methods for tensile properties of carbon fiber multifilament," GB/T3362-2005.
- [21] Chinese Standard, "Glassfiber reinforced cement lightweight hollow panel for partition," Tech. Rep. GB/T19631-2005, 2005.
- [22] B. Wei, H. Cao, and S. Song, "Degradation of basalt fibre and glass fibre/epoxy resin composites in seawater," *Corrosion Science*, vol. 53, no. 1, pp. 426–431, 2011.
- [23] B. Wei, H. Cao, and S. Song, "Environmental resistance and mechanical performance of basalt and glass fibers," *Materials Science and Engineering A*, vol. 527, no. 18-19, pp. 4708–4715, 2010.

Research Article

Mechanical Behavior and Chloride Penetration of Precracked Reinforced Concrete Beams with Externally Bonded CFRP Exposed to Marine Environment

Yan Xie, Kunhua Guan, Lei Zhan, and Qichen Wang

School of Civil and Transportation Engineering, Guangdong University of Technology, Guangzhou 510006, China

Correspondence should be addressed to Yan Xie; xieyan@gdut.edu.cn

Received 23 September 2016; Accepted 8 November 2016

Academic Editor: Baolin Wan

Copyright © 2016 Yan Xie et al. This is an open access article distributed under the Creative Commons Attribution License, which permits unrestricted use, distribution, and reproduction in any medium, provided the original work is properly cited.

Cracked reinforced concrete (RC) beams can be repaired effectively by using externally bonded CFRP sheets. However, when the strengthened beams are subjected to marine environment, long-term performance will be affected by the material and the interface deterioration of concrete and CFRP. Therefore, to evaluate the service life of the strengthened beams, this study investigates the behavior of precracked RC beams strengthened with CFRP sheets exposed to marine environment. Accelerated ageing experiments were carried out by exposing specimens to cyclic wetting in sea water and drying in 40°C air for 3 months and 6 months, respectively. After the environment exposure, four-point bending test was conducted and then the diffusion of chlorides in the strengthened beams was analysed. The results show that the bonding behavior of the adhesive was weakened and the ductility of the strengthened beams was slightly reduced due to the marine environment. But there is no obvious strength difference between the strengthened beams suffered from marine environment for 3 months and 6 months. Besides, the precracks in the RC beams accelerated the chloride diffusion, while CFRP bonding reduced the chloride penetration. In addition, NEL method was employed to validate the effect of the cracks on chloride permeability. The results showed that the chloride diffusion coefficients increased with the depth of the cracks.

1. Introduction

Fatigue damage is one of the main problems that occur in highway bridges [1]. Concrete cracks induced by fatigue loadings may decrease the strength and stiffness of the reinforced concrete (RC) beams and accelerate chloride migration in concrete. To repair the cracked RC beams in the damaged bridges, external bonding of carbon fiber reinforced polymer (CFRP) sheets to the tension face was applied [2]. However, because of the adhesive bonding deterioration, the composite structures may have mechanical degradation and durability problem when they are subjected to marine environment. Thus, there is a great need to understand the durability and corrosion mechanism of the repaired RC beams under the environmental conditions.

Choo et al. [3] present a study on a RC bridge subjected to extreme vehicular loads and retrofitted with CFRP laminates. The increase in flexural capacity provides an adequate margin

of safety against further overloading. The RC beams damaged by static loading repaired with externally bonded CFRP laminates were demonstrated to be effective for increasing the capacity and rigidity [4]. On the other hand, the durability of RC beams reinforced with GFRP laminates were investigated by Almusallam [5]. The test results show that none of the environmental conditions have a noticeable influence on the flexural strength of the retrofitted beams. Nevertheless, the experimental tests on the durability of the concrete strengthened with near-surface mounted CFRP laminates showed a decrease of around 12% in the maximum pull-out force due to the wetting-drying cycles [6]. Benzarti et al. [7] conducted an accelerated ageing experiment to investigate the durability of the adhesive bond between concrete and CFRP strengthening systems under 40°C and 95% relative humidity. The results showed that moisture diffusion from the superficial layer of concrete towards the adhesive joint is a key factor to reduce the adhesive bonding strength and degrade the behavior of

adhesive itself. The deterioration in the adhesive bonding under temperature and water-immersion ageing conditions were detected by a nondestructive ultrasonic evaluation technique as well [8].

Besides, the effect of moisture diffusion on the adhesive bonding and chloride induced corrosion of the steel bar are also major causes of the deterioration of CFRP flexurally strengthened RC beams under marine environment [9–11]. The chloride diffusion in concrete was accelerated due to the defects of the RC beams caused by the actions of loads, environments, and climate conditions [12]. For all actions, flexural cracks in RC beams are an unavoidable phenomenon and have a significant effect on chloride diffusion [13]. Some studies [14–16] reported that crack width and depth significantly influence the chloride permeability in concrete. In addition, the cracks caused by tensile fatigue loading can accelerate the chloride penetration in concrete by 1.5–3.0 times [17]. When the cracks were notched artificially, however, the influence of crack width on chloride penetration is less pronounced and crack depth is the key factor of the chloride penetration [18].

From the above, the previous research has shown the influence of the marine environmental exposure on the RC beams with externally bonded CFRP. However, the effects of precracks and CFRP bonding on the chloride penetration to the concrete, as well as the durability performance of the retrofitted precracked beams, still remains unclear. In this paper, experimental study on precracked RC beams strengthened with CFRP subjected to marine environmental exposure was conducted. The deterioration of the specimens was produced by placing the beams into salt water under wetting/drying cycles. The flexural capacity and chloride penetration were investigated after 3 and 6 months under environmental exposure. In addition, NEL method [19–21] was employed to measure the chloride permeability with the depth of the cracks in concrete.

2. Experimental Study

In total, 19 specimens distributed in eight series were tested, as summarized in Table 1. For each series, the specimens have equal characteristics. The series “C” represents control specimens. The references “D”; “F”; and “H” mean cracked status, strengthened status, and environmental exposure status, respectively. The suffixed digitals 3 and 6 indicate months of environmental exposure.

2.1. Specimens. All specimens were T cross section beams as shown in Figure 1, reinforced with 2 Φ 14 mm steel bars in tension side and 4 Φ 8 mm steel bars in compression side. They were provided with Φ 6 mm diameter steel stirrups at 100 mm center to center spacing and distributed over the span. The mix proportions used to cast all beams were 1 : 1.81 : 2.77 : 4.51 (water : cement : sand : aggregate). The average 28-day compressive strength of the concrete was 36.62 MPa. The yield and ultimate strengths of steel bars were 397 MPa and 535 MPa, respectively. The elastic modulus is 202 GPa. The CFRP sheet (UT70-30) used was a unidirectional CFRP supplied by Toray Industries, whose nominal thickness is 0.167 mm. The

ultimate strength and the elastic modulus of the CFRP were 3878 MPa and 244 GPa, respectively. The adhesive used was Lica-100 A/B, a two-part thixotropic epoxy resin. It had a modulus of elasticity of 3.2 GPa and a tensile strength of 55.5 MPa.

2.2. Preparation of Strengthened Specimens. All beams were cast from the same batch in the laboratory and thereafter cured for 28 days. The RC beams in the specimen series DF, DFH-3, and DFH-6 were precracked by fatigue overloading before CFRP strengthening. The tensile concrete surface of the strengthened RC beams was ground by a concrete scabblor until exposure of aggregate was achieved, then blown with clean air to remove dust, and cleaned by acetone to ensure a good bond between the concrete surface and adhesive. After mixing, the adhesive was applied to the beam and CFRP sheet. The excess adhesive was squeezed out along the edges of the sheet, assuming complete adhesive coverage. Two layers of CFRP sheet was bonded to the tension face of the strengthened specimens. In order to avoid CFRP sheet debonding at the ends during the testing, they were attached in three U-shapes with 50 mm extension on each side of the beams, as shown in Figure 1.

2.3. Marine Environmental Exposure. The marine environment was produced by placing specimens into salt water under wetting/drying cycles. The wetting/drying environmental chamber with a length of 3 m, a width of 2 m, and a depth of 1.5 m can automatically adjust the water content. The temperature control accuracy is $\pm 1^\circ\text{C}$. Each wetting/drying cycle was 24 h. The specimens were immersed in a 3.5% NaCl solution for 10 h, followed by drying at 40°C for 14 h. The specimen series FH-3 and DFH-3 and FH-6 and DFH-6 were exposed for 3 months and 6 months, respectively.

2.4. Bending Test Set-Up and Procedures. The tests were carried out in a servohydraulic SDS500 test machine with a maximum capacity of 500 kN, subjected to a four-point bending set-up as shown in Figure 2. Deflections were measured at middle of the specimens using a potentiometer. All data were automatically recorded by a data logging system (TDS-530). The crack width was observed by a microscope. During loading, the displacements and load were recorded every 1 second.

The RC beams were precracked under fatigue loading which is corresponding to vehicle overloading on a highway bridge during one year [22]. The fatigue loading parameters, including loading patterns and number of loading cycles and loading amplitude, were calculated according to the vehicle overloading spectra [22]. Loading was applied sinusoidally, with a frequency of 0.2 Hz. The minimum and maximum cycle loads are 16.8 kN and 73 kN, which convert into longitudinal stresses in steel bars of 60.3 MPa to 358.0 MPa. The number of cycles is 380.

All specimens were finally tested under static load, by displacement control at a rate of 0.05 mm/sec. Loading was stopped when compressive concrete was crushed in the unretrofitted specimens or when the CFRP sheet was tensile ruptured in retrofitted specimens.

TABLE I: Specimen details.

| Series | Damaged status | Strengthening status | Environmental status and age | Number of specimens |
|--------|----------------|----------------------|------------------------------|---------------------|
| C | / | / | / | 3 |
| D | Damaged | / | / | 2 |
| F | / | Strengthened | / | 3 |
| DF | Damaged | Strengthened | / | 4 |
| FH-3 | / | Strengthened | Exposed for 3 months | 1 |
| FH-6 | / | Strengthened | Exposed for 6 months | 1 |
| DFH-3 | Damaged | Strengthened | Exposed for 3 months | 2 |
| DFH-6 | Damaged | Strengthened | Exposed for 6 months | 3 |

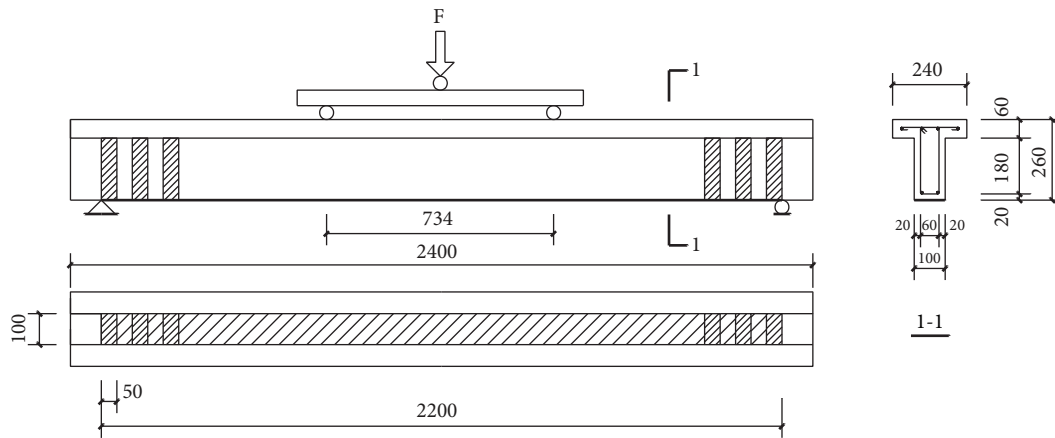


FIGURE 1: Details of the specimen (mm).

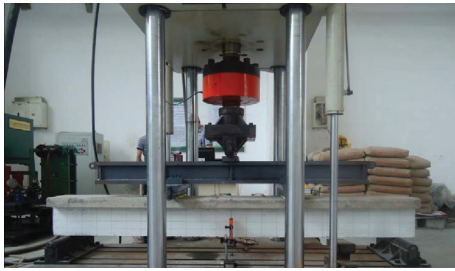


FIGURE 2: Bending test of the beam.

2.5. Chloride Penetration Tests. After bending tests, chloride penetration in specimens FH-3, FH-6, DFH-3, and DFH-6 was tested. The concrete samples were collected from 12 cross sections at 100 mm spacing in half beam due to symmetry as shown in Figure 3. In each cross section, three samples were collected from two sides and the middle of the web at the depth near the longitudinal steel bars. The locations of the samples were shown in Figure 3. The samples were oven-dried at 50°C for 24 h and thereafter were ground to powder which can pass through 0.15 mm sieve. Afterwards, concrete powder was dissolved [23] in the following procedures: 2.0 g powder was put into 40 mL solution which contains distilled water and concentrated nitric acid in proportion of 85 : 15 for 24 h

and then filtered. After the solution was analysed by AgNO_3 titration instrument (Automatic Potentiometric Titrator ZD-2), chloride contents in the concrete powder were calculated.

2.6. NEL Tests. NEL method [19–21] was employed to study the chloride diffusion coefficients of the concrete using a concrete electric flux measuring instrument (NEL-PEU), as shown in Figure 4. The mix proportions of the concrete in NEL test were 1 : 2.22 : 2.89 : 4.92 (water : cement : sand : aggregate). As shown in Figure 5, 15 concrete cylinders with a diameter of 100 mm and a thickness of 50 mm were casted as the samples. Thereafter, they were cured for 28 days. The concrete cylinders were equally distributed in five series with different crack depth. The series G-0 represents sound concrete. The series G-10, G-15, G-20, and G-25 represent the concrete with a 10 mm, 15 mm, 20 mm, and 25 mm depth crack, respectively. The width of the cracks is 0.2 mm which is the maximum allowed crack width in RC structures in Chinese bridge standard (JTG D60-2004) [24]. To artificially preset the crack, a stainless steel thin plate with 0.2 mm thickness was embedded in the concrete cylinders along a diameter when casting and was moved after 3-day curing. After immersed in a vacuumed instrument filled with water for 24 h, each specimen was fixed in a testing device. One side of the device was fulfilled with 0.3 mol/L NaOH solution and the other side was fulfilled with 3% NaCl

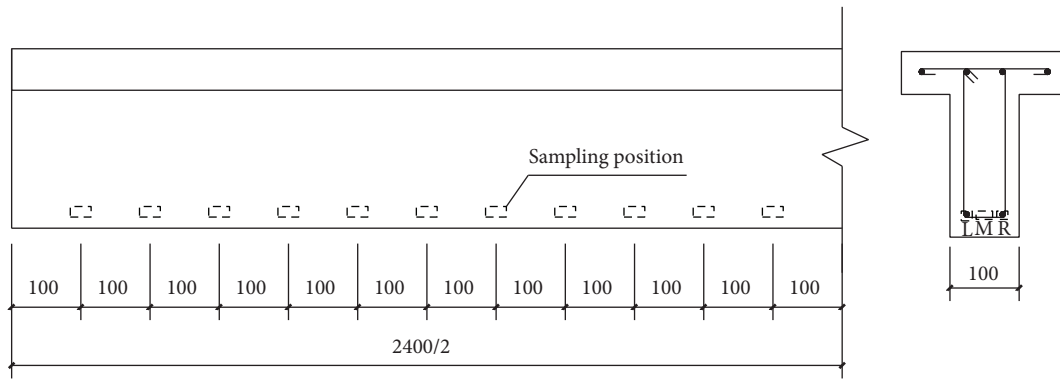


FIGURE 3: Sampling position (mm).



FIGURE 4: NEL-PEU instrument.



FIGURE 5: Specimen of NEL test.

solution. The electric flux values were recorded after being electrified for 6 h.

3. Experimental Results and Discussion

3.1. Precracking. The precracks in the RC beams were induced by fatigue loading. The damage of the specimens was identified by residual deflection and cracks, as shown in Table 2. The average residual deflections of the beams in series D, DF, and DFH were 0.91, 1.47, and 1.11 mm, respectively, which indicates that the fatigue loading weakened the stiffness of

TABLE 2: The results of precracking tests.

| Series | Residual crack width (mm) | Residual deflection (mm) |
|--------|---------------------------|--------------------------|
| D | 0.11 | 0.91 |
| DF | 0.28 | 1.47 |
| DFH | 0.26 | 1.11 |

the beams. The average width of the residual cracks in series DF and DFH was wider than 0.2 mm, which is the maximum allowed width of cracks in RC beams in Chinese bridge standard (JTG D60-2004) [24]. This indicates that these beams need to be repaired after the fatigue damage.

3.2. Flexural Capacity. All specimens were statically tested to determine the ultimate strength and deflections. The test results in the form of load-deflection behavior were presented in Figure 6. Average curves of each series were used to avoid cumbersome presentation. Two aspects were noted from Figure 6. Firstly, all the strengthened beams showed a strength enhancement over the unstrengthened beams, but the strengthened beams have very little enhancement in stiffness prior to the unstrengthened beams yielding. Secondly, the precracking and environmental exposure have only marginal effects on the load-deflection curves.

The average ultimate loads and deflections of each series are shown in Figures 7 and 8. The load-deflection curves of series C and D are equal, while the ultimate load of D is slightly higher than that of C. The CFRP strengthening increased the ultimate strength of the sound beams in series F by 85.7% and the precracked beams in series DF by 73.3% in comparison with series C and D, respectively. This indicates that the CFRP strengthening was less effective for the precracked RC beams compared to the unprecracked RC beams due to the residual deflection and cracks. In addition, the ultimate deflections of the specimens in series F and DF were decreased by 20.1% and 30.8% in comparison with C and D, respectively, which presents that the CFRP strengthening reduced the ductility of the RC beams. Comparing the specimens in series F and DF, the wetting/drying cycles for 3 and 6

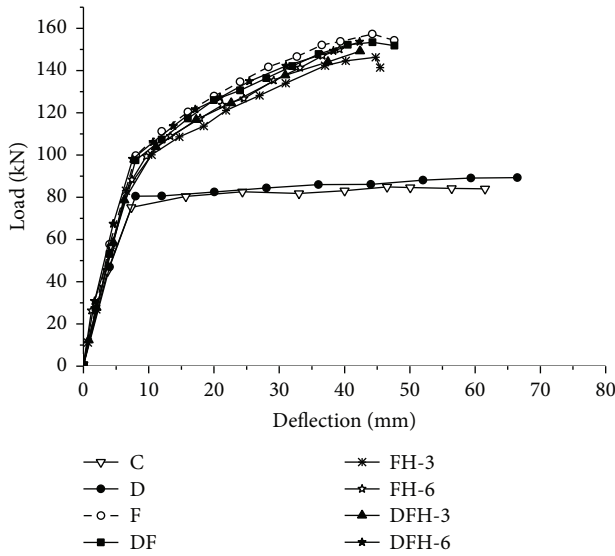


FIGURE 6: Load-deflection curves.

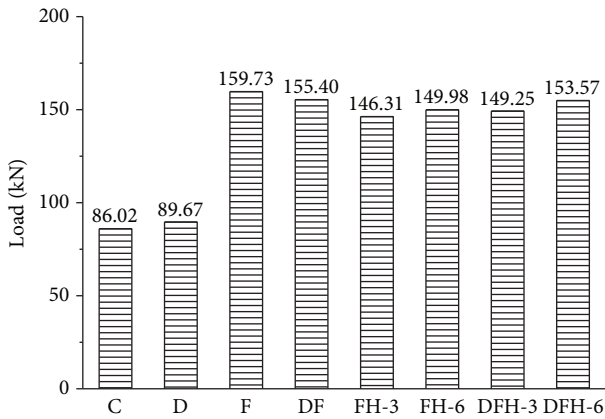


FIGURE 7: Ultimate loads.

months reduced the ultimate strength of the strengthened RC beams in series FH-3 and DFH-3 by 6.0% and in FH-6 and DFH-6 by 3.7%, respectively. These clarify that the strength of the specimens exposed to wetting/drying cycles decreased in the first 3 months and then slightly increased in the next 3 months. The environmental exposure has clear effect on the mechanical behavior of the CFRP reinforced concrete members for the first 3 months but this effect is marginal for the next 3 months and even longer period [25]. The strength of the concrete, meanwhile, increased during immersing in the water. The deflections of the specimens in series FH-6 and DFH-6 decreased slightly after 6 months of exposure to environmental condition in comparison with series FH and DFH. It showed that the hygrothermal environment has marginal effect on the ductility of the strengthened beams. The main cause of the decreases in the strength and ductility of the specimens under environmental exposure is the deterioration of the adhesive bonding caused by moisture diffusion into the adhesive joint [7, 8].

The width of the cracks in the middle of the specimens was measured at the load level of 79 kN. The average values of

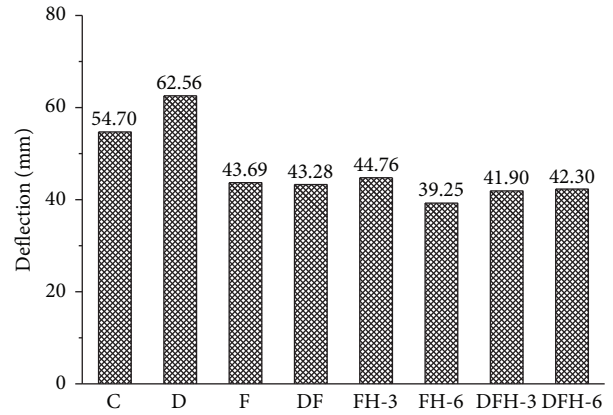


FIGURE 8: Ultimate deflections.

series C, F, DF, and DFH-3 are 0.22 mm, 0.12 mm, 0.19 mm, and 0.40 mm, respectively. The width of the cracks in the strengthened specimens in series F was about half of that in the plain control specimens in series C, which indicates that the CFRP strengthening effectively restricts the cracks opening. Due to the residual cracks caused by the fatigue overloading cycles, the strengthened damaged specimens in series DF have wider cracks than the specimens in series F. The width of the cracks in the specimens in series DFH-3 was about two times that of specimens in DF. The reason can be explained by the wetting/drying cycles, which weaken the bonding behavior of the adhesive, resulting in the significant increase of cracks width.

3.3. Chloride Penetration. The chloride profiles of specimens after wetting/drying cycles for 3 and 6 months were shown in Figure 9, from which the effect of the CFRP bonding, precracking, and exposing period on the chloride penetration can be observed.

3.3.1. CFRP Bonding Effect. The chloride contents in the sides of the web (samples L and R) are significantly higher than those in the middle of the web (samples M), which indicates that the CFRP bonding resisted the chloride penetration into the concrete. The chloride contents in the samples close to the ends of the strengthened beams (FH-3 and FH-6), especially in samples M, are obviously higher than those in other locations. This is because the CFRP bonding did not cover the ends of the specimens as shown in Figure 1. Thereby, it has higher chloride permeability.

3.3.2. Precracking Effect. The chloride contents fluctuated along the longitudinal direction in the strengthened precracked beams (DFH-3 and DFH-6). In addition, the average chloride contents in precracked beams (DFH-3 and DFH-6) are higher than those in the sound beams (FH-3 and FH-6). Furthermore, the chloride contents exactly in the crack location as shown in Figure 9(c) are significantly higher than others. Remarkable corrosion was observed on the steel bars located near this crack as well. As described above, it can be concluded that the cracks in the concrete accelerated the chloride penetration.

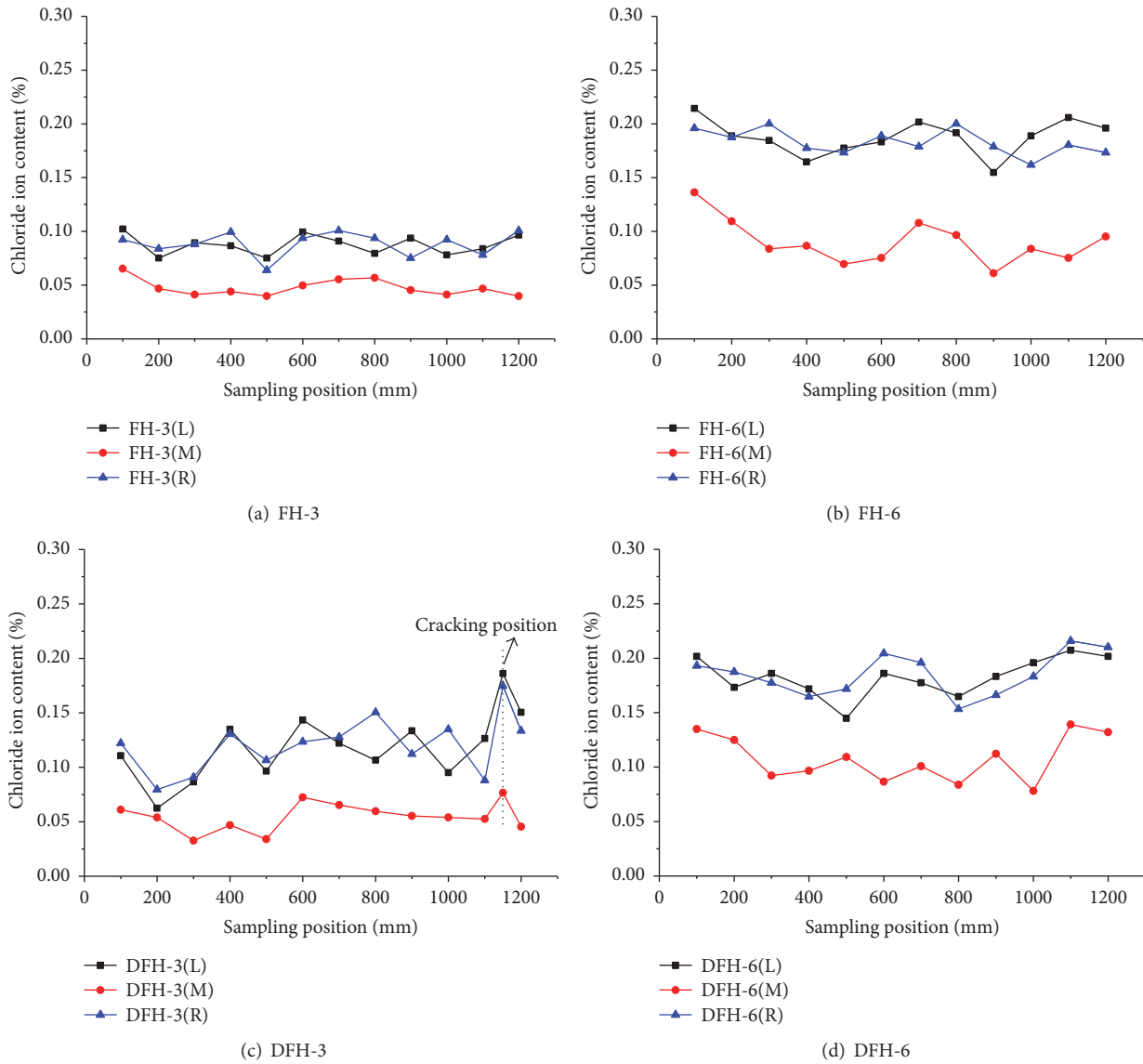


FIGURE 9: Chloride profiles of the specimens.

3.3.3. Exposing Period Effect. The average chloride contents in control specimen C, the specimens exposed to marine environment for 3 months (FH-3 and DFH-3) and 6 months (FH-6 and DFH-6), were 0.017%, 0.078%, and 0.142%, respectively. The chloride contents in the specimens subjected to environmental condition for 6 months are almost two times higher than those in the specimens for 3 months, which indicates that the chloride penetration increased with the period of the environmental exposure. Moreover, the chloride content in the specimens exposed for 6 months was higher than 0.1% which is the allowed value in Code for Construction of Concrete Structures (GB 50666-2011) [26].

3.4. Effect of Crack Depth on Chloride Diffusion Coefficients. The electric flux values Q of series G-0, G-10, G-15, G-20, and G-25 obtained by NEL tests were 2755.21C, 3276.17C,

3324.52C, 3543.57C, and 3751.45C, respectively. The chloride diffusion coefficients calculated by equation of Nernst-Einstein [20, 21] were shown in Figure 10.

The chloride diffusion coefficients of the specimens with 0.2 mm width crack (G-10, G-15, G-20, and G-25) were 16%–30% higher than that of the sound specimens (G-0). The chloride diffusion coefficients increased with the depth of the crack; however, the rate of increase was not pronounced. The chloride diffusion coefficient of the specimens with 25 mm depth crack (G-25) was only 12% higher than those with 10 mm depth crack (G-10).

The average width of the residual cracks in the specimens DFH was 0.26 mm. Meanwhile, the average chloride content in specimens DFH is about 18% higher than that in specimens FH without precracks. From the above NEL test results, the increasing rate is in the range of 16%–30%, which validates

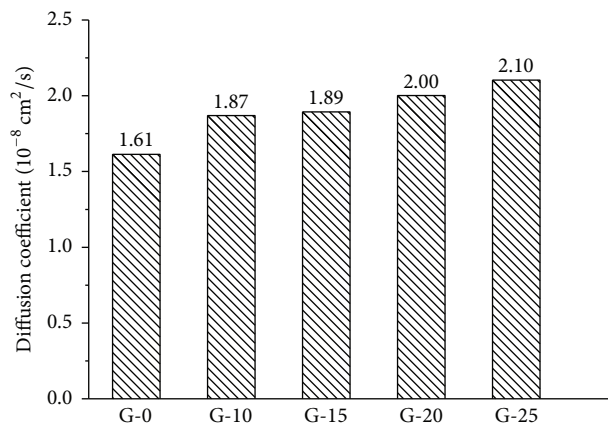


FIGURE 10: Chloride diffusion coefficients.

the effect of the precracking on chloride permeability in RC beams.

4. Conclusions

This paper presented an experimental study on precracked RC T-beams strengthened with CFRP subjected to marine environmental exposure. The RC beams were damaged under fatigue loading, resulting in cracks width in the range of 0.11~0.28 mm. The deterioration of the specimens was produced by placing the beams into salt water under wetting/drying cycles for 3 and 6 months. Flexural capacity and chloride penetration of the specimens were investigated. The following conclusions can be drawn from the experimental results:

- (1) The residual deflections and cracks in the RC T-beams damaged by fatigue loading cannot be ignored especially under chloride environment, and those repaired by CFRP can improve the strength significantly and decrease the permeability of chloride.
- (2) The strength of the CFRP retrofitted specimens reduced 6.0% by 3 months of wetting/drying cycles exposure while there was only 3.7% for specimens which were suffered for 6 months. It indicates that the wetting/drying environmental exposure has more obvious effect on the strength of CFRP strengthened beams in the first 3 months than in the 6 months.
- (3) The marine environment weakened the bonding strength of the adhesive and slightly reduced the ductility of the strengthened beams.
- (4) CFRP bonding can reduce the chloride penetration into the concrete, especially in the bonding interface, while the cracks in the concrete accelerated the chloride penetration.
- (5) NEL test results showed that the chloride diffusion coefficients of the concrete with 0.2 mm width crack were 16%–30% higher than that of the sound concrete, which also validates the effect of the precracking on chloride permeability in RC beams. In addition, the chloride diffusion coefficients slightly increased with the depth of the crack.

Competing Interests

The authors declare that there is no conflict of interests regarding the publication of this paper.

Acknowledgments

The authors thank the following groups for their financial support: National Natural Science Foundation of China (nos. 51278131 and 51202036), New Century Outstanding Talent Support Program Project of China (NCET-13-0739), and Guangdong Provincial Education Department Project of China (2012LYM. 0056).

References

- [1] G. C. Mays and G. P. Tilly, "Long endurance fatigue performance of bonded structural joints," *International Journal of Adhesion and Adhesives*, vol. 2, no. 2, pp. 109–113, 1982.
- [2] L. C. Hollaway and P. R. Head, *Advanced Polymer Composites and Polymers in the Civil Infrastructure*, Elsevier Science, Oxford, UK, 2001.
- [3] C. C. Choo, T. Zhao, and I. Harik, "Flexural retrofit of a bridge subjected to overweight trucks using CFRP laminates," *Composites Part B: Engineering*, vol. 38, no. 5-6, pp. 732–738, 2007.
- [4] O. Benjeddou, M. B. Ouezdou, and A. Bedday, "Damaged RC beams repaired by bonding of CFRP laminates," *Construction and Building Materials*, vol. 21, no. 6, pp. 1301–1310, 2007.
- [5] T. H. Almusallam, "Load-deflection behavior of RC beams strengthened with GFRP sheets subjected to different environmental conditions," *Cement and Concrete Composites*, vol. 28, no. 10, pp. 879–889, 2006.
- [6] J. Garzón-Roca, J. M. Sena-Cruz, P. Fernandes, and J. Xavier, "Effect of wet-dry cycles on the bond behaviour of concrete elements strengthened with NSM CFRP laminate strips," *Composite Structures*, vol. 132, no. 12, pp. 331–340, 2015.
- [7] K. Benzarti, S. Chataigner, M. Quiertant, C. Marty, and C. Aubagnac, "Accelerated ageing behaviour of the adhesive bond between concrete specimens and CFRP overlays," *Construction and Building Materials*, vol. 25, no. 2, pp. 523–538, 2011.
- [8] A. M. Mahmoud, H. H. Ammar, O. M. Mukdadi et al., "Non-destructive ultrasonic evaluation of CFRP-concrete specimens subjected to accelerated aging conditions," *NDT & E International*, vol. 43, no. 7, pp. 635–641, 2010.
- [9] D. Zhang, Y. Zhao, T. Ueda, X. Li, and Q. Xu, "CFRP strengthened RC beams with pre-strengthening non-uniform reinforcement corrosion subjected to post-strengthening wetting/drying cycles," *Engineering Structures*, vol. 127, pp. 331–343, 2016.
- [10] D. Zhang, S. Shen, Y. Zhao, W. Jin, and T. Ueda, "Cracking behavior of CFRP laminate-strengthened RC beams with pre-mechanical and post-mechanical environmental damage," *Journal of Composites for Construction*, vol. 19, no. 4, Article ID 04014066, 2014.
- [11] M. Otieno, H. Beushausen, and M. Alexander, "Chloride-induced corrosion of steel in cracked concrete—part I: experimental studies under accelerated and natural marine environments," *Cement and Concrete Research*, vol. 79, pp. 373–385, 2016.
- [12] J. Wu, H. Li, Z. Wang, and J. Liu, "Transport model of chloride ions in concrete under loads and drying-wetting cycles," *Construction and Building Materials*, vol. 112, pp. 733–738, 2016.

- [13] H.-L. Wang, J.-G. Dai, X.-Y. Sun, and X.-L. Zhang, "Characteristics of concrete cracks and their influence on chloride penetration," *Construction and Building Materials*, vol. 107, pp. 216–225, 2016.
- [14] H. Ye, Y. Tian, N. Jin, X. Jin, and C. Fu, "Influence of cracking on chloride diffusivity and moisture influential depth in concrete subjected to simulated environmental conditions," *Construction and Building Materials*, vol. 47, no. 5, pp. 66–79, 2013.
- [15] T. Ishida, P. O. N. Iqbal, and H. T. L. Anh, "Modeling of chloride diffusivity coupled with non-linear binding capacity in sound and cracked concrete," *Cement and Concrete Research*, vol. 39, no. 10, pp. 913–923, 2009.
- [16] K. Audenaert, G. D. Schutter, and L. Marsavina, "Influence of cracks and crack width on penetration depth of chlorides in concrete," *European Journal of Environmental and Civil Engineering*, vol. 13, no. 5, pp. 561–572, 2009.
- [17] C. Sosdean, L. Marsavina, and G. De Schutter, "Experimental and numerical determination of the chloride penetration in cracked mortar specimens," *European Journal of Environmental and Civil Engineering*, vol. 20, no. 2, pp. 231–249, 2016.
- [18] C. Fu, H. Ye, X. Jin, D. Yan, N. Jin, and Z. Peng, "Chloride penetration into concrete damaged by uniaxial tensile fatigue loading," *Construction and Building Materials*, vol. 125, no. 10, pp. 714–723, 2016.
- [19] H. G. Yin, Y. Li, H. Lv, and Q. Gao, "Durability of sea-sand containing concrete: effects of chloride ion penetration," *Mining Science and Technology*, vol. 21, no. 1, pp. 123–127, 2011.
- [20] X. Lu, "Application of the Nernst-Einstein equation to concrete," *Cement and Concrete Research*, vol. 27, no. 2, pp. 293–302, 1997.
- [21] C. L. Li, X. Y. Lu, and H. X. Zhang, "Rapid test method for determining chloride diffusivities in cementitious materials," *Industrial Construction*, vol. 628, no. 6, pp. 41–43, 1998 (Chinese).
- [22] Z. H. Wang, J. Deng, and D. Y. Wang, "Experimental study on bending capacity of reinforced T-beams after overloading damage," *Concrete*, no. 6, pp. 31–40, 2014 (Chinese).
- [23] Chinese standard, "Testing code of concrete for port and waterwog engineering," J TJ 270-98.
- [24] Chinese Standard, "General code for design of highway bridges and culverts," Tech. Rep. JTJ D60-2004, 2004.
- [25] Y. Huang, *Experimental study on durability of CFRP confined concrete subjected to hydrothermal environment [M.S. thesis]*, Guangdong University of Technology, Guangzhou, China, 2014.
- [26] Chinese Standard, "Code for Construction of Concrete Structures," GB 50666-2011.

Research Article

Effect of Temperature Variation on Bond Characteristics between CFRP and Steel Plate

Shan Li, Tao Zhu, Yiyang Lu, and Xiaojin Li

School of Civil Engineering, Wuhan University, Wuhan 430072, China

Correspondence should be addressed to Yiyang Lu; yylu901@163.com

Received 20 September 2016; Accepted 9 November 2016

Academic Editor: Jun Deng

Copyright © 2016 Shan Li et al. This is an open access article distributed under the Creative Commons Attribution License, which permits unrestricted use, distribution, and reproduction in any medium, provided the original work is properly cited.

In recent years, application of carbon fiber reinforced polymer (CFRP) composite materials in the strengthening of existing reinforced concrete structures has gained widespread attention, but the retrofitting of metallic buildings and bridges with CFRP is still in its early stages. In real life, these structures are possibly subjected to dry and hot climate. Therefore, it is necessary to understand the bond behavior between CFRP and steel at different temperatures. To examine the bond between CFRP and steel under hot climate, a total of twenty-one double strap joints divided into 7 groups were tested to failure at constant temperatures from 27°C to 120°C in this paper. The results showed that the joint failure mode changed from debonding along between steel and adhesive interface failure to debonding along between CFRP and adhesive interface failure as the temperature increased beyond the glass transition temperature (T_g) of the adhesive. The load carrying capacity decreased significantly at temperatures approaching or exceeding T_g . The interfacial fracture energy showed a similar degradation trend. Analytical models of the ultimate bearing capacity, interfacial fracture energy, and bond-slip relationship of CFRP-steel interface at elevated temperatures were presented.

1. Introduction

Carbon fiber reinforced polymer (CFRP) has been widely implemented in rehabilitating or strengthening deteriorating structures such as buildings and bridges in civil engineering due to its preferable mechanical properties, including high strength, light weight, corrosion resistance, and formability [1–3]. This has been particularly the case for concrete structures. However, the use of CFRP for strengthening or retrofitting metallic buildings and bridges is still in its early stages [4–6].

In the repair of steel structures with CFRP method, the CFRP is bonded to the steel surface using epoxy adhesives. The load is transferred to the CFRP material by epoxy adhesives. The performance of the CFRP-strengthened steel structures is governed by the effectiveness of interfacial bonding. Therefore, it is necessary to study the bond performance of CFRP-steel interface, through experimental studies on simple CFRP-steel bonded joints. According to it, some researches have been conducted at ambient temperature and revealed that the adhesive layer was the weak link in this composite

system, and one of the main failure modes observed was the debonding of CFRP from the steel substrate [7–12].

In some districts where the temperature may exceed 50°C or even higher, mechanical properties of epoxy adhesives may decrease considerably since their T_g are usually in the range from 55 to 120°C [13]. Beyond the T_g value, the adhesive transforms from a glassy state to a rubbery state accompanied with the degradation of the ability to transfer stress efficiently [14–16]. As a result, the mechanical performance of CFRP-strengthened steel structures subjected to elevated temperatures primarily depends on that of the thermoset adhesive. In order to investigate the bond behavior of CFRP-steel systems subjected to elevated-temperature exposure, a few researchers in recent years have undertaken relevant investigations. Nguyen et al. [17] studied the mechanical performance between normal modulus CFRP and steel plate at temperatures around the glass transition temperature (T_g) of the adhesive. A mechanism-based mode to describe the effective bond length, the strength, and the joint stiffness at elevated temperature was presented and verified. Al-Shawaf et al. [18] investigated the bond characteristics of

high modulus CFRP-steel bonded joints using three different epoxy resins at temperatures between 20°C and 60°C. At temperatures near and greater than T_g , as a result of increased adhesive's softening and degradation in properties, the prevailing failure mode was debonding failure, a significant decrease in the ultimate joint load was observed, and the strain level along the CFRP surface almost totally declined. But beyond these, studies on the bond behavior between CFRP and steel at elevated temperatures remain lacking, and further investigation is needed to better understand the performance of CFRP-steel interface at elevated temperatures.

This paper presents results concluded from a series of CFRP-steel double strap joints tested in tension at temperatures ranging from 27°C up to 120°C. Comparisons are presented on failure modes, joint ultimate bearing capacities between specimens at different temperatures. Combining the Chowdhury model [14] and Hart Smith model [19], an analytical model was developed for predicting the ultimate bearing capacity of CFRP-steel joints. Moreover, a model was proposed based on the literature [9, 20, 21] to characterize the temperature dependence of CFRP-steel joint behavior subjected to elevated temperatures.

2. Experimental Program

2.1. Test Specimens. A total of 21 double strap joints divided into 7 groups were tested. Three identical samples were prepared for each specific temperature. For each composite joint, the temperature is the only variable that is changed throughout the experiment (i.e., $T = 27, 40, 50, 60, 80, 100,$ and 120°C). All double strap bond specimens were named in the form of S-Tx. For example, specimen S-T50 strengthened with CFRP composite was tested at 50°C (T50).

2.2. Preparation of Specimens. Figure 1 shows a schematic view of the CFRP-steel double strap joints investigated in this study, including steel substrate, CFRP composite, and adhesive layer. For each specimen, two CFRP sheets were bonded symmetrically to the 3 mm thickness steel surface over a length of 150 mm. In the preparation of the specimen, the surface of the steel plate was uniformly roughened by emery wheel and cleaned with acetone to remove grease, oil, and rust to ensure proper bonding between the composite system and steel. Two CFRP sheets were first cut at 30 mm width and fully infiltrated. After the steel plate was placed in position and the adhesive was applied on the steel surface, the epoxy-bonded CFRP sheets were attached to the desired region and rolled on the adhesive until a uniform bonding layer was formed. All specimens were then cured in the laboratory at ambient temperature for a week.

2.3. Material Properties. Mechanical property of steel plate was obtained through tensile coupon test as per ISO 6892-1 [22]. CFRP sheet was a unidirectional material, and its properties were obtained in accordance with ASTM D3039 [23]. A two-part epoxy adhesive with the glass transition temperature (T_g) being 50°C was applied for all test specimens. The saturant resin (Part A) and hardener (Part B) were mixed

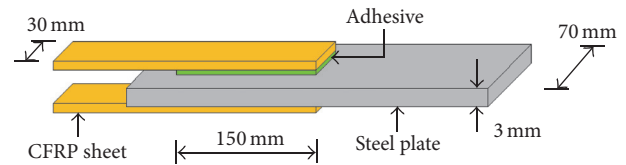


FIGURE 1: CFRP composite double strap joint specimen.

with a ratio of four to one by weight. Material properties of the two adherends and adhesive are summarized in Table 1.

2.4. Test Setup and Instrumentation. For control specimens, eight strain gauges were attached on the top of the CFRP sheet with spacing of 20 mm in the bonded zone, and one strain gauge in the unbonded zone was used to record the tensile load. For specimens at elevated temperatures, strain measure with adhesively bonded strain gauges is difficult due to the susceptibility of glue and strain gauge to heat. Nevertheless, the displacement values calculated from strain readings basically agree well with the LVDT readings reported by others [10]. Therefore, two L-shaped copper plates, which had a low coefficient of thermal expansion ($1.65 \times 10^{-5}/^\circ\text{C}$), were attached symmetrically for measuring displacement at the loaded end. A device using electric coil for heating was designed for elevated temperature tests. Specimens were preheated in the device to their target temperatures for a period of 20 minutes and kept inside throughout the test process. The arrangements of strain gauges and L-shaped copper plates are shown in Figure 2. All specimens were tested individually in direct tension to failure under displacement control (0.5 mm/min) using a universal hydraulic testing machine (capacity of 100 kN). The schematic view of test setup is shown in Figure 3.

3. Experimental Results

3.1. Failure Mode. Two predominant failure modes could be observed and described as failure Mode I and Mode II. Mode I failure refers to debonding between steel substrate and the adhesive. Mode II failure was debonding between CFRP sheet and the adhesive. The failure modes of all specimens were summarized in Table 2 with selective images of failed specimens presented in Figure 4. Specimens tested at temperatures between 27°C and 50°C were representative of Mode I failure. The debonding initiated from the loaded end and headed to the free end along the steel surface. The results suggest that, at temperatures below T_g , the adhesive used is brittle and glassy and has microcracking propensity, flaws, and imperfections. This will weaken the interfacial adhesive layer and lead to the debonding failure between steel and the adhesive [18]. When heated to tested temperatures from 60 to 120°C, the failure was characteristic of Mode II failure, with a little island-like adhesive left on the steel plate. In addition, more residual epoxy was attached on the surface of the steel plate as the temperature increased. A similar failure mode was observed in previous researches [9, 18, 24]. The epoxy remnant on the steel plate is indicative of poor

TABLE 1: Material properties.

| Material | Thickness (mm) | Young's modulus (GPa) | Yield strength (MPa) | Ultimate strength (MPa) | Failure strain (%) | Shear strength (MPa) |
|--------------------------|----------------|-----------------------|----------------------|-------------------------|--------------------|----------------------|
| Steel plate | 3 | 205.0 | 350.0 | 451.0 | 20.0 | — |
| CFRP | 0.111 | 252.0 | — | 3553.0 | 1.4 | — |
| Epoxy resin ^a | — | 2.4 | — | 33.0 | 1.4 | 21 |

^aManufacturer data.

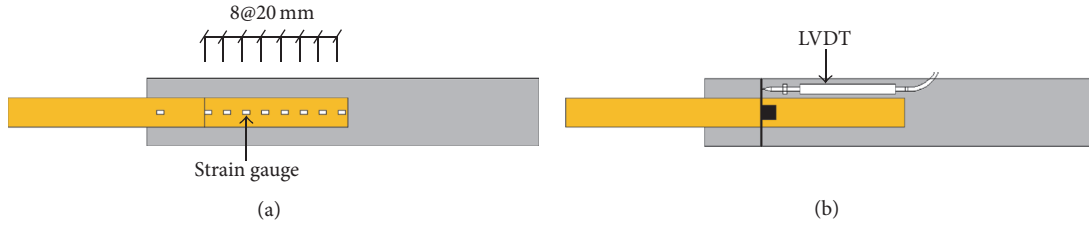


FIGURE 2: Instrumentation: (a) distribution of strain gauges; (b) layout of LVDTs.

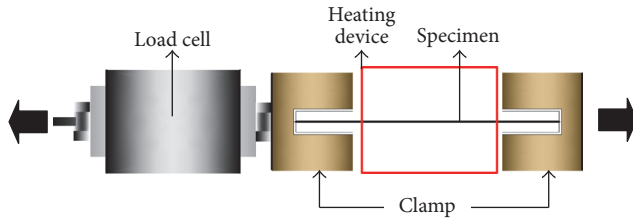


FIGURE 3: Test setup.

bonding between CFRP sheet and the adhesive. The steel plate and CFRP fibers can maintain their strengths at temperature above 120°C (maximum temperature in this study). This failure shift is believed to be dominated by the temperature dependence of the adhesive layer rather than the adherends. It is also suggested that the adhesive layer may degrade at a faster rate than the resin matrix in CFRP composites. Given that the adhesive and resin matrix were made of the same epoxy polymer, this different ratio in degradation may be because of the composite action between CFRP fibers and resin and different stress levels at adhesive layer and resin matrix [17].

3.2. Load-Displacement Behavior. Figure 5 shows the load-displacement curves for all the specimens. The displacement value for control specimen was calculated from readings of the strain gauges while those for specimens at elevated temperatures were obtained from the LVDT readings. All the curves behaved linearly in the initial loading, followed by a softening stage, and ended with a long plateau until final failure. It is evident from Figure 5 that the initial stiffness of specimens dropped with higher temperature. This degradation was pronounced at temperatures above T_g of the adhesive.

The term “bond strength” refers to the ultimate load that can be resisted by the CFRP sheet before the CFRP sheet debonds from the steel substrate. The bond strengths of all the specimens tabulated in Table 2 are the average values of each series. In the range from 27 to 50°C, the results showed a progressive decrease in bond strength as the temperature increased. The average strengths of S-T40 (10.000 kN) and S-T50 (8.950 kN) are 5.79% and 15.68% lower than that of S-T27 (10.614 kN), respectively. When the temperature exceeded T_g (50°C), a significant reduction of ultimate load was observed. The most drastic drop was seen on specimen S-T120 (0.360 kN), of which the remaining joint bond strength is only 3.39% of the initial strength at 27°C (10.614 kN). This means that there is hardly bond strength between the CFRP sheets and steel plate. This is in line with results reported by others [25]. The internal stress created within the interface due to the volatilization or decomposition as a result of adhesive volume decrease, together with the thermal stress caused by differences of the coefficients of linear thermal expansion of the adhesive and the adherends, would increase the porosity and flaws within the adhesive which, in turn, have a detrimental effect on adhesive-joint capacity.

4. Analysis on Test Results

4.1. Bond Strength Prediction. Based on the failure mode mentioned in Section 3.1, the bond strength of composite joint at ambient temperature can be predicted by the Hart Smith model [19], which was developed based on the adhesive failure of double strap joints. Because $E_s t_s > 2E_f t_f$ in this study, the ultimate load of double strap joint can be written as

$$P_u = \phi b_f \sqrt{2\tau_a t_a \left(\frac{1}{2}\gamma_e + \gamma_p \right) 4E_f t_f \left(1 + \frac{2E_f t_f}{E_s t_s} \right)} \quad (1)$$

TABLE 2: Test results of all specimens.

| Specimens | Composite | Temperature (°C) | Ultimate load (kN) | Predicted load (kN) | Failure mode |
|-----------|-----------|------------------|--------------------|---------------------|--------------|
| S-T27 | CFRP | 27 | 10.614 | 10.746 | I |
| S-T40 | CFRP | 40 | 10.000 | 10.149 | I |
| S-T50 | CFRP | 50 | 8.950 | 9.309 | I |
| S-T60 | CFRP | 60 | 8.056 | 7.661 | II |
| S-T80 | CFRP | 80 | 2.792 | 3.030 | II |
| S-T100 | CFRP | 100 | 1.162 | 0.901 | II |
| S-T120 | CFRP | 120 | 0.360 | 0.494 | II |

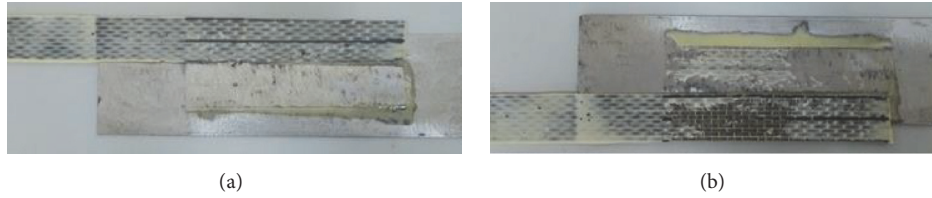


FIGURE 4: Typical failure modes: (a) Mode I; (b) Mode II.

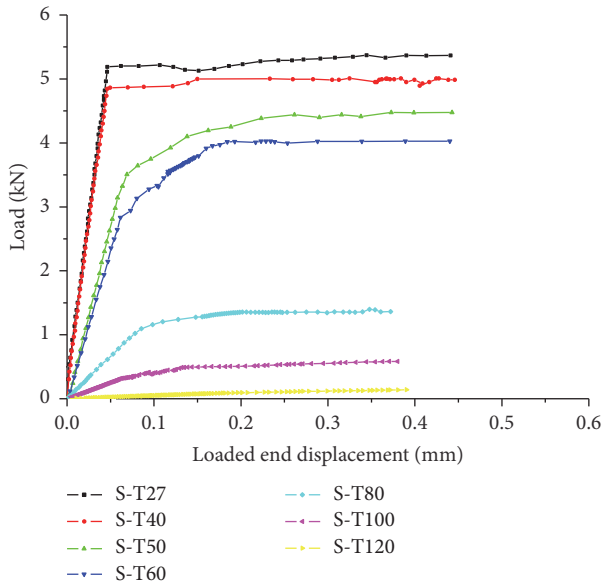


FIGURE 5: Load-displacement curves.

in which

$$\varphi = \begin{cases} 1 & L \geq L_e \\ \frac{L}{L_e} & L < L_e \end{cases} \quad (2)$$

$$L_e = \frac{P_u}{2\tau_a b_f} + \frac{2}{\lambda}$$

$$\lambda = \sqrt{\frac{G_a}{t_a} \left(\frac{1}{E_f t_f} + \frac{2}{E_s t_s} \right)},$$

where φ is the bond length factor; b_f is the width of CFRP composite; τ_a , t_a , γ_e , γ_p , and G_a are the shear strength, thickness, elastic shear strain, plastic shear strain, and shear modulus of adhesive, respectively; E_f , t_f and E_s , t_s are the elastic modulus and thickness of CFRP and steel adherends, respectively; L and L_e are the bond length and effective bond length.

On the other hand, the ultimate loads of specimens at elevated temperatures can be calculated by the Chowdhury model [14], which is given by

$$P_u(T) = \frac{P_u + P_R}{2} - \frac{P_u - P_R}{2} \tanh[k(T - T')], \quad (3)$$

where $P_u(T)$ is the ultimate load of specimen at specific temperature T ; P_u is the ultimate load at room temperature obtained by (1); P_R is the residual load capacity; k is a constant; T' is the temperature when a 50% reduction is observed. The values of parameters P_R , k , and T' achieved through regression analysis are equal to 0.422, 0.048, and 68.806, respectively.

All predicted ultimate loads are listed in Table 2. It should be noted that the value of γ_p is taken as $5\gamma_e$ in (1), because this assumption gives much better bond strength prediction in previous research [11]. The good agreement between prediction and test data shown in Figure 6 can be attributed to the fact that the relationship in (3) is totally empirical.

4.2. Discussion on the Interfacial Fracture Energy. The bond strength of a joint well established for CFRP-concrete joint is also applicable to CFRP-steel joint, which is in line with results reported by Xia and Teng [9]. And the double-lap shear test can be treated as two single-lap shear tests being

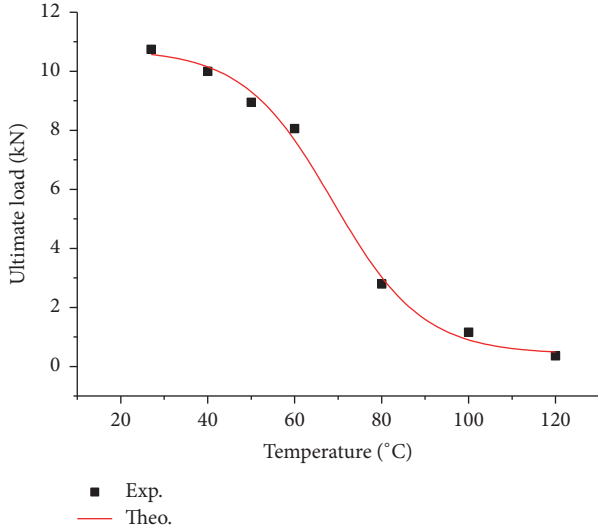


FIGURE 6: Ultimate load of specimens at elevated temperatures.

simultaneously conducted, and thus the ultimate load of double strap joint is given by

$$\frac{1}{2}P_u = b_f \sqrt{2G_f E_f t_f}. \quad (4)$$

Taking the effect of thermal exposure into consideration, thus the interfacial fracture energy of specimens at elevated temperatures can be calculated by

$$G_f(T) = \frac{[(1/2)P_u(T)]^2}{2b_f^2 E_f(T) t_f}. \quad (5)$$

The effect of elevated temperature is to degrade the mechanical properties of epoxy-impregnated CFRP composite, especially when the temperature exceeds the glass transition temperature, T_g . According to the degradation model by Bisby [20], the temperature-dependent elastic modulus of CFRP can be calculated by the following equation:

$$\frac{E_f(T)}{E_f} = \frac{1 - a_1}{2} \cdot \tanh[-a_2(T - a_3)] + \frac{1 + a_1}{2}, \quad (6)$$

where $E_f(T)$ is the tensile modulus of CFRP composite at specific temperature T ; E_f is the room-temperature modulus; a_1 , a_2 , and a_3 are the residual values of tensile modulus, constants that describe central temperature and severity of property degradation with temperature, which are 0.869, 0.106, and 52.207, respectively, according to the regression analysis.

Figure 7 depicts how the normalized interfacial fracture energy ($G_f(T)/G_f$) varies with the normalized temperature (T/T_g). A slight decrease of interfacial fracture energy $G_f(T)$ was observed before T_g approached, whereas a rapid decrease occurred when the temperature exceeds T_g of the adhesive.

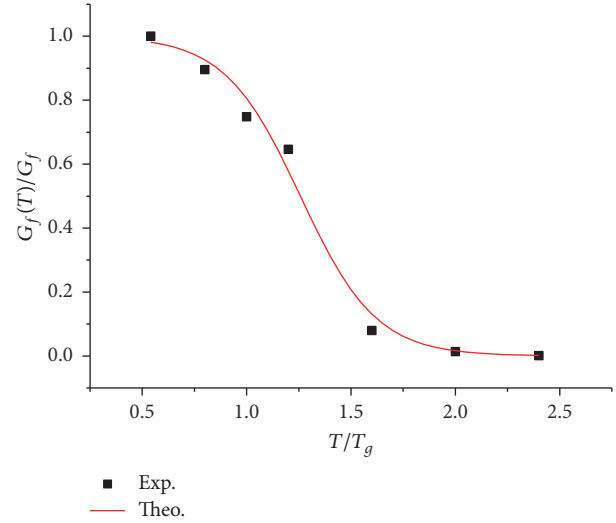


FIGURE 7: Interfacial fracture energy of specimens at elevated temperatures.

This decrease is mainly attributed to the mechanical degradation of the adhesive layer. According to the regression analysis, the temperature-dependent interfacial fracture energy can be written as

$$\frac{G_f(T)}{G_f} = \frac{1 - b_1}{2} \cdot \tanh\left[-b_2\left(\frac{T}{T_g} - b_3\right)\right] + \frac{1 + b_1}{2}, \quad (7)$$

where G_f refers to the interfacial fracture energy at ambient temperature and the regression values of parameters b_1 , b_2 , and b_3 are 0, 2.762, and 1.257, respectively.

4.3. Shear Stress-Slip Mode. The interfacial shear behavior of adhesively bonded joint is usually characterized by the relationship of the local shear stress and the relative slip between the two adherends. In the double strap joint test, the bond stress between the i -lth strain gauge and the i th strain gauge i , τ_i , can be obtained based on the internal force equilibrium:

$$\tau_i = \frac{E_f t_f (\varepsilon_i - \varepsilon_{i-1})}{\Delta x} \quad i \in (2, \dots, 8), \quad (8)$$

where ε_i and ε_{i-1} are measured strains in the CFRP sheet at adjacent strain gauge locations i and $i-1$ which are separated by a distance Δx .

Supposing that there is no relative slip at the free end of CFRP sheet, thus the relative slip s_i , at gauge location i , is expressed as

$$s_i = \frac{\Delta x}{2} \left(\varepsilon_1 + 2 \sum_{j=2}^{i-1} \varepsilon_j + \varepsilon_i \right) \quad (9)$$

$$i \in (2, \dots, 8), \quad j \in (2, \dots, 7),$$

where ε_1 is the strain at the free end of CFRP sheet; ε_j is the strain of the j th gauge attached on the CFRP sheet; ε_i is the

strain at the loaded end of CFRP sheet. Using (8) and (9), the local bond-slip relationships along the CFRP-steel interface can be obtained for specimens at ambient temperature.

For specimens at elevated temperatures without strain gauges, the bond-slip curve can be obtained from the relationship between the CFRP strain and slip at the loaded end. According to the literature [9, 10, 12, 21, 26–28], the bond-slip curves for CFRP-steel bonded joints are similar to those for CFRP-concrete bonded joints; both have a bilinear shape. And their developments of shear stress are the same. At a low load, the interface is in an elastic stage, during which the shear stress is the largest at or very close to the loaded end and gradually decreases towards the free end. As the load increases, part of the interface enters into softening stage, during which the shear stress at the loaded end decreases after it has approached its maximum value. When the shear stress at the loaded end reduces to zero, the ultimate load of the specimen is reached and keeps almost constant; debonding commences and propagates along the interface towards the free end with the peak shear stress moving gradually towards the free end. On the other hand, the strain-slip curves at the loaded end in this study derived from the load-slip relationship for CFRP-steel bonded joints are similar to those for CFRP-concrete bonded joints. Therefore, a similar expression linked to an exponential term is proposed for the relationship of the CFRP strain and interfacial slip in this section based on existing analytical model [21]:

$$\varepsilon = f(s) = \alpha(1 - e^{-\beta s}), \quad (10)$$

where α and β are regression parameters.

Figure 8 shows the comparison between regressing curves and experimentally observed relationships. It is found that all the ε - s curves predicted for specimens at elevated temperatures match well the experimental relationships plotted.

On the other hand, the equation of forces equilibrium acting on the CFRP sheet can be written as

$$\frac{d\sigma_f}{dx} - \frac{\tau}{t_f} = 0, \quad (11)$$

where σ_f and τ are the axial stress in the CFRP sheet and shear stress in the adhesive layer at any location, respectively. Combining (10) and (11) and neglecting the strain of the steel plate yield the following equation for the τ - s curve:

$$\begin{aligned} \tau &= t_f \frac{d\sigma_f}{dx} = E_f(T) t_f \frac{d\varepsilon}{dx} = E_f(T) t_f f'(s) \frac{df(s)}{ds} \\ &= \alpha^2 \beta E_f(T) t_f e^{-\beta s} (1 - e^{-\beta s}) \end{aligned} \quad (12)$$

because

$$G_f(T) = \int_0^{\infty} \tau ds = \frac{1}{2} \alpha^2 E_f(T) t_f. \quad (13)$$

The τ - s relationship can be rewritten as

$$\tau = 2G_f(T) \beta e^{-\beta s} (1 - e^{-\beta s}). \quad (14)$$

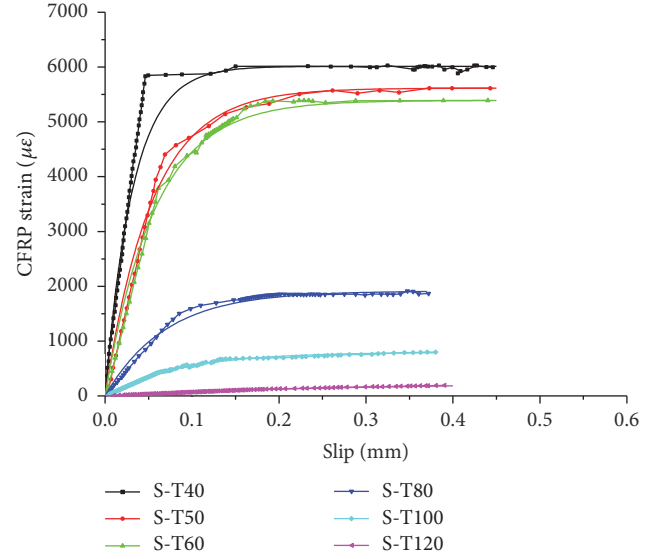


FIGURE 8: Relationships of CFRP strain and slip at loaded end.

Therefore, the shear stress as a function of relative slip can be determined with $G_f(T)$ calculated by (7) and regression parameter β .

Figure 9 shows how the normalized maximum shear stress ($\tau_{\max}(T)/\tau_{\max}$) and the corresponding normalized slip ($s_{\max}(T)/s_{\max}$) vary with the normalized temperature (T/T_g). The effect of elevated temperature is easier to characterize, showing typically a decrement of maximum shear stress with larger corresponding relative interfacial slip. The maximum bond stress decreased in agreement with the lower interfacial fracture energy, while the increase in slip meant degradation in the interfacial stiffness because of the softening of the adhesive.

5. Conclusions

The experimental results of 21 double strap joints subjected to elevated temperatures are presented. It is found that the CFRP-steel interface is significantly weakened and the degradation is affected by thermal exposure. The following conclusions are reached within the scope of this research:

- (1) The failure mode of specimens was affected by the elevated-temperature exposure. It was likely to change from debonding along steel-adhesive failure to debonding along CFRP-adhesive failure. The change of failure mode is dominated by the degradation and volume decrease of the adhesive.
- (2) The thermal exposure tended to decrease the initial stiffness and ultimate load for specimens, especially at temperatures above T_g of the adhesive.
- (3) A model was developed based on the Hart Smith model and the Chowdhury model for predicting the ultimate bearing capacity.
- (4) The interfacial fracture energy decreased gently at temperature below T_g , but much sharply when the

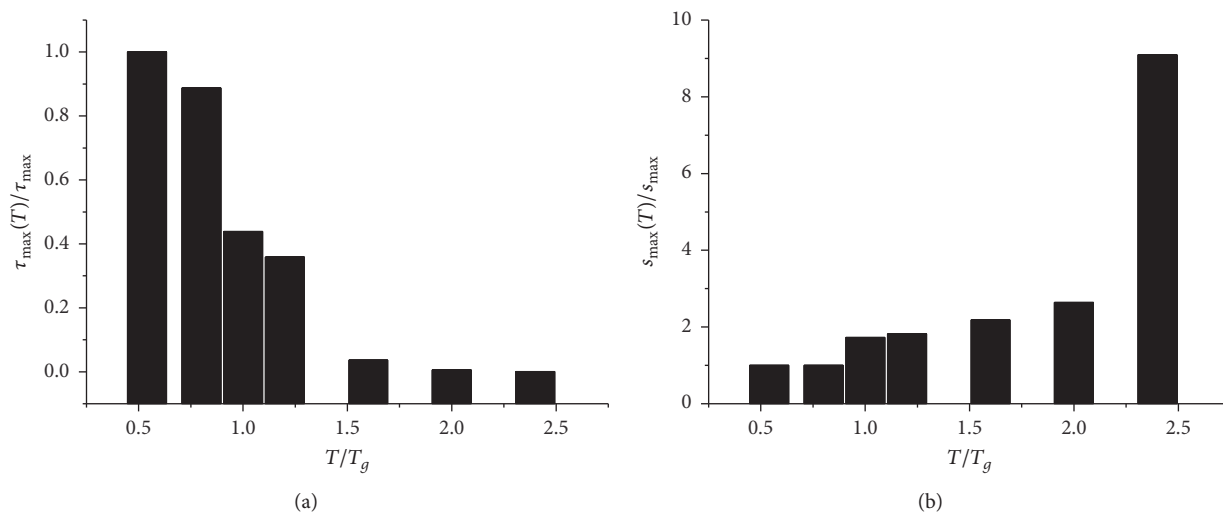


FIGURE 9: Effect of elevated temperatures on (a) τ_{\max} and (b) s_{\max} .

temperature exceeded T_g . A degradation model of interfacial fracture energy was presented.

- (5) Bond-slip relationship that approximates the effect of thermal exposure through regression parameters, calibrated by experimental data, was suggested. CFRP-steel interfaces at elevated temperatures showed a decrement of the maximum bond stress attained at a larger slip.

Competing Interests

The authors declare no competing interests.

Acknowledgments

The tests reported herein were made possible by the financial support from the Natural Science Foundation of China (51578428). The authors wish to thank the civil engineering technicians of Wuhan University for their help throughout the test process.

References

- [1] L. C. Hollaway, "A review of the present and future utilisation of FRP composites in the civil infrastructure with reference to their important in-service properties," *Construction and Building Materials*, vol. 24, no. 12, pp. 2419–2445, 2010.
- [2] J.-G. Dai, Y.-L. Bai, and J. G. Teng, "Behavior and modeling of concrete confined with FRP composites of large deformability," *Journal of Composites for Construction*, vol. 15, no. 6, pp. 963–973, 2011.
- [3] Y. Y. Lu, N. Li, and S. Li, "Behavior of FRP-confined concrete-filled steel tube columns," *Polymers*, vol. 6, no. 5, pp. 1333–1349, 2014.
- [4] D. Schnerch and S. Rizkalla, "Flexural strengthening of steel bridges with high modulus CFRP strips," *Journal of Bridge Engineering*, vol. 13, no. 2, pp. 192–201, 2008.
- [5] A. H. Al-Saidy, F. W. Klaiber, and T. J. Wipf, "Strengthening of steel-concrete composite girders using carbon fiber reinforced polymer plates," *Construction and Building Materials*, vol. 21, no. 2, pp. 295–302, 2007.
- [6] J. G. Teng, T. Yu, and D. Fernando, "Strengthening of steel structures with fiber-reinforced polymer composites," *Journal of Constructional Steel Research*, vol. 78, no. 6, pp. 131–143, 2012.
- [7] R. Haghani, "Analysis of adhesive joints used to bond FRP laminates to steel members—a numerical and experimental study," *Construction and Building Materials*, vol. 24, no. 11, pp. 2243–2251, 2010.
- [8] S. Fawzia, R. Al-Mahaidi, and X.-L. Zhao, "Experimental and finite element analysis of a double strap joint between steel plates and normal modulus CFRP," *Composite Structures*, vol. 75, no. 1–4, pp. 156–162, 2006.
- [9] S. H. Xia and J. G. Teng, "Behaviour of FRP-to-steel bonded joints," in *Proceedings of the International Symposium on Bond Behaviour of FRP in Structures (BBFS '05)*, pp. 411–418, Hong Kong, December 2005.
- [10] T. Yu, D. Fernando, J. G. Teng, and X. L. Zhao, "Experimental study on CFRP-to-steel bonded interfaces," *Composites Part B: Engineering*, vol. 43, no. 5, pp. 2279–2289, 2012.
- [11] C. Wu, X. L. Zhao, W. H. Duan, and R. Al-Mahaidi, "Bond characteristics between ultra high modulus CFRP laminates and steel," *Thin-Walled Structures*, vol. 51, no. 2, pp. 147–157, 2012.
- [12] S. Fawzia, X.-L. Zhao, and R. Al-Mahaidi, "Bond-slip models for double strap joints strengthened by CFRP," *Composite Structures*, vol. 92, no. 9, pp. 2137–2145, 2010.
- [13] D. Cree, T. Gamanouk, M. L. Loong, and M. F. Green, "Tensile and lap-splice shear strength properties of CFRP composites at high temperatures," *Journal of Composites for Construction*, vol. 19, no. 2, Article ID 04014043, 2015.
- [14] E. U. Chowdhury, R. Eedson, L. A. Bisby, M. F. Green, and N. Benichou, "Mechanical characterization of fibre reinforced polymers materials at high temperature," *Fire Technology*, vol. 47, no. 4, pp. 1063–1080, 2011.
- [15] A. P. Mouritz and A. G. Gibson, *Fire Properties of Polymer Composite Materials*, Springer, Dordrecht, The Netherlands, 2006.

- [16] S. Cao, Z. Wu, and X. Wang, "Tensile properties of CFRP and hybrid FRP composites at elevated temperatures," *Journal of Composite Materials*, vol. 43, no. 4, pp. 315–330, 2009.
- [17] T.-C. Nguyen, Y. Bai, X.-L. Zhao, and R. Al-Mahaidi, "Mechanical characterization of steel/CFRP double strap joints at elevated temperatures," *Composite Structures*, vol. 93, no. 6, pp. 1604–1612, 2011.
- [18] A. Al-Shawaf, R. Al-Mahaidi, and X.-L. Zhao, "Effect of elevated temperature on bond behaviour of high modulus CFRP/steel double-strap joints," *Australian Journal of Structural Engineering*, vol. 10, no. 1, pp. 63–74, 2009.
- [19] L. J. Hart Smith, "Adhesive-bonded double-lap joints," Tech. Rep. NASA CR-112235, Douglas Aircraft Company, Long Beach, Calif, USA, 1973.
- [20] L. Bisby, *Fire behavior of fiber-reinforced polymers (FRP) reinforced or confined concrete [Ph.D. thesis]*, Queens University, Ontario, Canada, 2003.
- [21] J.-G. Dai, W. Y. Gao, and J. G. Teng, "Bond-slip model for FRP laminates externally bonded to concrete at elevated temperature," *Journal of Composites for Construction*, vol. 17, no. 2, pp. 217–228, 2013.
- [22] ISO, "Metallic materials-tensile testing-part 1: method of test at room temperature," ISO 6892-1:2009, BSI, London, UK, 2009.
- [23] *Standard Test Method for Tensile Properties of Polymer Matrix Composite Materials; ASTM D3039-07*, ASTM, West Conshohocken, Pa, USA, 2008.
- [24] R. Haghani and M. Al-Emrani, "A new design model for adhesive joints used to bond FRP laminates to steel beams part B: experimental verification," *Construction and Building Materials*, vol. 30, no. 5, pp. 686–694, 2012.
- [25] Y. Y. Lu, W. J. Li, S. Li, X. Li, and T. Zhu, "Study of the tensile properties of CFRP strengthened steel plates," *Polymers*, vol. 7, no. 12, pp. 2595–2610, 2015.
- [26] H. Yuan, J. G. Teng, R. Seracino, Z. S. Wu, and J. Yao, "Full-range behavior of FRP-to-concrete bonded joints," *Engineering Structures*, vol. 26, no. 5, pp. 553–565, 2004.
- [27] J. G. Dai, T. Ueda, and Y. Sato, "Development of the nonlinear bond stress-slip model of fiber reinforced plastics sheet-concrete interfaces with a simple method," *Journal of Composites for Construction*, vol. 9, no. 1, pp. 52–62, 2005.
- [28] J. G. Dai, T. Ueda, and Y. Sato, "Unified analytical approaches for determining shear bond characteristics of FRP-concrete interfaces through pullout tests," *Journal of Advanced Concrete Technology*, vol. 4, no. 1, pp. 133–145, 2006.

Research Article

Discussion of a Coupled Strength Attenuation Model for GFRP Composites in Hydrothermal Environments

Wei Chen, Yongxin Yang, and Biao Li

Central Research Institute of Building and Construction Co., Ltd., MCC Group, Beijing 100088, China

Correspondence should be addressed to Wei Chen; 923248809@qq.com

Received 24 June 2016; Revised 9 August 2016; Accepted 23 August 2016

Academic Editor: Jun Deng

Copyright © 2016 Wei Chen et al. This is an open access article distributed under the Creative Commons Attribution License, which permits unrestricted use, distribution, and reproduction in any medium, provided the original work is properly cited.

The existing attenuation models for the durability of FRP (fiber-reinforced polymer) composites in hydrothermal environments were compared, and a new coupled strength attenuation model with a temperature parameter was proposed in this paper. A series of durability experiments on GFRP sheets in hydrothermal environments were conducted to validate the accuracy and rationality of the new model. A comparison between experimental data and the calculation results of the coupled model indicated that the new model can fit better with the experimental data and effectively reflect the convergence phenomenon in the strength attenuation of GFRP in hydrothermal environments. With a temperature parameter included, the new model can better predict the service life of GFRP composites at different aging temperatures. According to the coupled attenuation model proposed in this paper, a concept and calculation method of the slow-aging time point are put forward, which can be convenient for the evaluation and design of GFRP structures with long-term durability.

1. Introduction

Research shows that FRP (fiber-reinforced polymer) composites possess great durability performance [1] compared with traditional civil engineering materials (i.e., steel and concrete), but some problems remain for further study. The performance degradation of FRPs in hydrothermal aging environments has aroused the attention of many scholars. Zhou [2] carried out experiments on pultruded GFRP square tubes in distilled water under temperatures of 20°C, 40°C, and 60°C. After 6 months of degradation, the results show that the mechanical properties of the GFRP samples decreased. The higher the temperature is, the greater the decrease in the mechanical properties is, and the faster the decrease rate is. Sun and Li [3] conducted experiments on FRPs in hydrothermal environments, and a new attenuation model for FRPs was obtained and corrected based on experimental data and Williams's model. Zhang et al. [4] analysed the performance degradation of FRPs in hydrothermal environments and put forward a parabolic-linear model. Yang et al. [5] conducted hydrothermal aging experiments on BFRP by changing the content of basalt fiber cloth, infiltration of resin and other factors, and the variations of the tensile strength,

elongation ratio, and tensile elastic modulus were analysed. Berkettis and Tzetzis [6] conducted experiments on GFRP plates in distilled water, and the results indicated that the prophase quality rising rate increases with the temperature, while the elastic modulus decreases first rapidly and then slowly. FRPs can very easily be subjected to hydrothermal aging. In response to the call for further understanding, many other scholars [7–9] have also conducted aging experiments to study the mechanical properties of FRPs in hydrothermal environments.

A few researchers have already proposed strength attenuation models of FRPs in hydrothermal environments. Williams et al. [10] proposed the WLF empirical equation (1) based on the time-temperature equivalence principle:

$$\lg a_T = \lg \frac{t}{t_s} = \frac{-C_1(T - T_s)}{C_2 + T - T_s}, \quad (1)$$

where T_s and t_s denote the reference temperature and time, respectively, and C_1 and C_2 are empirical constants. The strength of FRPs under different temperatures could be translated into the strength under the same temperature based on the time-temperature equivalence principle. The

relationship between the residual strength and aging time can be presented as

$$P_t = \frac{P_0}{100} [a \ln(t) + b], \quad (2)$$

where P_t denotes the residual strength, P_0 denotes the initial strength, and a and b are undetermined constants.

Gunyaev et al. [11] established a semiempirical mathematical model for the median aging residual strength. The aging process of FRPs could be regarded as irreversible, and the strength attenuation model can be expressed as

$$S = S_0 + \eta(1 - e^{-\lambda}) - \beta \ln(1 + \theta t), \quad (3)$$

where S denotes the strength after aging time (t), S_0 denotes the initial strength, η and β are material parameters, and λ and θ are environmental parameters.

Guo [12] analysed the mechanical properties of FRPs in a hydrothermal environment and found that the mechanical properties first decrease rapidly and then slowly or even not at all. Based on this phenomenon, a bilinear attenuation model was proposed. Zhang et al. [3] improved the model by including the nonlinear law of the degradation of FRPs, such that the parabolic-linear attenuation model was proposed.

A comparison of the existing attenuation models indicates that Williams's model fits the experimental data well, but there is some error in the data of the later aging process. It is widely confirmed that Gunyaev et al.'s model fits better with the experimental data, while the complexity caused by a large number of parameters in the model makes it inconvenient to use. Guo bilinear model is easy to calculate, but it cannot reflect the nonlinear law of the performance degradation of FRPs. Zhang parabolic-linear model has a good prediction capability at early aging times, but the second stage of the linear part of the model cannot reflect the gradual convergence of the degradation. In addition, none of the models above contain a temperature parameter. Williams's model has to translate data of the strength reduction under different temperatures into that of the same temperature and then calculate a single-factor model that is only related to the aging time factor. The other three models lack consideration of the influence of temperature, as the parameters are different for the same material at different temperatures, making it inconvenient to predict the strength attenuation of FRPs under conditions of a specific temperature. Therefore, a more convenient and reasonable model is urgently needed. This paper proposes a new model for the strength attenuation of GFRP containing a temperature parameter. The parameters of the model remain unchanged for a single material or product. The coupled model was proposed based on previous studies and a mechanism analysis. A series of durability experiments under hydrothermal environments were conducted to verify the accuracy of the proposed model.

2. Single-Factor Model Analysis

2.1. Temperature-Factor Model. According to the Arrhenius formula, the relationship between the strength reduction

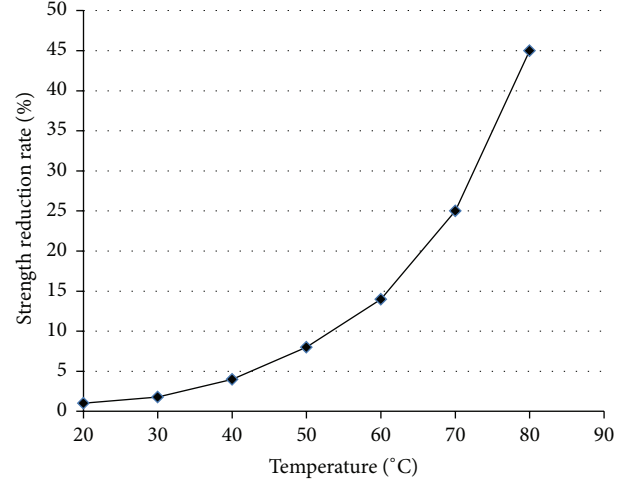


FIGURE 1: Relationship between strength reduction rate and temperature.

and temperature presents as the higher the temperature, the greater the strength reduction (within a certain temperature range). The slope of the tangent of the strength reduction curve as a function of temperature is gradually increasing. This indicates that the relationship between the strength reduction and temperature may be exponential or multinomial. Many scholars [13–17] reached the same conclusion in their research. It is widely believed that the increase in temperature can accelerate the aging of the GFRPs. Taking the natural index part of the Arrhenius formula into consideration, it is appropriate to assume that the strength reduction presents a natural exponential growth relationship with the temperature rising and that it can approximately simulate the influence of the temperature in the aging of FRPs. Robert and Fam [18] obtained experimental data from aging experiments of GFRP bars in a hydrothermal environment to support this opinion, as shown in Figure 1, from which it could be observed that the strength reduction shows an approximately exponential growth relationship with the temperature.

Therefore, assume that the strength reduction shows a natural exponential growth relationship with the temperature, and the attenuation model of the temperature can be expressed as

$$D = A \cdot e^{BT}, \quad (4)$$

where D denotes the strength reduction, T denotes the temperature, and A and B are undetermined constants related to the time and temperature, respectively.

According to (4), if the aging temperature increases from T_0 to T , the strength reduction should be multiplied by influence factor $\lambda_{\Delta T}$, whereas $\lambda_{\Delta T} = D_T/D_{T_0} = e^{B(T-T_0)}$. In this model, B can be considered as a constant for the same material, and all the time-dependent effects are included in parameter A . For certain materials and conditions, influence factor $\lambda_{\Delta T}$ is only affected by temperature difference ΔT .

To verify the accuracy of the model, a series of durability experiments on GFRP sheets under different temperatures were conducted. The specimens for the tests were made of

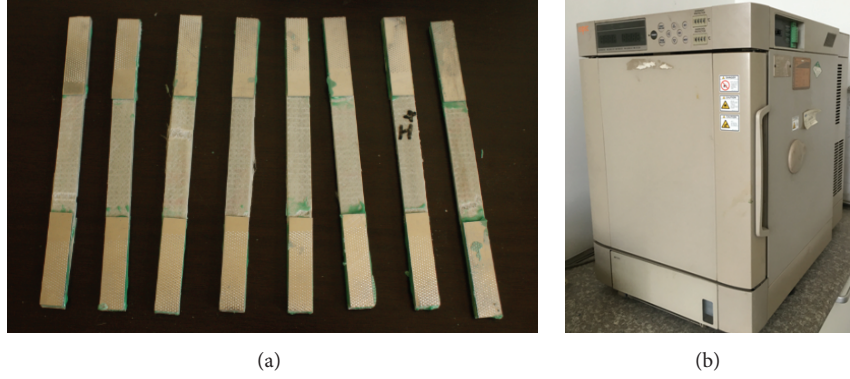


FIGURE 2: Experimental pictures: (a) samples of GFRP sheet and (b) the hydrothermal aging box.

TABLE 1: Strength of the samples after aging tests (MPa).

| Tem. | Time | | | | |
|------|------|------|-------|-------|-------|
| | 42 d | 83 d | 124 d | 185 d | 250 d |
| 25°C | 982 | 960 | 942 | 927 | 922 |
| 50°C | 1034 | 940 | 922 | 895 | 898 |
| 75°C | 958 | 912 | 890 | 856 | 854 |

TABLE 2: Strength reduction rates of the samples (%).

| Tem. | Time | | | | |
|------|-------|------|-------|-------|-------|
| | 42 d | 83 d | 124 d | 185 d | 250 d |
| 25°C | 2.87 | 5.06 | 6.82 | 8.31 | 8.51 |
| 50°C | -2.28 | 7.02 | 8.80 | 11.47 | 11.18 |
| 75°C | 5.12 | 9.79 | 11.97 | 15.33 | 15.53 |

glass fiber fabric embedded in epoxy matrix and then cured for 24 h in laboratory environment (a temperature of 23°C and a humidity of 50%) before the experiments. The aging temperatures of the experiments were set to 25°C, 50°C, and 75°C, and the environmental humidity was 95%. Figure 2 shows the samples of the GFRP sheets and the hydrothermal aging box that was used.

The average strength of the GFRP sheets before the aging tests (after curing for 24 h) is 1011 MPa. The strengths of the samples were tested after different aging times. The results of the tensile tests after aging are summarized in Table 1.

Based on the original data in Table 1, the strength reduction rates were calculated and are shown in Table 2.

It can be observed from Table 2 that after being exposed to a hydrothermal environment for 83 days, the strength reduction rates were 5.06%, 7.02%, and 9.79% at 25°C, 50°C, and 75°C, respectively. From the theoretical analysis of the new temperature model, the influence factor can be calculated as $\lambda_{\Delta T} = D_T/D_{T_0} = e^{B\Delta T}$. Combined with the strength reduction results above, the influence factor can be obtained as follows: $\lambda_{25}^1 = D_{50}/D_{25} = 7.02/5.06 = 1.387$ and $\lambda_{25}^2 = D_{75}/D_{50} = 9.79/7.02 = 1.395$. The two numbers are very close, which also reflects the reliability of the temperature attenuation model proposed by the authors. As for the data after 124 days, 185 days, and 250 days of aging,

the values of influence factor are calculated as $\lambda_{25}^1 = 1.290$, 1.381, and 1.314, respectively, and $\lambda_{25}^2 = 1.359$, 1.336, and 1.38, respectively. The values of the influence factor are close to those calculated after 83 days of aging, which proves the hypothesis that the influence factor and parameter B in the new model as well as the shape of the temperature model that is mainly determined by parameter B will not change with the change in the aging time. When the influence factor of the experiments is calculated, the data after 42 days of aging were ignored as abnormal data, which may be due to the second curing (i.e., postcuring) process which occurred in the specimens, and the average value of the influence factors can be obtained as $\bar{\lambda}_{25} = e^{B\Delta T} = e^{25B} = 1.357$, from which parameter B for the material used in the experiments can be obtained as $B = 0.012$. It must be clarified that, for different materials or different products, although the formula of the model is still applicable, the parameters in the model will change and need to be recalculated.

2.2. Aging Time-Factor Model. Extensive research has been conducted to study the attenuation law of strength for the GFRPs. Most of the studies [3, 13, 19–21] present the result that the strength of the GFRPs decreases rapidly at the early aging time and then goes slower and slower. To correspond with the natural index in the temperature model, a new model of aging for the time factor of GFRPs was proposed: $D = e^{-C/t}$. t denotes the aging time and C is a constant number for certain materials. It can be observed that in this model, D tends to be 0 when t tends to be 0, and D tends to be 1 when t tends to be infinity. Some FRP materials present an early convergence phenomenon, and the strength reduction cannot reach 1. Based on this situation, parameter M was introduced, and the new aging model can be represented by the following expression:

$$D = Me^{-C/t} \quad (0 < M < 1). \quad (5)$$

The new aging model can intuitively show the relationship between the strength reduction and the aging time, and it is more accurate than the linear model.

The experimental data under the temperature of 50°C (Table 2) were used to validate the accuracy of the model.

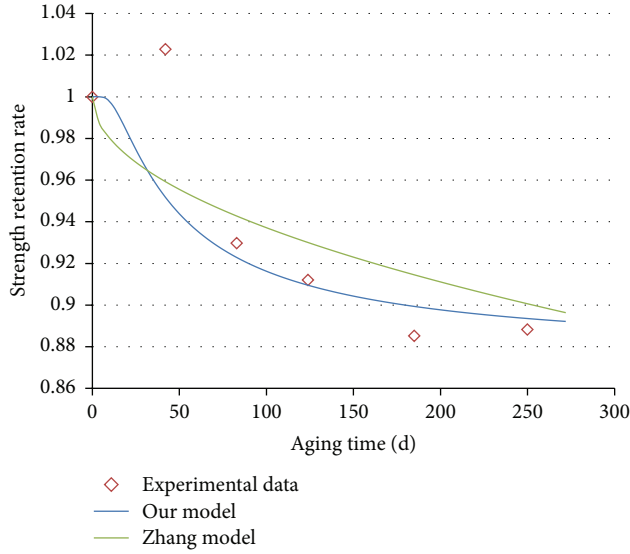


FIGURE 3: Comparison of models and experimental data at 50°C.

Through numerical fitting with (5), the values of the parameters were obtained: $M = 0.125$ and $C = 40$. Then, the strength attenuation model for the material used in the experiments is $D = 0.125e^{-40/t}$. This new model is presented in Figure 3 and compared with Zhang parabolic-linear model.

Generally speaking, the strength of the GFRPs decreases rapidly at first and then slowly, and the aging rate becomes slower and slower over the aging time with a trend of convergence. It could be learned from the experimental data that, at a condition of 50°C, the decrease of the strength began to slow down after exposure to a hydrothermal environment for 185 days, which indicates that the aging model proposed in this paper can better reflect this convergence phenomenon and can better fit the experimental data.

3. Coupled Model Analysis

From the analysis of the single-factor model, the relationship between the strength reduction and temperature could be expressed by (4). In this equation, A is a parameter related to the influence of aging time. Additionally, the influence of the aging time was analysed and a new model for the aging time factor was obtained (5). When considering the influences of both the temperature and aging time, parameter A in (4) could be replaced by the aging time factor model (5). After mathematical simplification, the following coupled model has been obtained:

$$D = N \cdot e^{BT-C/t}, \quad (6)$$

where N is a material parameter ($0 < N < 1$), and B and C are undetermined constants related to the temperature and time, respectively.

Equation (6) is the proposed coupled model of strength attenuation with a temperature parameter for GFRP composites. It shows that the strength reduction rate increases with the rise of temperature and the aging time. The sensitivity to

TABLE 3: Values of material parameter N .

| Tem. | Time | | | | |
|------|--------|-------|-------|-------|-------|
| | 42 d | 83 d | 124 d | 185 d | 250 d |
| 25°C | 0.054 | 0.063 | 0.070 | 0.076 | 0.074 |
| 50°C | -0.032 | 0.062 | 0.067 | 0.078 | 0.072 |
| 75°C | 0.053 | 0.064 | 0.067 | 0.077 | 0.074 |

these two factors can also be obtained. A larger value of B indicates a greater effect of the temperature, whereas a larger value of C represents a slower convergence of the material in the process of aging. The values of B and N can determine the approach limit value of the strength reduction under the assumption of the strength attenuation model: $D_{\max} = N \cdot e^{BT}$.

For the material used in our experiments, the value of parameter B was obtained in the analysis of the temperature model above ($B = 0.012$), and the value of parameter C was obtained in the analysis of the aging time model ($C = 40$). According to (6), the coupled model for our experiments can be expressed by the following equation:

$$D = Ne^{0.014T-40/t}. \quad (7)$$

There is only one undetermined parameter, N , in (7). The experimental data (shown in Table 2) of strength reduction rate under different aging times (t) and temperatures (T) were used to calculate the values of parameter N , which are shown in Table 3.

According to the results shown in Table 3, it is obvious that the values of N are close to each other (except for the abnormal data after 42 days of aging, which has been explained in the temperature-factor model), reflecting the feasibility and accuracy of the theoretical model proposed in this paper. The average value of N can be calculated as $\bar{N} = 0.070$. And (7) could be expressed by the following equation:

$$D = 0.070 \cdot e^{0.012 \cdot T - 40/t}. \quad (8)$$

It must be clarified that the parameters in (8) are only appropriate for the condition of our experiments. The experiments were conducted only as evidence to validate the accuracy and rationality of the model, and a specific model for the experiments (8) was used to present the superiority of the new proposed model. For other materials or products, although the formula of the model (6) is still applicable, the parameters of the model will change and need to be recalculated. According to (8), it will take 270 days for the strength to decrease by 11% at 50°C, whereas, in an 80°C environment, it will only take 80 days to reach the same strength reduction. The new coupled model can conveniently predict the durability of FRP materials under different temperatures. A strength reduction curve as a function of the aging time has been put forward based on the new coupled model (Figure 4) for the material used in our experiments. After comparison with the experimental data, it could be noted that despite the abnormal data after aging for 42 days, the experimental data can basically fit the coupled model proposed by the paper.

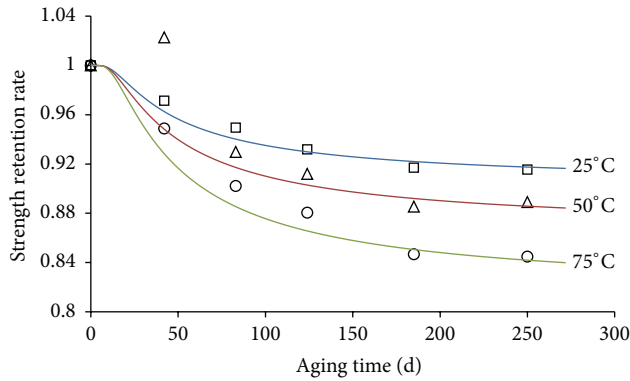


FIGURE 4: Strength decline rates under different temperatures.

From the aging experimental data and the strength attenuation curve given in Figure 4, it could be found that after aging for a certain time, the reduction rate slowed down and the strength gradually stabilized. Some scholars [22] believe that the product of the early reaction of aging in GFRPs plays a protective role in later reactions, such that the aging rate slows down. This convergence phenomenon could be well presented in the new coupled model (6). The aging time when the strength reduction reaches 90% of the approach limit reduction could be regarded as the transition point, after which the strength of the GFRPs could be regarded as stable. This transition point could be expressed as a slow-aging time point t_i . According to (6), $D_{\max} = N \cdot e^{BT}$, and $D_{90\%} = N \cdot e^{BT-C/t_i}$. If the conception of t_i indicates that $D_{\max}/D_{90\%} = 90\%$, then t_i could be calculated as the formula shown in (9). It is obvious that the value of t_i is only related to time parameter C . This is reasonable because, in the coupled model, the value of parameter C determines the variation trend of the strength reduction related to the aging time. For instance, the value of C has already been obtained ($C = 40$) for the material used in the experiments of this paper, so that the value of the slow-aging time point could be calculated as $t_i = 379.7d$, which means that, after 379.7 days of aging, the strength reduction had reached 90% of the approach limit reduction for the material used in the exposure environment. In practical engineering, if the strength of FRPs at t_i could be obtained, it can roughly represent the long-term strength of the material. Furthermore, if the strength of the material at t_i can meet the design requirements, it could be interpreted that the structure can meet the long-term service requirements. This can provide a reference for the evaluation and design of the long-term stability of FRP structures. It is important to note that for some FRP materials under certain conditions, the strength reduction rate does not slow down and there is no limit for strength reduction, so that the slow-aging time point becomes meaningless under this situation:

$$t_i = \frac{C}{\ln 10 - 2 \ln 3}. \quad (9)$$

In conclusion, not only can the new model in (6) be applied to analyse and predict the strength reduction of GFRP with a time factor, but it can also intuitively indicate the effect of

temperature, and its accuracy and rationality were verified by experimental data. It should be noted that, for different materials or products, the parameters in the equation will change and should be calculated by experiments. The model also provides a certain reference value for other materials (e.g., CFRP and BFRP) and corrosive environments (e.g., acid, alkali, and salt chemical corrosion solutions), but its accuracy remains for further study.

4. Conclusions

The paper proposes a coupled model of strength attenuation for GFRP composites in hydrothermal environments. Although the aging mechanism has not yet been confirmed, single-factor models of the temperature and aging time were proposed based on the existing research results, and the coupled model was then obtained. A series of durability experiments on GFRP sheets in hydrothermal environments were conducted to validate the accuracy and rationality of the model. On the basis of the coupled model, the concept and calculation method of the slow-aging time point were presented. The following conclusions can be drawn from this study:

- (1) A temperature-factor model was proposed based on the Arrhenius formula and existing studies, and it indicated that the strength reduction rate shows a natural exponential growth relationship with the temperature. The accuracy and rationality of the temperature were verified by the results of durability experiments, based on which the calculated values of influence factor $\lambda_{\Delta T}$ are close after different aging times.
- (2) A new strength attenuation model with aging time factor was proposed based on the data of previous studies. Experimental data were used to support the new model, and it was shown that the new model can fit the experimental data better than the parabolic-linear model. The new model can also reflect the convergence phenomenon found in the experimental data.
- (3) A coupled model for the strength attenuation of GFRP was obtained based on the single-factor models. According to the coupled model, the degradation curves of the strength of GFRP under 25°C, 50°C, and 75°C were obtained. Despite the abnormal data after 42 days of aging, the experimental data can basically fit the coupled model proposed by the paper.
- (4) According to the coupled model, the concept and calculation method of the slow-aging time point t_i were proposed, which can provide a reference for the evaluation and design of the long-term stability of FRP structures.

Competing Interests

The authors declare that there are no competing interests regarding the publication of this paper.

Acknowledgments

The authors gratefully acknowledge the financial support provided by the China 973 Program (Project no. 2012CB026205) and the Project of Water Conservancy Scientific Research and Technical Extension in Shandong Province (Project no. SDSLKY201407).

References

- [1] Q. R. Yue and Y. X. Yang, "Introduction to durability of concrete strengthened with fiber reinforced polymers," *Journal of Building Structures*, vol. 30, no. 6, pp. 8–15, 2009.
- [2] M. Zhou, *Study on the hydrothermal durability of GFRP and BFRP composites [Ph.D. thesis]*, Harbin Institute of Technology, Harbin, China, 2013.
- [3] B. Sun and Y. Li, "Study on the aging behavior of FRP materials and the prediction of its durability," *Fiber Reinforced Plastics/Composites*, vol. 4, pp. 29–35, 2013.
- [4] Y. H. Zhang, Y. X. Yang, Y. Yao et al., "The durability test and attenuation unified model of FRP performance at hot and humid environment," *Industrial Construction*, vol. 10, pp. 46–50, 2014.
- [5] Y. X. Yang, M. Yang, Y. Zhao et al., "Experimental study on durability of BFRP," *Industrial Construction*, vol. 6, pp. 11–13, 2007.
- [6] K. Berkettis and D. Tzetzis, "The compression-after-impact strength of woven and non-crimp fabric reinforced composites subjected to long-term water immersion ageing," *Journal of Materials Science*, vol. 45, no. 20, pp. 5611–5623, 2010.
- [7] H. Rahimi, "Environmental durability of materials and bonded joints involving fiber reinforced polymer and concrete," in *Proceedings of the 1st Conference on Application of FRP Composites in Construction and Rehabilitation of Structures*, pp. 76–80, 2004.
- [8] G. Xian, H. Li, and X. Su, "Effects of immersion and sustained bending on water absorption and thermomechanical properties of ultraviolet cured glass fiber-reinforced acrylate polymer composites," *Journal of Composite Materials*, vol. 47, no. 18, pp. 2275–2285, 2013.
- [9] A. R. Hutchinson and L. C. Hollaway, *Environmental Durability Strengthening Concrete Structures with Bonding Fiber-Reinforced Composites*, Wood Head Publishing, 1999.
- [10] M. J. He, W. X. Chen, and X. X. Dong, *Polymer Physics*, Fudan University Press, Shanghai, China, 2000.
- [11] G. M. Gunyaev, E. N. Kablov, and V. M. Aleksashin, "Modification of construction carbon-reinforced plastics with carbon nanoparticles," *Russian Journal of General Chemistry*, vol. 81, no. 5, pp. 970–977, 2011.
- [12] C. H. Guo, *Evaluation study on FRP mechanical properties and durability of FRP reinforced concrete [Ph.D. thesis]*, Central Research Institute of building and Construction CO. LTD, MCC Group, 2006.
- [13] S. Li, H. T. Ren, C. K. Huang, and M. H. Shi, "Durability research of FRP sheet under temperature and alkali factor," *Journal of Building Structures*, no. 1, pp. 94–99, 2010.
- [14] Z.-S. Guo, J. Feng, H. Wang, H. Hu, and J. Zhang, "A new temperature-dependent modulus model of glass/epoxy composite at elevated temperatures," *Journal of Composite Materials*, vol. 47, no. 26, pp. 3303–3310, 2013.
- [15] I. Nishizaki and S. Meiarashi, "Long-term deterioration of GFRP in water and moist environment," *Journal of Composites for Construction*, vol. 6, no. 1, pp. 21–27, 2002.
- [16] A. S. M. Kamal and M. Boulfiza, "Durability of GFRP rebars in simulated concrete solutions under accelerated aging conditions," *Journal of Composites for Construction*, vol. 15, no. 4, pp. 473–481, 2011.
- [17] F. Ellyin and C. Rohrbacher, "Effect of aqueous environment and temperature on glass-fibre epoxy resin composites," *Journal of Reinforced Plastics and Composites*, vol. 19, no. 17, pp. 1405–1427, 2000.
- [18] M. Robert and A. Fam, "Long-term performance of GFRP tubes filled with concrete and subjected to salt solution," *Journal of Composites for Construction*, vol. 16, no. 2, pp. 217–224, 2012.
- [19] W. C. Xue and K. Fu, "Experimental research on mechanical behaviors of GFRP bridge decks under alkaline solution," *Journal of Reinforced Plastics and Composites*, vol. 32, no. 23, pp. 1835–1841, 2013.
- [20] X. Jiang, H. Kolstein, F. Bijlaard, and X. Qiang, "Effects of hygrothermal aging on glass-fibre reinforced polymer laminates and adhesive of FRP composite bridge: moisture diffusion characteristics," *Composites Part A: Applied Science and Manufacturing*, vol. 57, pp. 49–58, 2014.
- [21] H.-C. Wu and A. Yan, "Durability simulation of FRP bridge decks subject to weathering," *Composites Part B: Engineering*, vol. 51, pp. 162–168, 2013.
- [22] M. Kotani, Y. Yasufuku, Y. Tamaishi, and H. Kawada, "Study of strength degradation mechanism of woven GFRP in water environment," *Journal of Solid Mechanics and Materials Engineering*, vol. 4, no. 11, pp. 1574–1584, 2010.

Research Article

Investigation of Mechanical Properties of Basalt Particle-Filled SMC Composites

Kadir Cavdar¹ and Mahmut Bingol^{2,3}

¹Mechanical Engineering Department, Uludağ University, Gorukle, 16059 Bursa, Turkey

²Mechanical Engineering Department, Institute of Science, Uludağ University, Gorukle, 16059 Bursa, Turkey

³Vocational School of Yalova, Yalova University, 77100 Yalova, Turkey

Correspondence should be addressed to Kadir Cavdar; cavdar@uludag.edu.tr

Received 9 June 2016; Revised 5 August 2016; Accepted 18 August 2016

Academic Editor: Jun Deng

Copyright © 2016 K. Cavdar and M. Bingol. This is an open access article distributed under the Creative Commons Attribution License, which permits unrestricted use, distribution, and reproduction in any medium, provided the original work is properly cited.

Basalt particles have been investigated as a novel additive for the production of glass fibre reinforced composite using sheet moulding compound (SMC) method. Compared to the CaCO_3 that are widely used as filler in the SMC composite, the resulting composites exhibit improved mechanical properties. The tensile strength increased by approximately 15%, whereas the flexural strength was enhanced by 8% in SMC composites prepared by basalt particles. Examination of the surface morphology and interfacial debonding of the specimens is also performed via scanning electron microscopy. Superior strength properties are observed in the basalt particle-reinforced composites compared to those with the CaCO_3 fillers.

1. Introduction

Polymer composites are composed of an inorganic reinforcement and a polymeric matrix, providing the desired combination of mechanical, chemical, and thermal resistance features. Due to its distinct advantages such as design flexibility, dimensional stability, consolidation of parts, high strength, light weight, moderate tooling and finishing costs, and corrosion resistance, sheet moulding compound (SMC) is one of the widely used composite preparation methods. The SMC method is a sheet of ready-to-mould composites containing uncured thermosetting resins and uniformly distributed short fibres and fillers. Commonly, glass fibre is used as a reinforcement material and unsaturated polyester as a matrix, along with various fillers and additives in the prepreg formulation. Calcium carbonate (CaCO_3) is cheap and easily available filler and thus is the most widely used filler in the composite preparation. Due to its high surface energy, the CaCO_3 reduces mechanical properties of the composite materials [1].

Basalt is a rigid, hard, and durable volcanic mineral which is dark grey or black in colour. It consists of approximately 50% SiO_2 basalt and originated from the solidification of hot magma flows rising from volcanoes or cracks in the earth's

crust. Recently, basalt fibre is used as an alternative reinforcement material, which exhibits exceptional characteristics and mechanical properties compared to those of glass fibres. Basalt-polymer materials are primarily used in building construction, and then they began to be employed in the automobile, machine, and aerospace industries as a replacement for traditional glass and carbon fibre reinforcements [2–5]. Moreover the basalt fibre is fire resistant and forms insulation against sound and heat and thus presents a more economical alternative to the carbon fibre. For instance, the chopped basalt fibre can also be mixed with cement to provide both lower weight and higher structural strength [6–8]. Similarly, basalt particles have also been used as fillers for polymer composites. An important feature of the basalt particle is its suitability for the moulding process. By adding basalt particles at a specific rate into the polymer matrix the corresponding composites were produced via moulding. The various properties of these materials involving wear, mechanical properties, and chemical resistance are remarkably enhanced and no bubbles or pores were observed in the structure [9, 10].

A novel strategy has been developed to improve the fibre reinforced composite properties by introduction of additional particles in the polymer matrix. For example, the

TABLE 1: Chemical compositions of basalt particle [12].

| Compound | Weight percentage in basalt (%) |
|--------------------------------|---------------------------------|
| SiO ₂ | 51.6–57.5 |
| Al ₂ O ₃ | 16.9–18.2 |
| CaO | 5.2–7.8 |
| MgO | 1.3–3.7 |
| Na ₂ O | 2.5–6.4 |
| K ₂ O | 0.8–4.5 |
| Fe ₂ O ₃ | 4.0–9.5 |

mechanical properties of carbon fibre reinforced epoxy composites have been enhanced by the addition of graphene nanoparticles, which enhance the interface mechanics via chemical bonding [11]. In another study, Ary Subagia et al. examined the effect of different tourmaline micro/nanoparticle fillers in basalt fibre reinforced epoxy composites produced via vacuum-assisted resin transfer moulding. With the addition of the particles, the composites gained increased tensile and flexural properties [2].

In this study, a comparative study for the SMC composites prepared with glass fibre reinforced composite containing either CaCO₃ or basalt particles has been reported based on their microstructure and mechanical properties. The composites produced from basalt particles had better mechanical properties compared with CaCO₃ particle-reinforced SMC composites. The mechanical properties of the specimens are investigated in accordance with the standard tests. The surface morphology of the specimens is examined in more detail via scanning electron microscopy.

2. Materials and Methods

2.1. Materials. The basalt particle is purchased from Basaltex (Masureel Group, Belgium) and its chemical composition is given in Table 1.

The E-glass fibre with bundle diameters of 15 μ m is provided by Cam Elyaf A.S. (SMC3-2400) and cut into 65 mm length and added into resin randomly at a concentration of 20% by weight. For the unsaturated polyester resin, Polipol™ 347-BMC-SMC (Poliya, Istanbul, Turkey) is used in the experiments, and the resin properties are given in Table 2.

2.2. Preparation of SMC Composites. The SMC composites are produced in two steps. In the first step, the prepreg formulation is prepared according to a given formulation (Table 3) and is incubated for a maturation period (Figure 1). This time period plays a vital role in the bonding between the resin and the fibre. Hence, this bonding also affects the mechanical properties of the composite material.

In the second step, the SMC plates were retained in a specially prepared 140 \times 280 mm² sheet mould at temperatures of 140–150°C under the effect of 80-bar constant pressure for about 4 min (Figure 2).

2.3. Characterization. A diamond saw is used to cut the manufactured plates and the specimens are prepared according to ISO527 and ISO178, respectively, for tensile and

TABLE 2: Polyester resin properties.

| Property | Value |
|---------------------|--------------------------|
| Density | 1.118 gr/cm ³ |
| Tensile strength | 52 MPa |
| Flexural strength | 117 MPa |
| Elongation at break | 3.86% |

TABLE 3: The formulation of SMC prepreg.

| Compound | Weight percentage (%) |
|--------------------------------------|-----------------------|
| Unsaturated polyester | 36 |
| Thermoplastic resin | 10 |
| Polymerization catalyst | 0.5 |
| CaCO ₃ or basalt particle | 30 |
| Glass fibre SMC3-2400 (65 mm) | 20 |
| Other additives | 3.5 |
| Total | 100 |

flexural strength tests. The tensile tests are performed with the Shimadzu-AG-I machine at a speed of 5 mm/min and the flexural tests are done using the Zwick-1446 machine (Figure 3) at 2 mm/min.

The morphological features of the broken composite surfaces obtained from the tensile and flexural tests are characterized by SEM (Carl Zeiss EVO 40) with accelerating voltage of 20 kV. The specimen surfaces are coated with gold palladium and observed under reduced pressure.

3. Results and Discussion

The strength of the composite materials is directly related to the interfacial mechanics between matrix and fibre. The interface strength increases the composite material strength. In recent years, some attempts have been made to improve these chemical and mechanical bonds. The particle additives are usually aimed at reducing the cost, but the chemical and physical properties of composite materials featuring particles produced with additives are also improved. Basalt fillers are used in road construction and, in mineral form, for heat and sound insulation. As a reinforcing filler material, it is used in composites where improved mechanical properties are desired. Moreover, it is also used to improve wear and corrosion resistance. In this study, the specimens were produced with basalt particles instead of the commonly used CaCO₃ filler and the mechanical properties of these new composite materials were investigated. The specimens were broken using testing equipment according to standard procedures, as shown in Figure 4.

Generally, glass fibre provides the greatest strength when used as the reinforcement material in SMC composites, whereas the CaCO₃ fillers are useful to tune the paste viscosity and reduce the cost. The main purpose of this study is to improve the mechanical properties of SMC composites through the improvement of matrix properties by the addition of basalt particles instead of CaCO₃ fillers. The replacement of CaCO₃ fillers with basalt particles brings



FIGURE 1: Prepreg formulations containing (a) CaCO₃ and (b) basalt particles.

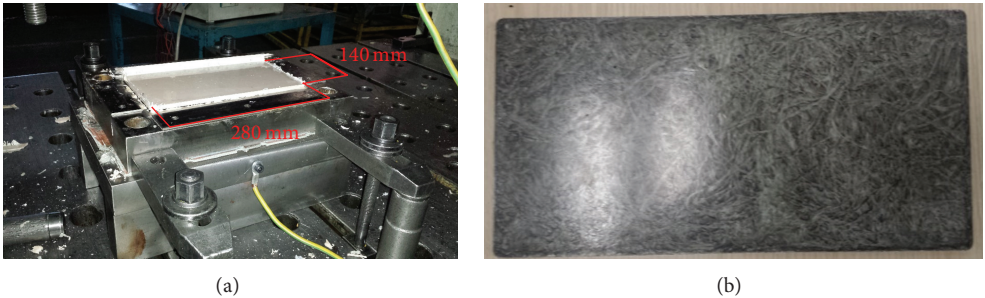


FIGURE 2: (a) SMC plate containing CaCO₃ filler in the mould and (b) SMC plate containing basalt filler.

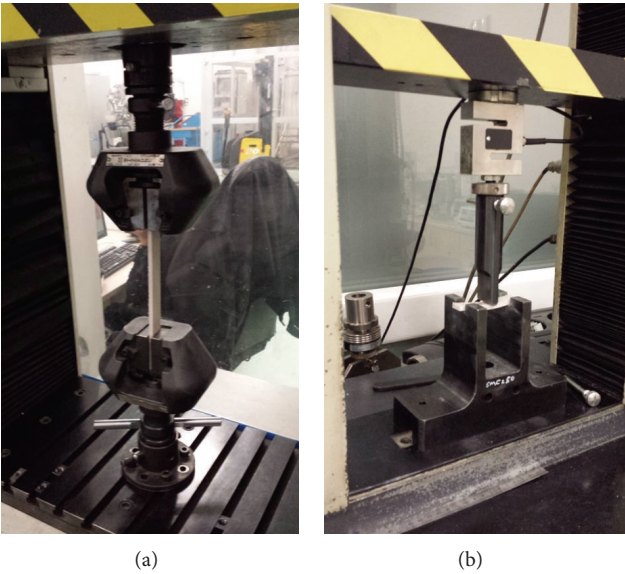


FIGURE 3: The specimens fixed the testing device (a) tensile and (b) flexural tests.

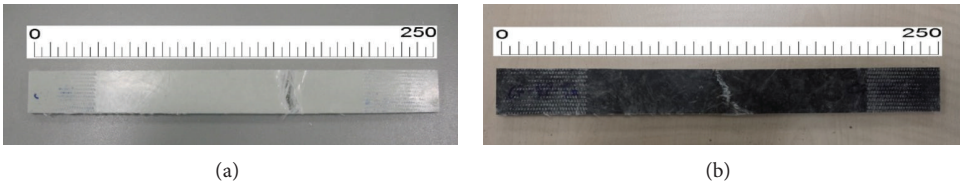


FIGURE 4: Broken test specimens, (a) filled with CaCO₃ and (b) filled with basalt particles.

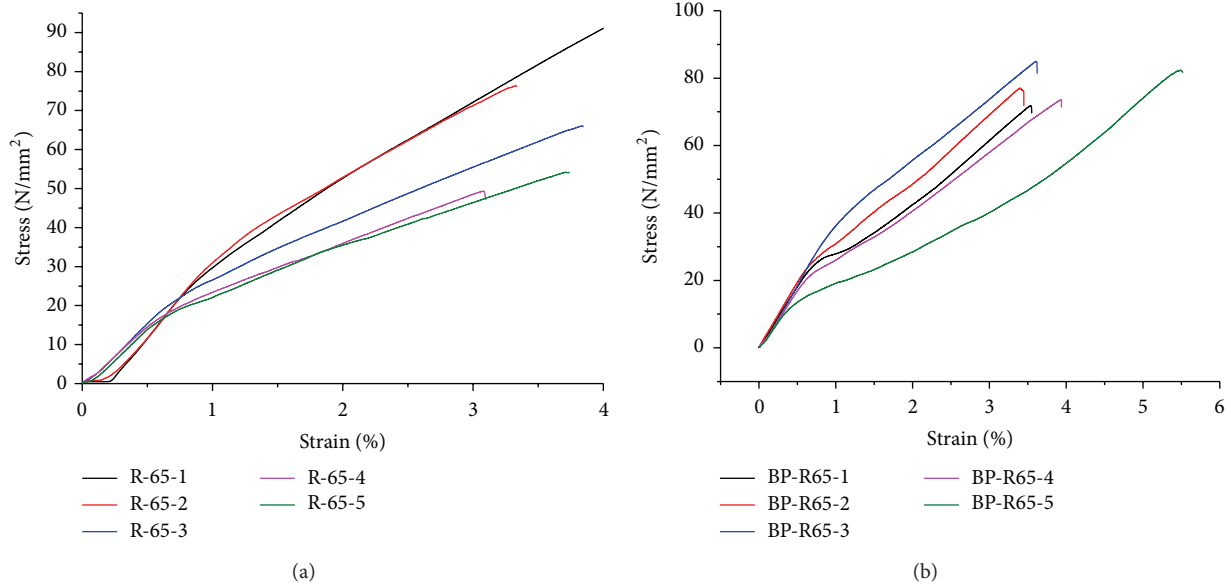


FIGURE 5: Tensile strength values of composite materials filled with CaCO₃ (a) and basalt particles (b).

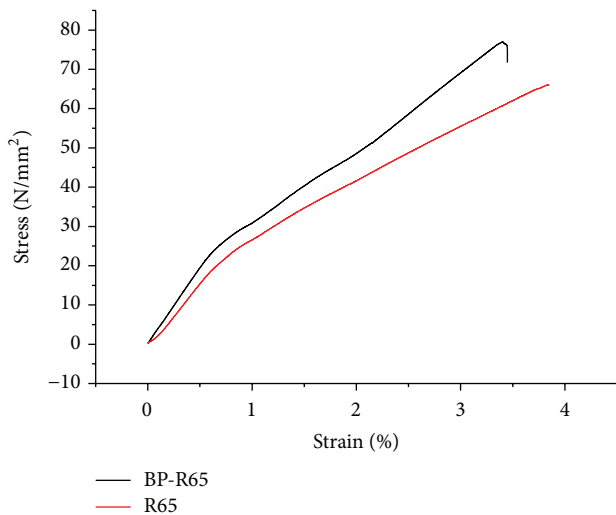


FIGURE 6: Sample tensile strength values of a specimen.

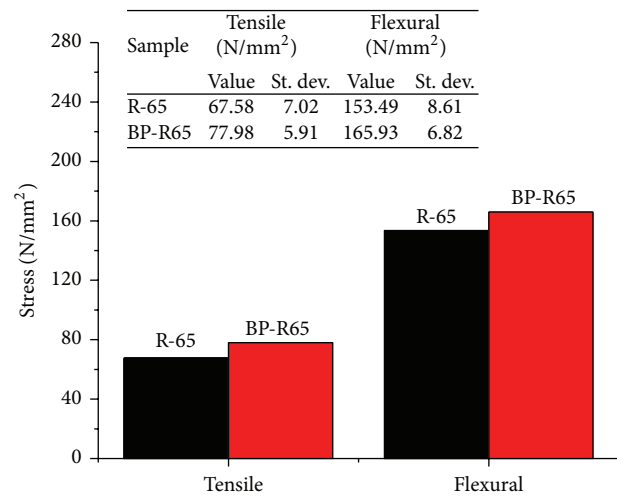


FIGURE 7: The average values for tensile and flexural strength values of R-65 and BP-R65 test specimens.

many outstanding features such as being fire resistant, explosion-proof, and nontoxic and not reacting with the air or water in the matrix. Both tensile and flexural tests confirmed that the SMC composite prepared by basalt fillers has better mechanical properties compared to the composite containing CaCO₃ fillers. Without changing the reinforcement material (glass fibre), this increase in the mechanical properties by simple matrix modification is a significant finding. The tensile and flexural test results can be found in Figures 5 and 6. The tensile strength increased by approximately 15%, whereas the flexural strength was enhanced by 8% (Figure 7).

In the literature, the failure mechanism of composite materials is usually explained in three stages. In the first stage, microcracks are formed in the matrix, followed by fibre-matrix debonding and interfacial decohesion and eventually

by fibre breakage [13–17]. In our case, the basalt particles not only prevent the microcracks of the final composites but also improve the cohesion between glass fibre and matrix; thus the mechanical properties of SMC composites are significantly enhanced. The average tensile and flexural strength values obtained with samples using CaCO₃ and basalt fillers are given in Figure 7. This graphic shows that an increment trend in both tensile and flexural stress is obtained.

The morphology of SMC composites is also investigated by SEM equipment using fracture surfaces of the tensile and flexural specimens. In the CaCO₃ filled SMC composite, it can be observed enveloping the fibre surface in Figure 8 and reducing the interfacial strength between the fibre and matrix. Due to insufficient interface strength, the pull-out of

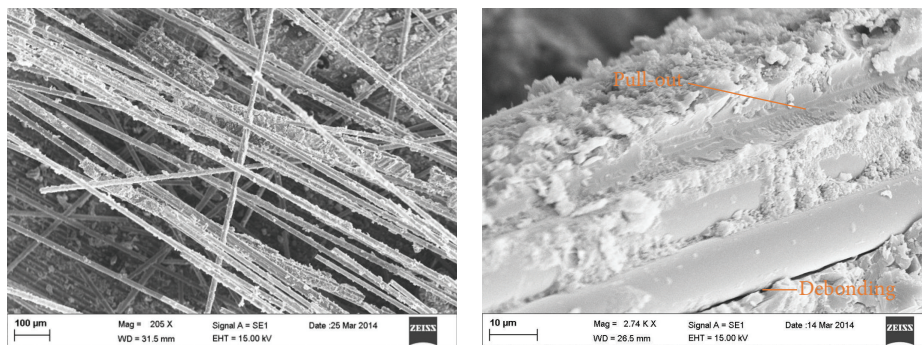


FIGURE 8: The SEM images of the SMC composite filled with CaCO_3 .

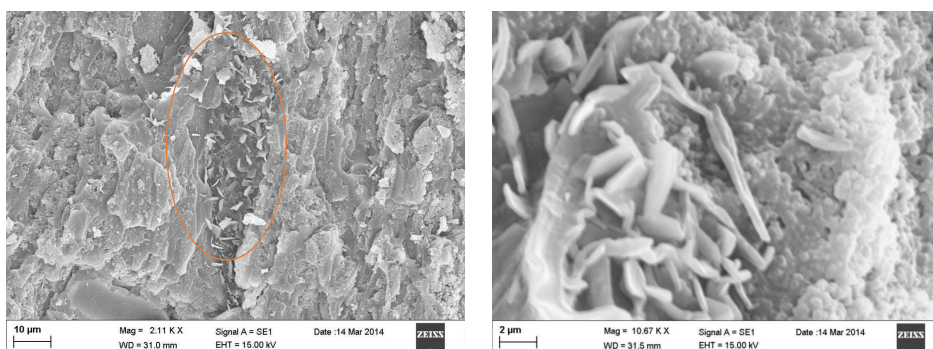


FIGURE 9: The SEM images of SMC composite filled with basalt particles.

glass fibre easily occurred in the matrix. Consequently, the interfacial debonding results in a decrease in both tensile and flexural strengths.

On the other hand, in the case of basalt particle-reinforced composite, the basalt particles help to hold the glass fibre together with matrix in the composite (Figure 9). Thus, the formation of microcracks in the matrix particles has been relatively delayed in the first stage of damage. Hence, the mechanical properties of the SMC plates are remarkably improved and the failure mechanism has been deferred.

4. Conclusions

In conclusion, basalt particles as an alternative filler for glass fibre reinforced SMC composite has been investigated. Compared to the CaCO_3 fillers that are generally used in the SMC composite, the basalt particles filled sample exhibits significant improvement on the tensile and flexural strengths. The morphologies of the obtained SMC materials are investigated by SEM analysis. In the CaCO_3 filled composites, fibre pull-out and interfacial debonding more easily occurred due to the high surface energy. This could be responsible for reducing the mechanical properties of the nonpolar matrices. Conversely, the basalt particles hold glass fibre and matrix together and resulted in improved strength properties. In the future studies, the proportion of basalt fillers and new SMC production methods will be examined in order to achieve better mechanical properties.

Competing Interests

The authors declare that there is no conflict of interests regarding the publication of this paper.

Acknowledgments

This paper is based upon work supported by Uludağ University (Research Grant no. UAP(M) 2011-29). The authors are grateful to Dr. Mehmet Atilla Tasdelen from Yalova University Polymer Engineering Department for his valuable contributions.

References

- [1] V. M. Tuan, D. W. Jeong, H. J. Yoon et al., "Using rutile TiO_2 nanoparticles reinforcing high density polyethylene resin," *International Journal of Polymer Science*, vol. 2014, Article ID 758351, 7 pages, 2014.
- [2] I. D. G. Ary Subagia, L. D. Tijing, Y. Kim, C. S. Kim, F. P. Vista IV, and H. K. Shon, "Mechanical performance of multiscale basalt fiber-epoxy laminates containing tourmaline micro/nano particles," *Composites Part B: Engineering*, vol. 58, pp. 611–617, 2014.
- [3] V. Lopresto, C. Leone, and I. De Iorio, "Mechanical characterisation of basalt fibre reinforced plastic," *Composites Part B: Engineering*, vol. 42, no. 4, pp. 717–723, 2011.
- [4] I. D. G. Ary Subagia, Y. Kim, L. D. Tijing, C. S. Kim, and H. K. Shon, "Effect of stacking sequence on the flexural properties

- of hybrid composites reinforced with carbon and basalt fibers,” *Composites Part B: Engineering*, vol. 58, pp. 251–258, 2014.
- [5] D. Asprone, E. Cadoni, F. Iucolano, and A. Prota, “Analysis of the strain-rate behavior of a basalt fiber reinforced natural hydraulic mortar,” *Cement and Concrete Composites*, vol. 53, pp. 52–58, 2014.
- [6] C. Colombo, L. Vergani, and M. Burman, “Static and fatigue characterisation of new basalt fibre reinforced composites,” *Composite Structures*, vol. 94, no. 3, pp. 1165–1174, 2012.
- [7] K. Singha, “A short review on basalt fiber,” *International Journal of Textile Science*, vol. 1, no. 4, pp. 19–28, 2012.
- [8] B. Wei, H. Cao, and S. Song, “Surface modification and characterization of basalt fibers with hybrid sizings,” *Composites Part A: Applied Science and Manufacturing*, vol. 42, no. 1, pp. 22–29, 2011.
- [9] A. Akinci, H. S. Yetgin, S. Yilmaz, and U. Sen, “The variation of pin-on-disc wear properties of particle filled polymer matrix composites with applied loads,” *Journal of Engineering and Natural Sciences*, vol. 27, pp. 129–138, 2009.
- [10] A. Todic, B. Nedeljkovic, D. Cikara, and I. Ristic, “Particulate basalt-polymer composites characteristics investigation,” *Materials & Design*, vol. 32, no. 3, pp. 1677–1683, 2011.
- [11] V. Acar, H. Akbulut, M. Sarikanat, O. M. Seydibeyoglu, Y. Seki, and S. Erden, “Karbon elyaf takviyeli prepreg kompozitlerde arayüzey mekaniğinin karbon nanoyapı katkısıyla iyileştirilmesi,” *Electronic Journal of Machine Technologies*, vol. 10, no. 3, pp. 43–51, 2013.
- [12] <http://www.basaltex.com/files/cms1/basalt-fibres-as-reinforcement-for-composites.ugent.pdf>.
- [13] J. Fitoussi, M. Bocquet, and F. Meraghni, “Effect of the matrix behavior on the damage of ethylene-propylene glass fiber reinforced composite subjected to high strain rate tension,” *Composites Part B: Engineering*, vol. 45, no. 1, pp. 1181–1191, 2013.
- [14] J. Fitoussi, F. Meraghni, Z. Jendli, G. Hug, and D. Baptiste, “Experimental methodology for high strain-rates tensile behaviour analysis of polymer matrix composites,” *Composites Science and Technology*, vol. 65, no. 14, pp. 2174–2188, 2005.
- [15] B.-Z. Huang and L.-J. Zhao, “Bridging and toughening of short fibers in SMC and parametric optimum,” *Composites Part B: Engineering*, vol. 43, no. 8, pp. 3146–3152, 2012.
- [16] R. O. Ochola, K. Marcus, G. N. Nurick, and T. Franz, “Mechanical behaviour of glass and carbon fibre reinforced composites at varying strain rates,” *Composite Structures*, vol. 63, no. 3-4, pp. 455–467, 2004.
- [17] K. Ogi and M. Yamanouchi, “Temperature dependence of flexural strength of a CF-SMC composite,” *Applied Composite Materials*, vol. 18, no. 5, pp. 397–408, 2011.